UNIVERSITÀ DEGLI STUDI DI ROMA "TOR VERGATA"

FACOLTA' DI INGEGNERIA
Dipartimento di Informatica, Sistemi e Produzione

Dottorato di Ricerca in
GEOINFORMAZIONE

XX° CICLO

Design of unconventional antennas for broadband naval communications

Lorenzo Mattioni

Relatore: Prof. Gaetano Marrocco

Coordinatore: Prof. Domenico Solimini

Marzo 2008

…to my parents…

This Ph.D. work was carried on within the framework of a long-term research activity funded by SELEX COMMUNICATIONS, Pomezia, Roma, Italia, concerning the study of new shipborne antennas for the Software Defined Radio technology.

Contents

Introduction

In the telecommunications context, a 'naval platform' is required to exchange information with mobile and fixed station such as other ships, airplanes, helicopters, satellites and ground stations. The operative requirements of a ship, therefore, comprise the capability to transmit/receive over a wide range of frequencies and to establish links at different elevation angles, using for instance Seawave, NVIS (Near Vertical Incidence Skyave), and BLOS (Beyond Line Of Sight) communications. NVIS links are generally used to go beyond an obstacle, such as a mountain or a piece of land, taking advantage of the ionospheric reflection at certain frequencies (typically 2-10 MHz). Moreover, the onboard antennas have to transmit limited levels of power in order to minimize the interferences with receivers and other electronic devices, causing co-location problems [1], and also to safeguard the people onboard. Recent advances in radio technologies and in mobile communication systems are generating a great interest in multiband and broadband antenna systems. The advent of the Software Defined Radio (SDR) technology [2]-[5], having the capability to simultaneously transmit/receive multiple-waveforms, of the same or different type, within the 2 MHz - 2 GHz band, of the Cognitive Radio (CR) [6], and the modern employment of spread-spectrum techniques, such as the frequency hopping, are only some examples of the growing demand for simultaneous operation over multiple-channels. To host multi-channel communications, actual naval systems employ either a multiplicity of narrow-band tunable antennas, or a small set of broadband antennas together with combining networks. In the first case, the most common antennas are whip-types, for communications at the horizon and BLOS, and fan-types antennas or loops for NVIS links [7], [8]. The main drawbacks of having a great number of antennas are the need of large spaces and complicated feeding networks onboard the ship and the increase of interferences among antennas and with the ship superstructures. This issue is particularly critical in the HF band since the size of the superstrucures are comparable with the wavelengths involved. In the other case, broadband antennas like discone, discage, log-periodic or loaded wire radiators [9]-[10] can mitigate the space requirements but require the use of power combiners to generate the multi-channel input signal. Because of the losses introduced by the combining networks, the resulting system efficiency is highly reduced; in particular, efficiency decreases with the increase of channels' number. As a consequence, innovative technological solutions are required to maximize the radiated power in multi-channel radiating systems.

The subject of this Ph.D. thesis deals with the study of design methodologies for broadband and multi-function antennas with application in HF-VHF/UHF naval communications.

The antenna impedance loading technique, that offers a multiplicity of degrees of freedom in the antenna synthesis procedure, is investigated to enlarge the antenna bandwidth and to synthesize the radiation pattern dinamically with frequency. This method can be also useful for antenna size miniaturization and has the advantage that the same antenna may be used in different electromagnetic scenarios by simply tuning the electric parameters of the loads, offering a great operational flexibility.

The concept of structural antenna is then investigated, consisting in the full integration of wire antennas with metallic existing structures such as funnels or big masts in the naval context. Besides to limited space requirements, this strategy offers the advantage to use existing structures as active part of the antenna. The presence of these large conductive bodies, that in general degrade the antenna features, is considered since the design stage and can be exploited to even improve the antenna performances.

Finally, the extension to multi-port structural antennas is considered and two different feeding strategies are investigated, consisting in exciting the antenna ports in incoherent and coherent manner. Since the radiating elements are placed at a close proximity compared with wavelength and are strongly coupled with the surrounding environment, the port-matching becomes a key issue. At this purpose, different design methodologies are proposed, in which the beam shaping and the antenna port matching are simultaneously considered.

Chapter 1 discusses the concept of structural antenna and introduces the physical rationale of the Naval Structural Antennas (NSA), Chapter 2 investigates the main electromagnetic features of different structural antennas by numerical simulations, Chapter 3 focuses on the design of the basic broadband element, denoted as single-feed Naval Structural Antenna, Chapter 4 extends the design to the multi-port NSA, that offers a great flexibility in terms of power handling and radiation pattern reconfigurability. Chapter 5 introduces a modal approach to the investigation of multi-port radiating structures and analyzes the performances of highly coupled circular arrays. Chapter 6 proposes two different methods of constrained radiation pattern synthesis for highly coupled circular arrays, and hence suitable for the NSA. Chapters 7 and 8 concern the shipborne application and the experimental evaluation of the proposed antennas.

Appendix A recalls the concepts of impedance loading, broadbanding and GA optimization, and describes the functionalities of the electromagnetic tool BLADE (Broadband Loaded Antenna DEsigner), parallely developed during my Ph.D. and used to perform all the antenna optimizations here presented.

Chapter 1

Structural antennas

This Chapter discusses the concept of structural antenna and recalls some papers of the 1950's in which the idea of exciting the wings or the fuselage of an aircraft without resorting to external structures was used. At the beginning, a quick review on the methods to obtain a structural antennas is presented, with particular care to the shunt-fed antennas, whose configuration can be associated to the theory of T/Γ-match. Then, the Naval Structural Antennas (*NSA*), obtained as the integration of a funnel-like cylindrical structure with a feeding wire, is introduced.

1.1 Methods to obtain a structural system

In a structural antenna system a significant part of a metallic existing structure is tightly integrated with a main radiator, which generally consists of some feeding wires or notches. If the size of the existing structure, e.g. a mobile platform, is comparable with the wavelength involved, it strongly contributes to the radiated field and to the input impedance, becoming therefore a real portion of the overall radiating system. The idea of exploiting the induced currents flowing on the structure hosting the antennas goes back to the 1950's, particularly in avionic environment [11], [12], [13] and [14]. The authors of these papers tried to overcome the mechanical problem of supporting a wire antenna, either fixed or trailing, onboard an aircraft. Utilization of the aircraft structure as an antenna in the HF band, where the fuselage and wings are comparable to a wavelength, could offer the possibility of reducing parasite drag, or wind resistance, that are very serious problems considering the high speed of an aircraft. In addition, the problems encountered in the use of conventional wire antennas with respect to icing, precipitation static and interference to the coverage of gun turrets in military aircraft would be largely removed by the use of the aicraft structure itself as an antenna. Basically, two methods for accomplishing the whole aircraft excitation without resort to external structures are possible: *electric-type* (high impedance) driving technique, which uses 'caps' or probes' on extremities, and *magnetic-type* (low impedance) driving technique. In the first case (wing-cap or tail-cap antennas [12]) excitation is accomplished by isolating one of the extremities of the aircraft and applying the driven voltage to the isolated portion. Fig.1.1 shows two examples of cap antennas obtained by means of isolating devices and voltage sources placed on the wing or the tail of the aircraft. Current amplitude on the whole structure can be observed at two different HF frequencies. Isolating devices can be obtained by using soft magnetic material layers as discussed in [15], where a voltage gap is created in the middle of an helicopter to use it as a big horizontal dipole.

The second case, in which coupling between the feed antenna and the aircraft structure is accompished magnetically, comprises the use of notch-fed and shunt-fed antennas (Fig.1.2), which electrically penetrate the airframe [11], [13], [16]. These antennas are most effective when located in regions of high current concentration, such as the extremities of a wing, because the strength of their coupling with the aircraft is proportional to the square of the normal mode current which they interrupt [13].

These two kinds of antennas, when they can be used, have a number of structural adavntages over cap-types antennas, and certain electrical advantages also. They require no special lightning protection and eliminate the need for special isolating devices. In the following paragraph the attention will be focused on the shunt-fed antennas. In particular, it will be seen how these antennas can be associated to the concept of T/Γ-*match* configuration [17].

For what concerns the vehicular environment, the concept of structural antenna is adopted in [18]. In the vehicular context, the problems concerning the platform aerodynamics, high-speed and icing are not so critical as in

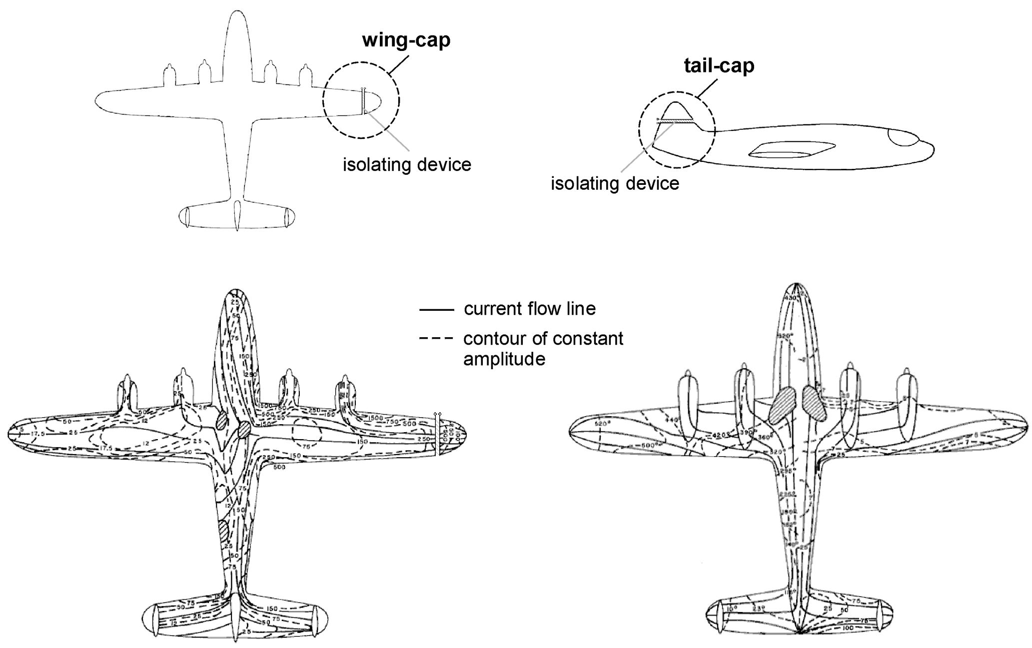

Figure 1.1: *left)* Currents on the aircraft excited by a wing-cap antenna at 11.2 MHz (L=λ). *right)* Currents on the aircraft excited by a tail-cap antenna at 15 MHz.

the avionic environment, however the use of a structural solution can be exploited at low HF frequencies in order to reduce the size of the antennas without compromising their efficiency or to emphasize the radiation along certain directions. Paper [18] presents an approach, based on characteristic modes [19], to the analysis and synthesis of HF antennas on vehicles. As an example, it is shown the possibility to maximize the radiation along the zenith by exciting certain modal currents on the vehicle by means of proper voltage sources (amplitude and phase) arranged *ad-hoc* on the vehicle itself (Fig.1.3).

Presently, structural antennas in naval environment are not so common although the strong interaction between naval superstructures and shipborne antennas has been widely argued in past and recent papers. For instance, the suitable integration of typical HF antennas into the ship's topside structure has been discussed in [7] and optimum performances are achieved by the simultaneous design of antennas and naval structures with the aid of scale

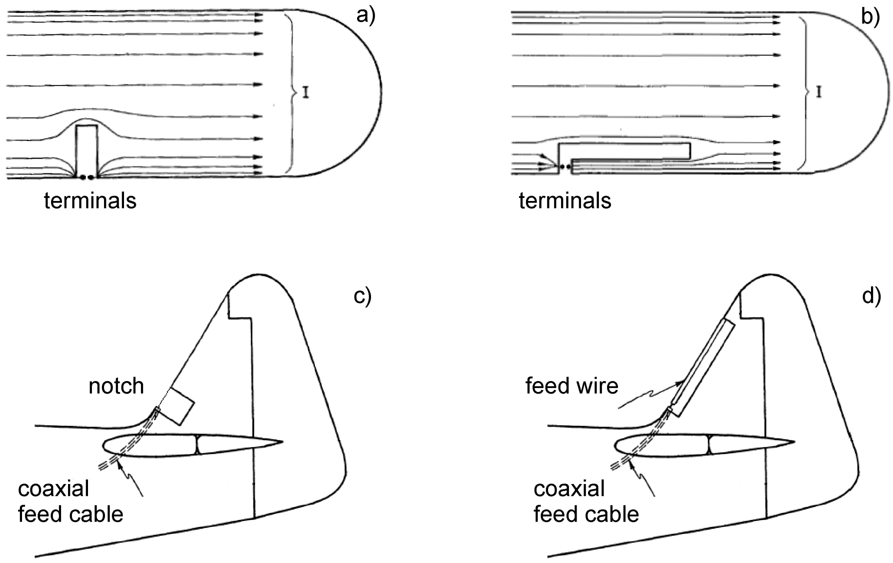

Figure 1.2: *a)* Notch antenna on a wing. *b)* Shunt antenna on a wing. *c)* Notch antenna on the tail. *d)* Shunt antenna on the tail. a) and b) are used to obtain an horizontal polarization, c) and d) for vertical polarization.

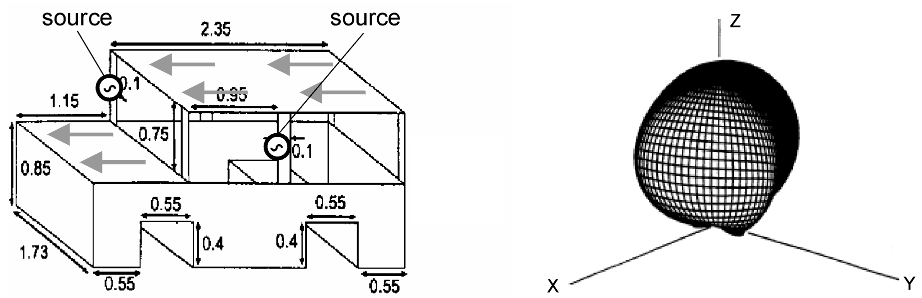

Figure 1.3: Excitation of modal currents on a jeep (dimensions in m) by means of voltage sources on the vehicle itself in order to maximize the radiation along the zenith.

brass models. Radiation pattern distortions of simple HF antennas, when embedded into the naval scenario, have been considered in [20]. Investigation in [21] addresses the possibility to place HF/VHF arrays, whose elements are electrically small loops or dipoles, on the deck, hull and/or gunwale of a ship with the purpose of sectorial coverage. The paper discusses the advantages and disadvantages of mounting these arrays on various parts of the ship on the basis of the electromagnetic performances and the interaction with the sea environment (Fig.1.4).

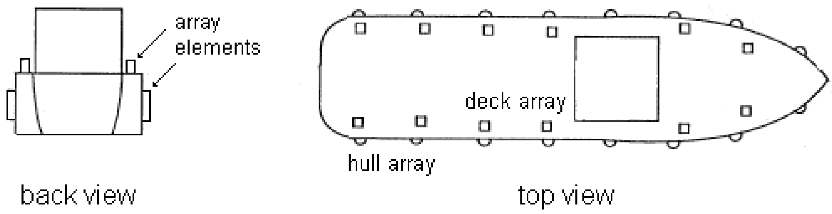

Figure 1.4: HF/VHF arrays on the deck and hull of a ship.

1.1.1 Shunt-fed antennas and the theory of T/Γ-match

The basic concept of a shunt-fed antenna can be directly derived from the theory of a conventional folded dipole or, more in general, from the theory of T/Γ-*match*. A folded dipole (or monopole) is a very thin rectangular loop which serves as a step-up impedance transformer (approximately by a factor of 4 at the first resonance) of the simple dipole (or monopole) impedance. It basically operates as an unbalanced transmission line and can be analyzed by assuming that its current is decomposed into two distinct modes: a transmission line mode and an antenna mode (Fig.1.5).

This analytic model can be used to accurately predict the input impedance [17] at the source terminals. A generalization of the folded dipole is the *T-match* technique, which is used to transform the input impedance of a conventional dipole by acting on a larger number of geometrical degrees of freedom. While in the folded dipole all the wires have the same diameter and parallel wires have the same length, in the T-match configuration the dipole of length l and radius a is connected to a balanced transmission line (such as the 'twin lead') by another dipole of length l' ($l' < l$) and radius a'. Dipoles are separated by a small distance s ($s < 0.05\lambda$) (Fig.1.6a).

As in the case of the folded dipole, the T-match is modeled by transmission line and antenna modes. The total current at the input terminals is divided between the two conductors in a way that depends on the relative radii of the two conductors and the spacing between them. Since the two

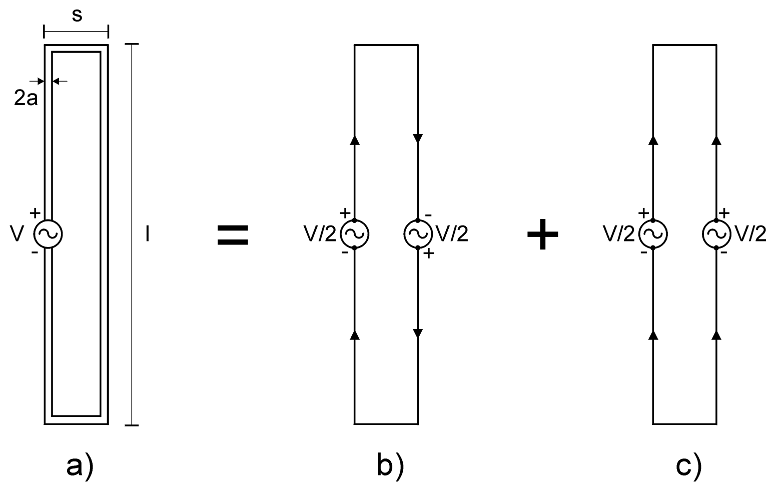

Figure 1.5: *a)* Folded dipole. *b)* Transmission line mode. *c)* Antenna mode.

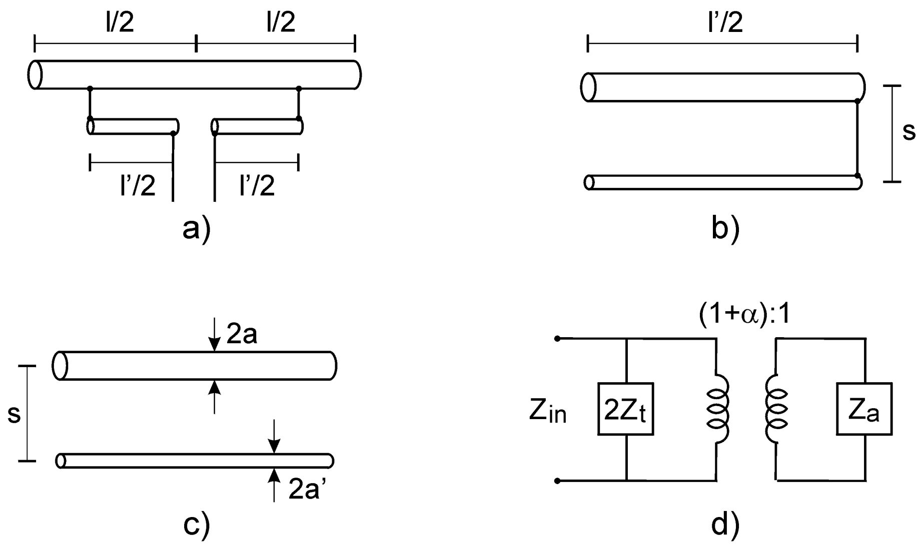

Figure 1.6: *a)* T-match structure. *b)* Shorted transmission line equivalent. *c)* Two-wire transmission line. *d)* Equivalent circuit for T-match.

conductors are not in general of the same radius, the antenna mode current division is not unity. The total input impedance, which is a combination of the antenna (radiating) and the transmission (non-radiating) modes, can be written as [17]

$$Z_{in} = \frac{2Z_t[(1+\alpha)^2 Z_a]}{2Z_t + (1+\alpha)^2 Z_a} \tag{1.1}$$

where Z_a is the center point free-space input impedance of the antenna (with equivalent radius a_e) in the absence of the T-match connection, $Z_t = jZ_0 tan(k\frac{l'}{2})$ is the impedance at the input terminals for the transmission line mode (i.e., two-wire shorted transmission line of length $l'/2$ with radii a, a' and separation s shown in Fig.1.6b), where Z_0 is the characteristic impedance of the two-wire transmission line, and α is the current division factor. An approximation of Z_0, a_e and α as functions of the geometrical parameters a, a' and s is given in [17]. Based on (1.1), the T-match behaves as the equivalent circuit of Fig.1.6d in which the antenna impedance is stepped up by a ratio of $(1+\alpha)$ and it is placed in shunt with twice the impedance of the non-radiating mode (transmission line) to result in the input impedance. It is worth noticing that, when $\alpha = 1$, that is the case of the folded monopole, (1.1) reduces to

$$Z_{in} = \frac{4Z_t Z_a}{2Z_a + Z_t} \tag{1.2}$$

and, if the folded dipole is resonant ($l = \lambda/2$), then $Z_t \to \infty$ and (1.2) becomes $R_{in} = 4R_a$.

Frequently, dipole antennas are fed by coaxial cables which are unbalanced transmission lines. A convenient method to match the dipole or other antennas (Yagi-Uda, log-periodic) to 50Ω or 75Ω is to use the Γ-*match* arrangement shown in Fig.1.7, which can be considered equivalent to half of the T-match [17].

If the original dipole of length l is replaced by a big plate (resembling an aircraft wing) or a large cylinder (resembling an aircraft fuselage), a structural antenna is obtained, whose configuration resembles the T/Γ-match structures.

In [11], a possible arrangement for shunt excitation of an aircraft as an HF antenna is presented. In particular, the feed wires are placed along the leading edge of the wings and at a short distance from them (Fig.1.8a).

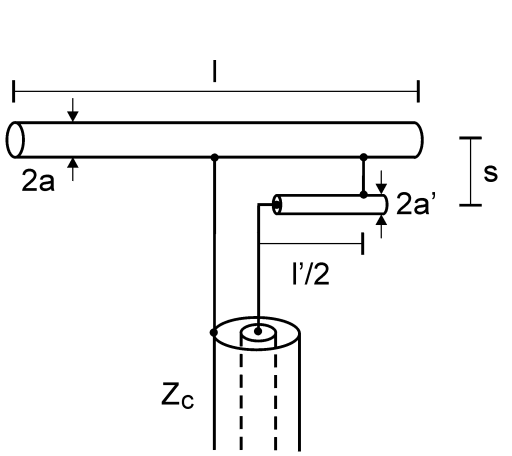

Figure 1.7: Γ-match structure.

The paper experimentally investigates the input resistance and reactance of shunt-excited flat plates for a variety of widths of plate (Fig.1.8b and Fig.1.8c). When $W = 0$, i.e. the plate degenerates in a wire, the conventional curves of resistance and reactance of a folded monopole are obtained. When W increases the curves become smoother, exhibit a smaller dynamics, and the antiresonances become closer. In other words the resulting structure has a broader bandwidth.

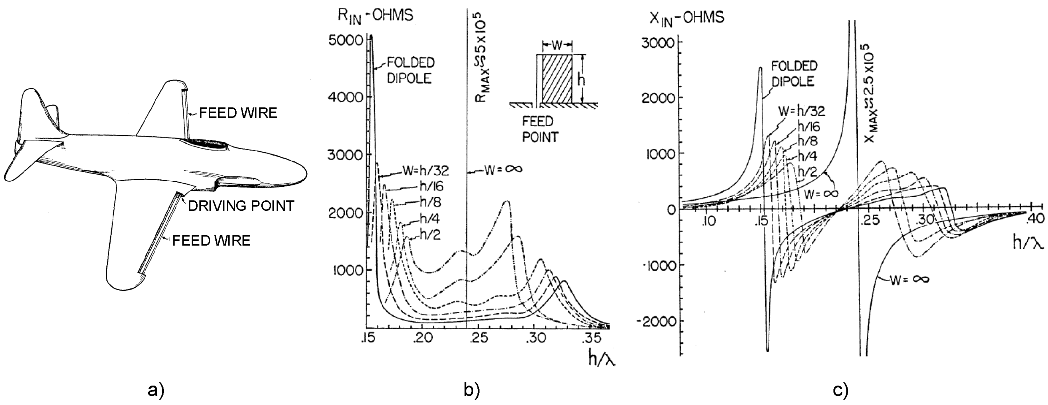

Figure 1.8: *a)* Shunt excitation on wings. *b)* Input resistance of a family of shunt-excited flat-plate dipoles when W is changed. *c)* Input reactance of a family of shunt-excited flat-plate dipoles when W is changed.

In [16], the study of multi-conductor transmission lines (MTL) as HF radiating elements on an aircraft fuselage is carried out. In particular, two parallel rectangular loops of the same length (also known as 'towel bar' antennas) are considered. The paper proposes a semi-analytical model for fast parametric analysis of antenna coupling and interaction with the surrounding environment. A generalization of the Γ/T-match feeding technique is employed and the three-conductor transmission line, originated by the fuselage and the two loops, is analyzed by the superimposition of an antenna mode and two transmission line modes. An equivalent circuit, incorporating transmission line sections, can be derived to perform fast optimization of antenna size and position (Fig.1.9). The influence of the aircraft body is taken into account by global electrical parameter Y_A obtained from a coarse-grid FDTD solution of the aircraft without loops.

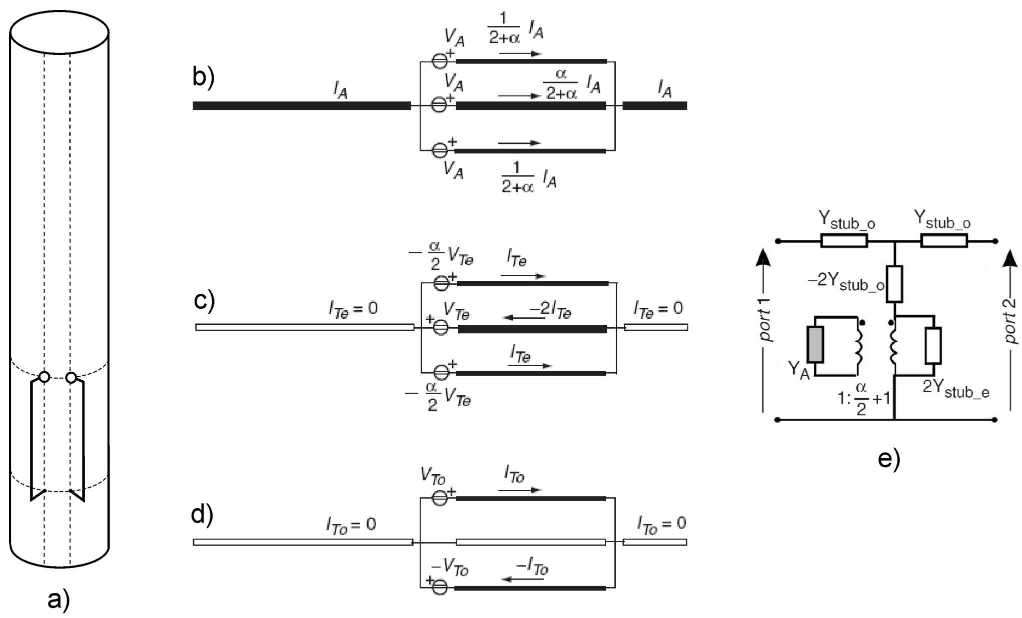

Figure 1.9: *a)* Geometry of the considered structure. *b)* Generalized Γ-match configuration, antenna mode. *c)* Transmission line mode (even excitation). *d)* Transmission line mode (odd excitation). *e)* Equivalent circuit.

1.2 Naval Structural Antenna (NSA): physical rationale

The challenge here introduced consists in turning an existing metallic naval superstructure such as a funnel or a big mast, which are rather common in many ship scenarios, into a Naval Structural Antenna for the HF band. The funnel in particular, has typically cylindrical, pyramidal as well as conical shape, diameter of 5-10 m and height of 10-25 m comparable with HF wavelength. Materials are generally made of aluminium alloys. Starting from a standard folded monopole antenna, which has been already considered as HF radiator in [22], a basic idea to obtain a structural antenna from a cylindrical funnel, for instance, consists in replacing one of the vertical conductors of the antenna with the funnel itself (Fig.1.10). The resulting structure recalls the shunt-fed antennas previously considered or the Γ/T-match configuration.

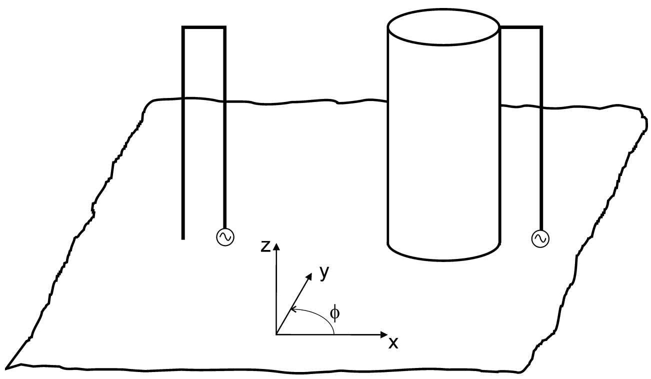

Figure 1.10: Basic idea to obtain a structural antenna from a folded monopole-like structure and a funnel-like cylindrical body.

To illustrate the concept, Fig.1.11 shows the normalized gain of a folded monopole of size $2m \times 10m$ and its combination with a hollow cylindrical body of height $10m$ and diameter $5m$. Results are obtained by means of the Method of Moments (MoM) [23], [24], considering both antennas on an infinite perfect ground plane. The 2 MHz patterns are quite similar: in particular, the structural antenna shows a nearly hemispherical coverage. The uniformity of its directivity at high elevation angles, as well as along the horizon, make this configuration rather attractive as a multi-function antenna in the sense that it combines the possibility to simultaneously provide Seawave and NVIS radiation.

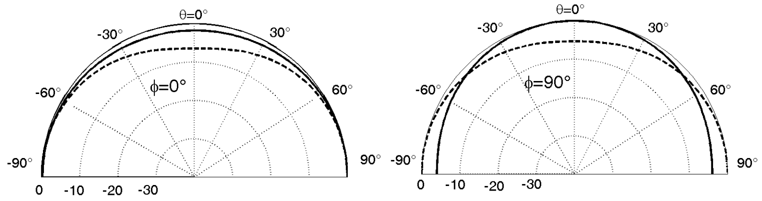

Figure 1.11: Normalized directivity at 2 MHz of the folded monopole (dashed lines) of size $2m \times 10m$ and of the structural antenna (solid lines) in Fig.1.10 including an hollow cylinder of size $5m \times 10m$.

Moreover, Fig.1.12 compares the input reactance of the structures in Fig.1.10. The curve of the structural antenna exhibits a smoother behavior than that of the folded monopole, particularly in the low HF range, and so an easier matching is expected for this antenna by using, for instance, the broadbanding strategy discussed in Appendix A.

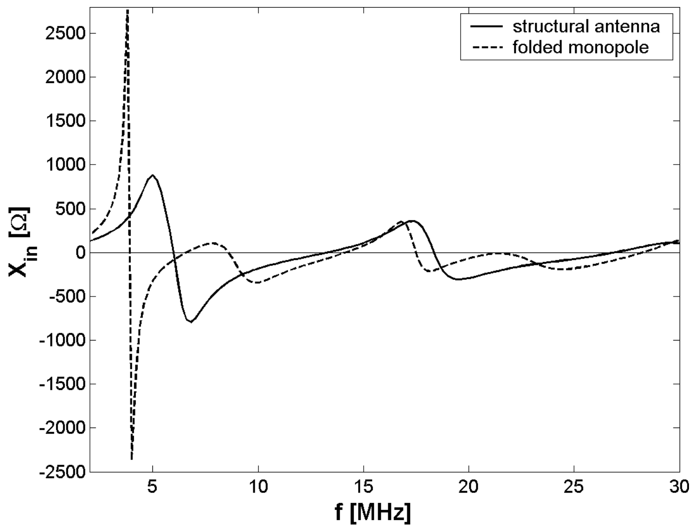

Figure 1.12: Input reactance of the folded monopole of size $2m \times 10m$ and of the structural antenna of size $5m \times 10m$.

Chapter 2

Analysis of structural antennas

In this Chapter the electromagnetic properties of a structural antenna are numerically analyzed in detail. At the beginning, the difference between a non-connected and a connected monopole to a cylindrical body is evaluated in terms of input impedance and radiation pattern. Then, these performances are investigated and compared for different shapes of the central structure.

2.1 Performances of non-structural and structural configurtions

The first comparison was performed by simulating (MoM) the antenna configurations in Fig.2.1 on an infinite perfect ground plane.

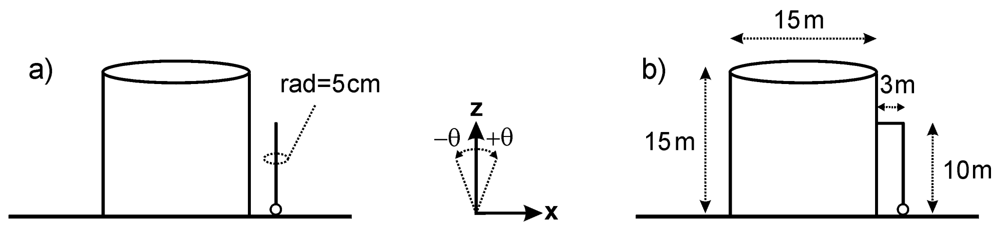

Figure 2.1: *a)* Monopole in front of a cylinder. *b)* Example of structural antenna. In both cases the source is placed alonf $\phi = 0°$.

Configuration b is considered a structural antenna because of the electrical connection between the wire and the cylinder. In this case, currents directly flow from the feeding wire to the cylinder and higher amplitude values can be appreciated on it. Fig.2.2 shows the real and imaginary parts of the input impedance of the configurations in Fig.2.1.

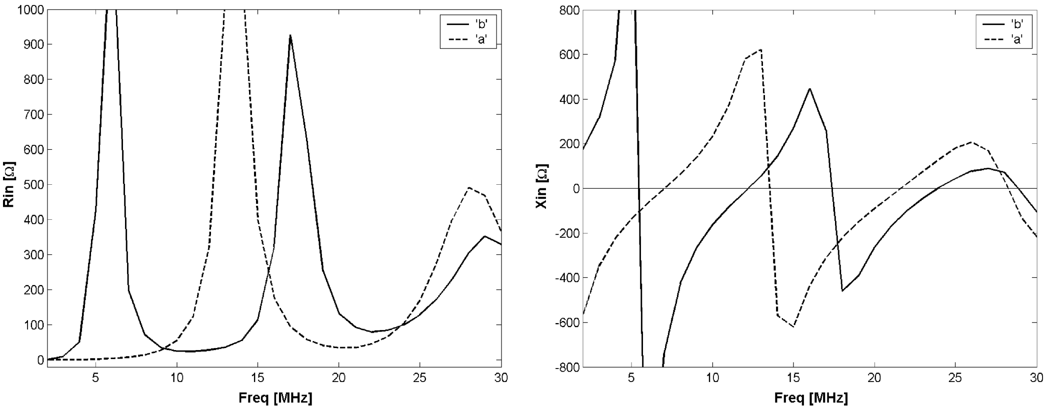

Figure 2.2: Input impedance in the HF band for the two configurations in Fig.2.1.

Configuration *a* has two series resonances in the HF band around 7 MHz and 22 MHz, corresponding to the series resonances of the monopole. At the first one, the input resistance is just 7 Ω and the antenna cannot be easily matched unless a sensible lowering of the efficiency, while at the second one it is about 42 Ω. Configuration *b* has two series resonances around 12 MHz and 24 MHz and the antenna can be matched at both frequencies because the input resistance is enough high (about 30 Ω and 100 Ω, respectively). By assuming the antennas perfectly matched to the characteristic impedance Z_c at each resonance, the values of percentage bandwidth (computed with respect to $|\Gamma|$<-10 dB) are shown in Tab.2.1.

For what concerns the radiation patterns on the horizontal plane, configuration *a* is nearly omnidirectional at 2 MHz, the cylinder behaves as a weak director at 3-4 MHz, and acts as a reflector in the large range 5-21 MHz enforcing the radiation in the monopole direction. In the range 22-30 MHz the horizontal gain approaches to zero and the main lobe is tilted to elevation angles around 30°.

Configuration *b*, instead, retains nearly omnidirectional features in the range 2-10 MHz, the cylinder behaves as a weak director at 11-12 MHz, and

Table 2.1: Percentage bandwidth of the structures a and b at their resonances. Antennas are supposed perfectly matched to the characteristic impedance Zc.

Conf.	**f (MHz)**	**B%**	$\mathbf{Z_c}$ **(Ω)**
a	7	10.1	7
a	21.6	3.8	42
b	12.2	4.0	30
b	23.9	12.5	100

it acts as a reflector in the range 13-22 MHz. In the range 22-30 MHz the behavior is similar to configuration *a*. Fig.2.3 compares the horizontal gain of structures *a* and *b* at some significant frequencies and the omnidirectionality of the structural antenna up to 10 MHz can be observed.

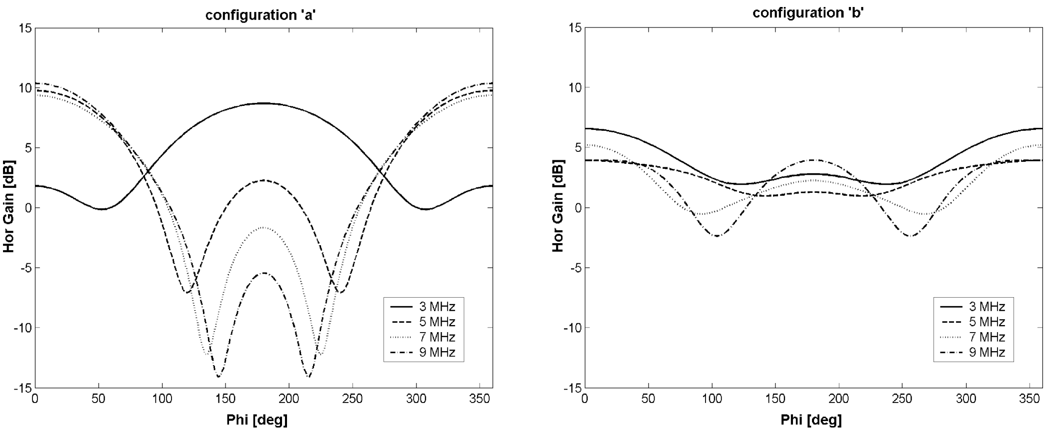

Figure 2.3: Horizontal gain at some significant frequencies for the two configurations in Fig.2.1. *left)* configuration *a*. *right)* configuration *b*.

For what concerns the radiation patterns on the vertical plane, configuration *a* has low gain values (lower than -5 dB) on the zenith in the whole NVIS range 2-10 MHz, substantially due to a monopole-like operation. At the contrary, configuration *b* shows high gain values (higher than 0 dB) on the zenith, as expected from the preliminary study in the last paragraph of previous Chapter. Fig.2.4 compares the vertical gain of the structures *a* and *b* at different frequencies.

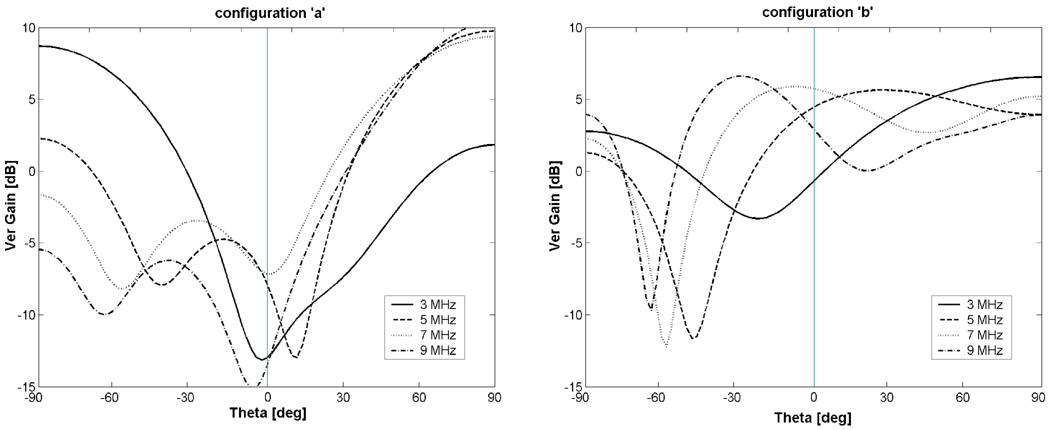

Figure 2.4: Vertical gain at some significant frequencies for the two configurations in Fig.2.1. *left)* configuration *a*. *right)* configuration *b*. The zenith is in $\theta = 0°$.

It has been shown that the structural antenna offers some benefits in terms of input impedance and radiation pattern. Besides an easier matching at two different resonant frequencies, the radiation patterns of the structural antenna exhibit omnidirectional features on the horizontal plane in the range 2–10 MHz; this property can be useful to efficiently shape the pattern of a circular array configuration by a synthesis of the excitations, as discussed in [25]. Moreover, high gain values along the zenith make this kind of antenna particularly suited to NVIS communications at lower HF frequencies.

2.2 Performances with different central structures

This paragraph focuses on the bandwidth performances of an HF structural antenna when the shape of the central conductor is modified. In order to compare the structures in Fig.2.5 only on the basis of their shape, some dimensions are fixed:

- height of the feeding wire: 10 m

- radius of the wires: 0.1 m
- height of the central object: 10 m
- distance of the vertical wire from the vertical axis of the central object: 13 m
- lateral surface of the central object: $\simeq$630 m^2

Four cases are considered in which the central body is a cylinder (c), a cone (d), a frustum of cone (e) and an half-sphere (f).

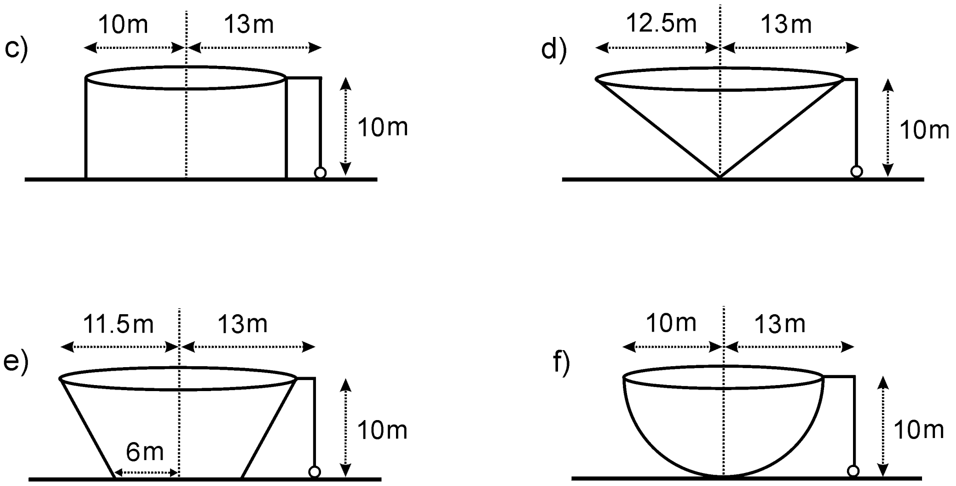

Figure 2.5: Structural antennas obtained for different shapes of the central object.

The input impedance curves of the structural antennas in Fig.2.5 are similar to that of the structural antenna in configuration b. As in the previous case, by assuming the antennas perfectly matched to the source at each resonant frequency, the values of percentage bandwidth are shown in Tab.2.2.

Structure f (half-sphere) seems to be the best among the considered cases. Its resonances are lower than those of the other structures and so, for a given frequency, this is the most compact antenna. Also, this configuration is the best in terms of percentage bandwidth.

By assuming an intermediate value of the characteristic impedance (Z_c = 85 Ω), the half-sphere structural antenna has a dual-band operation as

Table 2.2: Percentage bandwidth of the structures c, d, e and f at their resonances. Antennas are supposed perfectly matched to the characteristic impedance Zc.

Conf.	**f (MHz)**	**B%**	$\mathbf{Z_c}$ **(Ω)**
c	12.2	6.2	38
c	24.4	13.9	115
d	14.9	9.4	41
d	29.2	7.2	71
e	13.4	6.3	46
e	26.8	8.7	77
f	12.1	14.5	69
f	24.2	15.3	109

shown in Fig.2.6. In particular, the percentage bandwidth is about 15.5% around 12.1 MHz and 11.7% around 24.2 MHz.

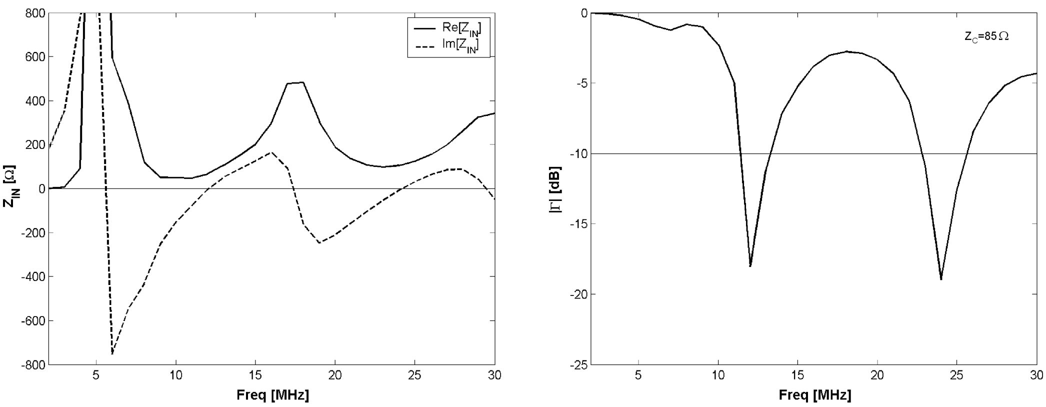

Figure 2.6: Input impedance and reflection coefficient for the configuration *f*.

In order to complete the analysis of configuration *f*, radiation patterns on vertical and horizontal cuts at different frequencies are shown (Fig.2.7 to Fig.2.9) and compared with those of configuration *c* (large cylinder).

The horizontal patterns at low HF frequencies (Fig.2.7) are not so uniform as in the configuration *c*, particularly at 3 MHz and 9 MHz. At higher

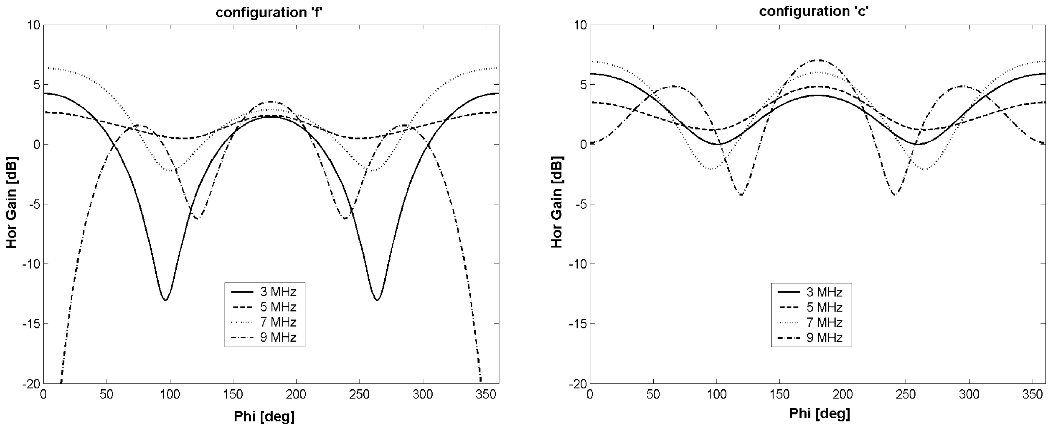

Figure 2.7: Horizontal gain at some frequencies. *left)* configuration *f*. *right)* configuration *c*.

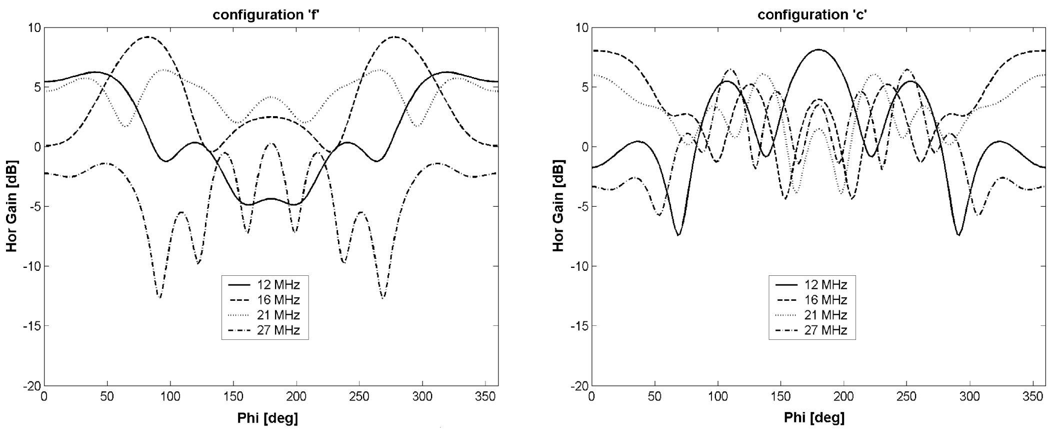

Figure 2.8: Horizontal gain at some frequencies. *left)* configuration *f*. *right)* configuration *c*.

frequencies (Fig.2.8) the horizontal patterns are similar to those of configuration *c* with differences between the maximum and minimum value less than 10-12 dB at each frequency. The vertical patterns (Fig.2.9) are better than those of the configuration *c* with values even higher than 5 dB along the zenith.

It can be observed that the height of the central body does not significantly affect the results (performances of configurations *b* and *c* are comparable). Moreover, it has been verified that simulations with top-closed and

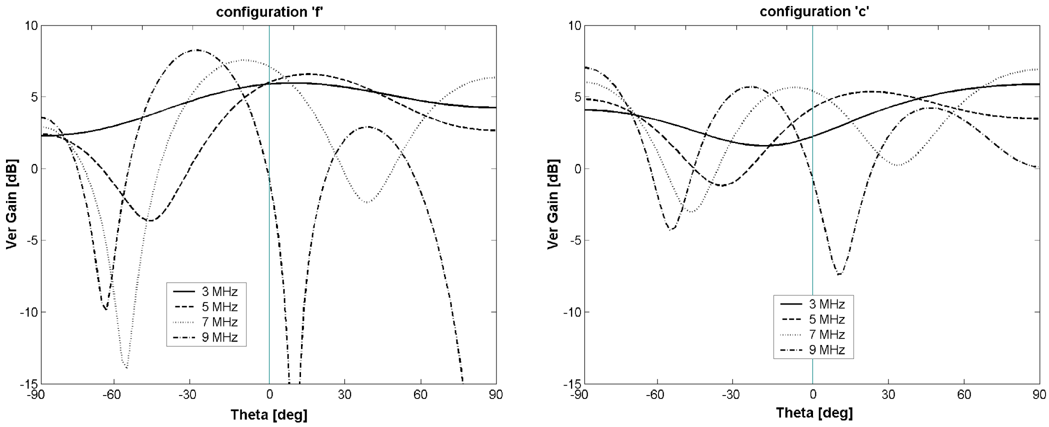

Figure 2.9: Vertical gain at some frequencies. *left)* configuration *f*. *right)* configuration *c*. The zenith is in $\theta = 0°$.

hollow central bodies lead to nearly the same results.

This analysis has shown some interesting properties of structural antennas and how the concept can be extended to different shapes and size of the central structure.

Since it is not so common to find an hemi-spherical structure onboard a ship, an hollow cylinder will be considered in the rest of the treatment.

Moreover, it is worth noticing that the structural antennas up to now considered have typically narrow bandwidths and a proper broadbanding strategy has to be chosen in order to perform broadband naval communications. Impedance loading method is generally employed together with the use of a matching network to achieve broadband wire antennas for the whole HF band. Such a strategy will be adopted in the following Chapters.

Chapter 3

Design of the basic broadband structural element (NSA_1)

This Chapter focuses on the design of the single-feed Naval Structural Antenna or NSA_1. At the beginning, a preparatory study to the NSA_1 is accomplished and, by using the impedance loading method discussed in Appendix A, a stand-alone broadband wire antenna for the whole HF band (2-40 MHz) is designed. This antenna, denoted as *bifolded*, has a simple wire geometry, only requires four lumped loads and an impedance transformer, and exhibits the capability to simultaneously perform Seawave and NVIS links [26], [27].

In order to obtain a structural antenna, the diameter of one of the bifolded vertical conductors is supposed to be enlarged as in Fig.1.10. At this point, the broadband NSA_1 is designed by modifying the wire shape and re-optimizing the antenna loading in order to take into account the presence of the large cylinder, resembling a funnel or a big mast. The resulting structure is a compact structural antenna for HF naval communication having the possibility to communicate at different elevation angles depending on the frequency.

The study of this and the next Chapter, will leave apart from a particular naval realization and will consider a canonical test-case with the purpose to investigate the feasibility and potentials of the naval structural antenna concept. The application to a realistic ship model will be discussed in Chapter 7.

3.1 Bifolded antenna

Bifolded is a new wire antenna of size suitable for naval installation and with multi-mode capabilities, in the sense that it combines the possibility to simultaneously provide Seawave and NVIS links with broadband features. Antenna geometry is obtained starting from a folded monopole and adding some horizontal and vertical wires in order to increase the number of current paths at different frequencies. Lumped impedances are placed on the antenna conductors with the twofold purpose of broadband radiation pattern synthesis and antenna matching (see Appendix A). Unlike conventional RLC trap loading, the proposed strategy involves the placing of isolated resistors, parallel and series LC circuits, by whose combination more complex topologies can be obtained. This strategy permits to minimize the components of the matching network which is practically distributed all over the antenna.

3.1.1 The unloaded bifolded monopole

To achieve multi-mode functionalities, the antenna geometry needs to include the shape of a monopole and that of a half loop for NVIS radiation. Accordingly, the proposed geometry is shown in Fig.3.1.

This is obtained as modification of a simple folded monopole, where the addition of a nested wire improves the space filling of the antenna and permits to create more complex meander paths useful for antenna miniaturization [28]. The expected benefit will be a bandwidth improvement or, from a different point of view, a simpler antenna broadbanding task.

Fig.3.2 shows the input impedance of the unloaded bifolded monopole in comparison with a folded monopole having same sizes, as computed by MoM [23], under the assumption that the antennas are placed on a perfect ground plane. It can be observed that the folded monopole exhibits a short-circuit condition around 12 MHz ($R_{in} \simeq 4\Omega$) corresponding to the loop anti-resonance ($2H + W \simeq \lambda$). Around this frequency it will be rather difficult to match the antenna, even with trap loading, unless a sensible lowering of the efficiency. On the contrary, the bifolded geometry does not show a so huge short-circuit around that frequency and the minimum value of its input resistance occurs around 24 MHz ($R_{in} \simeq 10\Omega$). Moreover, the impedance

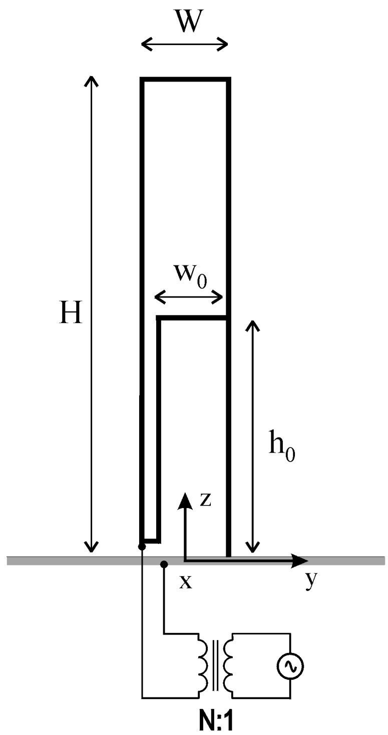

Figure 3.1: Geometry of the *bifolded* monopole over an infinite ground plane. The impedance transformer ratio N will be optimized together with antenna loading. Antenna size: $H = 12m$, $W = 2m$, $h_0 = H/2$, $w_0 = 1.6m$.

curves are less oscillating than that of the folded monopole and it is therefore expected that an easier matching will be possible for the new antenna.

3.1.2 Broadbanding Strategy

To achieve broadband features and a radiation pattern suitable to different kinds of services, the antenna in Fig.3.1 is loaded by means of passive lumped electric devices, which will enforce the most suitable current path at each frequency. Reasonable requirements for a loaded antenna system are VSWR<3 within the whole HF band, antenna efficiency larger than 50%, gain higher than $-20dB$ at NVIS, higher than $-10dB$ along the horizon for $2MHz \leq f \leq 5MHz$ and higher than $2dB$ above 5 MHz. The allowed range of the electric components needs to be properly defined at the purpose to obtain feasible values. In particular, large values of inductance or trans-

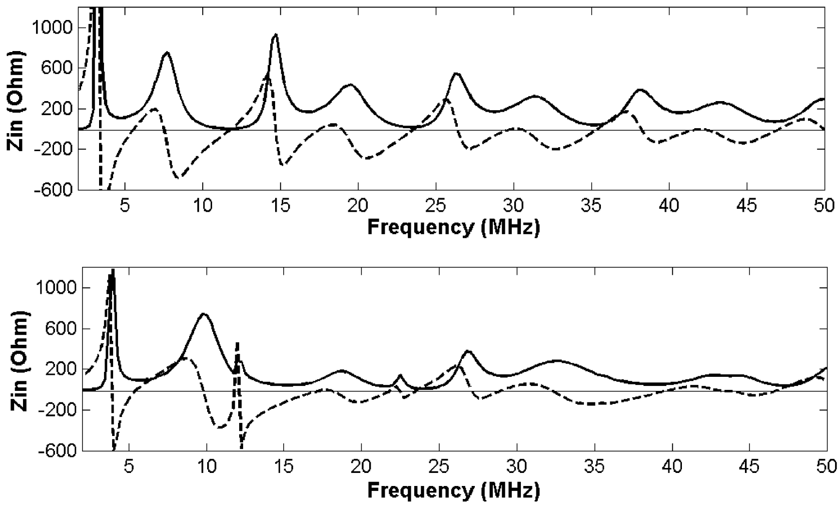

Figure 3.2: Input impedance in the band 2-50 MHz of the unloaded folded monopole (up) and of the new bifolded monopole (down) of size in Fig.3.1. Solid and dashed lines respectively refer to real and imaginary part of the input impedance.

formation ratio involve large coils which can get self-resonating [29] in the upper part of HF band. Concerning the resistor limitations, large resistances could require cooling systems to be distributed along the wires for high power dissipation at low frequencies where the antenna efficiency is small. The parameters' ranges which will be here considered are: $50nH \leq L \leq 3\mu H$, $5pF \leq C \leq 1nF$, $R \leq 100\Omega$. Within these constraints, it has been verified that the above gain and matching requirements can not be achieved, at a same time, by using conventional RLC traps and typical lossless networks [22], [30] plus a frequency-independent attenuator and an impedance transformer. Therefore, a different strategy is here adopted. The matching network only retains an impedance transformer while loading components are distributed along the antenna according to multiple topologies. The basic circuits are the isolated resistor and both the series and the parallel LCs, which can respectively act as short- and open-circuit at their natural frequency. By introducing also individual resistors it is possible to synthesize a proper frequency-dependent attenuator all over the antenna and, since more loading impedances are allowed to share a same position in the wire as series connection, more electrical topologies can be attained.

The optimization of antenna loads (number, topology, position and values) and of the impedance transformer is achieved with respect to the minimization of the following penalty function (see Appendix A) depending on matching, gain and efficiency requirements:

$$F = \frac{1}{N_f} \sum_{n=1}^{N_f} [w_1^{(n)} F_{VSWR}^{(n)} + w_2^{(n)} F_{\eta}^{(n)} + w_3^{(n)} F_{G\theta}^{(n)}] + w_6 F_{traps} \tag{3.1}$$

Here, N_f is the number of frequency samples in the HF band (tagged by index n), $F_{VSWR}^{(n)}$ is a normalized threshold function controlling the matching (VSWR<3), $F_{\eta}^{(n)}$ controls the system efficiency, $F_{G\theta}^{(n)}$ the system gain along the horizon ($\theta = 90°$) and at NVIS angles ($\theta = 20°$). Finally, F_{traps} tries to minimize the number of loading impedances. Details on these functions are given in Appendix B ('Bifolded antenna and NSA$_1$ loading' paragraph). Parameters $w_j^{(n)}$ are frequency-dependent in order to selectively weigh the gain and matching requirements in different parts of the band. For instance, at lower frequencies (2-4 MHz) the weight of matching penalty ($F_{VSWR}^{(n)}$) is more emphasized than that affecting the gain. The Genetic Algorithm (GA) [31], which is a commonly used tool to design loaded antennas, is applied for solving the optimization problem together with MoM for antenna analysis. The evaluation of the features of each population member (i.e. a loaded antenna) is achieved by the fast method described in [30] which requires the inversion of small matrices, of size depending only on the loads' number (Appendix A).

3.1.3 Results

The loading of the bifolded monopole has been optimized having set to 10 the maximum number of loads. Conductors are assumed to be aluminium pipes with diameter of 8.5 cm.

At purpose of comparison, also the folded monopole of same size has been optimized according to the proposed strategy. Fig.3.3 shows the loading topology of the bifolded monopole as found by GA. Four circuits have been required while seven circuits have been necessary for the folded monopole.

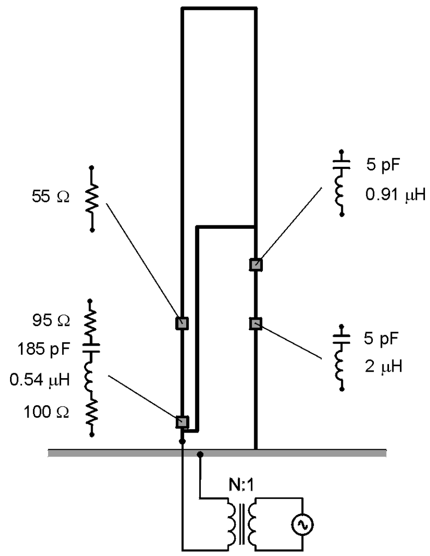

Figure 3.3: Optimized loads for the bifolded monopole. The transformation step-up ratio has been set to 3.4.

Although both the folded and the bifolded antennas are well matched in a band which is even larger than the required HF region, the proposed antenna shows superior performances, as concerns the gain and the efficiency (Fig.3.4). The ϕ-averaged gain of the bifolded is higher and more uniform up to 40 MHz whereas the folded monopole gain drops under 2 dB in many parts of the band. The efficiency of the new antenna is higher than that of the conventional folded monopole in particular for 7 MHz $\leq f \leq$ 15 MHz, i.e. around the sharp short-circuit effect which is present in the input impedance of the unloaded structure as discussed in the previous paragraph. In this case the low efficiency of the folded monopole is the price to pay to have the antenna matched.

By inspection of current patterns of the loaded bifolded monopole (Fig.3.5), it is evident the combination of the different current paths, loop and monopole modes in particular, allowed by the proposed geometry. At 2.5 MHz the equivalent electric monopole current is the difference between currents along segments a and b, while the magnetic dipole results from the current path c, d, e, f. The lower vertical wire, g, connected to ground is isolated by the two high-impedance series LC loads of Fig.3.3 (which resonate at $f = 50.3MHz$

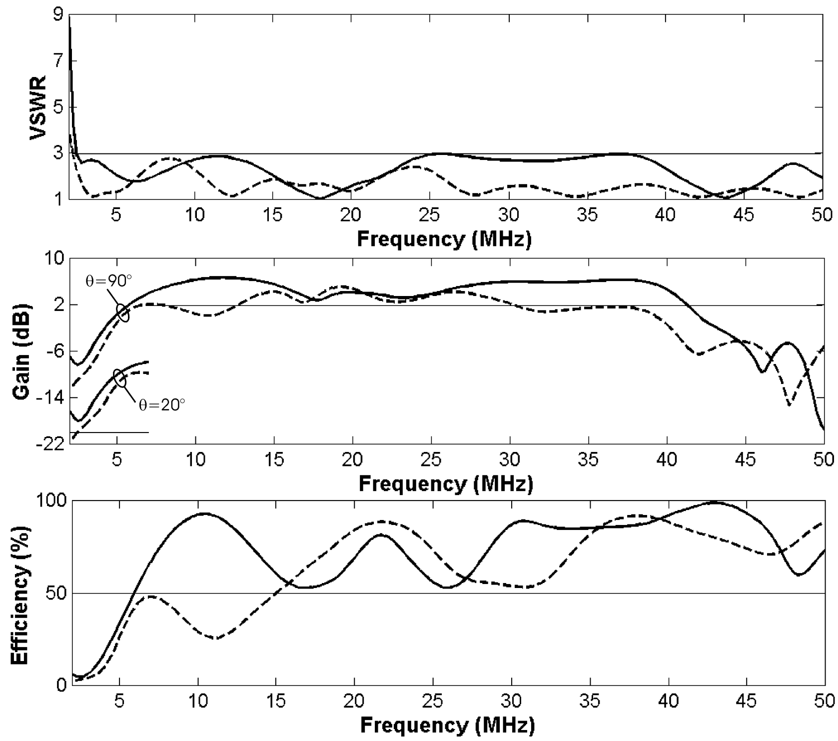

Figure 3.4: ϕ-averaged gain at the horizon and at $\theta = 20°$, and system efficiency after loading optimization in the range 2-50 MHz. Solid lines tag the loaded bifolded monopole with four circuits, while dashed curves are for the reference folded monopole having the same size of the proposed antenna, and loaded with seven circuits.

and $f = 74.6MHz$, respectively) and therefore it does not much contribute to radiation at low frequencies while it is active at higher frequencies. Radiation patterns in Fig.3.6 indicate NVIS gain performances and an almost omnidirectional radiation along the horizon.

A different optimized topology is presented in Fig.3.7 where the loading resistors are constrained to be placed only close to the ground plane: this condition could be useful whenever the antenna has to handle high power and cooling equipments need to be considered. In this case, the electromagnetic requirements previously introduced, are matched by using only three LC circuits on the right vertical conductor, two resistors close to the source and an impedance transformer of value $N = 4$. Due to its simpler practical

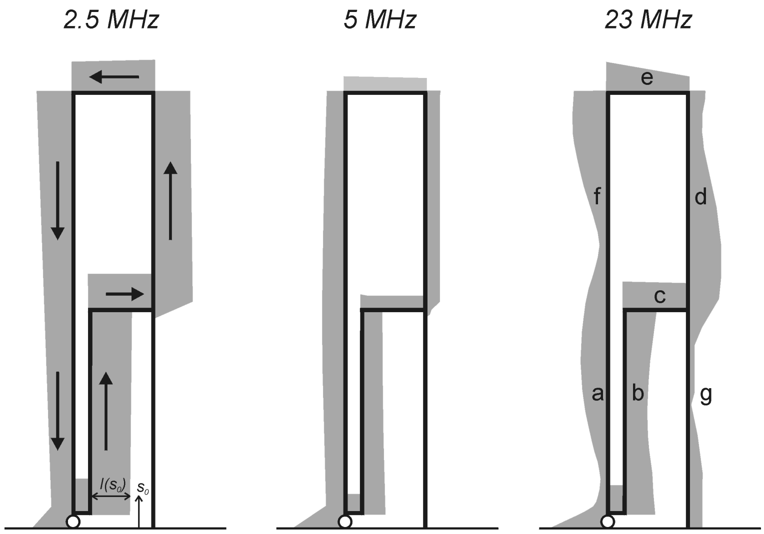

Figure 3.5: Current patterns (amplitude) at some frequencies. Arrows indicate the current direction.

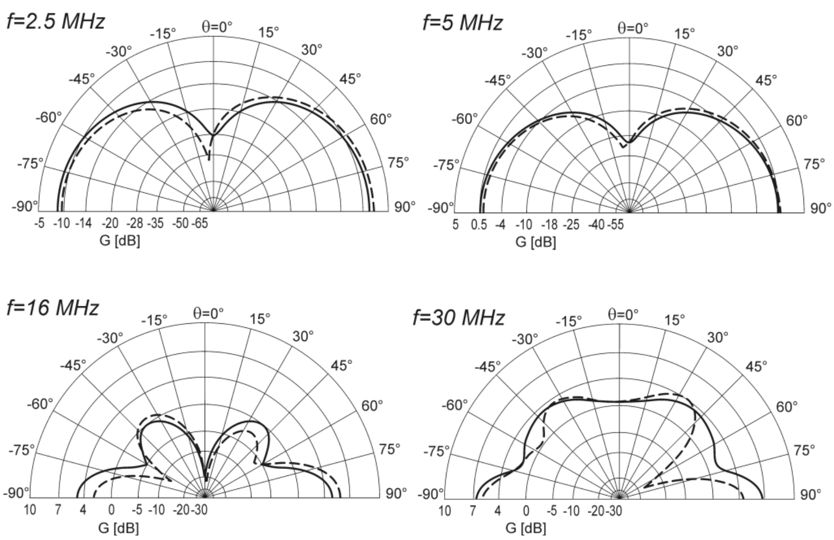

Figure 3.6: Radiation patterns at some frequencies. Solid line: $\phi = 0°$ cut; dashed line $\phi = 90°$ cut.

realization, this configuration of bifolded will be considered hereafter.

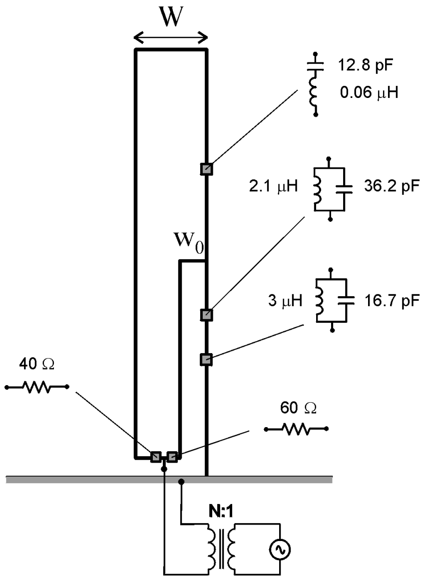

Figure 3.7: Loading topology of the bifolded monopole when resistors are constrained close to the ground plane. The transformation step-up ratio has been set to 4 and $w_0 = (2/5)W$.

3.1.4 Extension to higher frequencies

As stated in the introduction, broadband antennas, though not so common, are also used in naval environments, but their bandwidths are generally less than 10:1. Electrically loaded wire antennas can be used in the HF band while discone and log-periodic radiators typically serve the VHF/UHF ranges. Arrangements of different antennas to obtain a compact broadband radiator, have already been discussed in some papers [32], [33] but these solutions, however, refer to not so wide frequency ranges.

The following two paragraphs describe the extension of the bifolded operational bandwidth to the VHF/UHF bands [34]. This is accomplished by a mechanical and electrical integration of the basic antenna structure with a top-mounted VHF omnidirectional broadband radiator, such as a discone antenna. The novelty of this approach, which can be also applied to other antenna typologiesis, is the feeding strategy, which should minimize the inter-antenna coupling. In this context, the purpose of the integration consists in the design of a broadband system having two separate input ports for the HF and VHF channels, where each sub-antenna retains about the same electromagnetic performances as in the stand-alone configuration. This is a strong challenge, particularly in the HF band, since the VHF feeding cable could strongly interact with the HF antenna and the discone modifies the original bifolded geometry by extending its height. In this perspective, a solution involving the tuning of the HF antenna impedance loading is presented.

Integration strategy

With reference to the bifolded-discone arrangement of Fig.3.8, the new proposed integration requires the VHF feeding cable to run along (or inside) one of the vertical (hollow) conductors of the HF structure, which serves as a mechanical and electrical support.

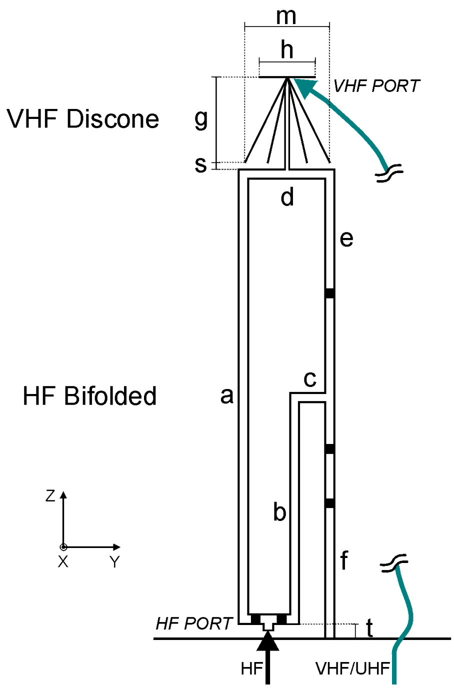

Figure 3.8: Two-ports antenna system obtained by combining the bifolded and the discone radiators. Dimensions (in $[m]$): $a = 12$, $b = 6$, $c = 0.8$, $d = 2$, $e = 6$, $f = 6$, $g = 2.17$, $h = 1.55$, $m = 1.9$, $s = 0.2$, $t = 0.4$. Bifolded pipes diameter $d_b = 0.1$. Discone wires diameter $d_d = 0.004$. Black squares indicate the impedance loads in the bifolded design in Fig.3.7.

Since the HF antenna is loaded by lumped circuits, which interrupt the bifolded, they could prevent the VHF feeding cable to reach the discone. In particular, the bifolded antenna of Fig.3.7 is equipped with three loads on the vertical right conductor ('e' and 'f' wires in Fig.3.8) and no load on the left branch 'a'. The VHF feeding cable cannot run inside the unloaded conductor 'a' because the HF source would be short-circuited. However, the VHF feeding cable may run inside the HF-grounded conductors 'e' and 'f', but the impedance loading of the antenna needs to be modified with the purpose to leave these wires unloaded or, at least, to load them with only parallel LC-type circuits. In the latter case, the required inductance may be obtained by twisting the VHF cable itself (Fig.3.9a).

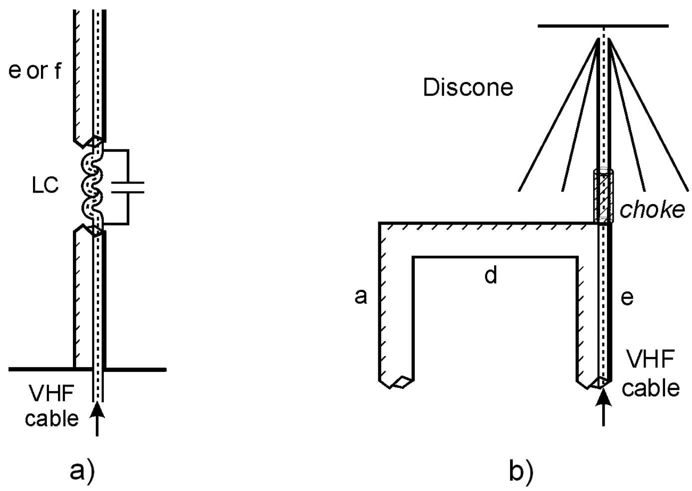

Figure 3.9: a) The inductor of the LC parallel circuit is obtained by twisting the VHF cable itself. b) HF-choke used to suppress the induced currents on the discone antenna.

Performances estimation

For the sake of simplicity, an 8-radials discone is considered. This antenna has a VSWR<3 in the 40-440 MHz range, but the proposed integration can be also applied to different and better performing monopole-like VHF antennas. It has been numerically verified that the inter-antenna isolation improves if the discone is placed far from the HF port, i.e. at the top of the right conductor 'e' (Fig.3.10).

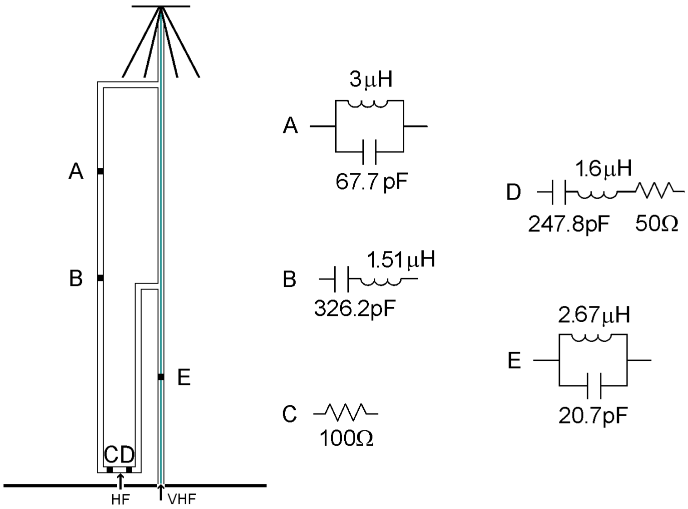

Figure 3.10: Re-optimized bifolded loading configuration. One LC-parallel circuit (tagged by 'E') was selected by the GA on the right vertical conductor. When using a coaxial cable of diameter 5 mm, for instance, the inductance in the circuit 'E' corresponds to a coil of 10 turns, of length 10 cm and diameter 5 cm. The HF transformation step-up ratio was set to 4 as in the previous case.

The tuning of the impedance loads on the HF antenna is achieved by the same GA approach as in the bifolded optimization.

The best re-optimized antenna requires one LC parallel circuit on the conductor 'f' (tagged with 'E' in Fig.3.10), while four circuits are placed on the other branches. The performances in the HF band are shown in Fig.3.11 and compared with those of the stand-alone bifolded.

Because of the induced currents on the discone, a slight degradation of the VSWR and a lowering of the gain occur between 8-20 MHz. This can be avoided by using HF-choke mechanisms (Fig.3.9b), for instance obtained by means of soft magnetic-material layers as suggested in [15].

The VHF antenna behaviour, instead, is substantially independent on the particular HF antenna impedance loading configuration. The discone VSWR and averaged horizontal gain after the integration were computed and compared with those obtained at the same height from the ground plane,

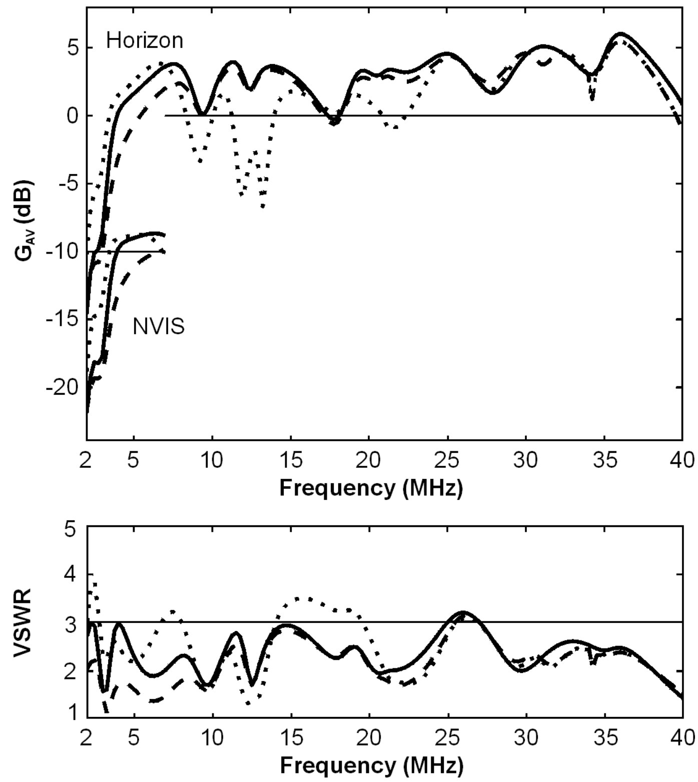

Figure 3.11: *HF performances*: ϕ-averaged gain at horizon ($\theta = 90°$) and NVIS ($\theta = 20°$), and VSWR of the following antenna systems: stand-alone re-optimized bifolded (solid line), un-choked bifolded + discone (dotted line), bifolded + discone and finite impedance model (|Zs|/sq=500 as in [15]) for the HF-choke in Fig.3.9b (dashed line).

without the supporting HF structure. As shown in Fig.3.12, the VHF antenna is well matched in the whole 40-440 MHz frequency range.

The nulls in the gain around 200 MHz and 400 MHz are due to the intrinsic discone anti-resonances rather than to the coupling with the bifolded antenna.

The resulting VSWR of the integrated antenna system is shown in Fig.3.13.

Because of its low VSWR values, the bifolded antenna could be used up to 45 MHz. The normalized radiation patterns on the horizontal plane are represented in Fig.3.14, where a good omnidirectionality can be observed at all the considered frequencies.

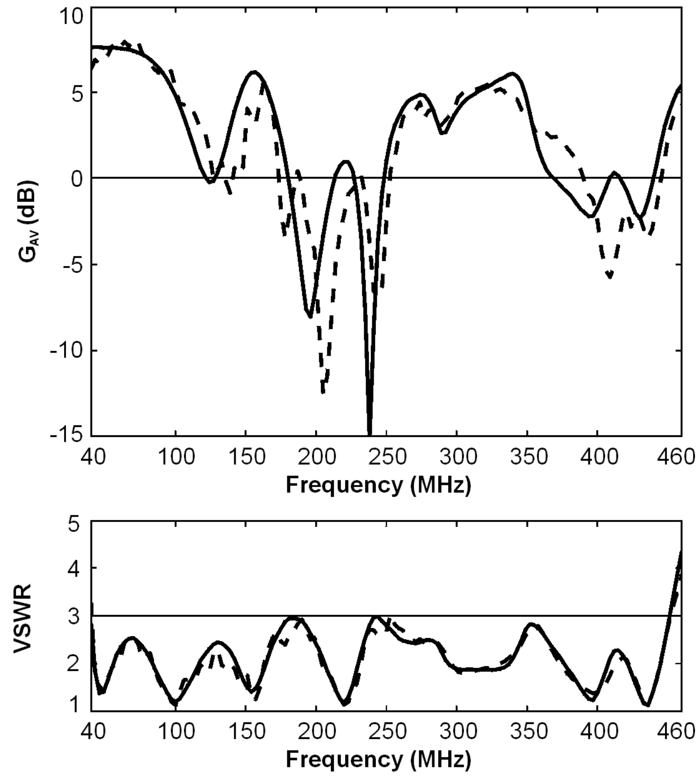

Figure 3.12: *VHF performances*: ϕ-averaged gain at horizon ($\theta = 90°$) and VSWR of the discone antenna in two different configurations: top-mounted discone in Fig.3.10 (dashed line), and stand-alone discone placed at the same height from the ground plane (solid line).

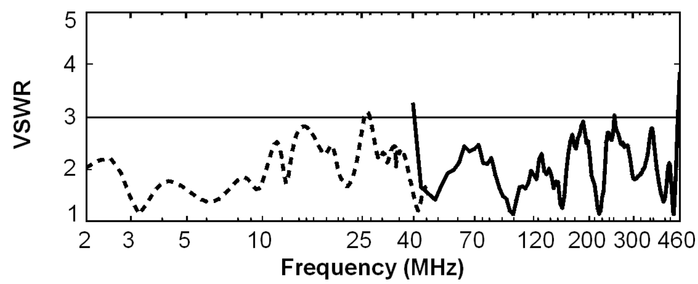

Figure 3.13: VSWR of the integrated antenna system in Fig.3.10 in the overall 2-460 MHz. Bifolded VSWR (dotted line) was extended up to 45 MHz.

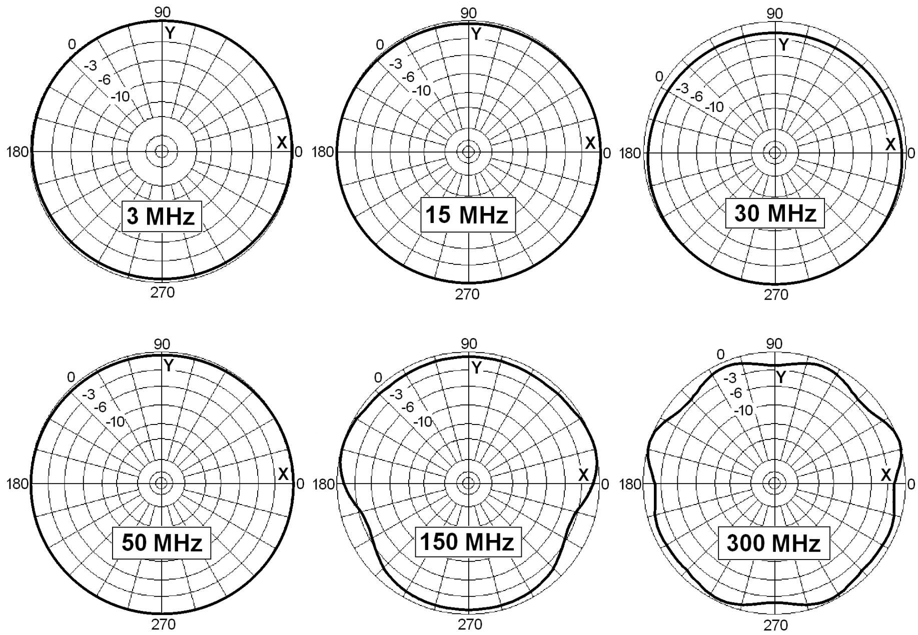

Figure 3.14: Normalized horizontal gain at different frequencies for the integrated antenna system in Fig.3.10.

3.2 Single-feed broadband NSA

The structural antennas considered in the first two Chapters (Fig.1.10 and Fig.2.5) have narrow bandwidths around their resonances and they have been verified not to possess broadband features, as required to serve the whole HF range, even if the wires were loaded by lumped impedances. In order to design the NSA_1 in the overall HF band, the bifolded layout of Fig.3.7 can be chosen as a starting point. In fact, since its left vertical conductor is unloaded, it can be supposed to be replaced by a large cylinder resulting in a typical structural configuration. The presence of the large metallic object, however, perturbs the electromagnetic behavior of the resulting antenna and, therefore, the wire shape and loading need to be re-optimized. Among the various considered, an interesting geometry for the wire part of the structure, hereafter denoted as *sub-radiator,* is shown in Fig.3.15. This shape is conceptually similar to that of the bifolded in the sense that it embodies nested closed-loops and, if properly loaded, permits to excite different current patterns, and hence different radiation patterns, at different frequencies. The vertical conductor up above the cylinder will be useful to enhance the radiation in the highest part of the HF range, as shown later on.

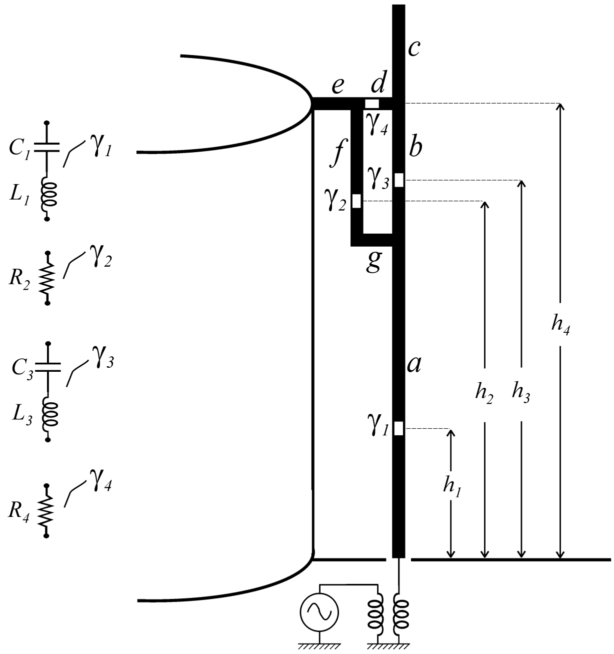

Figure 3.15: Example of structural antenna (single-feed NSA) with a shaped wire *sub-radiator*. Segment size (in $[m]$): $a = 7, b = 3, c = 2, d = 1, e = 1, f = 3, g = 1$. The RF source is connected to the antenna by means of an impedance transformer with step-up ratio $N = 4$. Geometrical (in $[m]$) and electrical parameters of the circuits γ_n are: $h_1 = 3.25$, $h_2 = 7.75$, $h_3 = 8.25$, $h_4 = 10$, $C_1 = 569.1pF$, $L_1 = 1.12\mu H$, $R_2 = 61\Omega$, $C_3 = 59.8pF$, $L_3 = 0.073\mu H$, $R_4 = 48.6\Omega$.

An impedance transformer, of step-up ratio to be optimized, is connected between the wire-radiator and the RF source generator. The parameters of the broadband system are chosen again by a GA driven optimization with the purpose of minimizing the same penalty function found in (3.1) for the case of the bifolded antenna.

An example of optimized structure requires four loading impedances as in Fig.3.15 [35], [36] and the resulting antenna is well matched in the whole HF band as visible in Fig.3.16. The shadowed region gives the sensitivity of the VSWR to a random $\pm 10\%$ deviation of the electric components values from the optimized results. As expected from the GA paradigm, the optimized antenna appears rather robust to fabrication uncertainties.

The inspection of the antenna current in Fig.3.17 reveals the presence, at lower frequencies (2 MHz), of two nested rectangular loops. The smaller one consists of the b, d, f, g segments and mainly radiates toward the zenith. The external loop acts as a folded monopole of segments a, b, d, e together with the cylindrical body, with main radiation toward the horizon. The vertical wire c is nearly isolated. The resulting radiation pattern (Fig.3.18) still retains hemispherical coverage. As frequency increases (15 MHz) the current pattern becomes more complex, the internal loop mode vanishes, the segment c start to be energized and the radiation is similar to that of a whip antenna, i.e. with nearly omnidirectional pattern on the horizontal plane without the presence of nulls.

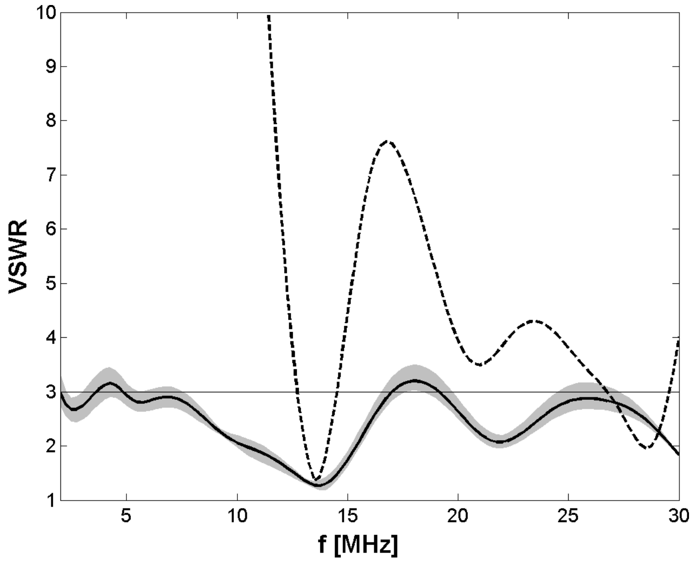

Figure 3.16: VSWR for the single-feed NSA of Fig.3.15 without (dashed line) and with (solid line) optimized broadbanding loads and transformer. The shadowed region gives the sensitivity of the VSWR to a random ±10% deviation of the electric components values from the optimized results.

The frequency-dependent ϕ-averaged gain (Fig.3.19) shows values larger than 0 dB at horizon above 5 MHz with peak values of about 5dB beyond 15 MHz. It can be also appreciated a reasonable high gain in the NVIS frequency

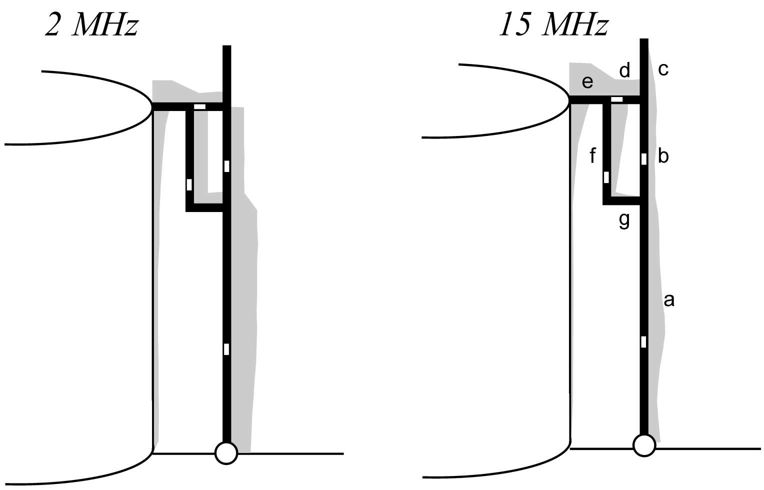

Figure 3.17: Currents on the single-feed loaded NSA at two different frequencies. Shadowed regions indicate the current amplitude at wire location.

range. Finally, except for 2 MHz, where the efficiency is between 0.2% and 0.5%, acceptable values are obtained in the whole HF range, and in particular beyond 5 MHz where the efficiency ranges between 30% and 80% (Fig.3.20).

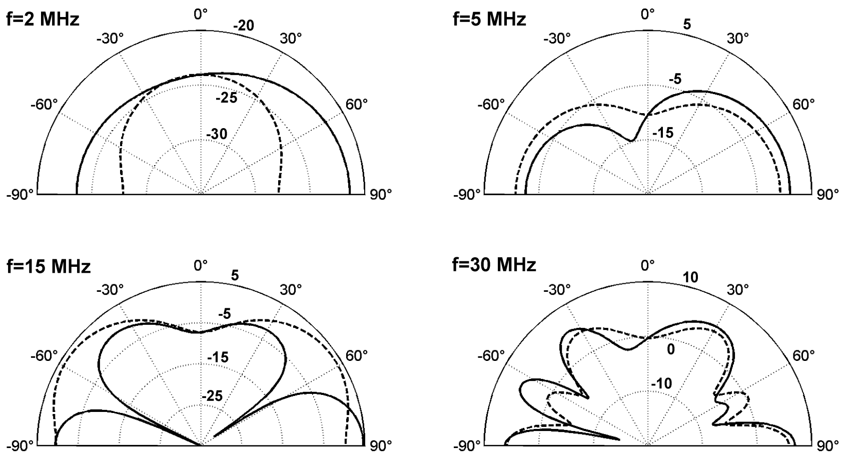

Figure 3.18: Gain of the single-feed loaded NSA at some frequencies; solid line: $\phi = 0°$, dashed line: $\phi = 90°$.

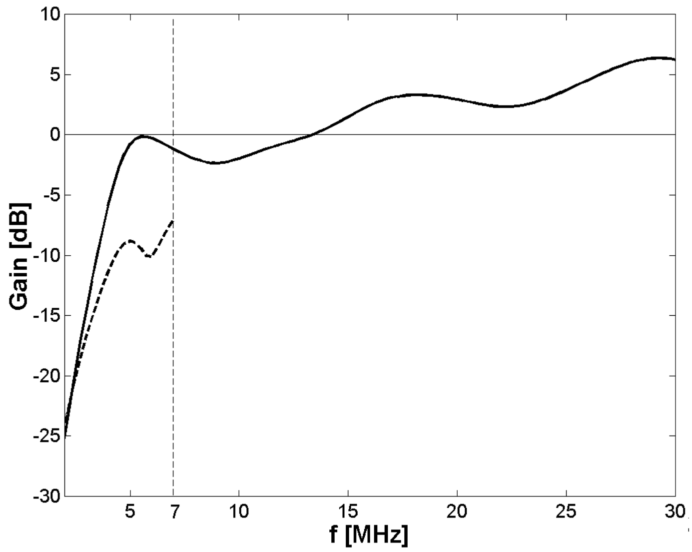

Figure 3.19: Frequency-dependent ϕ-averaged gain for the single-feed loaded NSA along the horizon ($\theta = 90°$, solid line) and at NVIS ($\theta = 20°$, dashed line).

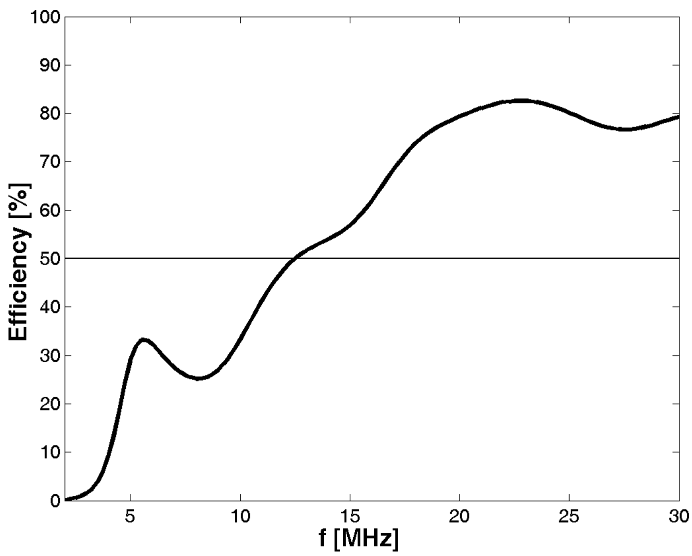

Figure 3.20: Efficiency of the single-feed loaded NSA.

Chapter 4

Multi-port Naval Structural Antenna ($\mathbf{NSA}_N$)

This Chapter extends the design of the single-feed NSA to that of multi-port NSA or NSA_N. The inclusion of more than a single loaded wire sub-radiator on the cylindrical body yields a multiple-feed compact antenna system which can be used in two different configurations: *multi-channel* (or *incoherent*) and *mono-channel* (or *coherent*). In this way, a great flexibility in terms of power handling and radiation pattern reconfigurability can be achieved [35], [36]. In particular, in the first case a huge efficiency improvement over the conventional broadband antenna systems, equipped with lossy combining networks as discussed in the introduction, can be obtained. In the second case, the NSA_N can be used as an array and a moderate shape of the beam is possible in the HF band.

As an example, Fig.4.1 shows the NSA_4 configuration including four equi-spaced wire sub-radiators ($\Delta\phi = 2\pi/N = \pi/2$). Since wires are placed at a close proximity compared with the HF wavelengths, the mutual coupling effects need to be carefully taken into account in the system performance evaluation, not only for what concerns the radiation properties but also for the electrical mismatch at each port.

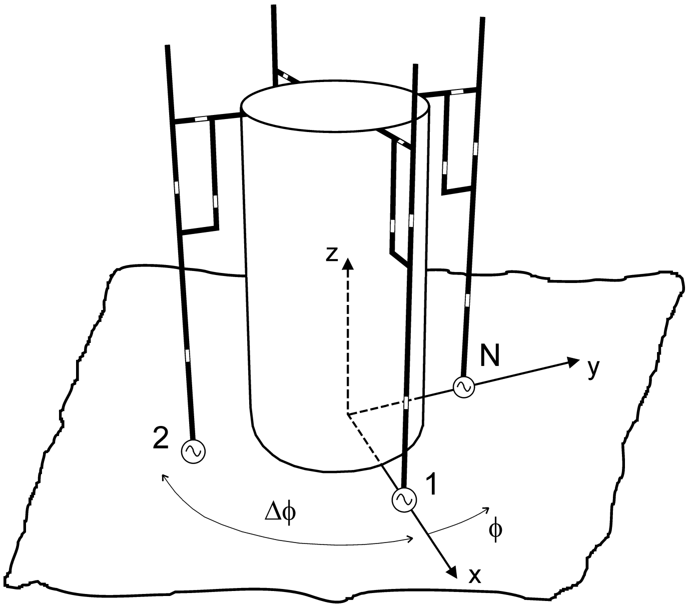

Figure 4.1: Multiple-feed NSA_4. The four wire sub-radiators are clockwise numbered.

4.1 Multi-channel mode

This feeding strategy allows the antenna to simultaneously communicate on multiple-channels. Each port of the structure can be directly excited by a different narrow-band signal. In this way a set of signals is combined *on air*, avoiding the use of lossy combining networks that are generally adopted together with broadband radiators. In general, the efficiency of a broadband antenna equipped with a signal combiner is $\eta_{A+C} = \eta_A \eta_C$, where η_A is the antenna efficiency, $\eta_C = 1/N$ is the combiner efficiency and $N = 2^p$ is the total number of channels to be combined. In other words, each combination stage causes a loss of 3 dB on each channel. Tab.4.1 shows that η_C sensibly reduces with the increase of channels' number and, therefore, the resulting system efficiency η_{A+C} can be very low.

Multi-channel strategy significantly improves the system efficiency with respect to the traditional broadband systems, as explained in the following example. Three antenna systems (Fig.4.2) are considered: *a)* a single-feed broadband NSA with a single-channel, *b)* the same antenna equipped with

Table 4.1: Efficiency of combining networks for different numbers of channels.

channels	**losses**	η_C
1	0 dB	100%
2	3 dB	50%
4	6 dB	25%
8	9 dB	12.5%

a broadband combiner of 4-channels, *c)* a 4-port NSA used in multi-channel mode.

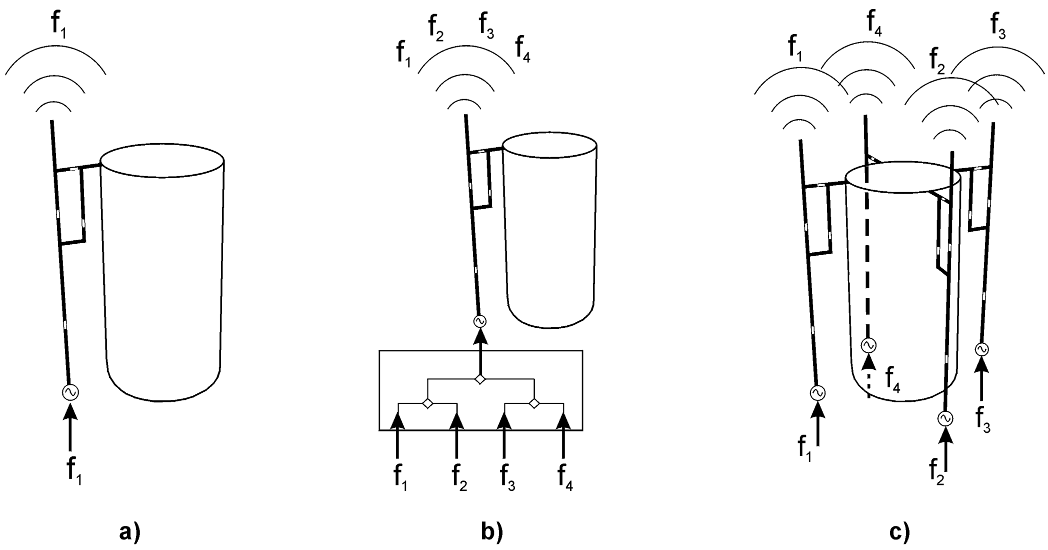

Figure 4.2: *a)* NSA_1 single-channel. *b)* NSA_1+4-channel combiner. *c)* NSA_4 multi-channel.

While the efficiency of the NSA_1 plus the combiner network managing N channels is $\eta_{A+C} = \eta_{NSA_1}/N$, the exclusive allocation of each sub-radiator of the NSA_N to a single channel is expected to ideally give a higher system efficiency, close to η_{NSA_1}. However, because of the coupling among sub-radiators, the efficiency of the NSA_N on each channel is slightly smaller than η_{NSA_1}, as shown in Fig.4.3 for the case $N = 4$. Anyway, it can be appreciated up to 400% improvement in the most part of the band with respect to the NSA_1

plus the power combiner network. At those frequencies where the port coupling is more effective, the above improvement is smaller but always larger than about 300%.

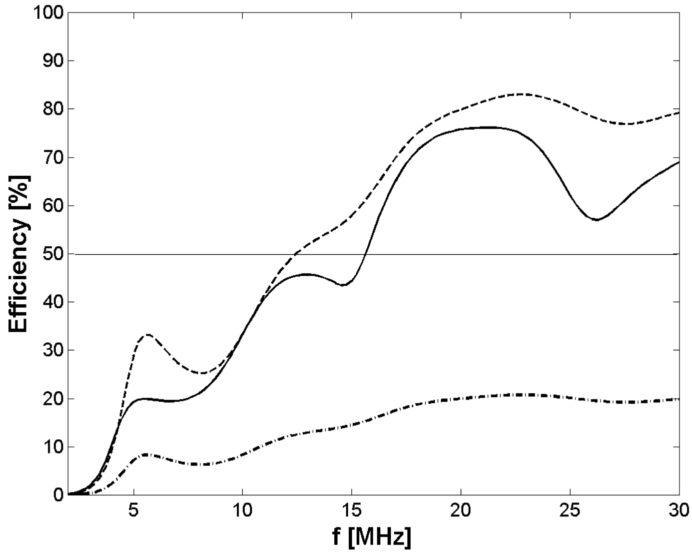

Figure 4.3: System efficiency of the NSA_4 in *multi-channel* mode (solid line), of the NSA_1 with a single-channel (dashed line), and of the NSA_1 connected to a power combiner for a simultaneous 4-channels communication (dash-dotted line).

The *embedded* VSWR, gain and efficiency, i.e. input and radiation characteristics of the multiple-feed NSA when a single source is excited and the remainings are turned off and terminated to the nominal line-impedance, have been numerically computed and can be compared with those of the NSA_1 depicted in Fig.3.15. Fig.4.4 shows the embedded VSWR for N=4 and N=6 equi-spaced elements. In both configurations, the mutual coupling among wire sub-radiators is not so strong to sensibly modify the antenna matching in comparison with the single-feed loaded NSA (see Fig.3.16).

Fig.4.5 and Fig.4.6 represent the embedded gain at different frequencies on both horizontal and vertical cuts for the NSA_4. The azimuthal patterns, particularly at higher frequencies, retain omnidirectional features as in the NSA_1, and NVIS links are still possible due to the acceptable radiation close to the zenith at lower frequencies.

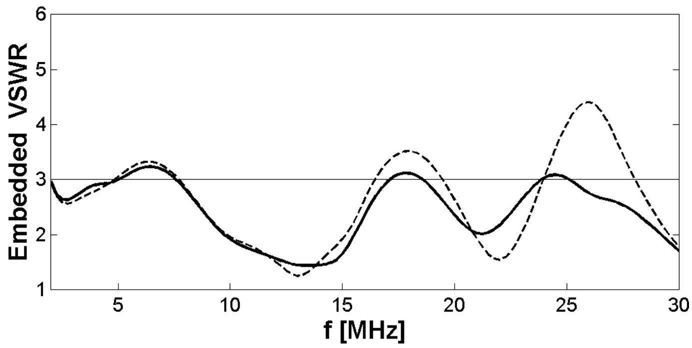

Figure 4.4: *Embedded* VSWR of the NSA_4 (solid line) and NSA_6 (dashed line) with respect to 200Ω.

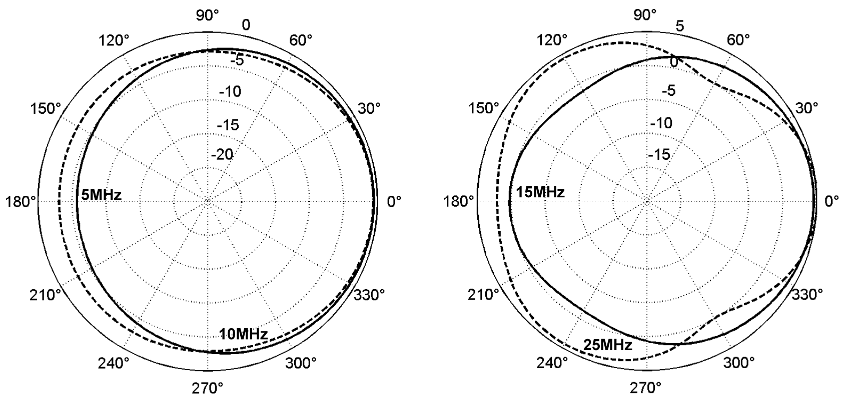

Figure 4.5: *Embedded* gain of the NSA_4 at different frequencies on the horizontal cut ($\theta = 90°$ plane). The source is assumed to be placed in $\phi = 0°$.

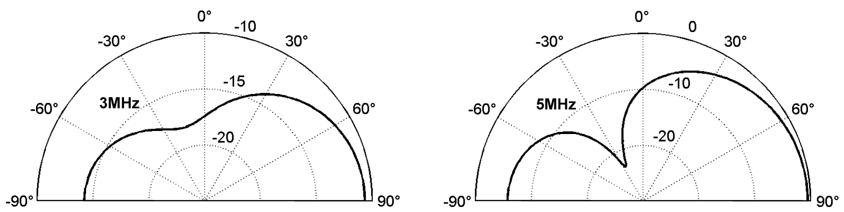

Figure 4.6: *Embedded* gain of the NSA_4 at different frequencies on the vertical cut ($\phi = 0°$ plane). The source is assumed to be placed in $\theta = 90°$.

NSA_N with $N \leq 6$ sub-radiators can be therefore used in multi-channel configuration maintaining about the same input and radiation characteristics as the single-feed NSA. For a larger number of elements, the distance between adjacent sub-radiators reduces and the mutual coupling effects can start to degrade the antenna matching.

In order to quantify the inter-port coupling, the scattering matrix [S] has been calculated for $N = 4$. Because of the periodicity of the structure, the scattering matrix is *circulant*, i.e., every row is obtained from the previous one through a cyclic permutation. If in the antenna structure only reciprocal elements are present, [S] is also a symmetric matrix as indicated below. Moreover, since $S_{12} = S_{14}$, the following relation holds:

$$[S] = \begin{bmatrix} S_{11} & S_{12} & S_{13} & S_{14} \\ S_{21} & S_{22} & S_{23} & S_{24} \\ S_{31} & S_{32} & S_{33} & S_{34} \\ S_{41} & S_{42} & S_{43} & S_{44} \end{bmatrix} = \begin{bmatrix} S_{11} & S_{12} & S_{13} & S_{12} \\ S_{12} & S_{11} & S_{12} & S_{13} \\ S_{13} & S_{12} & S_{11} & S_{12} \\ S_{12} & S_{13} & S_{12} & S_{11} \end{bmatrix} \tag{4.1}$$

The scattering matrix is completely characterized by the scattering coefficients S_{11}, S_{12}, S_{13}, whose values in the HF band are shown in Fig.4.7.

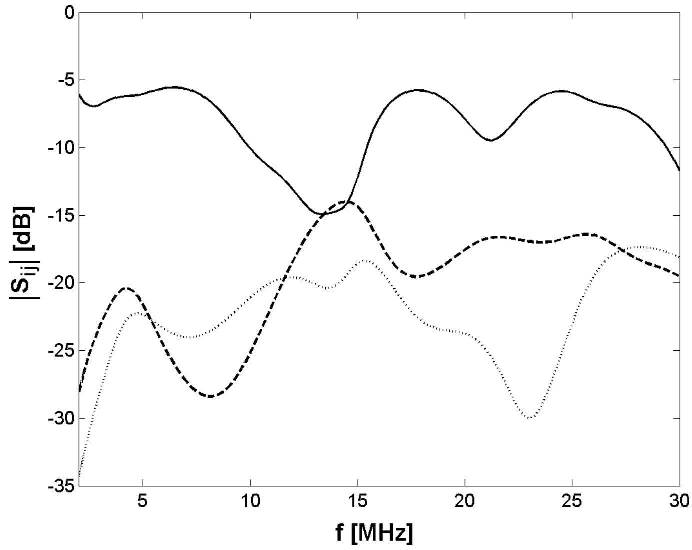

Figure 4.7: Scattering coefficients for the NSA$_4$.

The inter-port coupling is weak and values lower than -15 dB can be observed in almost the whole HF band. It was also verified that, by terminating the ports on an impedance different from the optimized nominal value, for instance a short- or an open-circuit, the embedded performances are not sensibly modified because of the low inter-port coupling.

4.1.1 Performances with different superstructures

It is here investigated the extension of the NSA_N concept to different superstructures in order to better understand the role of the thickness and shape of the central conductor with respect to the broadband performances. Three geometries have been considered (Fig.4.8): a 5m-square cross-section cylinder having wire sub-radiators in front of the wedges, a 1m-diameter cylinder representative of a naval mast, and a simple wire which may yield a stand-alone general purpose multi-port broadband antenna system. Four ports are allocated in each configuration (NSA_4). Wire sub-radiators retain the same shape as in the original NSA while the loading impedances are re-optimized, only for what concerns their values, having fixed the topology and positions as before. The embedded performances are calculated by means of the usual numerical models. It is however expected that even better results could be obtained with an *ad-hoc* design of the wire sub-radiators.

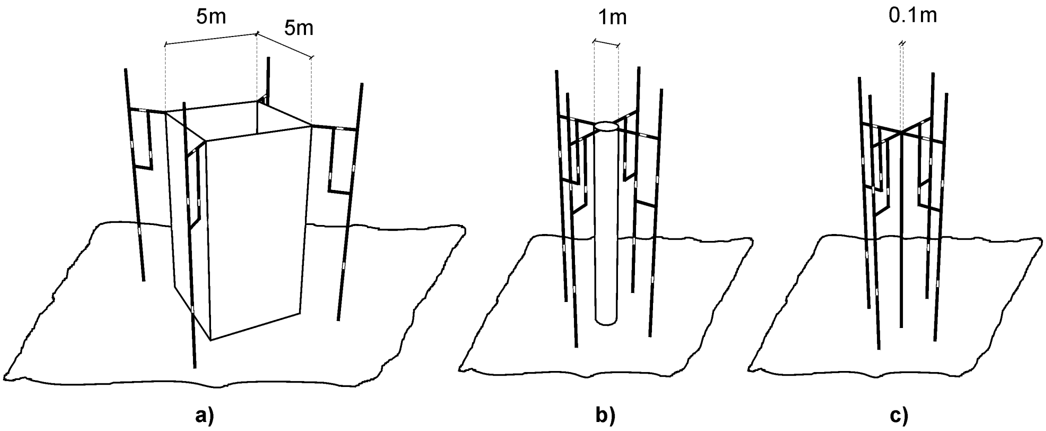

Figure 4.8: Three alternative geometries for the multiport NSA system. The central conductor is a fat hollow square-size cylinder of $5m$-side, a thin circular hollow cilinder of $1m$-diameter and a simple $0.1m$-thickness wire. The wire sub-radiators geometry is the same as in Fig.3.15.

In all the geometries the ports are well matched (Fig.4.9) with VSWR<3 in most part of the HF band, quite apart from the size and shape of the central structure. The average embedded gains along the horizon (Fig.4.10) reveal some differences, particularly at low frequencies (2-5 MHz). As the size of the central conductor is reduced, the embedded gain at the horizon increases since the structure acts more as a monopole rather than as an isotropic antenna, that is instead a feature of large central conductors. The thick circular- and square-section NSAs perform similar, while systems with thinner central conductors exhibit a less uniform gain with the frequency.

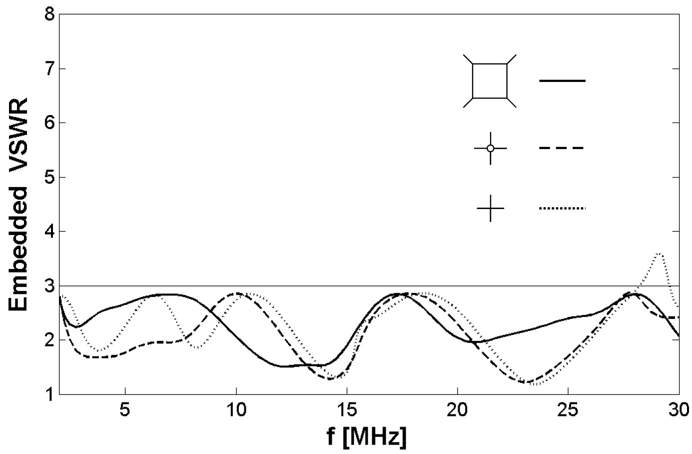

Figure 4.9: Embedded VSWR of the three NSA_4 systems in Fig.4.8 when the loading impedances have been re-optimized, according to the penalty function in (3.1), only for what concerns their values, while the topology and positions are the same as in Fig.3.15.

More evident differences in antenna performances appear in the embedded efficiency diagrams of Fig.4.11, where the NSAs with a thinner central conductor are less efficient in most part of the HF band. This effect is due to the overall reduced size of the antenna system and, hence, to a coupling among sub-radiators larger than that of the 5m structure. For instance, as it is visible in Fig.4.12, the S_{13} scattering parameters between antipodal ports reveal a stronger interaction for thinner structures. In this case, part of the current injected by the excited port in a sub-radiator will be both dissipated by the loading resistors of other sub-radiators and collected at the passive ports. The increase of inter-port coupling could also forbid the multi-channel usage of the system with thin central conductors.

It was finally verified that even removing the central conductor, the resulting antenna system still retain the same features of the NSA_4 equipped

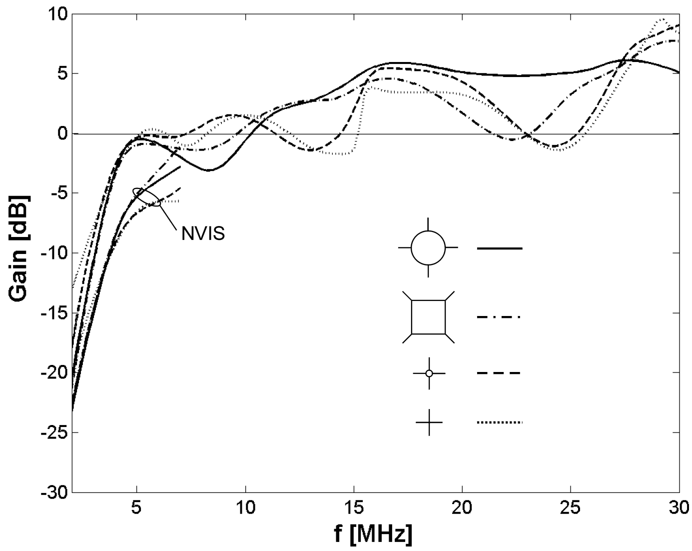

Figure 4.10: ϕ-averaged embedded gain of three NSA_4 systems in Fig.4.8 after loading impedance re-optimization.

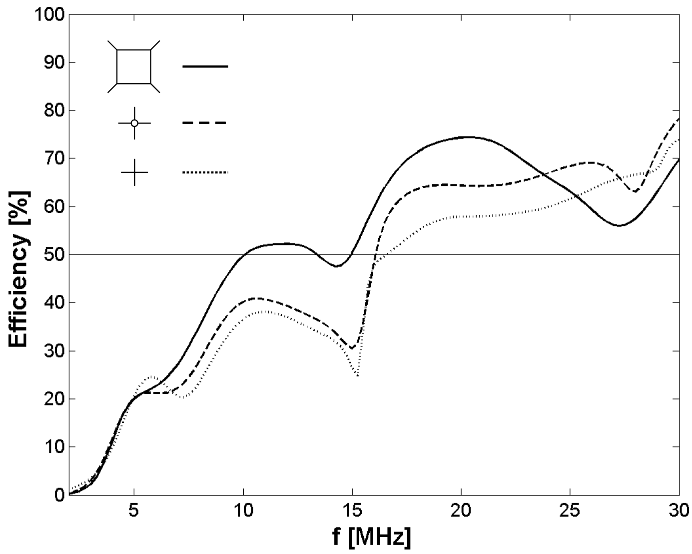

Figure 4.11: Embedded efficiency of the NSA_4 systems in Fig.4.8 after loading impedance re-optimization. Curves have to be compared with the solid line in Fig.4.3.

with a thin central conductor. The presence of a fat central structure seems therefore to be required to obtain high efficiency and a reasonable decoupling

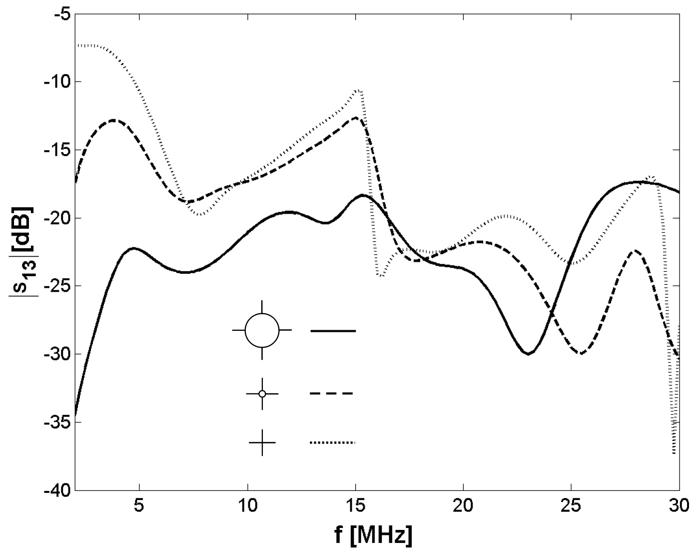

Figure 4.12: Coupling parameters (S_{13}) among antipodal ports for circular cylidrical NSAs with diameter $5m$, $1m$ and $0.1m$.

among ports rather than for broadbanding purposes.

4.2 Mono-channel mode

In this feeding strategy, the N ports are simultaneously allocated to the same channel as in array configurations. The following investigation will address the sectorial coverage properties of the NSA_N, that can be achieved by a simple phase synthesis, and will analyze the degradation of the system broadband features in comparison with the single-feed NSA (see Fig.3.16). Although the overall structure is not properly an array, since there is a tight electrical contiguity among all the radiating elements, nevertheless the system can be considered as a single antenna equipped with N ports having the possibility to host different current patterns depending on the particular feeding strategy. An active element factor $\overrightarrow{E}_n(r, \theta, \phi, f)$ can be associated to the unitary excitation of the nth port when the other ports are turned off. The total radiated field of the NSA_N when the ports are excited by

$A_n(f) = C_n(f)e^{j\alpha_n(f)}$, $\{C_n, \alpha_n\} \in \mathbb{R}$, can be written [25] as

$$\overrightarrow{E}(r, \theta, \phi, f) = \sum_{n=1}^{N} A_n(f)\overrightarrow{E}_n(r, \theta, \phi, f) \tag{4.2}$$

Due to the rotational periodicity of the considered structure, $\overrightarrow{E}_n(r, \theta, \phi, f)$ $=\overrightarrow{E}_1(r, \theta, \phi + (n-1)\Delta\phi, f)$, and (4.2) becomes

$$\overrightarrow{E}(r, \theta, \phi, f) = \sum_{n=1}^{N} C_n(f)e^{j\alpha_n(f)}\overrightarrow{E}_1(r, \theta, \phi + (n-1)\Delta\phi, f) \tag{4.3}$$

with $\Delta\phi = 2\pi/N$. It is easy to observe that beam steering on the horizontal plane ($\theta = 90°$) at ϕ_0 direction can be simply achieved choosing $C_n(f) = C_0(f)$ and

$$\alpha_n(f) = -\angle\overrightarrow{E}_1(r, 90°, \phi_0 + (n-1)\Delta\phi, f) \tag{4.4}$$

where "$\angle$" denotes the phase operator.

Fig.4.13 and Fig.4.14 show the gain of the NSA_N on the horizontal plane at different frequencies respectively for the cases $N = 4$, with beam steering in $\phi_0 = 45°$, and for the case $N = 6$, $\phi_0 = 30°$. Azimuthal patterns, which are symmetric as regards ϕ_0, have been compared with those of the NSA_1 rotated of ϕ_0. As visible in Fig.4.13, at 2 MHz and 10 MHz the NSA_4 exhibits sectorial coverage capabilities and the radiation is principally confined in the half-space centered on ϕ_0 with a front-to-back ratio of about 10 dB. Moreover, it can be also observed an improvement on the maximum gain performance of about 5-6 dB with respect to the NSA_1. As the frequency increases, the front-to-back ratio of the NSA_4 tends to reduce but this configuration still presents a better gain than that of the single-feed structure along ϕ_0. Using $N = 6$ sub-radiators (Fig.4.14) it can be noted a further improvement on the maximum gain performance at all HF frequencies (about 9 dB at 25 MHz) and a better front-to-back ratio at 15 MHz and 25 MHz than that found in the NSA_4.

Antenna matching can be still considered acceptable for the NSA_4 (Fig.4.15), while some *blind sub-bands* appear for the NSA_6 (Fig.4.16). Hence, it can be

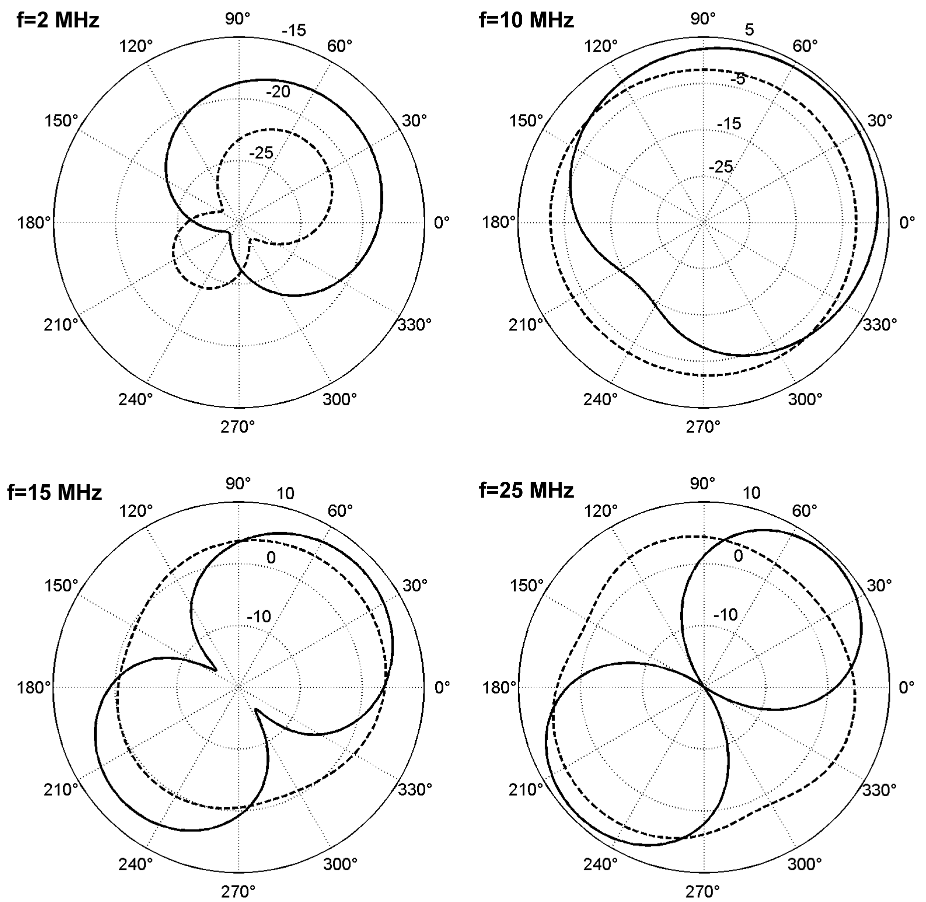

Figure 4.13: Azimuthal gain patterns of the NSA_4 steered to $\phi_0 = 45°$ (solid line) compared with those of the NSA_1 oriented along ϕ_0 (dashed lines).

necessary to compensate this behaviour by introducing a proper matching network or by means of a more efficient array synthesis strategy, also accounting for matching requirements, as it will be discussed in Chapter 6.

The choice $\phi_0 = (m + 1/2)\Delta\phi$ permits to obtain symmetric patterns and to simultaneously minimize the mutual coupling among sub-radiators. In particular, it was verified that antenna matching degrades as ϕ_0 moves from the central position between two adjacent sub-radiators towards one of them, as it will be shown in detail again in Chapter 6 (Fig.6.6).

Finally, the NSA_N in mono-channel configuration can be even used to emphasize the radiation towards the zenith for NVIS links in the range 2-10 MHz. By feeding a pair of opposite sub-radiators with equal signal ampli-

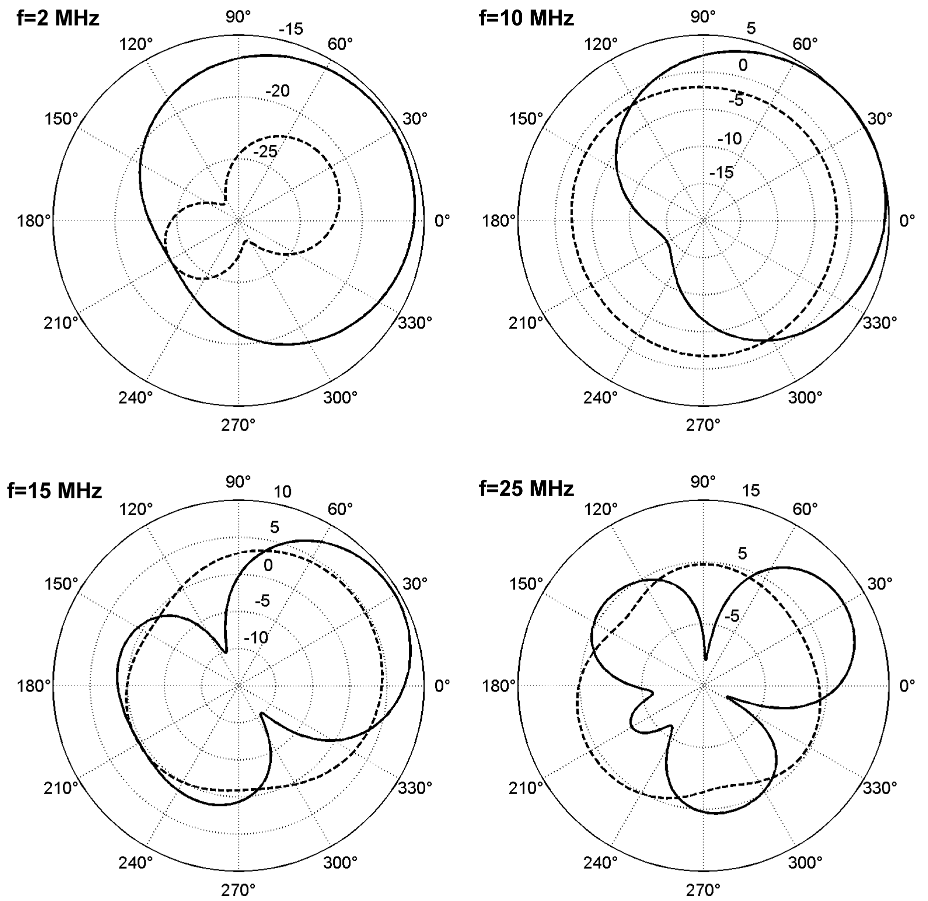

Figure 4.14: Azimuthal gain patterns of the NSA_6 steered to $\phi_0 = 30°$ (solid line) compared with those of the NSA_1 oriented along ϕ_0 (dashed lines).

tudes and opposite phases, the current on the antenna (Fig.4.17) assumes the same distribution as on a large half-loop. Comparing the resulting 2 MHz pattern with that of the single-feed NSA (Fig.3.18), it can be observed a gain improvement of about 3-4 dB on the zenith and a more uniform radiation close to it. It was also verified that the active sub-radiators still retain an acceptable matching (VSWR<3.5).

It was finally verified that using the same superstructures as the previous paragraph in mono-channel mode, blind sub-bands are visible again, the efficiency is poor (<40%) in the whole HF band for the NSAs with thinner central conductors, and sectorial coverage is not possible at lower frequencies because of the very weak array effect due to the close proximity of the

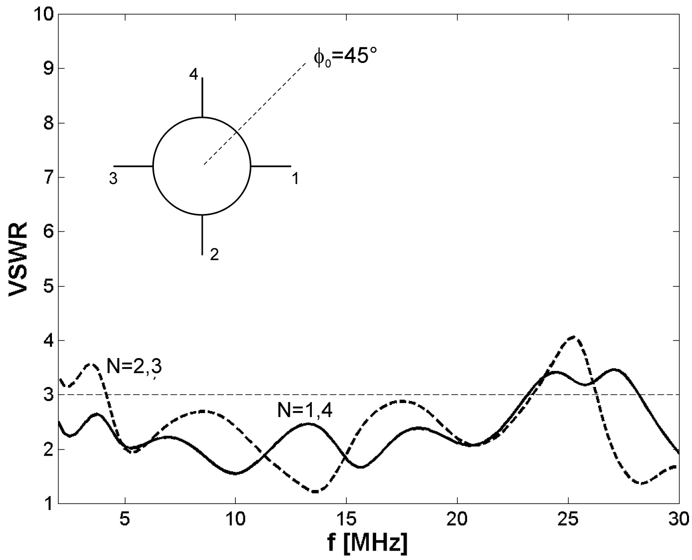

Figure 4.15: VSWR at each port of the NSA_4 when $\phi_0 = 45°$; due to the antenna rotational symmetry as regards ϕ_0, pairs of symmetric sources share the same VSWR curve. VSWR is referred to 200Ω.

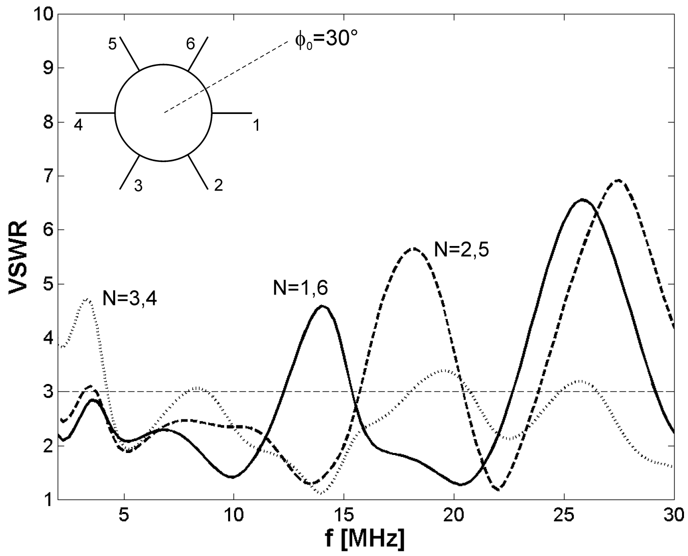

Figure 4.16: VSWR at each port of the NSA_6 when $\phi_0 = 30°$; due to antenna simmetry as regards ϕ_0, pairs of symmetric sources share the same VSWR curve. VSWR is referred to 200Ω.

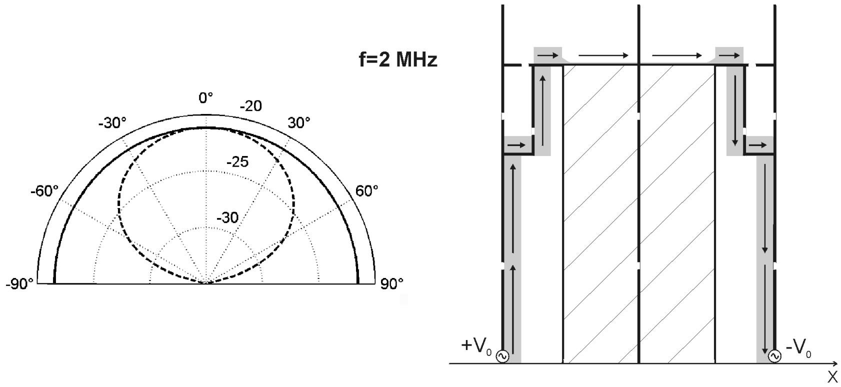

Figure 4.17: Vertical gain pattern and current distribution on the NSA_4 at 2 MHz when a half-loop mode is excited; solid line: $\phi = 0°$, dashed line: $\phi = 90°$; arrows indicate the current direction.

sub-radiators compared with the wavelength.

Chapter 5

Modal study of highly coupled circular arrays

This Chapter introduces a modal approach of general interest for the investigation of multi-port radiating structures. The basic concepts are derived from [37] and [38] and are here extended and treated in a unitary way keeping in mind the application to structural antenna systems; some new interesting results are found and shown. The presented method is particularly suited for the analysis and synthesis of highly coupled circular arrays, such as the NSA, and will be here applied to analyze the main properties of some unloaded multi-port structures with circular periodicity and to show a simple way to achieve a moderate beam focusing from this kind of antennas. In the next Chapter the theory will be used to perform NSA radiation pattern synthesis.

5.1 Modal theory formulation

Given an N-port antenna, this method is based on the study of the admittance matrix [Y] (or, equivalently, the scattering or impedance matrix) and its eigenvectors $\overrightarrow{v}^{(i)}$ and eigenvalues $\lambda^{(i)}$, related by the following well-known relation:

$$[Y]\,\overrightarrow{v}^{(i)} = \lambda^{(i)}\overrightarrow{v}^{(i)} \qquad i = 1, 2, ..., N \tag{5.1}$$

In this particular problem, the eigenvectors $\overrightarrow{v}^{(i)}$ are also called *eigenexcitations* of the N-port antenna. Each eigenexcitation excites a mode of the radiating structure. The physical meaning of the eigenvalues $\lambda^{(i)}$ is that of *active input admittance*, the same at each port, when the N-port antenna is excited by the eigenexcitation $\overrightarrow{v}^{(i)}$ [37]. It can be verified by expanding (5.1):

$$\begin{cases} Y_{11}v_1^{(i)} + Y_{12}v_2^{(i)} + ... + Y_{1N}v_N^{(i)} = \lambda^{(i)}v_1^{(i)} \\ Y_{21}v_1^{(i)} + Y_{22}v_2^{(i)} + ... + Y_{2N}v_N^{(i)} = \lambda^{(i)}v_2^{(i)} \\ \quad ... \\ Y_{N1}v_1^{(i)} + Y_{N2}v_2^{(i)} + ... + Y_{NN}v_N^{(i)} = \lambda^{(i)}v_N^{(i)} \end{cases} \qquad i = 1, 2, ..., N \tag{5.2}$$

The eigenvalue $\lambda^{(i)}$ is found by inverting (5.2):

$$\begin{cases} \lambda^{(i)} = \frac{Y_{11}v_1^{(i)}+Y_{12}v_2^{(i)}+...+Y_{1N}v_N^{(i)}}{v_1^{(i)}} = \frac{\sum_{k=1}^{N} Y_{1k}v_k^{(i)}}{v_1^{(i)}} = \frac{I_{TOT,1}^{(i)}}{v_1^{(i)}} = Y_{IN,1}^{(i)} \\ \lambda^{(i)} = \frac{Y_{21}v_1^{(i)}+Y_{22}v_2^{(i)}+...+Y_{2N}v_N^{(i)}}{v_2^{(i)}} = \frac{\sum_{k=1}^{N} Y_{2k}v_k^{(i)}}{v_2^{(i)}} = \frac{I_{TOT,2}^{(i)}}{v_2^{(i)}} = Y_{IN,2}^{(i)} \\ \quad ... \\ \lambda^{(i)} = \frac{Y_{N1}v_1^{(i)}+Y_{N2}v_2^{(i)}+...+Y_{NN}v_N^{(i)}}{v_N^{(i)}} = \frac{\sum_{k=1}^{N} Y_{Nk}v_k^{(i)}}{v_N^{(i)}} = \frac{I_{TOT,N}^{(i)}}{v_N^{(i)}} = Y_{IN,N}^{(i)} \end{cases} \tag{5.3}$$

where $I_{TOT,k}^{(i)}$ and $Y_{IN,k}^{(i)}$ are the total current and the active input admittance at the kth-port when the ports are excited by the eigenexcitation $\overrightarrow{v}^{(i)}$.

As discussed in [37], the eigenexcitations can be *orthonormalized*:

$$\left\langle \overrightarrow{v}^{(i)}, \overrightarrow{v}^{(j)*} \right\rangle = \sum_{k=1}^{N} v_k^{(i)} v_k^{(j)*} = \delta_{ij} \tag{5.4}$$

where δ_{ij} is the Kronecker symbol, and an *arbitrary excitation* $\overrightarrow{v}$ can be expressed as a linear combination of the eigenexcitations:

$$\overrightarrow{v} = \sum_{i=1}^{N} c_i \overrightarrow{v}^{(i)} \tag{5.5}$$

where c_i are complex weighing coefficients given by the scalar product:

$$c_i = \left\langle \overrightarrow{v}, \overrightarrow{v}^{(i)*} \right\rangle \tag{5.6}$$

Starting from these basic concepts, an important equation will be now found, relating the active input admittance at the kth-port due to an arbitrary excitation, to the eigenvalues, eigenvectors and the weighing coefficients.

According to (5.5) an arbitrary voltage at the kth-port (the kth-component of vector $\overrightarrow{v}$) is given by:

$$v_k = \sum_{i=1}^{N} c_i v_k^{(i)} \tag{5.7}$$

By multiplying both members of (5.2) by c_i and applying the sum operator, these relations hold:

$$\begin{cases} Y_{11} \sum_{i=1}^{N} c_i v_1^{(i)} + Y_{12} \sum_{i=1}^{N} c_i v_2^{(i)} + ... + Y_{1N} \sum_{i=1}^{N} c_i v_N^{(i)} = \sum_{i=1}^{N} \lambda^{(i)} c_i v_1^{(i)} \\ Y_{21} \sum_{i=1}^{N} c_i v_1^{(i)} + Y_{22} \sum_{i=1}^{N} c_i v_2^{(i)} + ... + Y_{2N} \sum_{i=1}^{N} c_i v_N^{(i)} = \sum_{i=1}^{N} \lambda^{(i)} c_i v_2^{(i)} \\ ... \\ Y_{N1} \sum_{i=1}^{N} c_i v_1^{(i)} + Y_{N2} \sum_{i=1}^{N} c_i v_2^{(i)} + ... + Y_{NN} \sum_{i=1}^{N} c_i v_N^{(i)} = \sum_{i=1}^{N} \lambda^{(i)} c_i v_N^{(i)} \end{cases} \tag{5.8}$$

By using (5.7), equation (5.8) can by written as:

$$\begin{cases} Y_{11} v_1 + Y_{12} v_2 + ... + Y_{1N} v_N = \sum_{i=1}^{N} \lambda^{(i)} c_i v_1^{(i)} \\ Y_{21} v_1 + Y_{22} v_2 + ... + Y_{2N} v_N = \sum_{i=1}^{N} \lambda^{(i)} c_i v_2^{(i)} \\ ... \\ Y_{N1} v_1 + Y_{N2} v_2 + ... + Y_{NN} v_N = \sum_{i=1}^{N} \lambda^{(i)} c_i v_N^{(i)} \end{cases} \tag{5.9}$$

The kth-row of the left-hand member of (5.9) is the total current at the kth-port due to an arbitrary excitation $\overrightarrow{v}$. This current can be expressed as the product between the *active input admittance* at the kth-port and the voltage at the kth-port. In other words, the kth-row of the left-hand member of (5.9) can be written as:

$$Y_{k1}v_1 + Y_{k2}v_2 + ... + Y_{kN}v_N = \sum_{i=1}^{N} Y_{ki}v_i = I_{TOT,k} = Y^a_{IN,k}v_k \tag{5.10}$$

By using (5.9) and (5.10), for the kth-row it holds:

$$Y^a_{IN,k}v_k = \sum_{i=1}^{N} \lambda^{(i)} c_i v_k^{(i)} \tag{5.11}$$

Finally, by using (5.7), the expression of the *active input admittance* at the kth-port due to an arbitrary excitation $\overrightarrow{v}$ is obtained:

$$Y^a_{IN,k} = \frac{\sum_{i=1}^{N} \lambda^{(i)} c_i v_k^{(i)}}{\sum_{i=1}^{N} c_i v_k^{(i)}} \tag{5.12}$$

It is worth noticing that, while $\lambda^{(i)}$ is the active input admittance, the same at each port, when the array is excited by the eigenexcitation $\overrightarrow{v}^{(i)}$, $Y^a_{IN,k}$ is the active input admittance at the kth-port when the array is excited by an arbitrary excitation $\overrightarrow{v}$.

At this point, the expression of the *active reflection coefficient* at the kth-port due to an arbitrary excitation $\overrightarrow{v}$ is easily obtained:

$$\Gamma^a_k = \frac{Y_{g,k} - Y^a_{IN,k}}{Y_{g,k} + Y^a_{IN,k}} \tag{5.13}$$

where $Y_{g,k}$ is the line admittance of the kth-source.

5.1.1 Eigenpatterns

The radiated far-field of the N-port antenna produced by the orthonormalized eigenexcitation $\overrightarrow{v}^{(i)}$ is called *eigenpattern* [37] and it will be denoted as $\overrightarrow{E}^{(i)}(\theta,\phi) = E_\theta^{(i)}(\theta,\phi)\widehat{\theta} + E_\phi^{(i)}(\theta,\phi)\widehat{\phi}$. The eigenpatterns satisfy the following orthogonality relation on the sphere at infinity [38]:

$$\left\langle \overrightarrow{E}^{(m)}, \overrightarrow{E}^{(n)*} \right\rangle = \iint_{4\pi} \overrightarrow{E}^{(m)}(\theta,\phi)\cdot \overrightarrow{E}^{(n)*}(\theta,\phi) \sin\theta d\theta d\phi = K_{mn}\delta_{mn} \quad (5.14)$$

that is, by expanding (5.14):

$$\left\langle \overrightarrow{E}^{(m)}, \overrightarrow{E}^{(n)*} \right\rangle = \iint_{4\pi} (\mathrm{E}_\theta^{(m)}\mathrm{E}_\theta^{(n)*} + \mathrm{E}_\phi^{(m)}\mathrm{E}_\phi^{(n)*}) \sin\theta \mathrm{d}\theta \mathrm{d}\phi = (\mathrm{K}_{\theta mn} + \mathrm{K}_{\phi mn})\delta_{mn} \quad (5.15)$$

where:

$$\mathrm{K}_{\theta nn} = \iint_{4\pi} \left| E_\theta^{(n)} \right|^2 \sin\theta d\theta d\phi \quad (5.16)$$

$$\mathrm{K}_{\phi nn} = \iint_{4\pi} \left| E_\phi^{(n)} \right|^2 \sin\theta d\theta d\phi \quad (5.17)$$

and:

$$K_{nn} = \mathrm{K}_{\theta nn} + \mathrm{K}_{\phi nn} \quad (5.18)$$

By the superposition principle, the radiated field due to an *arbitrary excitation* $\overrightarrow{v}$ can be expressed as the linear combination of the eigenpatterns [37]:

$$\overrightarrow{E}(\theta,\phi) = \sum_{i=1}^{N} c_i \overrightarrow{E}^{(i)}(\theta,\phi) \quad (5.19)$$

where c_i are shown in (5.6).

It has to be oserved that, by using the linearity of the scalar product and equations (5.14) and (5.19), the scalar product between $\overrightarrow{E}(\theta,\phi)$ and the ith-eigenpattern gives:

$$\left\langle \overrightarrow{E}, \overrightarrow{E}^{(i)*} \right\rangle = \left\langle \sum_{j=1}^{N} c_j \overrightarrow{E}^{(j)}, \overrightarrow{E}^{(i)*} \right\rangle = \sum_{j=1}^{N} c_j \left\langle \overrightarrow{E}^{(j)}, \overrightarrow{E}^{(i)*} \right\rangle = \sum_{j=1}^{N} c_j K_{ji}\delta_{ji} = c_i K_{ii}$$

$$(5.20)$$

Therefore, another definition of the coefficients c_i has been here found, based on the eigenpatterns rather than on the eigenexcitations:

$$c_i = \frac{1}{K_{ii}} \left\langle \overrightarrow{E}, \overrightarrow{E}^{(i)*} \right\rangle \tag{5.21}$$

Such a definition is useful when a pattern synthesis has to be performed, as it will be shown in the next Chapter. In this case, $\overrightarrow{E}(\theta, \phi)$ is the desired pattern and c_i are the synthesized coefficients that give the array excitation vector according to (5.5).

5.1.2 Case of circular array

For an array of 4 radiators *angularly equispaced* on a circle (UCA) and in which only reciprocal elements are present, the admittance matrix [Y] is circulant and symmetric as found in (4.1):

$$[Y] = \begin{bmatrix} Y_{11} & Y_{12} & Y_{13} & Y_{12} \\ Y_{12} & Y_{11} & Y_{12} & Y_{13} \\ Y_{13} & Y_{12} & Y_{11} & Y_{12} \\ Y_{12} & Y_{13} & Y_{12} & Y_{11} \end{bmatrix} \tag{5.22}$$

It has to be observed that Y_{14} is replaced by Y_{12} due to the periodicity of the structure.

The matrix in (5.22) has the following set of *orthonormalized* eigenvectors [37]:

$$v_k^{(i)} = \frac{e^{j[2\pi(i-1)(k-1)/N]}}{\sqrt{N}} \qquad \text{i,k=1,2,...,N} \tag{5.23}$$

where (5.23) represents the kth-component of the ith-eigenvector.

For a given eigenvector, which is independent on the frequency, the amplitude of each component is constant end equal to $1/\sqrt{N}$, while the phase changes with constant step. In particular, the ith-eigenexcitation represents a uniform phasing of the array with step $\Delta\phi_i = \frac{2\pi}{N}(i-1)$:

$$\overrightarrow{v}^{(i)} = \frac{1}{\sqrt{N}} \begin{pmatrix} 1 \\ e^{j\Delta\phi_i} \\ e^{j2\Delta\phi_i} \\ \ldots \\ e^{j(N-1)\Delta\phi_i} \end{pmatrix} \qquad \text{i=1,2,...,N} \tag{5.24}$$

It can be observed that $\Delta\phi_i = 0$ when $i = 1$ and the array ports are excited with the same phase.

According to (5.24), eigenvectors can be real or complex. In particular, when the number of ports N is even, there are 2 real eigenvectors and $\frac{N}{2} - 1$ pairs of complex and conjugate eigenvectors. When N is odd, there is one real eigenvector and $\lfloor \frac{N}{2} \rfloor$ pairs of complex and conjugate eigenvectors (Tab.5.1).

Table 5.1: Real and complex conjugate orthonormalized eigenvectors as a function of the number of ports N.

N	$\boldsymbol{\Delta\phi}$	**eigenvectors**
2	180°	$2 \in R$
3	120°	$1 \in R$, 1 pair *c.c.*
4	90°	$2 \in R$, 1 pair *c.c.*
5	72°	$1 \in R$, 2 pairs *c.c.*
6	60°	$2 \in R$, 2 pairs *c.c.*
8	45°	$2 \in R$, 3 pairs *c.c.*
10	36°	$2 \in R$, 4 pairs *c.c.*

As discussed in [37] the eigenvalues of [Y] are, instead, given by:

$$\lambda^{(i)} = \sum_{k=1}^{N} Y_{1k} e^{j[2\pi(i-1)(k-1)/N]} \qquad \text{i=1,2,...,N} \tag{5.25}$$

Expression (5.25) has the form of a discrete Fourier transform of Y_k. It may be inverted, giving the values of Y_{1k} as functions of $\lambda^{(i)}$:

$$Y_{1k} = \frac{1}{N} \sum_{i=1}^{N} \lambda^{(i)} e^{-j[2\pi(i-1)(k-1)/N]} \tag{5.26}$$

It is here finally found that the field produced by the sum of the N eigenexcitations is a quantity proportional to the *active element factor* $\overrightarrow{E}^a_1$, that is the field obtained by exciting the array with $\overrightarrow{v}^a_1 = (1, 0, 0, .., 0)$. In fact, from (5.24) and $\Delta\phi_i = \frac{2\pi}{N}(i-1)$:

$$\sum_{i=1}^{N} \overrightarrow{v}^{(i)} = \sum_{i=1}^{N} \frac{1}{\sqrt{N}} \begin{pmatrix} 1 \\ e^{j\Delta\phi_i} \\ e^{j2\Delta\phi_i} \\ ... \\ e^{j(N-1)\Delta\phi_i} \end{pmatrix} = \frac{1}{\sqrt{N}} \begin{pmatrix} N \\ \sum_{i=0}^{N-1} e^{j\frac{2\pi}{N}i} \\ \sum_{i=0}^{N-1} e^{j2\frac{2\pi}{N}i} \\ ... \\ \sum_{i=0}^{N-1} e^{j(N-1)\frac{2\pi}{N}i} \end{pmatrix} \tag{5.27}$$

By using the well-known summation of the geometric series

$$\sum_{m=0}^{M-1} r^m = \frac{1-r^M}{1-r} \tag{5.28}$$

(5.27) becomes

$$\sum_{i=1}^{N} \overrightarrow{v}^{(i)} = \frac{1}{\sqrt{N}} \begin{pmatrix} N \\ \frac{1-e^{j2\pi}}{1-e^{j\frac{2\pi}{N}}} \\ \frac{1-e^{j4\pi}}{1-e^{j\frac{4\pi}{N}}} \\ ... \\ \frac{1-e^{j(N-1)2\pi}}{1-e^{j(N-1)\frac{2\pi}{N}}} \end{pmatrix} = \begin{pmatrix} \sqrt{N} \\ 0 \\ 0 \\ ... \\ 0 \end{pmatrix} = \sqrt{N}\overrightarrow{v}^a_1 \tag{5.29}$$

The sum of the N eigenexcitations gives $\sqrt{N}\overrightarrow{v}^a_1$ and, therefore, produces a far-field equal to $\sqrt{N}\overrightarrow{E}^a_1$. It was verified that the same field is given by the sum of the eigenpatterns, that is $\sum_{i=1}^{N} \overrightarrow{E}^{(i)} = \sqrt{N}\overrightarrow{E}^a_1$.

5.2 Application

5.2.1 Modal analysis of highly coupled circular arrays

The theory formulated in the previous paragraph is here applied to investigate the main electromagnetic properties of three different multi-port radiating structures: a circular array of eight monopoles in absence and in presence of a central cylindrical conductor, and an eight-port structural antenna of the same size where the monopoles are connected to the cylinder (Fig.5.1). The height of the structures is $\lambda/15$ @$2MHz$ and $4\lambda/3$ @$40MHz$, the radius of the arrays is about $\lambda/33$ @$2MHz$ and 0.6λ @$40MHz$, the distance between two adjacent radiating elements is about $\lambda/44$ @$2MHz$ and 0.46λ @$40MHz$.

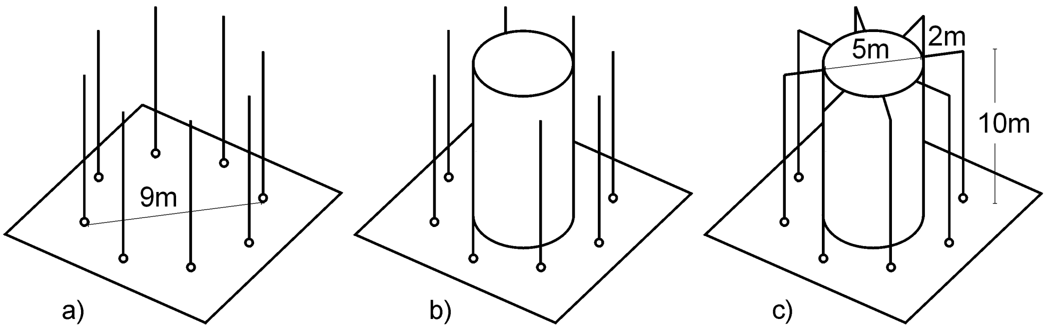

Figure 5.1: Example of three different multi-port radiating structures.

The set of orthonormalized eigenexcitations is the same for the three arrays and is independent on the frequency since, as shown in (5.23), it only depends on the properties of the [Y] matrix, which is circulant and symmetric in the three considered configurations as in (5.22). All the eigenexcitations have the same amplitude as shown in (5.24), while the values of the phases are summarized in Fig.5.2 for the 8-monopoles circular array reference case.

In this paragraph the eigenvalues of the scattering matrix [S] and the eigenpatterns, that is the active reflection coefficients and the gain associated to each eigenexcitation, respectively, are investigated in the HF band. All the simulations are carried out by MoM, assuming the antennas made of aluminium and placed over an infinite perfect ground plane.

In Fig.5.3 the half-sphere averaged gain and the active reflection coefficients (equal at all ports) are plotted for each eigenexcitation (or mode). Eigenexcitations 1 and 5 are real while the pairs of eigenexcitations (2;8), (3;7) and (4;6) are complex conjugate (Tab.5.1). Since complex conjugate eigenexcitations have the same gain and reflection coefficient amplitude, only five different curves appear.

A sort of cut-off frequencies can be observed in the gain of the modes (3;7), (4;6) and 5 in all the three configurations. Before their cut-off, modes

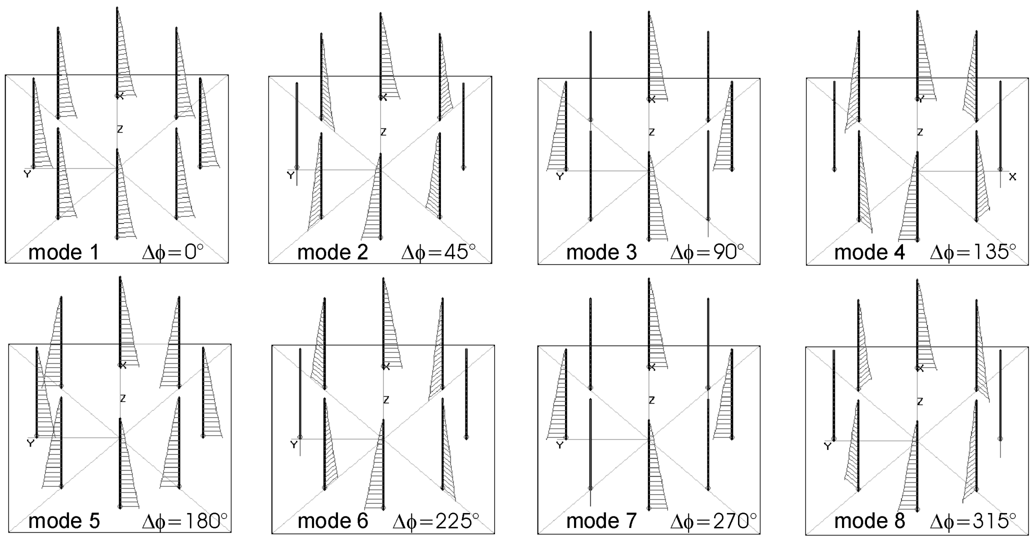

Figure 5.2: Phase relationships between the elements in each eigenexcitation or mode. Current amplitude and phase on each monopole are shown at 3 MHz. $\Delta\phi$ is the phase difference between two adjacent elements.

seem to contribute in negligible way to the radiation and the resulting antenna efficiency approaches to zero because of the ohmic losses. At lower frequencies, in fact, the array elements are very close with respect to the wavelength, and for certain phase relationships between adjacent elements, the transmission line mode can be very dominant on the antenna mode. For instance, in mode 5, which is that with the higher cut-off frequency, adjacent radiating elements are excited with opposite phase (Fig.5.2) and they behave as an actual transmission line. After 12-15 MHz all modes exhibit an averaged gain higher than 0 dB, which retains rather uniform in the rest of the HF band. In all considered cases, the higher gain is achieved by modes 1, where the radiating elements excitation is cophasal and of equal amplitude (Fig.5.2), and (2;8).

For what concerns the active reflection coefficients, modes mainly resonate around the series resonances of the 10m-monopoles (7, 21 and 35 MHz) for the configurations *a* and *b*, while resonate at different frequencies in the structural array (c). From the $|S_{11}|$ curves of case *b*, it is evident that only around 21 and 35 MHz most of the modes are simultaneously matched and therefore

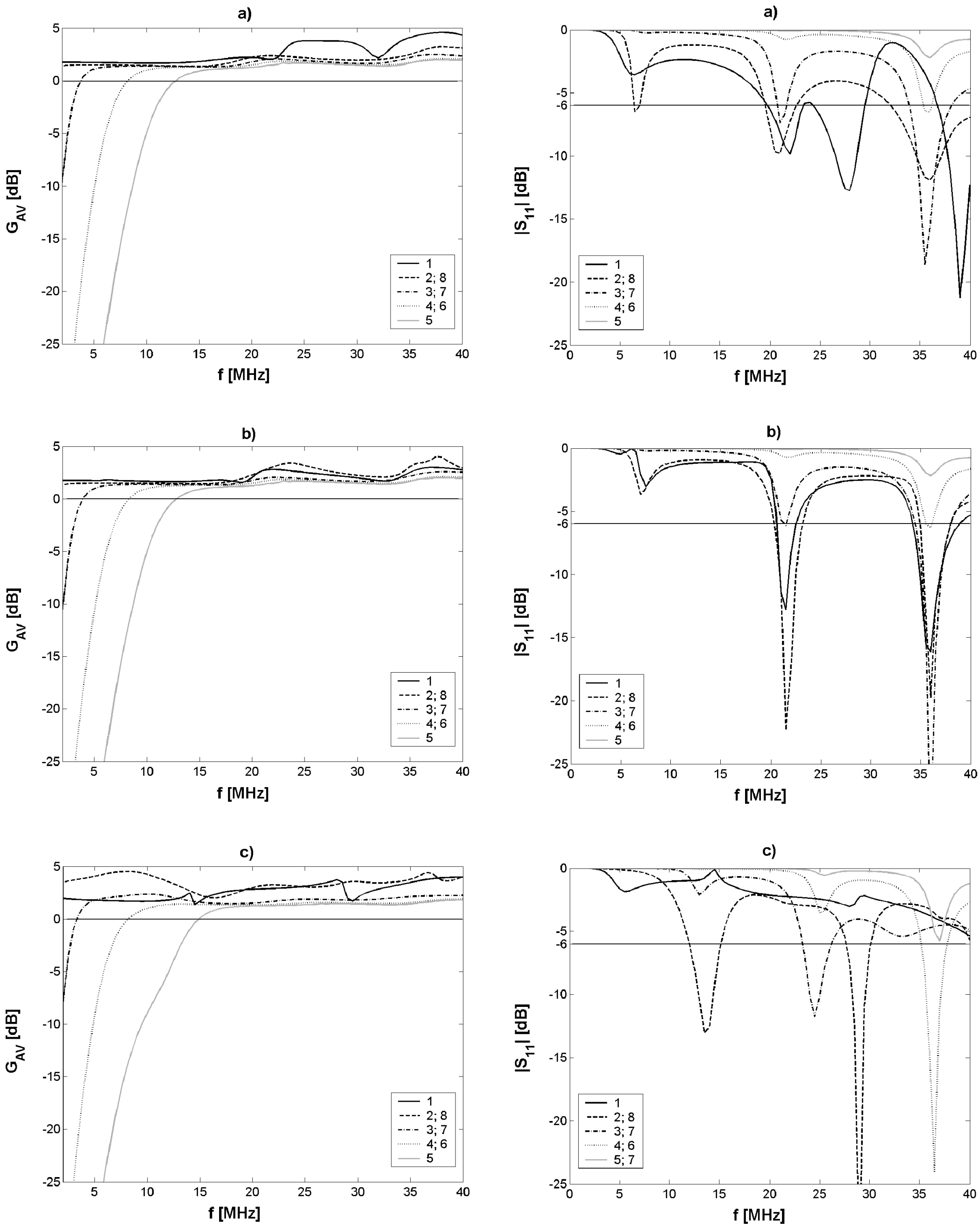

Figure 5.3: Averaged eigenpatterns (left) and eigenvalues of [S] (right) for the structures in Fig.5.1. Curves of $|S_{11}|$ refer to 50Ω; $|S_{11}| < -6dB$ corresponds to VSWR<3.

they can contribute to the total radiation according to the superposition principle in (5.19). In case *c*, the situation is worse because at the frequency where a mode is matched, the others are strongly mismatched and their contribution to the total radiated field is negligible. Such a phenomenon can be also discussed from the point of view of the array degrees of freedom. Using the array at those frequencies where one or more modes are strongly mismatched, and hence are not sensibly contributing to the radiation pattern, is the same as using the array without exploiting all the available degrees of freedom, with a consequent reduction of the shaping capabilities. The array degrees of freedom are fully exploited only at those frequencies where all modes are well matched. In this perspective, the impedance loading or, in general, the antenna broadbanding strategies, can help to take advantage of all the available degrees of freedom for radiation pattern shaping. In the next paragraph a simple way to focus the beam of the loaded NSA_4 system in the HF band is shown, while the radiation pattern synthesis of the NSA will be discussed in detail in the next Chapter.

The half-sphere averaged gain gives an idea of the global radiation of each mode but it does not provide information on how each mode redistributes the power in the half-space. At this purpose, the gain on the principal cuts will be considered.

The first two graphs of Fig.5.4 show the ϕ-averaged gain at the horizon of each mode in the HF band. In particular, the graph on the left refers to the array of monopoles in presence of the cylindrical structure (b) and that on the right corresponds to the structural configuration (c). The graph of the simple array of monopoles (a) is omitted since it is very similar to that of configuration b. In both cases, at lower frequencies the cut-off effect previously discussed is visible, and around 15 MHz all the modes have an horizontal gain higher than 0 dB. Moreover, the gains of configuration b are more uniform than those of configuration c and the nulls around 30 MHz are due to the anti-resonance of the monopoles and the cylindrical structure, whose height is λ at this frequency.

In the middle of Fig.5.4, the horizontal gain at 15 MHz (left) and the vertical gain at 25 MHz (right) of each mode are plotted with respect to ϕ and θ, respectively, for the array of monopoles (a).

The horizontal gain of modes 1, (2;8), (3;7) is fully omnidirectional, modes (4;6) exhibit slight oscillations, while mode 5 strongly oscillates in the range -

20 dB to 10 dB. In this case, as shown in the 3D-radiation-pattern in the inset, the maximum values correspond to the angular positions of the radiating elements, while the nulls occur between two adjacent elements. This general behavior of the modal gains at the horizon is about the same for the structures b and c, and it is not sensibly affected by the presence of the central cylinder. Such a behavior is also rather stable with frequency and it was observed that when the frequency is changed, only the oscillation's dynamics of modes are slightly modified. For instance, if the frequency increases, the oscillation of modes (4;6) becomes more appreciable.

The vertical gains of all modes exhibit a deep null on the zenith for the structure a at all frequencies of the HF band and, therefore, no mode radiates isotropically. The figure on the right shows that, at 25 MHz, modes mainly radiate at elevation angles between 20° and 70° because of the previously mentioned monopoles antiresonance around this frequency, which causes low gain values at the horizon.

Finally, the last two graphs of Fig.5.4, investigate the radiation towards the zenith obtained from modes (2;8) when the cylindrical body is present. In these cases, all the other modes have a deep null in the vertical direction as in the array of monopoles.

The graph on the left shows the gain on the zenith with respect to the frequency, obtained from modes (2;8) in configuration b and c. As expected, the structural array (c) can strongly radiate toward the zenith because of the physical connection of the monopoles to the cylinder that originates a plurality of closed paths operating as loop-like shapes of different size with respect to the wavelengths of the HF band. It is worth noticing that also the array in which the monopoles are not connected to the cylinder (b) radiates toward the zenith, although the gain is lower than that of the structural array. In particular, in the range 20-25 MHz, modes (2;8) exhibit values of gain higher than 0 dB; this effect is due to the excitation of the circular top-edge of the cylinder, whose circumference is about one wavelenght at these frequencies and therefore it behaves as a loop of lenght λ. In Fig.5.5 the current distribution on a loop of length λ and the related radiation pattern in the free space are shown. The currents on the semi-circumferences approximately radiate as a broadside array of two dipoles, having the same current amplitude and phase, and therefore maximizing the gain along the zenith. Moreover, it has been found that the radiation of configuration b and c due to modes (2;8) is circularly polarized on the zenith with an axial ratio $AR = 1$. Such a polarization is caused by the progressive phase difference $\Delta\phi = 45°$ associated to these modes in the case of 8 elements.

The last graph on the right of Fig.5.4 shows the gain on the vertical plane of modes (2;8) at 25 MHz for the three considered structures. The array of monopoles has the null on the zenith, configuration b has a gain of about 1.1 dB in this direction, and the structural array has a null at the horizon and a gain of about 3.9 dB on the zenith, as visible in the nearly spherical 3D-radiation-pattern in the inset.

In order to excite a radiated field $\overrightarrow{E}(\theta,\phi) = \sum_{i=1}^{N} c_i \overrightarrow{E}^{(i)}(\theta,\phi)$ without a null towards the zenith, one or both the eigenexcitations (2;8) will have to be included in the linear combination $\overrightarrow{v} = \sum_{i=1}^{N} c_i \overrightarrow{v}^{(i)}$ presented in (5.5). Any superimposition of all other modes will yield a radiation pattern with a null in the vertical direction at all frequencies.

The discussions made in this paragraph also hold for multi-port NSA systems with loaded sub-radiators. In particular, this analysis corroborates some results found in the previous Chapters concerning NSA radiators:

- The strong coupling among the sub-radiators and the associated cut-off effects degrade the NSA performances at low frequencies (2-5 MHz).
- The broadband behaviour of the NSA corresponds to have all modes well-matched in the HF band and so many degrees of freedom are available to shape the beam at each frequency.
- The presence of the cylindrical structure contributes to the radiation toward the zenith and produces a nearly isotropic radiation at low HF frequencies.

5.2.2 Simple beam focusing of the NSA_4

The modal theory is here used to achieve a beam focusing at the horizon from the NSA_4 in Fig.5.6 placed over an infinite perfect ground plane.

The admittance matrix is circulant and symmetric as in (5.22) and its orthonormalized eigenvectors and eigenvalues are given by equations (5.23) and (5.25). In particular, the eigenexcitations are the following:

$$\overrightarrow{v}^{(1)}=\frac{1}{2}\begin{pmatrix}1\\1\\1\\1\end{pmatrix},\ \overrightarrow{v}^{(2)}=\frac{1}{2}\begin{pmatrix}1\\-1\\1\\-1\end{pmatrix},\ \overrightarrow{v}^{(3)}=\frac{1}{2}\begin{pmatrix}1\\j\\-1\\-j\end{pmatrix},\ \overrightarrow{v}^{(4)}=\frac{1}{2}\begin{pmatrix}1\\-j\\-1\\j\end{pmatrix} \tag{5.30}$$

According to Tab.5.1, $\overrightarrow{v}^{(1)}$, $\overrightarrow{v}^{(2)} \in R$ and $\overrightarrow{v}^{(3)} = \overrightarrow{v}^{(4)*}$. In the first eigenexcitation all the ports are in phase, in the second one adjacent ports have opposite phase, in the third and fourth adjacent ports are in quadrature.

Fig.5.7 shows the eigenpatterns $\overrightarrow{E}^{(i)}(\theta,\phi)$ of the NSA_4, that is the electric far-field radiated by each eigenexcitation. In particular, the amplitudes and phases of the eigenpatterns are plotted at the horizon, where $\overrightarrow{E}^{(i)} = E_\theta^{(i)}\widehat{\theta}$, with respect to the azimuth (abscissa) and frequency (ordinate) in the HF band. Due to the periodicity of the structure, also the eigenpatterns have a periodic azimuthal behavior with a period of 90° in this case of four sub-radiators. The first eigenpattern exhibits a nearly omnidirectional azimuthal radiation up to 28 MHz and a uniform phase up to 20 MHz; the second plot shows low values of radiated field below 10 MHz, high values above 15 MHz where four lobes appear and the phase exhibts four discontinuities of 180°; the third and fourth diagrams show, for a fixed frequency, a gradual phase variation with the azimuth. It can be observed that eigenpatterns 3 and 4 have the same amplitude.

In Fig.5.8 the eigenvalues of the scattering matrix are shown, that is the amplitude of the reflection coefficient, equal at all ports, when the array is driven by each eigenexcitation. Since NSA_4 was loaded to achieve a broad-band behavior, all the modes are matched with a reflection coefficient lower than -6 dB (VSWR<3) in nearly the whole HF band and, therefore, they will all contribute to some extent to the radiation pattern at each frequency. According to $\overrightarrow{E} = \sum_{i=1}^{N} c_i \overrightarrow{E}^{(i)}$, an arbitrary radiated field can be achieved by properly weighing each eigenpattern in amplitude and phase.

The simplest kind of pattern synthesis, without any control on the pattern shape, consists in choosing, for each frequency, $|c_i| = 1$ and $\angle c_i$ so that all the eigenpatterns sum with the same phase along a desired azimuthal direction ϕ_0. For example, for the phases of c_i it can be chosen

$$\angle c_i(f) = -\angle \overrightarrow{E}^{(i)}(90°, \phi_0, f) \tag{5.31}$$

In this way, only the maximum radiation along a given direction is imposed and in Fig.5.9 the resulting patterns when ϕ_0=135° and ϕ_0=180° are shown. In both cases it can be observed that, also by imposing the constructive interference of the eigenpatterns in a given direction, at lower frequencies (f<10 MHz) the array effect is very weak, due to the close proximity of the radiating elements with respect to λ, and the synthesized patterns retain nearly omnidirectional. At intermediate frequencies (10 MHz<f<18 MHz) the array starts to be effective and a single lobe is visible. At higher frequencies secondary lobes appear due to the higher electrical spacing between radiating elements. However, in the whole frequency range the focusing capabilities of the array are limited by the small number of sub-radiators and, therefore, of degrees of freedom.

By using the same c_i coefficients in $\overrightarrow{v} = \sum_{i=1}^{N} c_i \overrightarrow{v}^{(i)}$ at each frequency, the array excitations that give the radiation patterns in Fig.5.9 can be found.

Moreover, by using equation (5.12), here reported for clarity in (5.32), the active input admittance at each port is obtained when the array is focusing along ϕ_0; then, the active reflection coefficients Γ_k^a at each port can be easily calculated by (5.13).

$$Y_{IN,k}^a = \frac{\sum_{i=1}^{N} \lambda^{(i)} c_i v_k^{(i)}}{\sum_{i=1}^{N} c_i v_k^{(i)}} \tag{5.32}$$

Fig.5.10 shows the active VSWR at each port, given by $\frac{1+|\Gamma_k^a|}{1-|\Gamma_k^a|}$, when the array is focusing along $\phi_0 = 180°$. As already found in the 'mono-channel mode' paragraph of Chapter 4, some blind sub-bands appear in the VSWR curves with values higher than 3. Hence, in order to maximize the array performances, it can be necessary to compensate this behaviour by means of more efficient array synthesis strategies, also accounting for matching requirements, as discussed in the next Chapter.

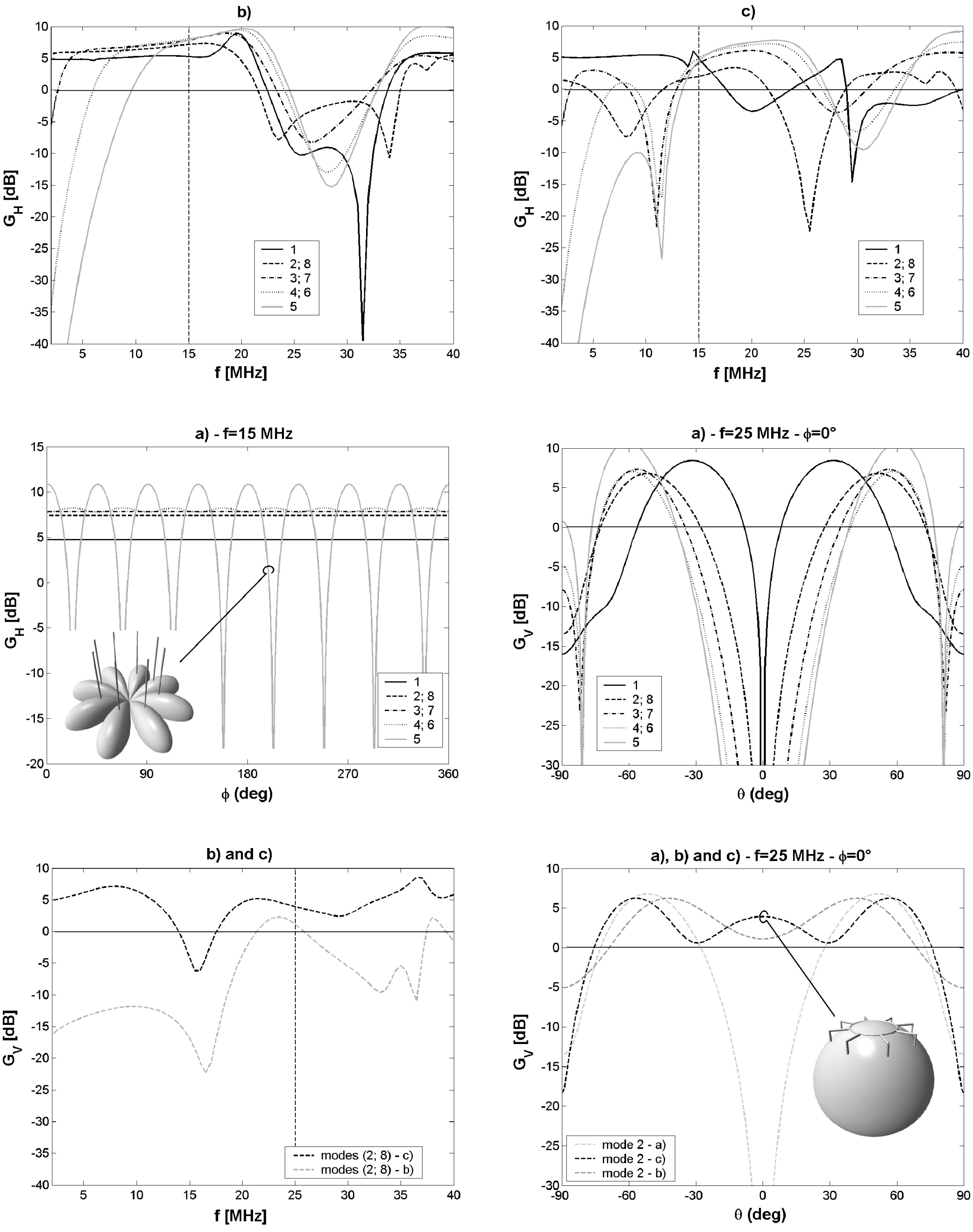

Figure 5.4: *up*) ϕ-averaged gain at the horizon for configurations b (left) and c (right). *middle*) horizontal gain at 15 MHz (left) and vertical gain ($\phi = 0°$) at 25 MHz (right) for configuration a. *down*) gain on the zenith with respect to the frequency achieved by modes (2;8) for configurations b and c (left); vertical gain ($\phi = 0°$) at 25 MHz for the three configurations (right).

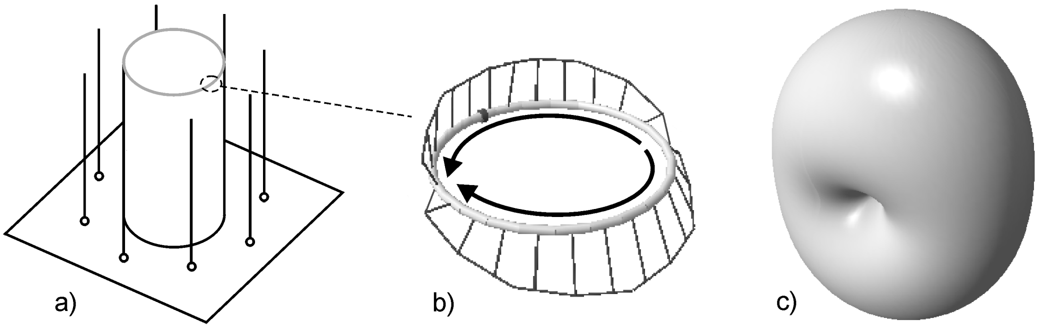

Figure 5.5: *a*) Array of configuration *b*. *b*) excitation of the loop mode at 25 MHz where the top-edge circumference is about λ. *c*) Radiation pattern of a loop of length λ in the free space.

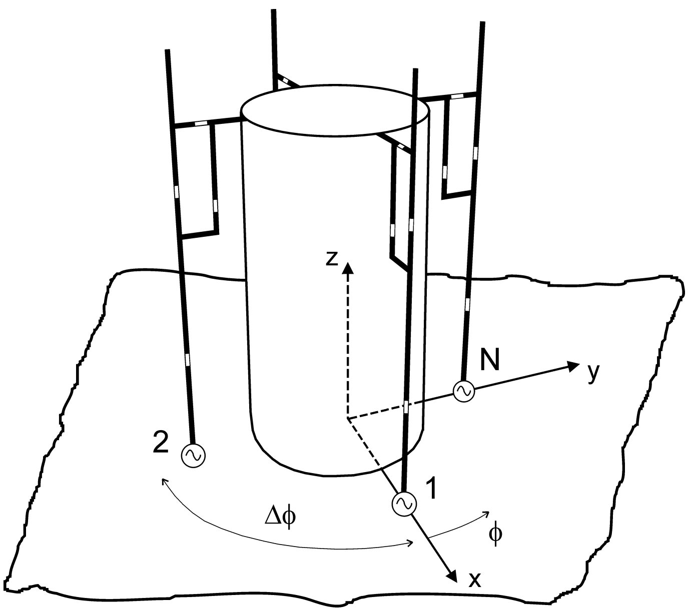

Figure 5.6: Multiple-feed loaded NSA_4 over an infinite perfect ground plane.

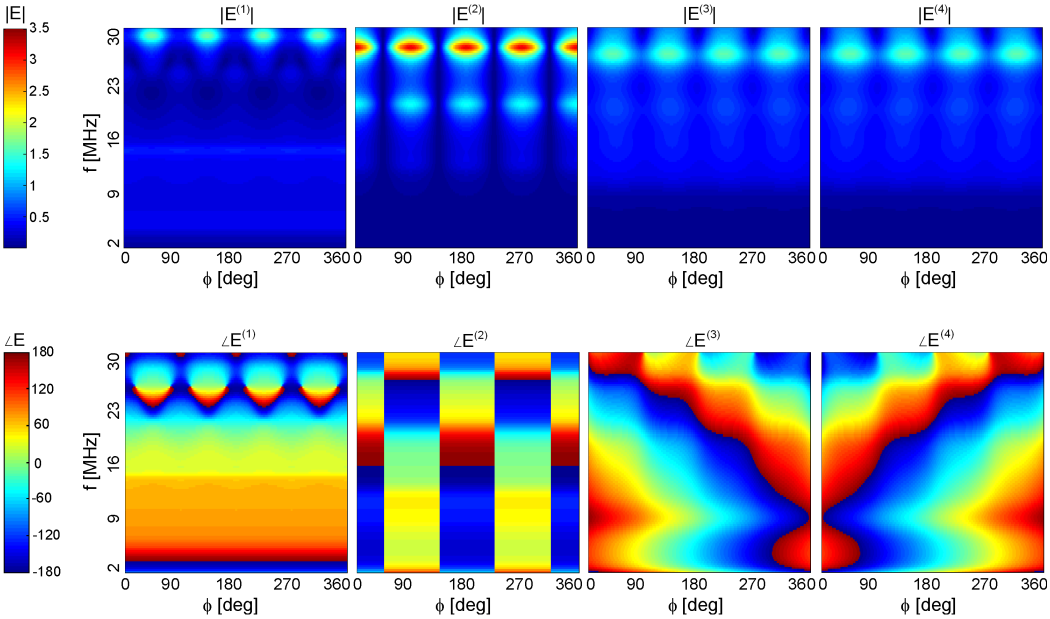

Figure 5.7: Eigenpatterns of the NSA_4 in Fig.5.6. Plots are independent on the distance r. *up*) Amplitude patterns of $rE_\theta^{(i)}$. *down*) Phase patterns of $re^{jkr}E_\theta^{(i)}$.

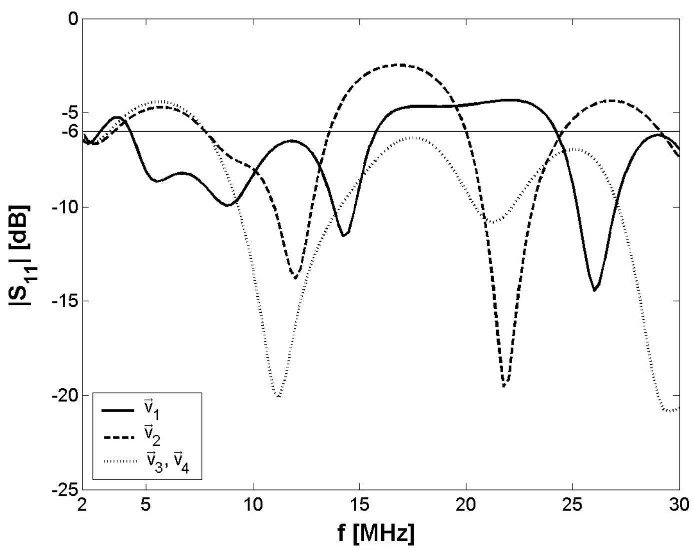

Figure 5.8: Amplitude of the reflection coefficient (eigenvalues of the scattering matrix [S]), referred to 200Ω and equal at all ports, for each eigenexcitation.

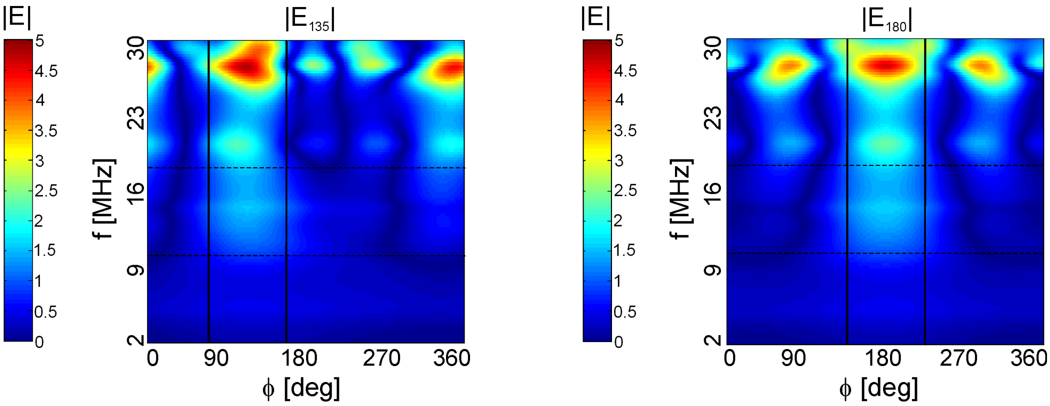

Figure 5.9: Pattern synthesis obtained by properly choosing, at each HF frequency, the phases of c_i. *left*) beam focusing on ϕ_0=135°.*right*) beam focusing on ϕ_0=180°.

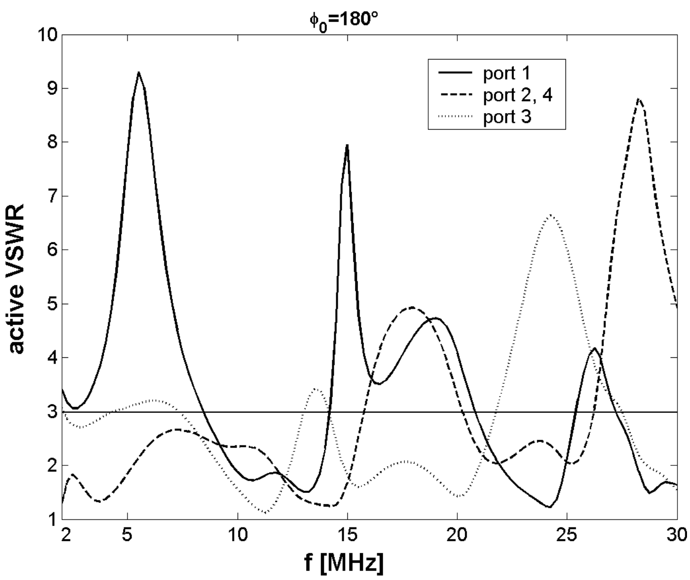

Figure 5.10: Active VSWR (referred to 200Ω) at the ports when the array is focusing on $\phi_0 = 180°$ (see Fig.5.6).

Chapter 6

Design of highly coupled circular arrays

After a short recall of the main properties and the basic theory of the circular array, this Chapter considers the radiation pattern synthesis of the NSA in coherent configuration.

When the geometry of the array is known, a problem of synthesis consists of determining the element excitations (amplitudes and phases) in such a way that the corresponding pattern satisfies prescribed conditions.

The basic theory of the circular array neglects the inter-element couplings and assumes that all the radiating elements have the same radiation patterns. Such a theory is not applicable to the NSA because the sub-radiators are placed at a close proximity with respect to the wavelength and, therefore, they are highly coupled; moreover, the radiation patterns of the sub-radiators connected to the cylinder are not omnidirectional and are not the same because they are reciprocally rotated in azimuth. For these reasons it is not possible to extract a true array factor from the total radiated field expression of the NSA and the conventional beam synthesis techniques, e.g. Chebyshev, Taylor, Schelkunoff, cannot be exploited.

In this case, the synthesis has to be directly performed on the total radiated far-field expression and two different methods are here considered, both taking into account the inter-port coupling. The first one is based on the active element factor concept, already introduced in Chapter 4, the second one on the modal approach fomulated in the previous Chapter. These methods have the additional advantage to directly synthesize the array in its real environment, for instance a complex naval scenario, without assuming the approximated hypothesis of free space as the conventional beam synthesis techniques do.

In order to control the beam shaping of the NSA, and not only the direction of maximum radiation, a mask for the desired radiation pattern has to be defined. Moreover, it may be desirable that array ports retain well-matched (active VSWR<3) in order to maximize the use of the available power, or that the ratio between the maximum and minimum excitation amplitudes be limited for feasibility reasons. At this purpose, two kinds of constrained optimizations are considered: in the first case the active element factor theory is used together with a stochastic optimizer based on a Genetic Algorithm, in the second case the modal synthesis is combined with a deterministic and iteratve algorithm.

6.1 Circular arrays

6.1.1 Main properties and applications

Array configurations in which the elements are placed in a circular ring are of very practical interest. They find applications in radio direction finding, smart antennas, air, space and coastal navigation, underground propagation, radar, sonar and many other systems. An application example is the development of the Traffic Collision-Avoidance and Alert System (TCAS), started in the early 1970's, whose function is to help aircraft pilots to avoid mid-air collisions. TCAS systems generally consist of a pair of eight-elements circular arrays, placed on the top and the bottom of the aircraft fuselage [39].

Uniform circular array (UCA), in which the radiating elements are uniformly disposed on a circle, has some important advantages over uniform linear array (ULA) and uniform retangular array (URA) [40]. For instance, though a uniform linear array exhibits excellent directivity and can form a very narrow main lobe in a given direction, it does not work equally well in all azimuthal directions. In this case, scanning of the radiation beam can be obtained by combining a few linear phased arrays, whose sectorial coverages add to give the desired 360° scan, which is required in many applications. At the contrary, due to its intrinsic symmetry and to the absence of edge elements, the UCA has the capability to azimuthally scan the beam through 360° with little change in either the beamwidth or the sidelobe level, and the beam steering can be simply achieved by circularly shifting the array excitations. Although mechanical scanning antennas can be used at this purpose, phased circular arrays can be particularly useful to satisfy the need for high speed scanning or when a fast reconfigurability of the main-lobe direction is required, as in the case of smart antenna systems [41]. Another important feature of the UCA, coming from its symmetry, is the possibility of producing patterns which are omnidirectional in azimuth.

Besides the radiation pattern invariance with the scan angle, circular arrays have the interesting characteristic to generate a main beam and sidelobes that are also independent on frequency. This is due to the fact that the far field pattern can be represented in terms of orthogonal phase modes (modes of unit amplitude and linear-phase-azimuth variation) and, so long as the relative amplitudes of these modes are controlled to be constant, the entire pattern retains constant with frequency as discussed in [42].

On the other hand, a circular array is a high-sidelobe geometry. In particular, the radiation pattern of rather large structures has -8 dB sidelobes when the element excitation is cophasal and of equal amplitude [43]. Sidelobes can be reduced by tapering the excitation amplitudes, by appropriate phase adjustment, by adding additional concentric rings to obtain spatial tapering, or by decreasing the distance of array elements [44], [45]. In this case, however, the mutual coupling effects, that in general are more severe than in ULAs beacause of the array geometry, can become more significant and difficult to be handled.

6.1.2 Array factor of a circular array

As shown in [17], by neglecting the coupling between the elements, the array factor of a circular array of N equally spaced elements on a ring of radius a, is given by

$$AF(\theta,\phi)=\sum_{n=1}^{N} I_n e^{j[ka\sin\theta\cos(\phi-\phi_n)+\alpha_n]} \tag{6.1}$$

where I_n and α_n are, respectively, the amplitude and phase excitation of the nth element and ϕ_n $=2\pi(n-1)/N$ is its angular position in the array; the first element is supposed to be in $\phi_1 = 0°$. To direct the peak of the main beam in the (θ_0, ϕ_0) direction, the phase excitation of the nth element can be chosen to be

$$\alpha_n = -ka\sin\theta_0\cos(\phi_0-\phi_n) \tag{6.2}$$

By supposing to have isotropic elements, assuming a uniform excitation ($I_n = I_0$) and using (6.1) and (6.2), the performances of the circular array radiation at the horizon (θ_0=90°) are investigated for a different number of radiating elements N and for different values of the array radius a. In Tab.6.1 d is the distance between two adjacent array elements, BW_{-3dB} is the half-power beamwidth of the main beam, SSL indicates the level of the sidelobes with respect to the main lobe, $FTBR$ is the front to back ratio and GL indicates the numer of grating lobes in the azimuthal $2\pi-$angle. As expected from the general array theory, for a small number of elements ($N = 4$ and 6) some grating lobes appear when $d > \lambda/2$ and high levels of sidelobes, low values of FTBR and large beamwidths can be observed. Also, the radiation pattern modifies for what concerns SLL and FTBR when the focusing direction is changed. For a larger number of elements ($N > 10$), and hence for large structures with respect to the wavelength, the array effect is more evident and better performances are obtained. In particular, the level of the sidelobes assumes the typical -8dB value, FTBR improves and the main lobe becomes very narrow. Moreover, the beamwidth of the main lobe and the sidelobe levels become nearly invariant with the scan angle (as indicated with '$\forall\phi_0$' in the Table).

In Fig.6.1 the normalized array factors of four configurations in Tab.6.1 are shown. In the first two cases (N = 10 and 20), two different plots are represented, referring to the focusing on ϕ_0 and ϕ_0+$\Delta\phi/2$, where $\Delta\phi = 2\pi/N$ is the angle between two adjacent elements. When the main lobe moves from

Table 6.1: Array Factor performances for different values of N and a

N	**a**	$\boldsymbol{\phi_0}$	**d**	**BW**$_{-3dB}$	**SLL**	**FTBR**	**GL**
4	$\lambda/2$	$0°$	0.7λ	$42°$	0 dB	0 dB	4
4	$\lambda/2$	$45°$	0.7λ	$41°$	-5.8 dB	11.5 dB	–
4	λ	$0°$	1.41λ	$21°$	-11.5 dB	0 dB	4
4	λ	$45°$	1.41λ	$20°$	-1.3 dB	1.3 dB	–
6	$\lambda/2$	$0°$	0.5λ	$41°$	-6.8 dB	9.5 dB	–
6	$\lambda/2$	$30°$	0.5λ	$41°$	-2.2 dB	2.2 dB	–
6	λ	$0°$	λ	$21°$	-7.3 dB	0 dB	1
6	λ	$30°$	λ	$21°$	-0.6 dB	11.7 dB	–
10	$\lambda/2$	$\forall\phi_0$	0.31λ	$42°$	-7.9 dB	$12-14$ dB	–
10	λ	$\forall\phi_0$	0.62λ	$21°$	-3 dB	*variable*	–
20	λ	$\forall\phi_0$	0.31λ	$21°$	-7.9 dB	$\simeq 16$ dB	–
20	$3\lambda/2$	$\forall\phi_0$	0.47λ	$13.6°$	$-7.9dB$	*variable*	–
50	2λ	$\forall\phi_0$	0.25λ	$10.2°$	-8 dB	$\simeq 19$ dB	–
50	3λ	$\forall\phi_0$	0.37λ	$6.7°$	-8 dB	$\simeq 21$ dB	–
50	4λ	$\forall\phi_0$	0.5λ	$5°$	-8 dB	$10-15$ dB	–
100	4λ	$\forall\phi_0$	0.25λ	$5°$	-8 dB	22 dB	–
100	5λ	$\forall\phi_0$	0.31λ	$4°$	-7.9 dB	23 dB	–
200	8λ	$\forall\phi_0$	0.25λ	$2.4°$	-8.4 dB	25 dB	–

ϕ_0 to $\phi_0 + \Delta\phi/2$, the beamwidth and the level of the secondary lobes remain unchanged, while some variations can be in general observed in the FTBR, as also indicated in the Table. It is worth noticing that the array factor when focusing on a given direction ϕ_0 is a periodic function and therefore its properties can be investigated only in the angular region $[\phi_0, \phi_0 \pm \Delta\phi/2]$, then they periodically repeat. Fig.6.1 also shows the array factor in the cases of $N = 100$ and 200 radiating elements, where very narrow main lobes and high values of FTBR can be achieved.

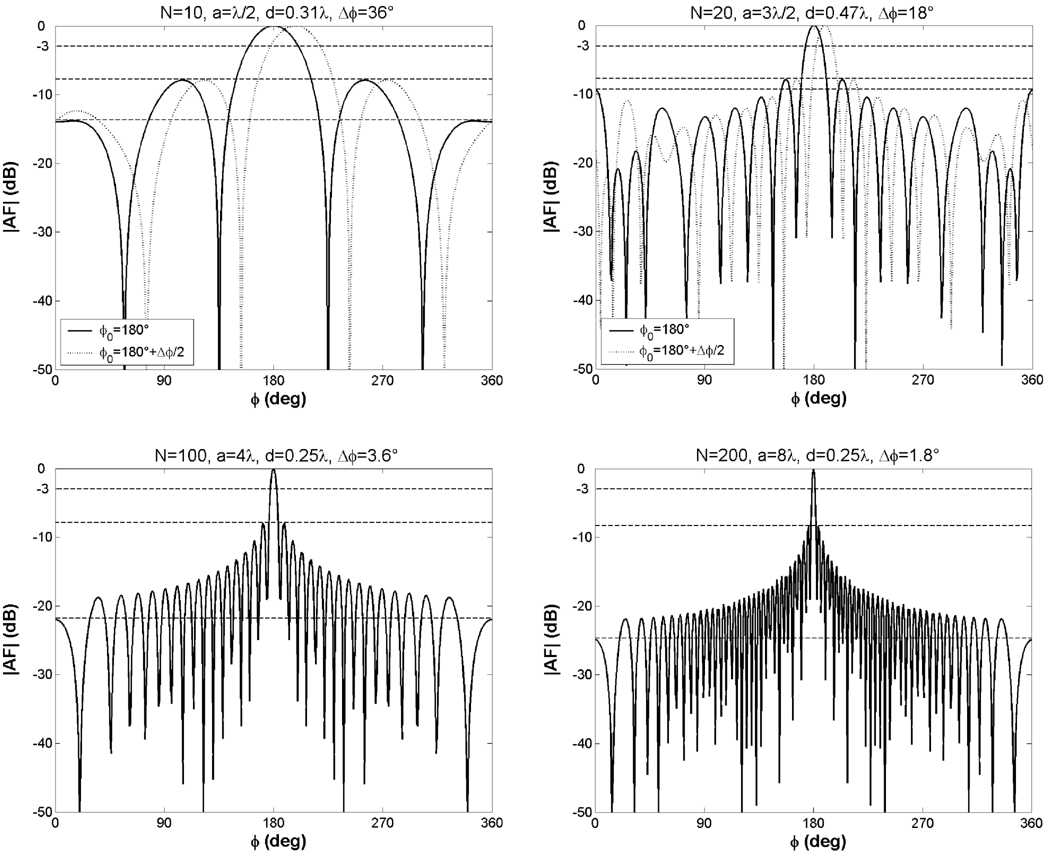

Figure 6.1: Array factors on the array plane (horizontal plane) for different values of N and a. The four configurations corresponds to the rows in italic in Tab.6.1.

6.2 Design methods

In the previous Chapters two simple kinds of NSA radiation pattern synthesis were introduced.

In the 'mono-channel mode' paragraph of Chapter 4 the active element factor theory [25] was used to obtain the expression of the total radiated far-field in (4.3) taking into account the inter-port coupling. The beam focusing at the horizon on a desired direction ϕ_0 was then obtained by choosing the excitation phases as in (4.4). In such a way the active element factors associated to each port could constructively interact along this direction. No control of the pattern shaping, active port-matching and excitation amplitude was performed. The horizontal radiation patterns obtained at some HF frequencies in the case of NSA equipped with 6 elements and focusing on $\phi_0 = 30°$ are reported for clarity in Fig.6.2. Fig.6.3 reports the active VSWR at each port where blind sub-bands with values higher than 3 were found.

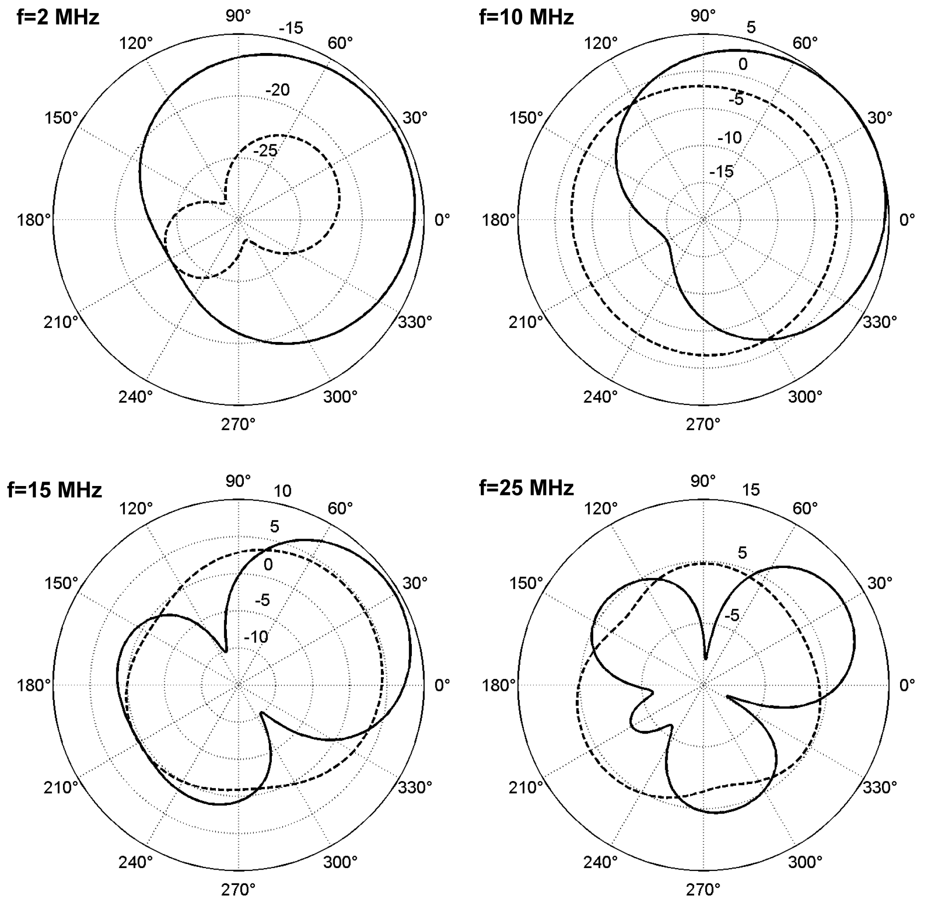

Figure 6.2: Azimuthal gain patterns of the NSA_6 steered to $\phi_0 = 30°$ (solid line) compared with those of the NSA_1 oriented alog ϕ_0 (dashed lines).

In the last paragraph of the previous Chapter, instead, the modal approach was used to obtain the expression of the total radiated far-field of the NSA equipped with 4 sub-radiators. Also this method considers the inter-port coupling and expresses the total far-field as the linear combination of an orthogonal set of eigenpatterns according to (5.19). The simplest kind of pattern synthesis, without any control of the pattern shaping, port matching and excitation amplitude consists in choosing $|c_i| = 1$ and $\angle c_i$ according to

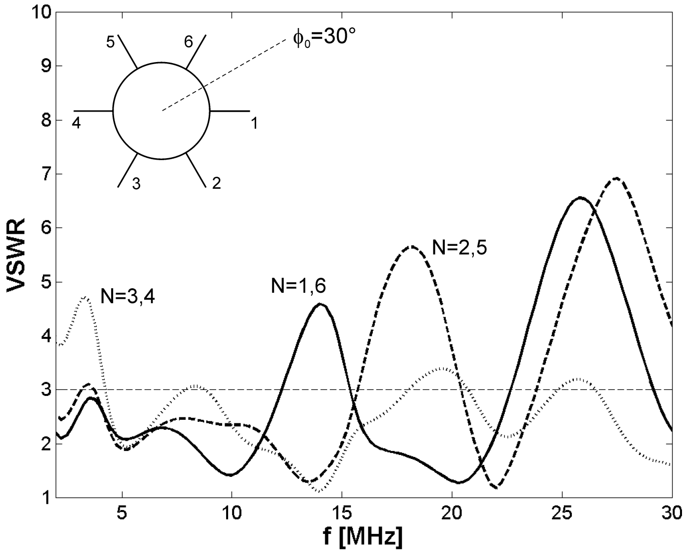

Figure 6.3: VSWR at each port of the NSA_6 on-PEC when $\phi_0 = 30°$; due to antenna simmetry as regards ϕ_0, pairs of symmetric sources share the same VSWR curve. VSWR is referred to 200Ω.

(5.31). In this way all the eigenpatterns sum with the same phase along a desired azimuthal direction ϕ_0. The beam focusing on the horizontal plane at each frequency for two different directions of ϕ_0 and the active VSWR at each port when the array is focusing on $\phi_0 = 180°$ were shown in Fig.5.9 and Fig.5.10. Also in this case blind sub-bands were visible with values of VSWR higher than 3.

In order to compensate this behaviour, two efficient constrained synthesis strategies are presented in the following paragraphs, also accounting for radiation pattern shaping, port-matching and excitation amplitude requirements.

Coupling-constrained array pattern synthesis have received considerable interest starting from the late 1960 [46]. Different techniques [47], [48], have been used to shape the pattern and, at the same time, to design matching networks able to mitigate the impedance change of the radiating elements in steerable-beam arrays. In the Software Defined Radio context, signal waveforms to be transmitted can be easily managed by the processing unit with the possibility to digitally set their amplitude and phases [49]. The impedance-matching and radiation-pattern constraints optimization can be therefore more easily formulated straight in terms of amplitudes and phases.

6.2.1 GA synthesis

This is a multi-objective optimization strategy that permits to control not only the pattern shaping, but also the active port matching. The method is based on the theory of the active element factor [25] combined with a Genetic Algorithm for the opimization of the array excitations.

The overall radiated field can be expressed in terms of the active element factors $\overrightarrow{E}_n(r,\theta,\phi,f)$, as found in (4.2) and (4.3), and it is here repeated for clarity:

$$\overrightarrow{E}(r,\theta,\phi,f) = \sum_{n=1}^{N} A_n(f)\overrightarrow{E}_n(r,\theta,\phi,f) \tag{6.3}$$

The objective function here considered for the solution of the $\{A_n\}$ excitation coefficients is composed by two terms, referring to pattern shaping and port matching at a given frequency:

$$F = w_{Gh}F_{Gh} + w_{VSWR}F_{VSWR} \tag{6.4}$$

F_{Gh} and F_{VSWR} are the normalized functions described in Appendix B ('On-PEC NSA$_N$ excitation' paragraph), respectively controlling the horizontal gain and the port matching; w_{Gh} and w_{VSWR} are the related weighing coefficients. In order to perform an unconstrained optimization of the radiation pattern, without any control of the port matching, the coefficient w_{VSWR} can be set to zero.

As an example, in Fig.6.4 gray regions represent the penalty associated to the horizontal gain and VSWR. In particular, on the left the horizontal gain mask used in the following examples is shown, characterized by three parameters: main lobe level (MLL), side-lobe level (SLL), and angular region where the main lobe is desired (BW). On the right, the threshold s_0 for the active VSWR can be seen.

Now it will be shown how the synthesis here considered has the capability to eliminate the NSA$_6$ blind sub-bands of Fig.6.3 and to moderately shape

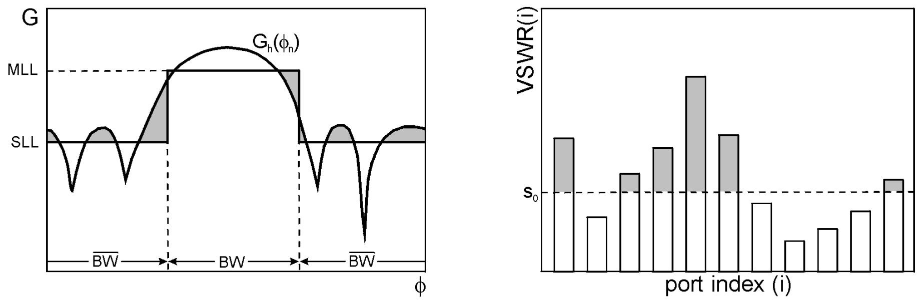

Figure 6.4: Example of penalty associated to the horizontal gain and VSWR with respect to the gain mask and VSWR threshold.

the beam improving, for example, the FTBR or modifying the main lobe beamwidth.

In general, supposing to optimize both the amplitudes and phases of the excitations, $D = 2N-2$ degrees of freedom are available (the amplitude and phase of one port are fixed as a reference); in the considered case $N = 6$ and $D = 10$. By imposing the symmetry of the radiation pattern with respect to ϕ_0=30° direction, and hence the symmetry of the excitations, the degrees of freedom reduce to $D = 2(N/2) - 2 = N - 2$; in the considered case $D = 4$. The synthesis, with the constraint of VSWR<3 at each port, is performed at those frequencies where the mismatching is more evident in Fig.6.3, that is at 3.5, 14, 18 and 27.5 MHz. The synthesized radiation patterns are shown in Fig.6.5.

Despite the small number of degrees of freedom ($D = 4$) and the constraint on the port matching, acceptable gain values are obtained. Moreover, due to the choice of a gain mask, better values of FTBR than those of Fig.6.2 are in general achieved. The corresponding values of VSWR (GA) at the various ports are shown in Tab.6.2 and are compared with those obtained in Fig.6.3 (*phase*).

With the proposed method of synthesis, the achieved VSWR values in Tab.6.2 are always lowen than 3.15. In this way, array performances are optimized since the input power and, therefore, the radiated power are maximized. It can be observed that ports 3 and 4 are turned off at 18 MHz; in this case the optimizer is not able to simultaneously lower the active VSWR on all ports and, so, the highly mismatched ports can be turned off without

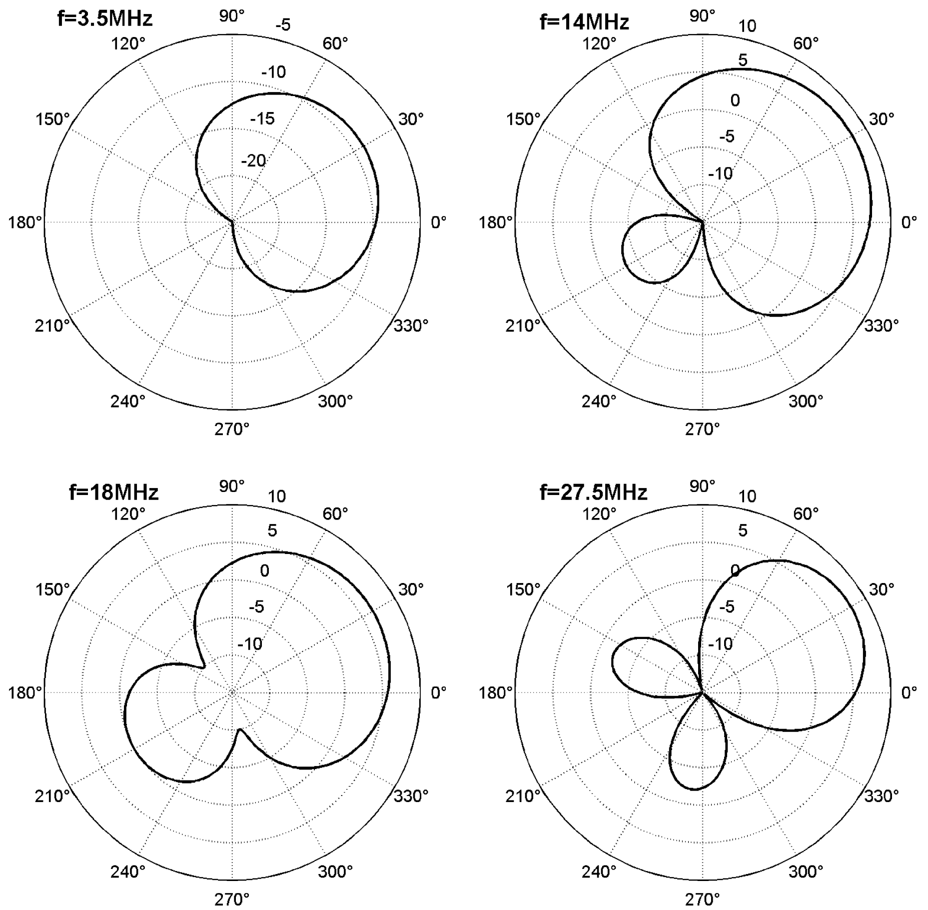

Figure 6.5: Synthesized pattern obtained with $D = 4$ degrees of freedom and with the constraint of port matching (VSWR<3.5).

sensibly affecting the radiation pattern.

In order to focus the beam in angles that differ from the intermediate direction between two sub-radiators, the symmetry of the excitations has to be removed and a greater number of degrees of freedom can be exploited. Using the simple phase synthesis of Chapter 4, it was verified that antenna matching degrades as ϕ_0 moves from the central position between two adjacent sub-radiators towards one of them (Fig.6.6).

This problem can be solved again by a GA synthesis as shown in Tab.6.3 at 14 MHz. The high values of VSWR on port-1 (*phase*) are lowered under 3 (*GA*) without sensibly affecting the radiation patterns (Fig.6.7).

In conclusion, the constrained GA optimzation can be very useful to

Table 6.2: VSWR at the ports when the array is focusing on 30°. 'GA' indicates the constrained optimization method here proposed, 'phase' indicates the simple phase synthesis described in 'mono-channel mode' paragraph of Chapter 4.

f [MHz]	method	ϕ_0	port-1	port-2	port-3	port-4	port-5	port-6
3.5	*GA*	30°	2.92	3.11	3.08	3.08	3.11	2.92
	phase	30°	<3	<3	**4.64**	**4.64**	<3	<3
14	*GA*	30°	2.77	2.93	1.32	1.32	2.93	2.77
	phase	30°	**4.59**	<3	<3	<3	<3	**4.59**
18	*GA*	30°	2.30	3.14	Off	Off	3.14	2.30
	phase	30°	<3	**5.63**	<3	<3	**5.63**	<3
27.5	*GA*	30°	2.14	2.59	2.36	2.36	2.59	2.14
	phase	30°	**5.16**	**6.92**	<3	<3	**6.92**	**5.16**

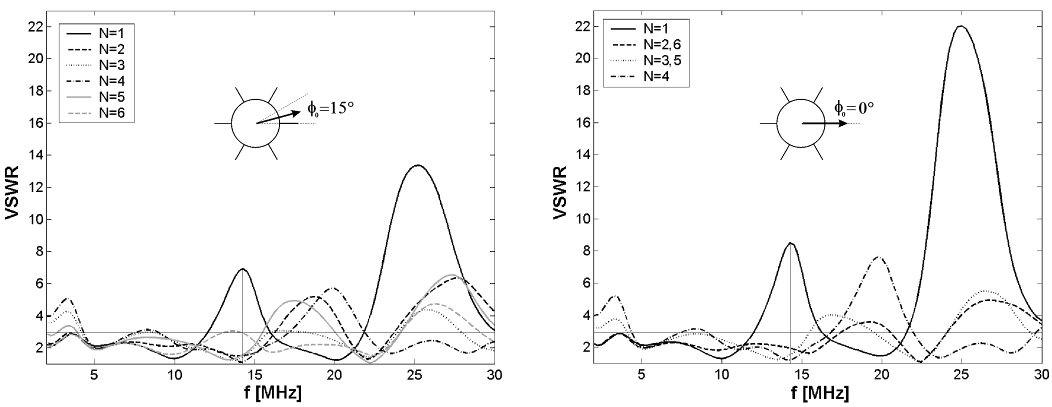

Figure 6.6: Active VSWR obtained with method 'phase'. *left)* focusing on $\phi_0 = 15°$. *right)* focusing on $\phi_0 = 0°$.

achieve sectorial coverage around a given angular direction controlling at the same time the port matching. However, there is a small set of frequencies, for instance 26 MHz, in which it was verified that the array ports cannot be simultaneously matched even if the gain requirement in (6.4) is strongly relaxed.

Finally, it is worth noticing that in all the considered optimizations, the ratio between the maximum and minimum voltage amplitude of the array

Table 6.3: VSWR at the ports when the array is focusing on 15° and 30° at f=14 MHz using methods 'GA' and 'phase'.

f [MHz]	method	ϕ_0	port-1	port-2	port-3	port-4	port-5	port-6
14	*GA*	15°	2.24	1.98	1.06	2.80	2.17	2.03
	phase	15°	**6.77**	<3	<3	<3	<3	<3
14	*GA*	0°	2.88	2.87	1.29	1.22	1.75	2.27
	phase	0°	**8.14**	<3	<3	<3	<3	<3

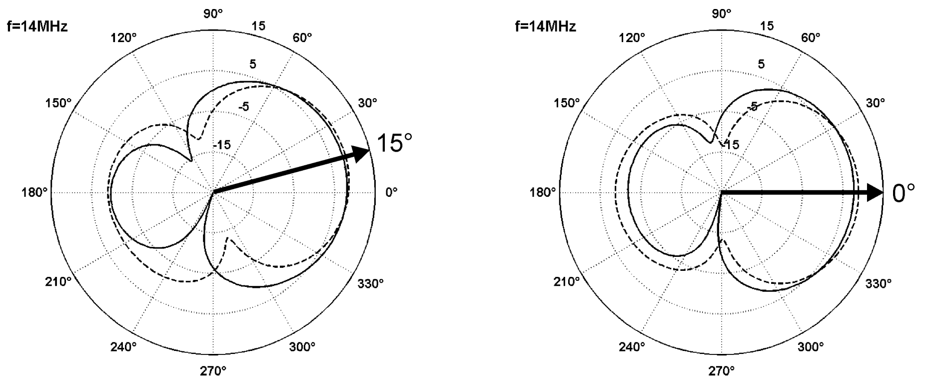

Figure 6.7: Focusing on $\phi_0 = 15°$ (left) and $\phi_0 = 0°$ (right). Solid lines tag '*GA*' method, dashed lines tag '*phase*' method.

excitations is completely acceptable and feasible without performing any control on it. In particular, it was found $\frac{|V\max|}{|V\min|} < 5$.

6.2.2 Modal synthesis

This method is based on the theory formulated in the previous Chapter and utilizes the orthogonality properties of characteristic modes to synthesize the desidered radiation pattern over all space in a mean square error sense. This feature may be desirable in some cases, but the method suffers from the disadvantage of computational complexity when the radiation pattern is required to be optimized, for instance, along a particular cut.

In the following paragraphs, at first an unconstrained modal synthesis is considered, where a desired pattern is given and synthesized. In the second paragraph a constrained optimization is proposed combining the modal synthesis with the iterative method of the alternate projections [50], [51]. In this case, the radiation pattern can be optimized together with the port voltage-amplitude or port matching control. Some examples are shown for a canonical circular array of monopoles and for the NSA above an infinite perect ground plane.

The main differences between modal and GA synthesis are that in the first method a bidimensional gain mask is required even if the radiation pattern has to be shaped along a particular cut, and the optimization process is deterministic, and hence faster, instead of stochastic.

Unconstrained modal synthesis

The modal synthesis of the radiation pattern at a given frequency is composed of three main steps:

1. Assignment of the desired bidimensional far-field mask $\overrightarrow{E}_d(\theta,\phi)$. In general $\overrightarrow{E}_d(\theta,\phi) = E_{d\theta}(\theta,\phi)\widehat{\theta} + E_{d\phi}(\theta,\phi)\widehat{\phi}$ and, therefore, two bidimensional masks can be assigned; moreover, each mask $E_{d\theta}(\theta,\phi)$ and $E_{d\phi}(\theta,\phi)$ can be specified in amplitude and phase. In the following examples of this Chapter, without loss of generality $E_{d\phi}(\theta,\phi) = 0$ will be assumed and only the amplitude $|E_{d\theta}(\theta,\phi)|$ will be assigned, by supposing $\angle E_{d\theta}(\theta,\phi) = 0$.

2. Computation of c_i coefficients according to (5.21), here reported for clarity for what concerns the general case:

$$c_i = \frac{1}{K_{ii}} \left\langle \overrightarrow{E}_d, \overrightarrow{E}^{(i)*} \right\rangle \tag{6.5}$$

where

$$K_{ii} = \mathrm{K}_{\theta ii} + \mathrm{K}_{\phi ii} = \iint\limits_{4\pi} \left|E_\theta^{(i)}\right|^2 \sin\theta d\theta d\phi + \iint\limits_{4\pi} \left|E_\phi^{(i)}\right|^2 \sin\theta d\theta d\phi \tag{6.6}$$

and

$$\left\langle \overrightarrow{E}_d, \overrightarrow{E}^{(i)*} \right\rangle = \iint\limits_{4\pi} \overrightarrow{E}_d(\theta,\phi)\cdot\overrightarrow{E}^{(i)*}(\theta,\phi)\sin\theta d\theta d\phi \tag{6.7}$$

that is

$$\left\langle \overrightarrow{E}_d, \overrightarrow{E}^{(i)*} \right\rangle = \iint\limits_{4\pi} (E_{d\theta}E_\theta^{(i)*} + E_{d\phi}E_\phi^{(i)*})\sin\theta d\theta d\phi \tag{6.8}$$

3. Computation of the synthesized excitation vector $\overrightarrow{v}_s$ by (5.5), here reported for clarity:

$$\overrightarrow{v}_s = \sum_{i=1}^{N} c_i \overrightarrow{v}^{(i)} \tag{6.9}$$

The excitation vector $\overrightarrow{v}_s$ will produce a field $\overrightarrow{E}_s(\theta, \phi)$ which synthesizes the mask $\overrightarrow{E}_d(\theta, \phi)$ in a mean square error sense. It has to be observed that the double integrals in (6.6) and (6.7) will be computed on the 4π-sphere if the array is in the free space and on the 2π-half-sphere in presence of an infinite perfect ground plane.

In Fig.6.8 a simple scheme for the unconstrained modal synthesis is summarized. In particular, T operator gives the far-field produced by a given excitation vector, while T^{-1} is the inverse transformation which, starting from a far-field mask and passing through the computation of c_i coefficients, synthesizes the corresponding excitation vector.

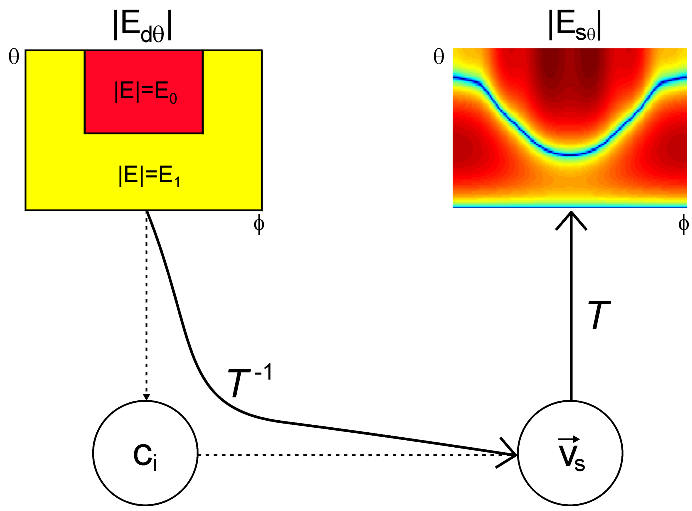

Figure 6.8: Scheme for the unconstrained modal synthesis. For the desired far-field mask it is here assumed $E_{d\phi}(\theta, \phi) = 0$ and $\angle E_{d\theta}(\theta, \phi) = 0$.

In order to demonstrate the effectiveness of the method, some examples are shown considering a circular array of monopoles above an infinite perfect ground plane. In this case, for any array excitation, and hence also for the eigenexcitations, the far-field has only the θ-component ($\overrightarrow{E}(\theta, \phi) =$

$E_\theta(\theta,\phi)\widehat{\theta})$ and exhibits a null along the zenith (θ=0°), as found in the modal analysis of Chapter 5. Consequently, (6.6) reduces to:

$$K_{ii} = \mathrm{K}_{\theta ii} = \iint\limits_{2\pi} \left| E_\theta^{(i)} \right|^2 \sin\theta d\theta d\phi \qquad (6.10)$$

and (6.8) becomes:

$$\left\langle \overrightarrow{E}_d, \overrightarrow{E}^{(i)*} \right\rangle = \iint\limits_{2\pi} E_{d\theta} E_\theta^{(i)*} \sin\theta d\theta d\phi \qquad (6.11)$$

In this configuration the computation of coefficients c_i by (6.5) is simplified.

Moreover, due to the antenna geometry, the array effect is stronger on the horizontal plane (θ=90°) and, therefore, the far-field masks are expected to be better matched for high values of theta ($60° \lesssim \theta \leq 90°$); at higher elevation angles the radiation pattern control is expected to be weak.

In the following examples the normalized desired and synthesized far-fields ($|E_{d\theta}|$ and $|E_{S\theta}|$) are shown together with the synthesized horizontal and 3D-total-gain. For each configuration, the synthesized values of c_i and $\overrightarrow{v}_i$, the ratio $\frac{|V\max|}{|V\min|}$, FTBR, SLL and maximum gain on the horizontal plane are reported. The monopoles' height is fixed to $h = \lambda/4$.

In the first case, the number of array elements is $N = 6$, the array radius is $a = \lambda/2$ and the inter-element spacing is $d = \lambda/2$. The desired mask imposes a single lobe in the angular region $45° \leq \theta \leq 90°$, $0° \leq \phi \leq 180°$. The mask and the synthesized radiation patterns are shown in Fig.6.9.

The amplitudes and phases of c_i and $\overrightarrow{v}_i$ are reported in Tab.6.4

Eigenpattern 1 (uniform excitation) provides the maximum contribution to the radiated field ($|c_1|$=1), while eigenpatterns 3 and 5 ($|c_{3,5}|$=6e-3) and eigenpattern 4 pratically do not contribute to the total riated field ($|c_4| \simeq$0). It can be observed that coefficients c_2, c_6 have a phase difference of 180°. For what concerns the excitations, symmetric with respect to ϕ_0=90°, all the ports are active and a tapering of the amplitudes can be observed. Moreover, with reference to Fig.6.9, while ports 2, 3, 1 and 4 radiate nearly with the same phase, ports 5 and 6 are shifted of 90°.

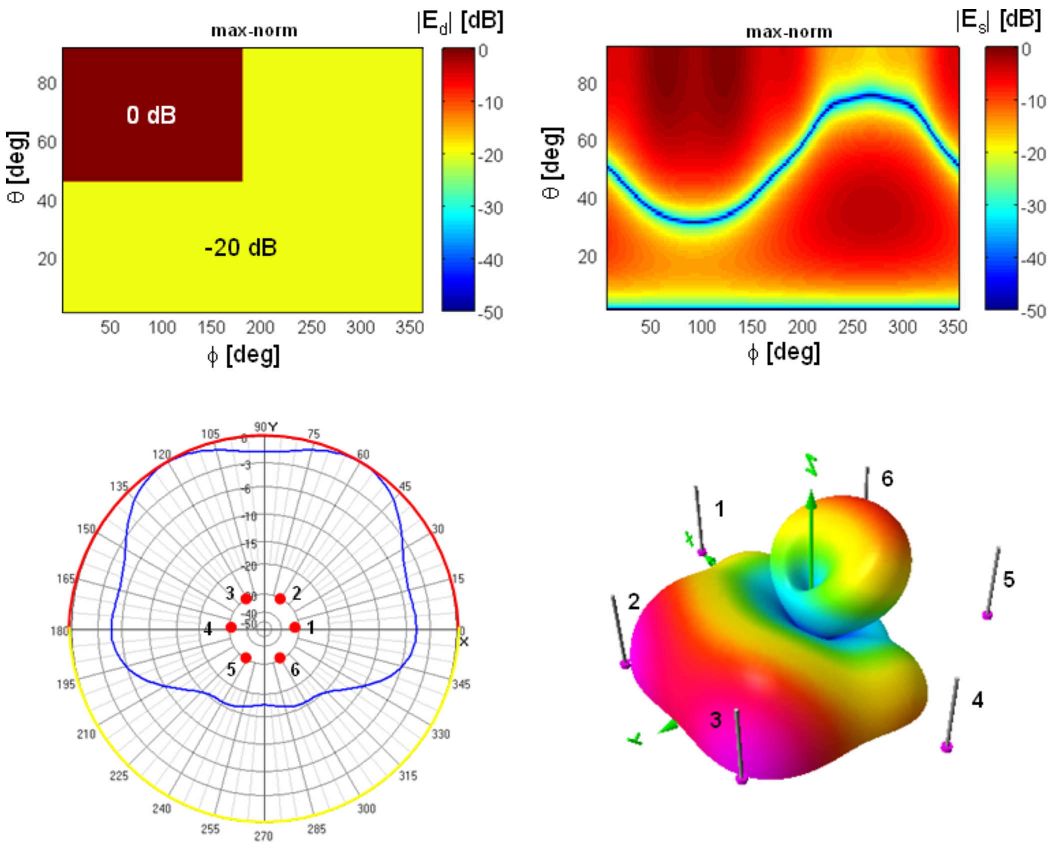

Figure 6.9: *up)* Mask of the desired far-field (left) and synthesized far-field (right). *down)* Synthesized horizontal gain (left) and synthesized 3D-gain (right).

The ratio $\frac{|V\max|}{|V\min|}$ is about 5.2, FTBR is about $15dB$ (intended as the ratio between tha gain in ϕ=90° and ϕ=270°) and maximum gain is $9.5dB$.

In the second case, the same configuration as before is considered but a different far-field mask is given. In particular, since the array cannot control the radiation pattern at high elevation angles, the isolated monopole far-field (element factor) is assumed for $0° \leq \theta \leq 45°$ instead of the value $-20dB$. In this way a more accurate synthesized field is expected at low elevation angles. The mask and the synthesized radiation patterns are shown in Fig.6.10.

The amplitudes and phases of c_i and $\overrightarrow{v}_i$ are reported in Tab.6.5

The c_i phases are the same as in the previous case, while the amplitudes give more weight to eigenpatterns 2 and 6. The ports are all active and the

Table 6.4: Normalized values of the synthesized weighing coefficients and array excitations.

i	$\lvert c_i \rvert$	$\angle c_i$	$\lvert v_i \rvert$	$\angle v_i$
1	1	-144.3°	*0.52*	*144.2°*
2	0.57	-76.4°	*1*	*155.4°*
3	6e-3	-127.7°	*1*	*155.4°*
4	$\simeq 0$	117.7°	*0.52*	*144.2°*
5	6e-3	-127.7°	*0.19*	*65.2°*
6	0.57	103.6°	*0.19*	*65.2°*

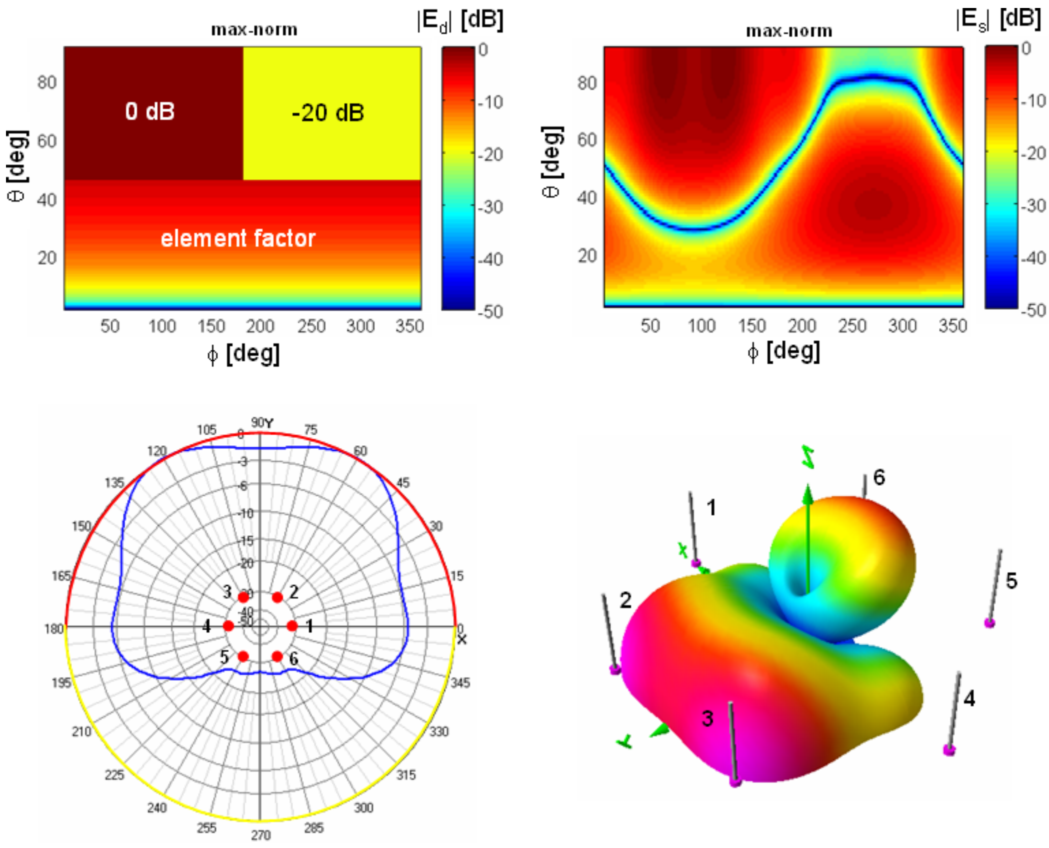

Figure 6.10: *up)* Mask of the desired far-field (left) and synthesized far-field (right). *down)* Synthesized horizontal gain (left) and synthesized 3D-gain (right).

Table 6.5: Normalized values of the synthesized weighing coefficients and array excitations.

i	$\lvert c_i \rvert$	$\angle c_i$	$\lvert v_i \rvert$	$\angle v_i$
1	1	-144.3°	*0.46*	*144.2°*
2	0.71	-76.4°	*1*	*156.6°*
3	7e-3	-127.7°	*1*	*156.6°*
4	$\simeq 0$	117.7°	*0.46*	*144.2°*
5	7e-3	-127.7°	*0.22*	*36.8°*
6	0.71	103.6°	*0.22*	*36.8°*

same tapering of the amplitudes as before is visible.

The ratio $\frac{|V\max|}{|V\min|}$ is about 4.5, FTBR is about $25dB$ (intended as the ratio between tha gain in ϕ=90° and ϕ=270°) and maximum gain is $9.4dB$. Using this different mask FTBR is improved of about $10dB$.

In the third case, the same configuration as before is considered but a new far-field mask is given. In particular, two symmetric lobes are required in the angular regions $45° \leq \theta \leq 90°$, $45° \leq \phi \leq 135°$ and $45° \leq \theta \leq 90°$, $225° \leq \phi \leq 315°$. The mask and the synthesized radiation patterns are shown in Fig.6.11.

The amplitudes and phases of c_i and $\overrightarrow{v}_i$ are reported in Tab.6.6

Table 6.6: Normalized values of the synthesized weighing coefficients and array excitations.

i	$\lvert c_i \rvert$	$\angle c_i$	$\lvert v_i \rvert$	$\angle v_i$
1	1	-144.4°	*0.46*	*-71.4°*
2	$\simeq 0$	84.9°	*1*	*136.5°*
3	0.89	52.3°	*1*	*136.5°*
4	$\simeq 0$	119.8°	*0.46*	*-71.4°*
5	0.89	52.3°	*1*	*136.5°*
6	$\simeq 0$	87.7°	*1*	*136.5°*

Only eigenpatterns 1, 3 and 5 contribute to the radiated field. For what

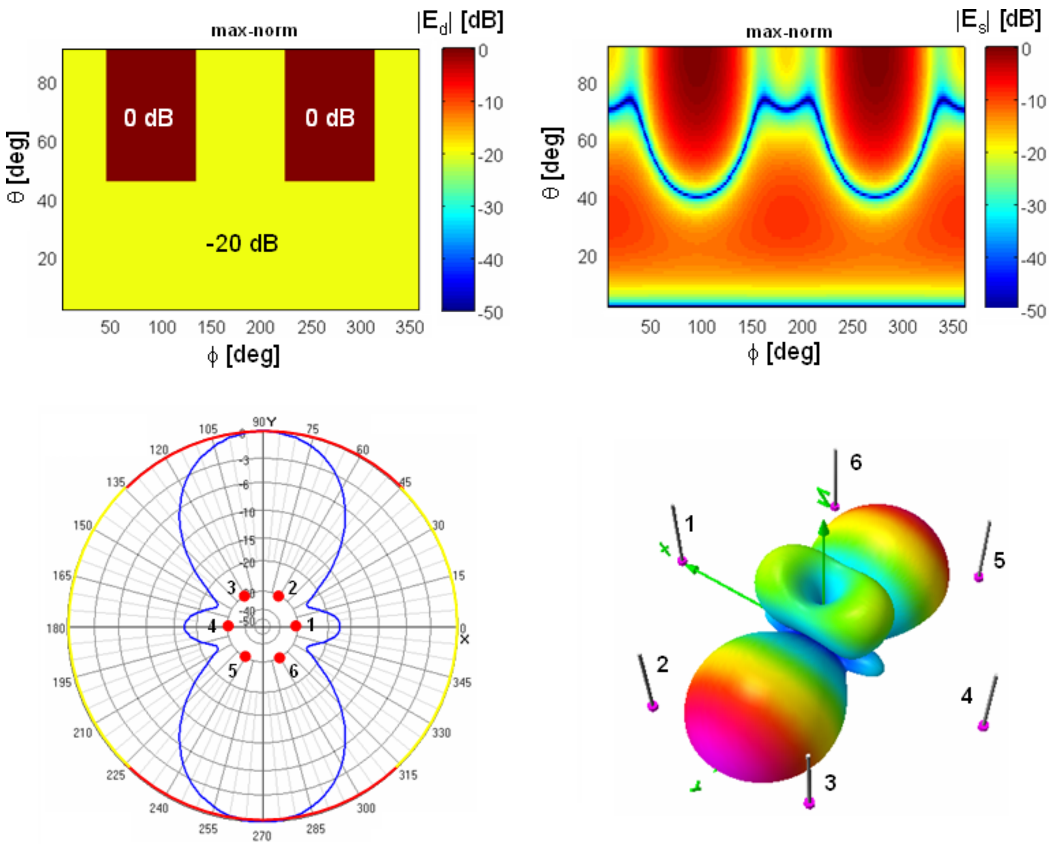

Figure 6.11: *up)* Mask of the desired far-field (left) and synthesized far-field (right). *down)* Synthesized horizontal gain (left) and synthesized 3D-gain (right).

concerns the excitations, symmetric with respect to ϕ_0=90°, all the ports are active. According to Fig.6.11, ports 2, 3 and 5, 6 radiates the maximum power and have the same amplitudes and phases.

The ratio $\frac{|V\max|}{|V\min|}$ is about 2.1, the ratio between the main lobes and the perpendicular side lobes is $17dB$ and the maximum gain is $11.4dB$.

In the last case, the number of array elements is $N = 20$, the array radius is $a = \lambda$ and the inter-element spacing is $d \simeq 0.31\lambda$. According to Tab.6.1, by a simple phase synthesis of the excitations, the following performances were found for the considered array: $BW_{-3dB} = 21°$, $SLL = -8dB$, $FTBR = 16dB$. By the modal synthesis also the amplitudes of the excitations are optimized and, therefore, better performances are expected. The desired mask imposes a main lobe in the angular region $60° \leq \theta \leq 90°$, $75° \leq \phi \leq 105°$ (ϕ_0=90° and $\Delta\phi$=30°) and tries to minimize the back radiaton. The mask and the synthesized radiation patterns are shown in Fig.6.12.

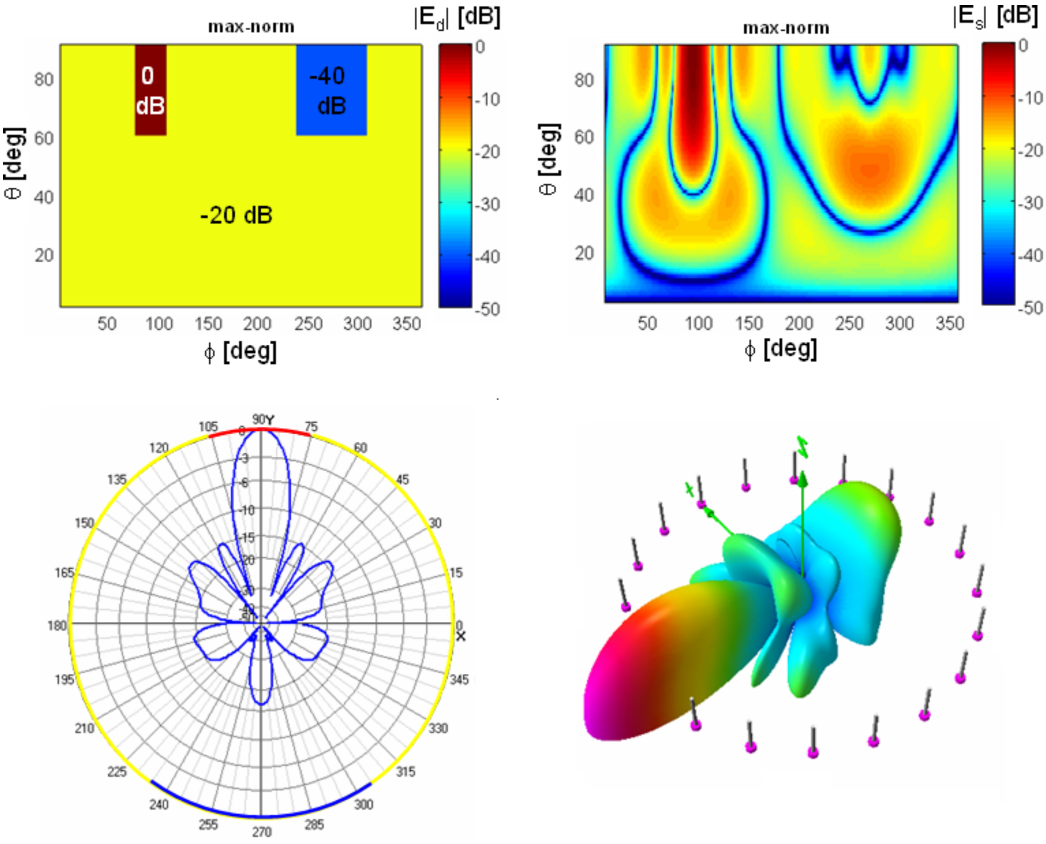

Figure 6.12: *up)* Mask of the desired far-field (left) and synthesized far-field (right). *down)* Synthesized horizontal gain (left) and synthesized 3D-gain (right).

The amplitudes and phases of c_i and $\overrightarrow{v}_i$ are not reported for brevity. However, some observations can be made: eigenpattern 11 gives the maximum contribution to the radiated field ($|c_{11}|$=1) and all the other eigenpatterns contribute in a comparable way ($0.1 \leq |c_i| \leq 0.52$). The array excitations are symmetric with respect to the focusing direction $\phi_0 = 90°$ and their amplitudes are tapered with values $0.35 \leq |v_i| \leq 1$.

The ratio $\frac{|V\max|}{|V\min|}$ is about 2.8, FTBR is about $16dB$ (intended as the ratio between the gain in ϕ=90° and ϕ=270°), SLL is about $-14dB$, BW$_{-3dB}$=16°

and maximum gain is nearly $18dB$. The degrees of freedom given by the excitation amplitudes permit to improve the side-lobe-level and to reduce the beamwidth with respect to the performances in Tab.6.1.

In all the considered cases the ratio $\frac{|V\max|}{|V\min|}$ is completely acceptable. It is finally worth noticing that, by using a greater number of elements, better array performances can be achieved because of the greater number of available degrees of freedom for the synthesis.

Constrained modal synthesis

Fig.6.13 proposes a scheme for the constrained modal synthesis based on the iterative projection method [50], [51]. The problem is formulated as the search of the intersection between two suitable sets. When a given radiation pattern is synthesized, it may be required to control the dynamic range of the array excitations, i.e. the ratio between the largest and smallest amplitude excitation, or to control the port-matching. The solution will be found as the intersection between the following two sets:

1. The set of array excitations that satisfy the requirements specified by a desired far-field mask.

2. The set of array excitations that satisfy the dynamic range or the port-matching constraints.

The iterative process in Fig.6.13 begins with the choice of an arbitrary array excitation $\overrightarrow{v}_0$ as a starting solution, for instance the uniform excitation. The corresponding field $\overrightarrow{E}_0$ is obtained by using the operator T previously introduced. At this point the first iteration starts and $|E_{0\theta}|$ (it is assumed $E_{0\phi} = 0$) is compared with the desired field mask $|E_{d\theta}|$ and corrected by the operator C_E in the following way:

$$E_{1\theta}(\theta,\phi) = \begin{cases} E_{\max}(\theta,\phi)\frac{E_{0\theta}(\theta,\phi)}{|E_{0\theta}(\theta,\phi)|} & |E_{0\theta}(\theta,\phi)| > \mathrm{E}_{\max}(\theta,\phi) \\ E_{0\theta}(\theta,\phi) & \mathrm{E}_{\min}(\theta,\phi) \leq |E_{0\theta}(\theta,\phi)| \leq \mathrm{E}_{\max}(\theta,\phi) \\ E_{\min}(\theta,\phi)\frac{E_{0\theta}(\theta,\phi)}{|E_{0\theta}(\theta,\phi)|} & |E_{0\theta}(\theta,\phi)| < \mathrm{E}_{\min}(\theta,\phi) \end{cases} \quad (6.12)$$

where E_{max} and $\mathrm{E}_{min} \in R$ define the maximum and minimum desired field amplitude in each direction (θ,ϕ) according to the assigned mask. The

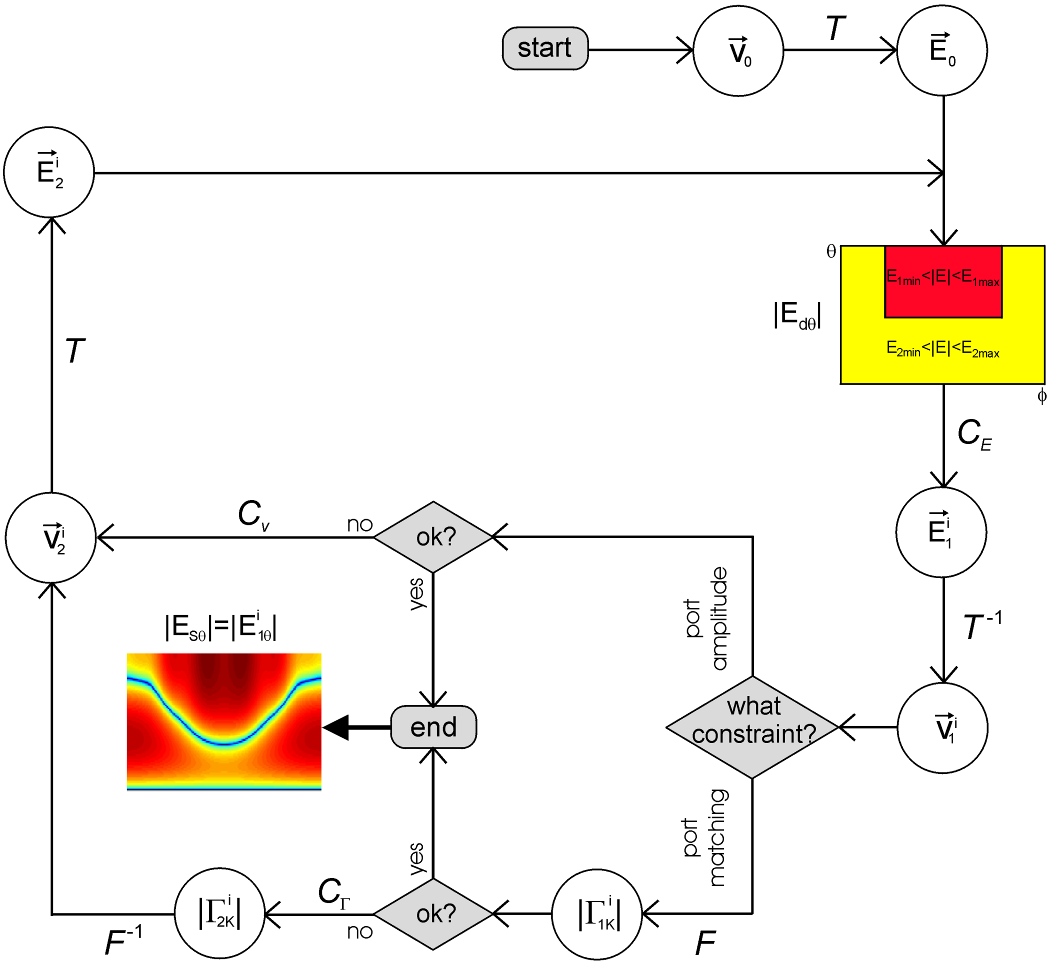

Figure 6.13: Scheme for the constrained modal synthesis. For the desired far-field mask it is here assumed $E_{d\phi}(\theta, \phi) = 0$ and $\angle E_{d\theta}(\theta, \phi) = 0$.

ratio $\frac{E_{0\theta}(\theta,\phi)}{|E_{0\theta}(\theta,\phi)|}$ indicates the term $e^{j\angle E_{0\theta}(\theta,\phi)}$. From the resulting field $\overrightarrow{E}_1$, the corresponding array excitation $\overrightarrow{v}_1$ is found by operator T^{-1}.

Now the scheme offers the possibility to include a constraint on the port-amplitude or port-matching.

In the first case (port-amplitude), if the constraint is satisfied the algorithm ends, otherwise each component of the excitation vector $\overrightarrow{v}_1$ is corrected by operator C_v in the following way:

$$v_{2,k} = \begin{cases} V_{\max}\frac{v_{1,k}}{|v_{1,k}|} & |v_{1,k}| > \mathrm{V}_{\max} \\ v_{1,k} & \mathrm{V}_{\min} \leq |v_{1,k}| \leq \mathrm{V}_{\max} \\ V_{\min}\frac{v_{1,k}}{|v_{1,k}|} & |v_{1,k}| < \mathrm{V}_{\min} \end{cases} \tag{6.13}$$

where V_{max} and $\mathrm{V}_{min} \in R$ are the maximum and minimum desired voltage-amplitude. The ratio $\frac{v_{1,k}}{|v_{1,k}|}$ indicates the term $e^{j\angle v_{1,k}}$, $v_{2,k}$ is the corrected excitation at kth-port and $\overrightarrow{v}_2$ is the corrected excitation vector.

In the second case (port-matching), at first the reflection coefficient at each port $\Gamma_{1,k}$ is computed by operator F, given by (5.12) and (5.13); then, if the constraint on $|\Gamma_k|$ is satisfied $\forall k$ the algorithm ends, otherwise $\Gamma_{1,k}$ is corrected by operator C_Γ in the following way:

$$\Gamma_{2,k} = \begin{cases} \Gamma_{\max}\frac{\Gamma_{1,k}}{|\Gamma_{1,k}|} & |\Gamma_{1,k}| > \Gamma_{\max} \\ \Gamma_{1,k} & |\Gamma_{1,k}| \leq \Gamma_{\max} \end{cases} \tag{6.14}$$

where $\Gamma_{max} \in R$ is the maximum desired amplitude of the reflection coefficient. The ratio $\frac{\Gamma_{1,k}}{|\Gamma_{1,k}|}$ indicates the term $e^{j\angle\Gamma_{1,k}}$, while $\Gamma_{2,k}$ is the corrected reflection coefficient at kth-port.

Once $\Gamma_{2,k}$ are computed $\forall k$, excitation $\overrightarrow{v}_2$ is obtained by inverting operator F. In particulare, the inversion of (5.13) is simple, while the inversion of (5.12) to find coefficients c_i leads to the solution of an homogeneous linear system $Ax = 0$, that can be more complicated.

The final step consists in the computation, by means of operator T, of field $\overrightarrow{E}_2$ that will be the input to the next iteration.

In the following example, the radiation pattern is synthesized with the constraint on the excitation voltage-amplitude.

The number of array elements is $N = 20$, the array radius is $a = \lambda$ and the inter-element spacing is $d \simeq 0.31\lambda$. At first, Fig.6.14 shows the performances obtained by the unconstrained synthesis discussed in the previous paragraph when the main lobe is required to be in the wide angular region $65° \leq \theta \leq 90°$, $0° \leq \phi \leq 180°$.

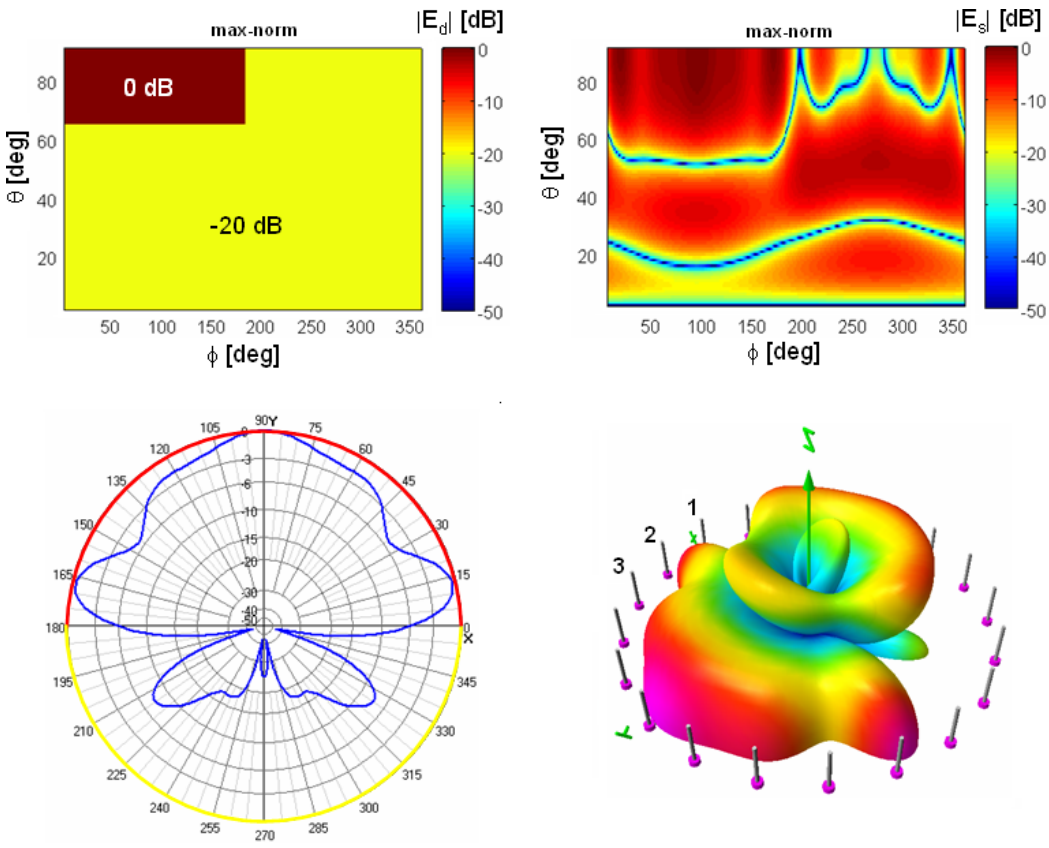

Figure 6.14: *up)* Mask of the desired far-field (left) and synthesized far-field (right). *down)* Synthesized horizontal gain (left) and synthesized 3D-gain (right). The $\frac{|V\max|}{|V\min|}$ ratio is about 32.

A maximum gain of $9.7dB$ and a FTBR of about -$24dB$ are found. The radiation is well confined and rather uniform in the desired half space and the back lobes level is about $-7.7dB$. These performances are achieved by a $\frac{|V\max|}{|V\min|}$ ratio of about 32.

In order to lower this ratio without sensibly affecting the radiation pattern, the constrained synthesis of Fig.6.13 is performed. In particular, $\frac{|V\max|}{|V\min|} = 5$ is imposed and the following normalized mask is chosen:

$$\begin{cases} E_{\min} = -2dB, \quad E_{\max} = 0dB & \text{if } 65^\circ \leq \theta \leq 90^\circ \cap 0^\circ \leq \phi \leq 180^\circ \\ E_{\min} = -\infty, \quad E_{\max} = -20dB & \text{otherwise} \end{cases} \tag{6.15}$$

A uniform excitation, producing an azimuthal omnidirectional far-field, is used as starting point and after i = 10 iterations the results in Fig.6.15 are obtained.

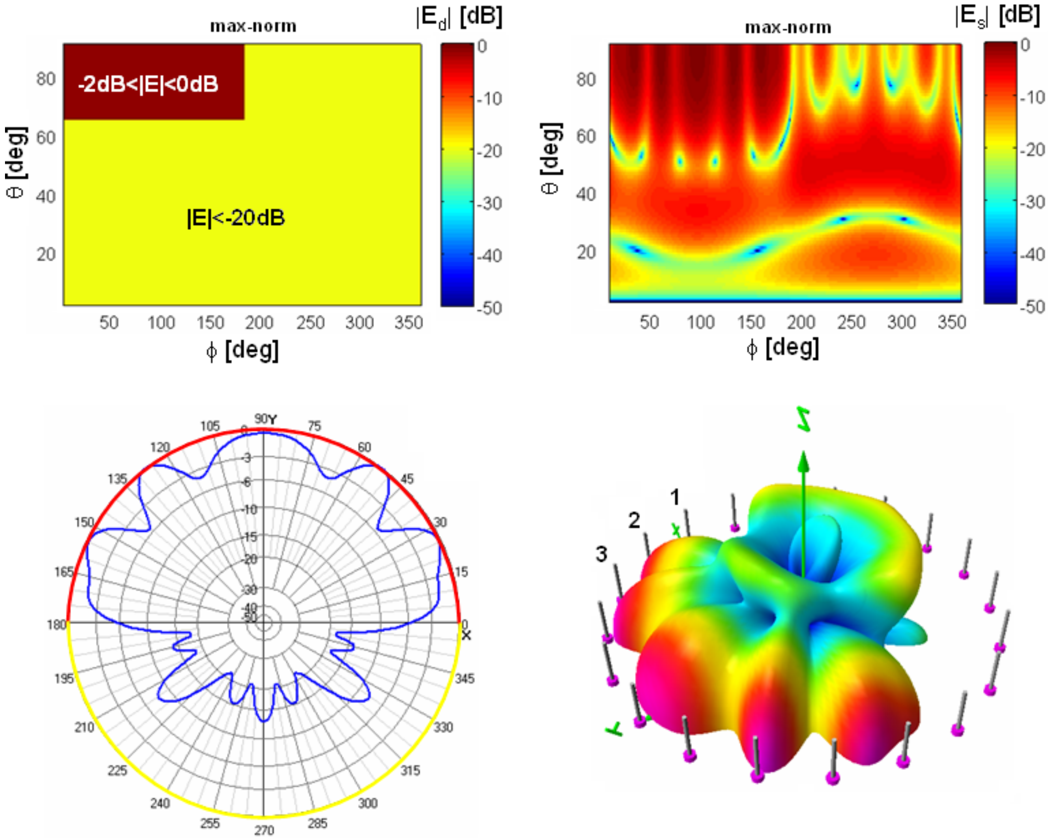

Figure 6.15: *up)* Mask of the desired far-field (left) and synthesized far-field (right). *down)* Synthesized horizontal gain (left) and synthesized 3D-gain (right). The $\frac{|V \max|}{|V \min|}$ ratio is about 4.8.

The maximum gain is 9.9dB and the FTBR is about -13dB. The radiation retains well confined in the desired half space but exhibits a lobed shape and the back radiation level is increased. These performances are however comparable with those obtained by the unconstrained synthesis, but $\frac{|V \max|}{|V \min|}$ = 4.8.

Fig.6.16 shows the voltage amplitudes at each port in the considered cases of unconstrained and constrained synthesis.

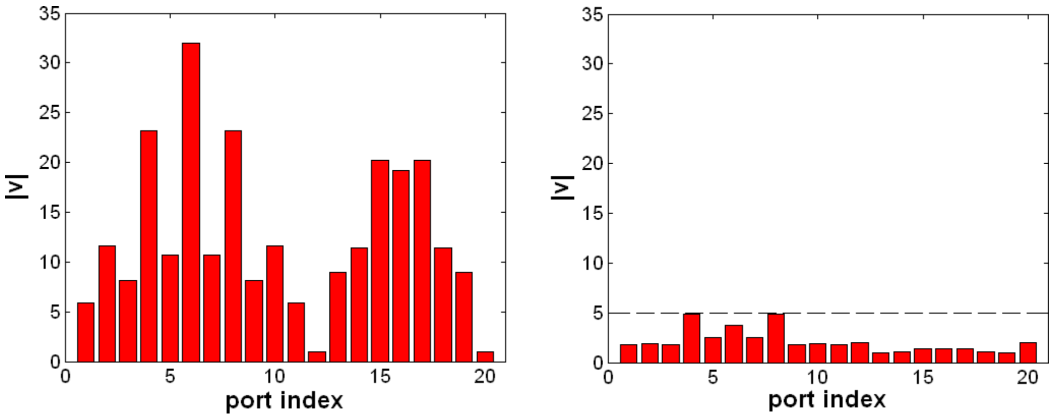

Figure 6.16: *left)* Array voltage amplitudes obtained by the unconstrained synthesis. *right)* Array voltage amplitudes obtained by the constrained synthesis. In both cases $|V_{\text{min}}| = 1$.

Application to the NSA

In this paragraph the modal synthesis is applied to the NSA system of Chapter 4. This configuration is different from the simple array of monopoles previously considered and, in general, the radiated fields (and hence the eigenpatterns) have the ϕ-component, and the radiation along the zenith can also be significant.

In the following examples, only the amplitude of the θ-component of the desired field is assigned and, therefore, it is implicitly assumed $\angle E_{d\theta}(\theta, \phi) = 0$ and $E_{d\phi}(\theta, \phi) = 0$ for each direction (θ, ϕ). In this case, equations (6.5)-(6.8) become:

$$c_i = \frac{1}{K_{ii}} \left\langle \overrightarrow{E}_d, \overrightarrow{E}^{(i)*} \right\rangle \tag{6.16}$$

where

$$K_{ii} = \mathrm{K}_{\theta ii} + \mathrm{K}_{\phi ii} = \iint\limits_{2\pi} \left| E_\theta^{(i)} \right|^2 \sin\theta d\theta d\phi + \iint\limits_{2\pi} \left| E_\phi^{(i)} \right|^2 \sin\theta d\theta d\phi \tag{6.17}$$

and

$$\left\langle \overrightarrow{E}_d, \overrightarrow{E}^{(i)*} \right\rangle = \iint\limits_{2\pi} E_{d\theta} E_\theta^{(i)*} \sin\theta d\theta d\phi \tag{6.18}$$

In the first example the NSA$_4$ is considered at $f = 15MHz$. At this frequency the height of the overall structure is about $\lambda/2$. The mask and the synthesized radiation patterns are shown in Fig.6.17. The main lobe is required in the angular region $65° \leq \theta \leq 90°$, $45° \leq \phi \leq 135°$.

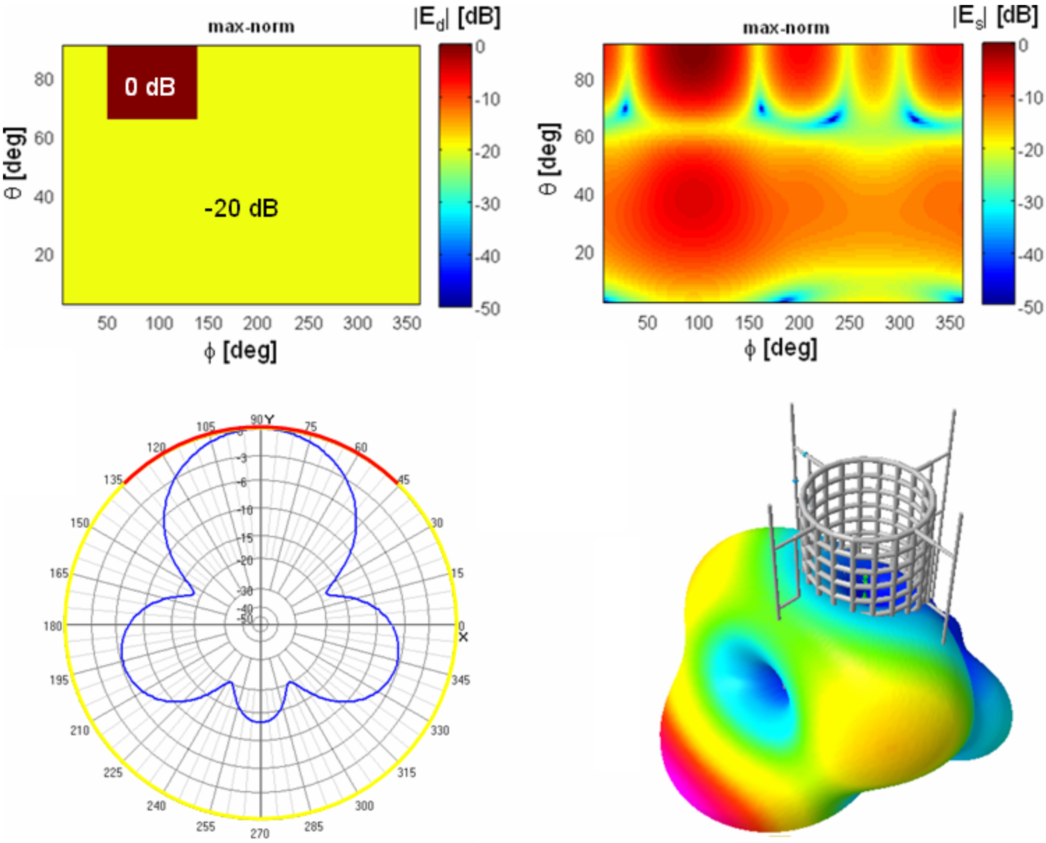

Figure 6.17: *up)* Mask of the desired far-field (left) and synthesized far-field (right). *down)* Synthesized horizontal gain (left) and synthesized 3D-gain (right).

After the synthesis, the ratio $\frac{|V\max|}{|V\min|}$ is about 2.5, FTBR is about $13dB$ (intended as the ratio between the gain in ϕ=90° and ϕ=270°), SLL is about $-6dB$, and maximum gain is nearly $9.8dB$.

In the second case the NSA$_6$ is considered at $f = 15MHz$. The mask and the synthesized radiation patterns are shown in Fig.6.18. The main lobe is required in the angular region $65° \leq \theta \leq 90°$, $45° \leq \phi \leq 135°$ and a value of $-40dB$ is imposed in the angular region $45° \leq \theta \leq 90°$, $225° \leq \phi \leq 315°$ in order to minimize the back radiation.

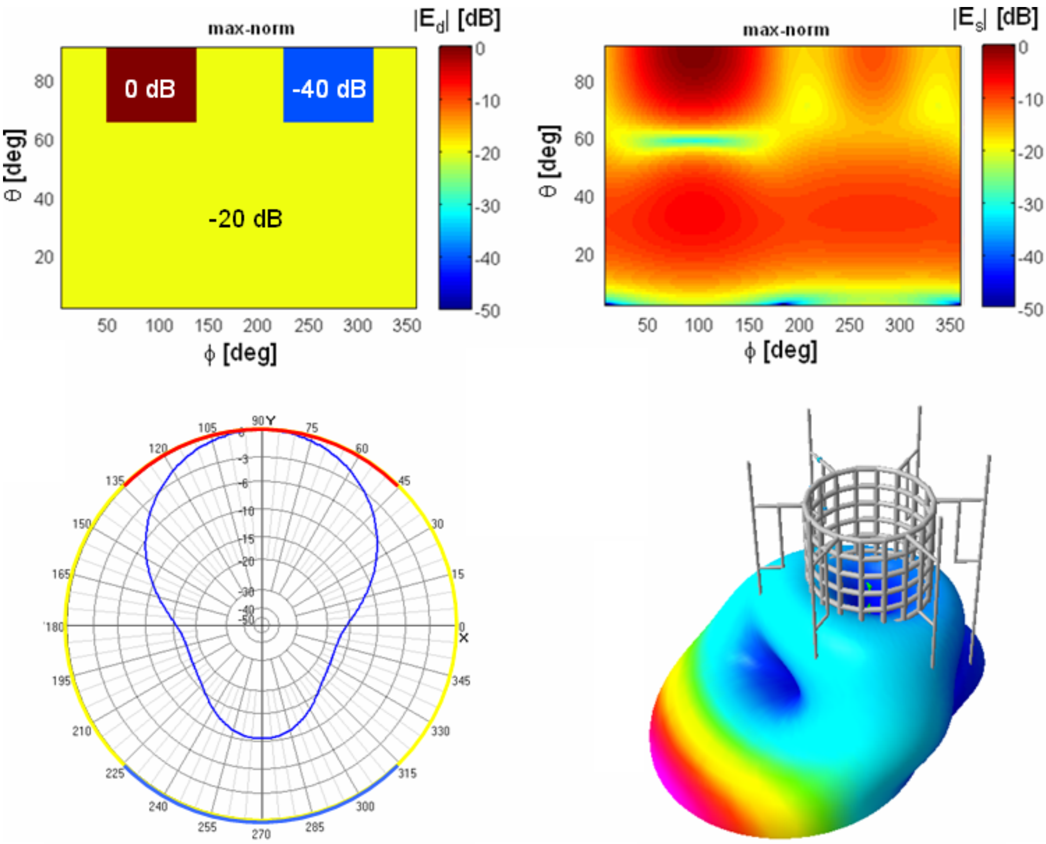

Figure 6.18: *up)* Mask of the desired far-field (left) and synthesized far-field (right). *down)* Synthesized horizontal gain (left) and synthesized 3D-gain (right).

The obtained ratio $\frac{|V\max|}{|V\min|}$ is about 2.4, FTBR is about $10.4dB$ (intended as the ratio between the gain in ϕ=90° and ϕ=270°), and maximum gain is nearly $10.4dB$.

Chapter 7

Shipborne application

HF antennas for naval communications are generally designed over an infinite ground plane assuming the sea as a perfect conductor due to its high conductivity. In this Chapter, the previously considered radiating structures are investigated in a realistic naval environment so that control and compensation techniques can be developed in order to minimize the interactions with the ship superstructures. Such interactions can be very strong in the HF domain where the antenna resonant length could be of similar size as the whole platform, as discussed in Chapter 1. Therefore, a strong pattern distortion [20] and source mismatch may occur, demanding multiple antennas and encouraging *ad-hoc* solutions [7].

The first part of this Chapter concerns the numerical analysis of the bifolded antenna onboard a realistic ship model, the aircraft carrier G. Garibaldi, in order to investigate the changes of its performances with respect to the infinite perfect ground plane case.

In the second part, the critical aspects concerning the extension of the NSA concept to a realistic ship environment is discussed with the purpose to define a general ship-suited design strategy [52]. In the previous Chapters the concept of Naval Structural Antenna was introduced and it was shown how the interactions of the HF source with a part of the ship, such as a funnel or a big mast, which in general produces undesired effects, can be instead steered to give unconventional performances and to reduce the number of antennas onboard. Up to now, however, this idea was investigated with reference to canonical geometries over a perfect ground plane. The discussions and the results here presented will be referred to a realistic ship model resembling a frigate where the challenge is to transform the big central mast into a broadband multi-port HF antenna system with a really limited use of the available space. The considered scenario is rather common and therefore the design methodology which will be developed, although experimented with a bechkmark ship, is of general interest and can be extended to several installation typologies.

7.1 Bifolded analysis on a realistic ship model

Numerical simulations of the bifolded monopole when embedded on a real ship model, the aircraft-carrier G. Garibaldi (Fig.7.1), are here carried out in order to investigate the antenna performances' modifications with respect to the infinite perfect ground plane configuration considered in Chapter 3. The large electric dimensions of the structure ($12\lambda@20MHz$ with 17500 unknowns) prevent a full-MoM analysis in the whole HF band. Therefore, MoM is used up to 16 MHz and the Multi-Level Fast Multipole Method (MLFMM) [53], an algorithm to quickly solve the MoM in presence of large size objects, is used in the upper range 16-40 MHz. The sea is modelled as a perfect ground plane and the bifolded antenna replaces a typical twin whip antenna mounted in the considered ship.

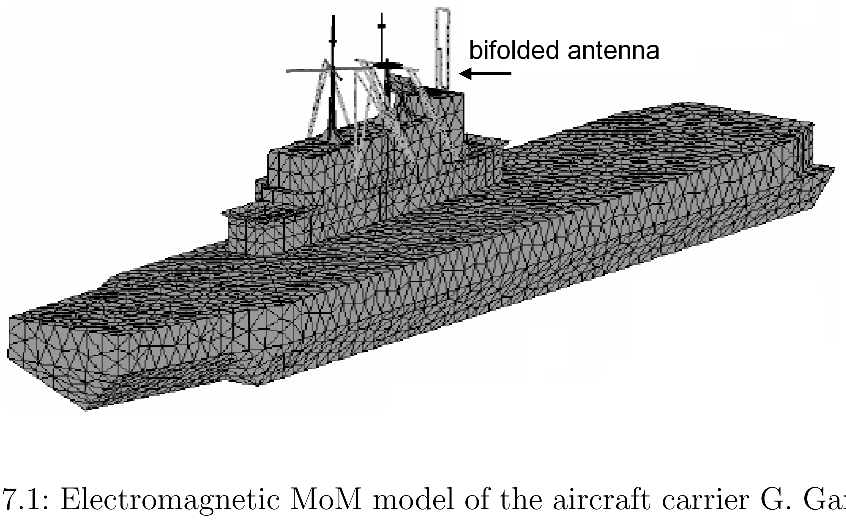

Figure 7.1: Electromagnetic MoM model of the aircraft carrier G. Garibaldi. Bifolded antenna is indicated by the arrow.

As visible in Fig.7.2, the antenna input impedance after the on-ship installation is not sensibly modified with respect to the simulation over a perfect ground and the VSWR is lower than 3 in almost the whole HF band. The ϕ-averaged gain at the horizon is enforced by the ship superstructure, particularly in the range 2-8 MHz, with improvements up to 10 dB. The most evident result, however, is the improvement of more than 10 dB of the NVIS radiation. This effect is substantially due to the antenna position within the ship environment. In this case, strong currents are induced by the radiator on the edges of the ship hull that behave as horizontal dipoles emphasizing the radiated field toward the zenith.

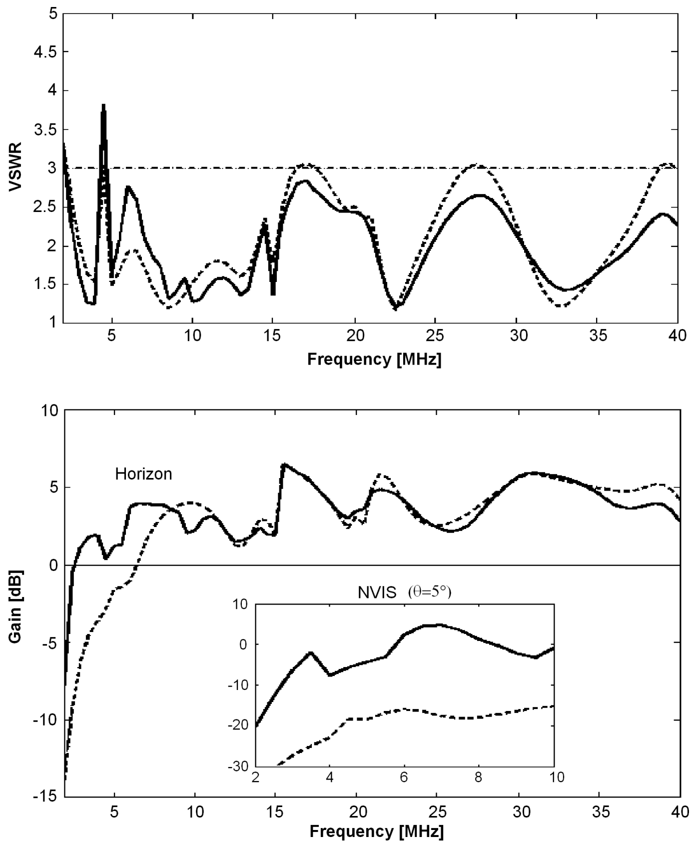

Figure 7.2: Bifolded performances over an infinite ground plane (dashed line) and on the ship (solid line). *up*) VSWR. *down*) ϕ-averaged gain at the horizon and at NVIS.

The radiation patterns at some HF frequencies are shown in Fig.7.3. The lobes and nulls at higher frequencies are due to the scattering effects caused by the complex electromagnetic scenario.

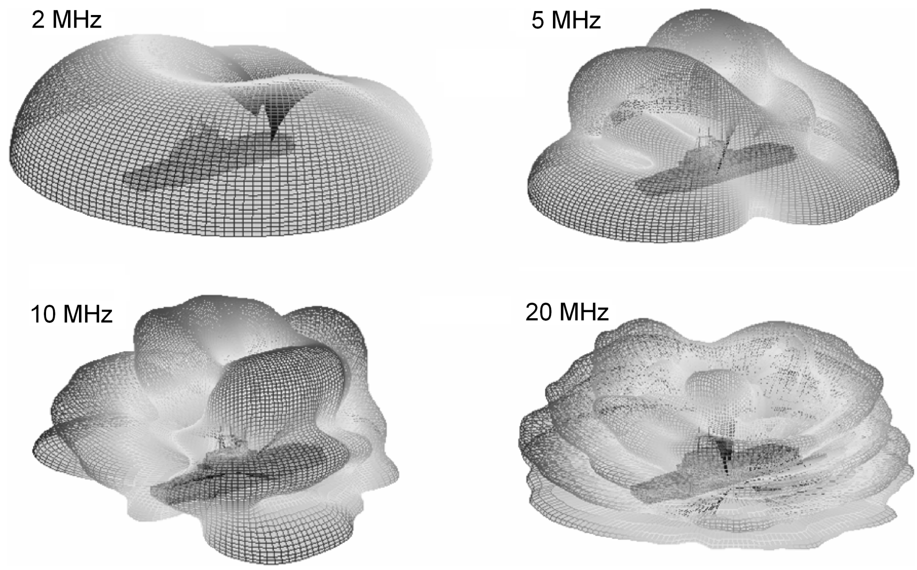

Figure 7.3: Radiation patterns of the bifolded antenna onboard the ship at different frequencies.

Finally, it is worth noticing that also the antenna efficiency improves in the range 2-10 MHz after the on-ship installation.

In conclusion, the input impedance of the antenna is not sensibly modified by the presence of the ship and it has been verified to hold also for other antenna positions on the ship. Therefore, in a first approximation, the antenna can be simply designed over an infinite perfect ground plane. For what concerns the radiation pattern, instead, it is strongly affected by the antenna position because of the electromagnetic interactions with the ship and its superstructures. In particular, the gain improvement at NVIS is nearly independent on the antenna typology and particularly depends on the induced currents on the ship itself. Therefore, the NVIS requirement can be relaxed in favour of other performances during the antenna design over an infinite perfect ground plane.

7.2 NSA design on a realistic ship model

This paragraph opens with the definition of reference performance indicators for onboard HF naval antennas and introduces the optimization problem for loaded broadband antennas including the ship superstructures. As a second step, details are given about the design of a single-feed NSA *on the mast* by a modification of the sub-radiators in Chapters 3 and 4, for what concerns topology, position and electrical values of the loading impedances. Then, the extension to the 4-port NSA is discussed with a particular attention to the embedded patterns features. Finally, the pattern synthesis optimization problem, with the additional constraint of the impedance matching at the antenna ports, is considered and solved by GA approach. By a proper control of port excitations, it is demonstrated how to improve the pattern uniformity at the horizon, caused by the shadowing effects of the surrounding deck objects, and how to enhance the system radiation toward a given angular sector having all the active ports matched with VSWR<3.

7.2.1 Statement of the problem

The reference naval platform, considered to illustrate the design methodology, is a typical frigate-like geometry containing a funnel, a big mast and a radar tower (Fig.7.4).

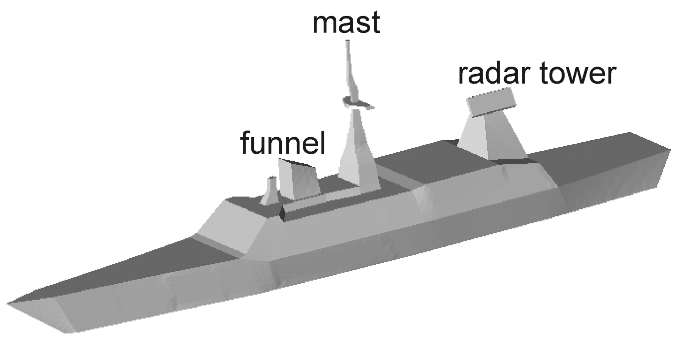

Figure 7.4: Simplified model of a frigate where the NSA concept will be experimented. The ship is 120m-long and 15m-wide.

The mast to be turned into an antenna is enlarged in Fig.7.5a. The non-uniform cross-section, tapered from the ground to the top, ranges from

7m×4m at the base, to 0.7m×0.7m at the top, and the overall height is more than twice the size of the canonical cylinders (height 10m) previously considered. In this case the mast becomes one of the vertical conductors of a folded-monopole-like geometry, and the wires are loaded by lumped electric circuits. Based on the previous experience, the same wire geometry as in the cylindrical NSA structure is connected to an edge of the mast while the loading circuits are re-optimized by GA for what concerns topology, position and electrical values.

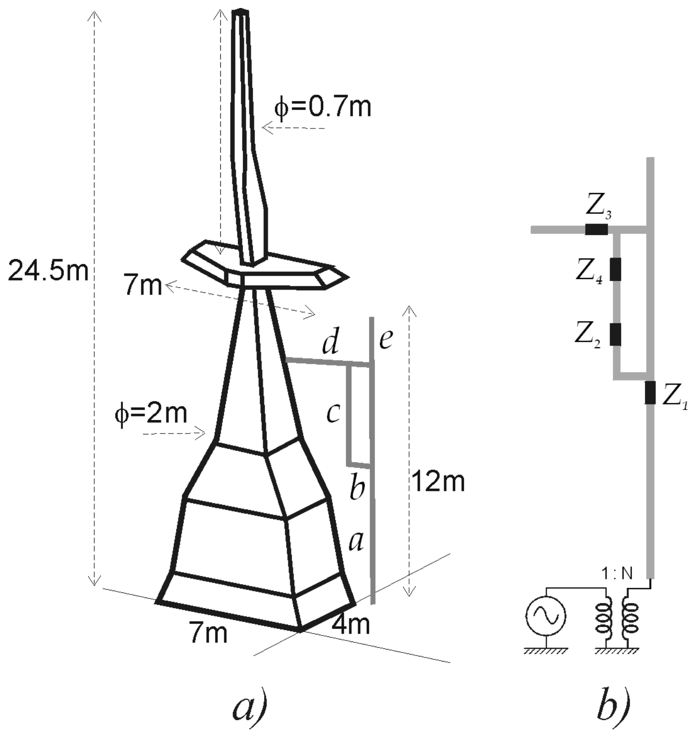

Figure 7.5: *a)* Transforming the mast into an NSA_1 by loaded-wires feeding. Size are: $a = 6m$, $b = 1m$, $c = 4m$, $d = 3.5m$, $e = 2m$. *b)* Loading impedances optimized by GA for the case of the mast over a perfect ground: Z_1 is the series connection of $L_1 = 0.23\mu H$ and $C_1 = 506pF$; Z_2 is the series connection of $L_2 = 0.77\mu H$ and $C_2 = 561pF$; Z_3 and Z_4 are resistors of value 54Ω and 9Ω. The impedance transformer ratio is $N = 4$.

Some of the performances to be met have been already introduced in the previous Chapters, the others are borrowed from [7]:

- VSWR<3 (line impedance 50Ω).
- ϕ-averaged gain at the horizon ($\theta = 90°$) more than $-10dB$ for 2 MHz$\leq f \leq$ 5 MHz and higher than $2dB$ above 5 MHz.
- ϕ-averaged gain at high elevation angles ($\theta = 10°$) more than $-20dB$ to perform Near Vertical Incidence Skywave (NVIS) communications.
- Gain variation on the horizontal plane with respect to the peak value, less than $10dB$ in the 80% of the whole azimuthal angle. The functions $U(f)$ and $\bar{U}$, referred to as *pattern uniformity* (see Appendix B, equation B.13) and *global pattern uniformity*, respectively, indicate the percentage of the whole azimuthal angle at the frequency f, and the percentage of the whole band ($\bar{U}$), where the gain requirement is met.

In the given examples, all the objects are considered made of aluminium and the wires are 10cm-cross-section pipes. The electromagnetic models of the mast equipped with wires and of the surrounding environment required for the GA optimization are achieved by MoM [54]. In the second half of the band (20-40 MHz), the huge size of the unknowns requires a combined MoM and MLFMM approach [53], as in the case of the bifolded on the aircraft carrier. The sea is modelled again as a perfect ground plane.

7.2.2 Design of the NSA on-the-mast

The considered problem is a rather hard challenge since additional difficulties are now present in comparison with the simplified structures in Chapter 4 due to the high extension of the mast, to the absence of azimuthal periodicity as in a cylinder, and to the interactions with large objects on the ship, such as the funnel and the radar tower placed at a close proximity to the mast. To isolate the features of the *mast-as-antenna* from the interactions with the ship environments, a preliminary optimization assumes the mast to be placed over a perfect ground plane. Since the overall height of the wire radiator is 12m, it is expected that the current over a consistent portion of the mast, from the horizontal platform up to the tip, will be out of any control. By previous experiences, having fixed to four the maximum number of loading impedances, the optimizer has selected two series LC circuits and two resistors placed as in Fig.7.5b and a nearly omnidirectional pattern is obtained with variations smaller than 10dB in the most part of the band (global uniformity $\bar{U} = 87\%$). The other results are shown in Fig.7.6. Besides a good matching in the whole HF band, it can be observed that the $\phi-$averaged gain at the horizon reduces around 8 MHz. At this frequency, the mast electrical height, including the overlength due to the horizontal platform, is roughly λ, and the current exhibits two oscillations. The upper part of the mast radiates with a 180° phase difference with respect to the current on the wires and on the lower part of the mast and therefore the gain at the horizon is lowered. To overcome this problem, some choke mechanisms could be introduced in the upper part of the mast with the purpose to suppress, or at least to reduce, the induced currents as in [15]. In the following part of the paper an un-choked mast is nevertheless considered since, as shown later on, the multiresonance behavior of the mast is less effective when the NSA is installed on the ship due to the interactions with the naval structure.

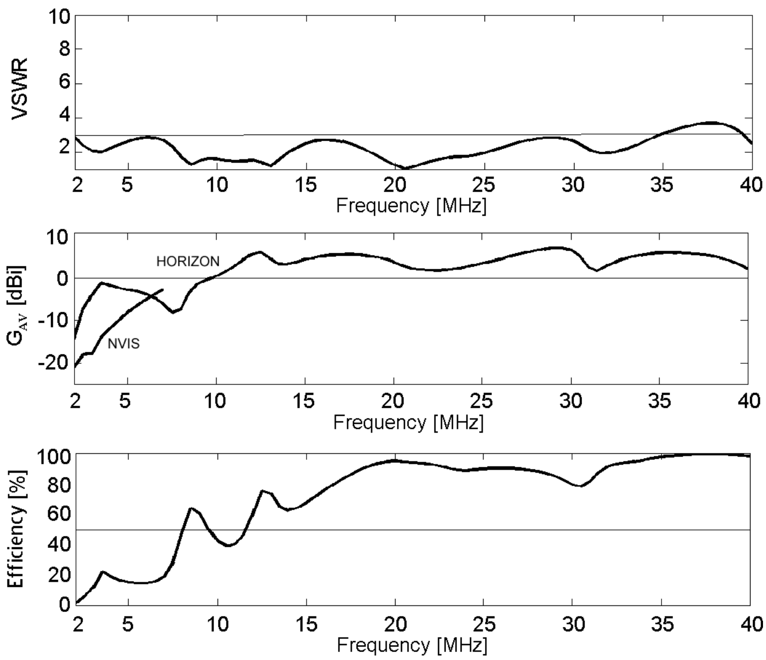

Figure 7.6: NSA_1 over a perfect ground plane. VSWR, $\phi-$averaged gain at the horizon and at NVIS (θ =10°), and efficiency.

When the NSA_1 without chokes, and provided with the loads optimized in the perfect ground configuration, is placed in the real position over the ship, some changes in the antenna features occur due to the electromagnetic coupling with the surrounding environment. The VSWR (Fig.7.7, dashed line) reveals a slight mismatch at low frequencies (VSWR<4), while the $\phi-$averaged gain does not any longer exhibit the reduction around 8 MHz, as in the perfect ground case. After a new optimization of a same number of loads, involving the full electromagnetic model of the antenna together with the naval platform, the NSA_1 becomes well matched in the whole HF band (Fig.7.7, solid line). Nevertheless, because of the ship-to-sea discontinuity and the presence of other deck objects, such as the funnel and the radar tower (Fig.7.4), the global pattern uniformity gets worse ($\bar{U} = 70\%$) with respect to the perfect ground case (it was $\bar{U} = 87\%$). The most penalized frequencies, in the HF band, are close to 8 MHz and 28 MHz.

7.2.3 Design of multi-port configuration

Multi-port configuration (NSA_N) requires that multiple wires and feeding points are connected to the central thick superstructure (the mast in the reference geometry). The resulting arrangement should minimize the coupling of the sub-radiators with the surrounding deck objects. Fig.7.8 shows an example of NSA_4 on the frigate, where the wires share the same loading set (topology, values and positions) of the NSA_1 on the ship. Additional degrees of freedom could be included if the loading impedances of each wire were independently chosen at the cost of a not negligible increase in the optimization times.

As stated in Chapter 4, this system can be used in multi-channel mode, where each port is instantaneously allocated to a single channel, or in mono-channel mode, where all the ports are instantaneously allocated to a single channel.

The incoherent management of the NSA for a realistic installation is here discussed, while the coherent case is addressed in the next paragraphs.

The independent excitation of the antenna ports to host multiple channels at a same time without the use of signal combiners is feasible if *i)* the radiation patterns of the system, when a single port is fed (embedded

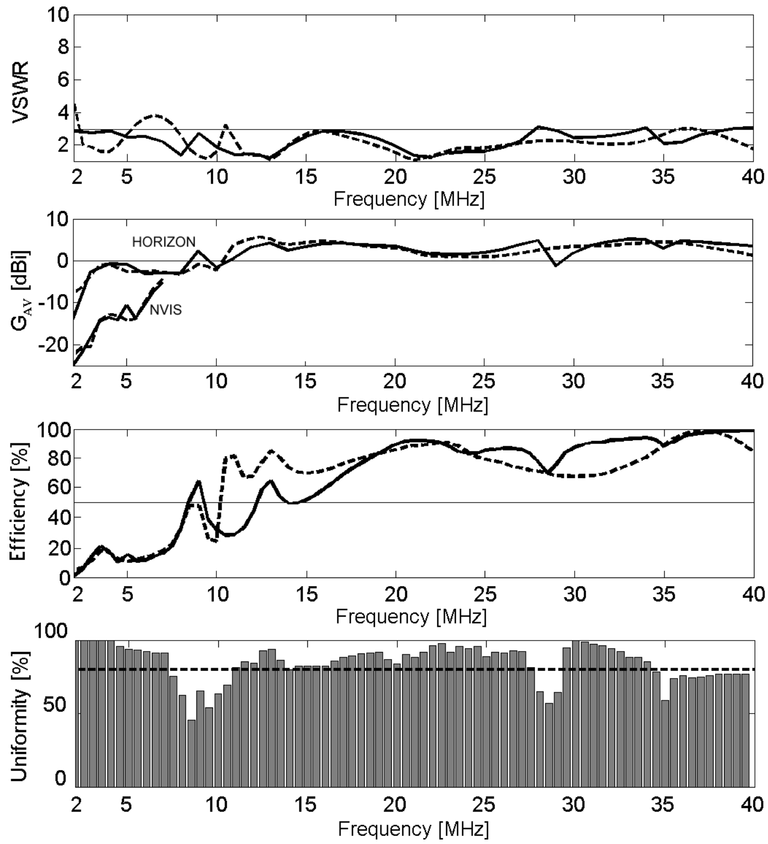

Figure 7.7: NSA_1 on the ship. VSWR, $\phi-$averaged gain at the horizon and at the NVIS (θ =10°), and efficiency. Dashed lines tag the performances with loading impedances borrowed from the mast-plus-perfect ground model, while continuous lines refer to the case where the loading impedances are those re-optimized for the must-plus-ship model. The histogram describes the pattern uniformity $U(f)$ referred to 10dB gain difference from the peak value.

radiation pattern), retain reasonable omnidirectional features and *ii)* the excited port is still matched. It has been verified that also for the NSA_4 on the ship the embedded VSWR at the system ports remains well matched in the whole HF band (Fig.7.9). When compared with diagrams of Fig.7.7, referring to the NSA_1 performances, the NSA_4 embedded average gain and efficiency show similar values in the most part of the HF band. As explained in 'multi-channel mode' paragraph of Chapter 4, this means that an improvement in

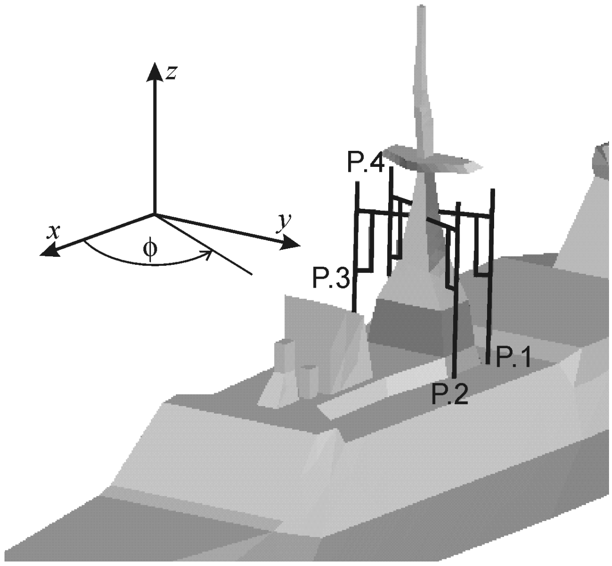

Figure 7.8: NSA_4 on the ship. The four wire radiators are connected to the mast edges.

the system efficiency of about four times can be theoretically achieved when four channels are simultaneously allocated to the NSA_4, one for each port, instead of using the NSA_1 equipped with a 4-channel signal combiner.

The embedded radiation patterns, nevertheless, deserve some discussions. By the geometrical symmetry with respect to the xz-plane, the embedded element factors associated with port $P.1$ and port $P.2$ are mirror images of ports $P.4$ and $P.3$, respectively (Fig.7.8). However, due to the strong interactions among wires, the overall pattern uniformity of each port is worse than the NSA_1 arrangement ($\bar{U} = 40\%$ instead of 70%) and some blind directions appear at different angles and frequencies depending on the excited port (Fig.7.10). The versatility of a NSA_N on a real ship, as a multi-channel system, is hence reduced in comparison with the ideal case of the perfect ground plane since the channels need to be properly distributed over the antenna ports taking into account the angular sector for the communication. For instance, if it is required to activate the NSA_4 on the frigate for a communication at 10 MHz along $\phi = 90°$, the port $P.1$ or $P.2$ have to be used since the others have low values of gain, while for communications at 15 MHz along $\phi = -60°$ both $P.3$ and $P.4$ ports can be chosen.

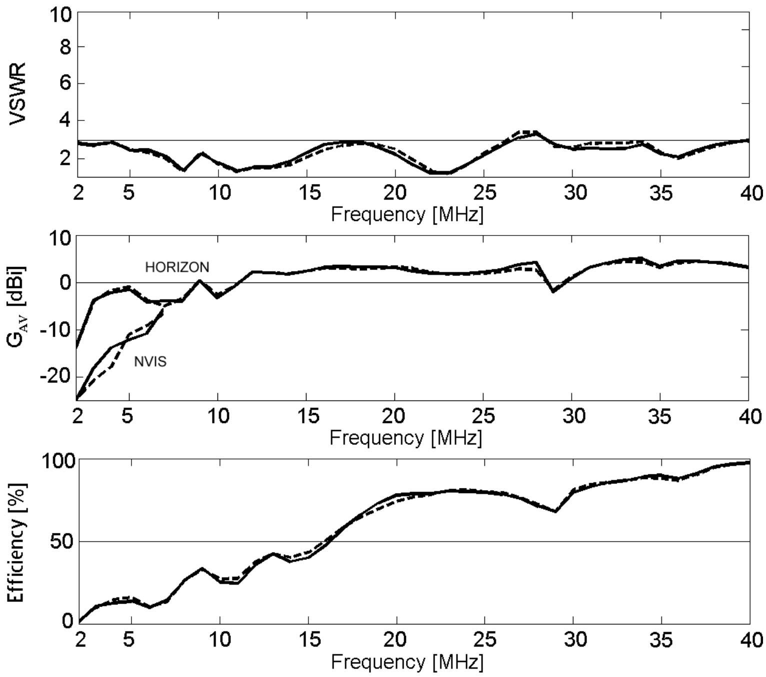

Figure 7.9: NSA_4 on the ship. Embedded VSWR, ϕ−averaged gain and efficiency. Due to the nearly symmetry with respect to the xz-plane of the geometry and the scenario (Fig.7.8), curves related to port $P.1$ (continuous lines) and port $P.2$ (dashed lines) are completely superimposed to those of port $P.4$ and port $P.3$, respectively.

Radiation pattern shaping

The use of the multi-port NSA as an array (coherent mode) promises a moderate degree of pattern shaping with the purpose to improve the gain uniformity or concentrate the radiation toward a given angular sector. The overall radiated field is expressed in terms of active element factor as in (4.2) and, due to the high inter-port coupling, the impedance matching is controlled together with the pattern shaping.

Similarly to the GA synthesis in Chapter 6, it is here formulated a general multi-objective constrained optimization problem for the solution of the excitation coefficients in order to achieve different kinds of performances, such as *i)* the excitation of uniform patterns on the horizontal plane, *ii)* the radiation enhancement within a particular azimuthal angular sector and *iii)*

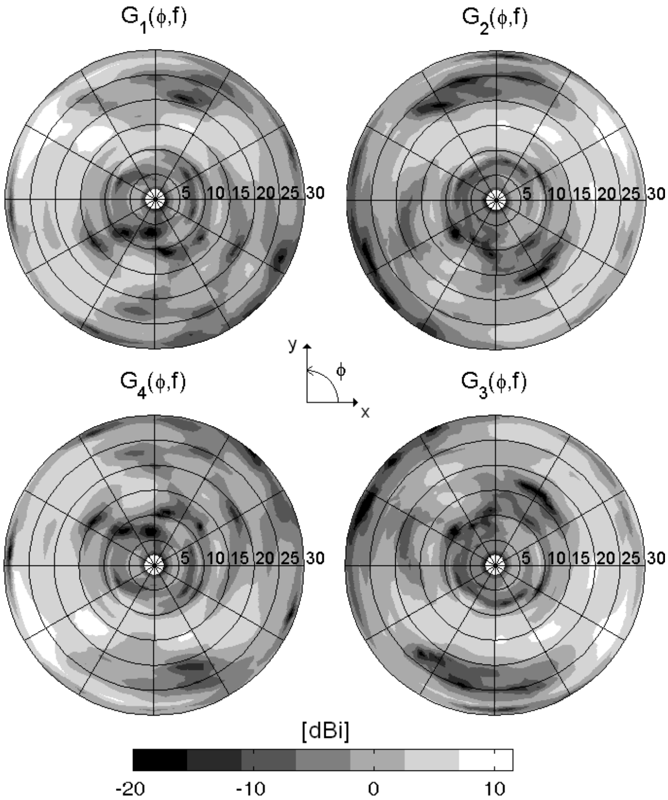

Figure 7.10: NSA_4 on the ship. Embedded gain patterns at the horizon related to each port. Labels on the horizontal axis tag the frequency. Since the ship is almost symmetrical with respect to $\phi = 0°$ (corresponding to the ship bow), G_3 and G_4 are the mirror image of G_2 and G_1, respectively.

the improvement of NVIS radiation. The optimization is performed by controlling not only the pattern shaping, but also the port matching and the number of excited ports.

In order to have the transmitters working with the maximum power, only a phase synthesis will be considered. It is assumed that $C_n = \{0, 1\}$ and, in the general case of N excited ports, i.e. $A_n = e^{j\alpha_n(f)}$, $N-1$ degrees of freedom are available. The multi-objective optimization requires the minimization, at each frequency, of the following penalty function

$$F = w_S F_S + w_U F_U + w_A F_A + w_V F_V + w_N F_N \tag{7.1}$$

where, depending on the particular requirements to be met, only some of the weight coefficients $\{w_x\}$ are different than zero. F_S, F_U, F_A, F_V and F_N

are the normalized functions ($0 < F_x < 1$) described in detail in Appendix B ('On-ship NSA$_N$ excitation' paragraph), respectively controlling the port matching (F_S), the uniformity of the azimuthal pattern at horizon (F_U), the horizontal gain in a defined azimuthal sector (F_A), the NVIS gain (F_V), and the number of excited ports (F_N). In particular, F_U function controls the effective average gain, $G_{EFF} = G_{AV}U$, which is a measure of the pattern uniformity weighed by the average gain G_{AV}, that correctly penalizes those patterns which, although uniform in azimuth, exhibit a low average gain.

Excitation of uniform patterns - A proper choice of the NSA$_N$ phases can mitigate the pattern distortion of the NSA$_1$ radiator caused by the ship interactions, with the purpose to achieve a pattern uniformity $U(f) > 80\%$. Accordingly, the penalty function (7.1) is customized by setting $w_V = w_A = 0$. The reference configuration for the evaluation of the uniformity enhancement is the NSA$_1$ on the frigate corresponding to port P.1 which, from Fig.7.7, suggests some improvements around 8 MHz, 10 MHz, 14 MHz and 29 MHz. After the phase optimization, the azimuthal patterns of Fig.7.11 are obtained for the NSA$_4$, having all the excited ports well matched with VSWR<3. In all the cases the effective average gain G_{EFF} has been highly improved as shown in Tab.7.1. The uniformity requirement is met at all the frequencies with a reasonable high $\phi-$averaged gain at the expenses of the maximum gain which is generally penalized in favour of a raising of the minimum values. It is finally interesting to note that not all ports are always excited: for instance, at 10 MHz and 28.5 MHz only two of them are required to achieve pattern uniformity. In such a case the remaining ports could be allocated to other services, improving the system flexibility, or dedicated to the same channel with higher performances (for instance, the effective gain at 10 MHz can be improved from $G_{EFF} = -1.8dB$ to $G_{EFF} = 1.2dB$).

Improving radiation within an angular sector - To achieve directional properties with the NSA$_4$ *on the mast*, within an azimuthal sector at the horizon, centered at ϕ_0 [$\theta_0 = 90°$, $|\phi - \phi_0| < \Delta\phi/2$], the penalty function in (7.1) is customized by setting $w_V = w_U = 0$. The effectiveness of the optimization results is quantified by a global indicator $I(\theta_0,\phi_0,\Delta\phi)$ giving

Table 7.1: Gain parameters when the NSA is phased for horizontal pattern uniformity

		a)	*b)*	*c)*	*d)*
		8.5MHz	10MHz	14MHz	28.5MHz
		4 ports	2 ports	4 ports	2 ports
G_{MAX}	NSA_1	5.6	4.5	7.5	9.1
[dB]	NSA_4	5.9	2.4	7.2	6.6
G_{AV}	NSA_1	-4.7	-4.3	1.9	1.5
[dB]	NSA_4	0	-1.4	3.8	2
U	NSA_1	45	63	80	57
[%]	NSA_4	85	92	100	80
G_{EFF}	NSA_1	-8.2	-6.3	0.9	-0.9
[dB]	NSA_4	-0.6	-1.8	3.8	1

the relative increase of the radiated power in that angular sector with respect to the pth embedded pattern having the best gain, G_p, toward the steering direction ϕ_0:

$$I(\theta_0,\phi_0,\Delta\phi) = \frac{\int_{\phi_0-\Delta\phi/2}^{\phi_0+\Delta\phi/2} |G_{NSA_4}(\theta_0,\phi) - G_p(\theta_0,\phi)|d\phi}{\int_{\phi_0-\Delta\phi/2}^{\phi_0+\Delta\phi/2} G_p(\theta,\phi_0)d\phi} \tag{7.2}$$

For the NSA_4 on the frigate, it has been found that the gain improvement is evident above 15 MHz, where the NSA ports begin to be electrically far enough to produce an array behavior. Additionally, since the embedded gain patterns (Fig.7.10) are not azimuthally uniform in the whole HF band, there are some frequencies and angles, for instance $\phi = \pm 90°$, where their radiation is simultaneously low and therefore only negligible gain improvement can be achieved by phasing the NSA_4. Fig.7.12 gives some examples of radiation enforcement along the ship bow ($\phi_0 = 0°$) and stern ($\phi_0 = 180°$), and along intermediate directions ($\phi_0 = 330°$ and $\phi_0 = 210°$). The shadowed regions are representative of the radiation power improvement, $I(90°, \phi_0, 90°)$ in $|\phi - \phi_0| < 45°$, ranging from 50% up to more than 200%.

Beyond 30 MHz the mast starts to act as a reflector and the embedded gains are mainly confined within a half space. In this case interesting results can be achieved by turning on that pair of ports having high gain in the required angular sector.

Enhancement of NVIS radiation - The multi-objective optimization of the NSA_N excitation is finally applied to the enhancement of the NVIS radiation which can be obtained within a given azimuthal direction by using a phased NSA_N. This feature can be useful when an obstacle, e.g. a mountain, prevents the sea-wave propagation in a given direction. The penalty function in (7.1) is customized by setting $w_A = w_U = 0$. As in the previous paragraph, the optimized results for the NSA_4 on the frigate model are compared with the embedded gain pattern having the best radiation in $|\phi - \phi_0| \leq 45°$ at $\theta_0 = 10°$ (Fig.7.13). An average 3 dB improvement in the peak gain can be appreciated at the considered frequencies, while the radiated power has been nearly doubled.

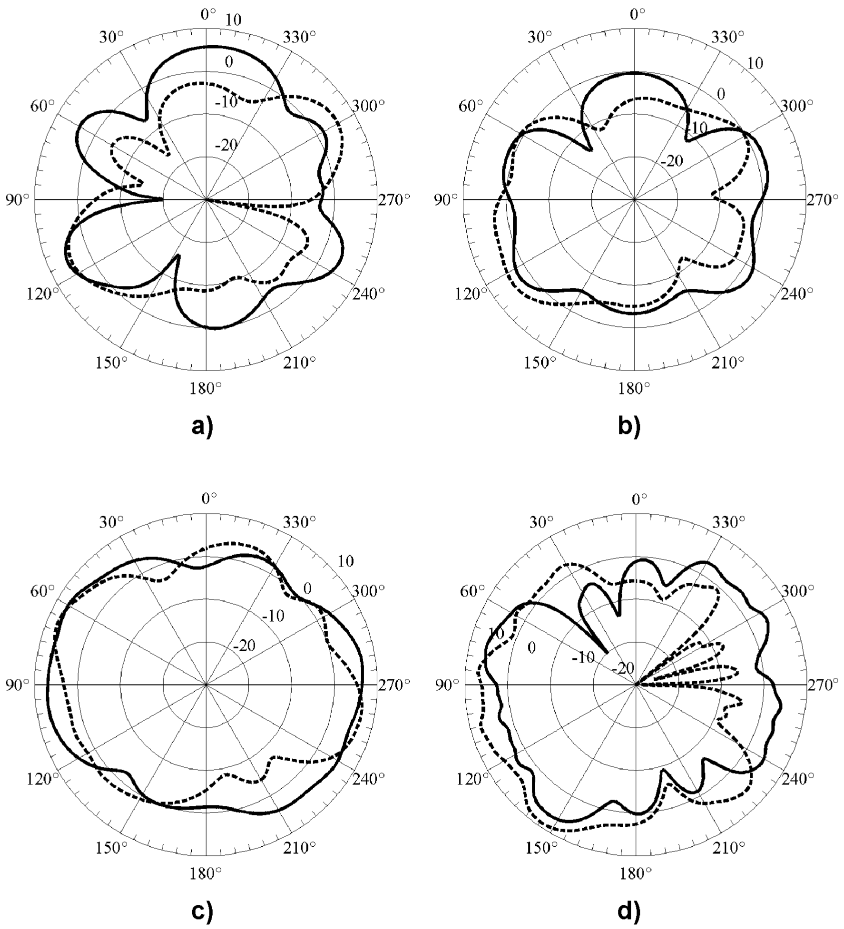

Figure 7.11: Phased NSA_4 (continuous lines) for uniform pattern synthesis at the horizon ($\theta_0 = 90°$) compared with the azimuthal gain pattern of NSA_1 corresponding to port $P.1$ (dashed line). *a)* $f = 8.5MHz$, four ports used, $\alpha_1 = 0°$, $\alpha_2 = 24°$, $\alpha_3 = 325°$, $\alpha_4 = 315°$, $1.7 < VSWR < 2.2$. *b)* $f = 10MHz$, two ports used, $\alpha_2 = 0°$, $\alpha_3 = 5°$, $1.5 < VSWR < 1.7$. *c)* $f = 14MHz$, four ports used, $\alpha_1 = 0°$, $\alpha_2 = 296°$, $\alpha_3 = 164°$, $\alpha_4 = 121°$, $1.7 < VSWR < 2.5$. *d)* $f = 28.5MHz$, two ports used, $\alpha_1 = 0°$, $\alpha_3 = 150°$, $3.1 < VSWR < 3.2$. The direction $\phi = 0°$ corresponds to the ship bow. Details about gain improvements in Tab.7.1.

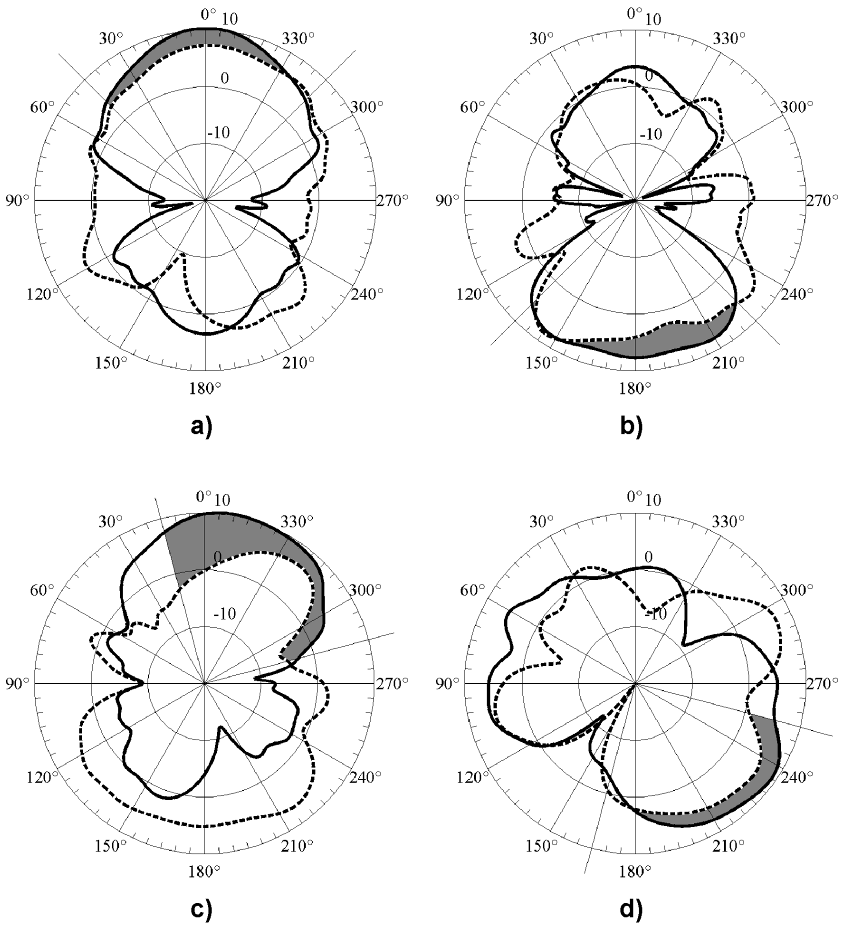

Figure 7.12: Phased NSA_4 (continuous lines) for sectorial pattern synthesis at the horizon ($\theta_0 = 90°$) compared with the embedded pattern having the highest gain at ϕ_0 (dashed lines) *a)* $\phi_0 = 0°$, $f = 20MHz$, two ports used, $\alpha_2 = \alpha_3$, $VSWR = 2.6$, $I = 61\%$. *b)* $\phi_0 = 180°$, $f = 25MHz$, two ports used, $\alpha_4 = \alpha_1$, $VSWR = 2.1$, $I = 56\%$. *c)* $\phi_0 = 330°$, $f = 20MHz$, three ports used, $\alpha_4 = 0°$, $\alpha_2 = 297°$, $\alpha_3 = 289°$, $1.6 < VSWR < 3$, $I = 230\%$. *d)* $\phi_0 = 210°$, $f = 15MHz$, three ports used, $\alpha_4 = 0°$, $\alpha_2 = 200°$, $\alpha_3 = 96°$, $2.3 < VSWR < 3$, $I = 66\%$.

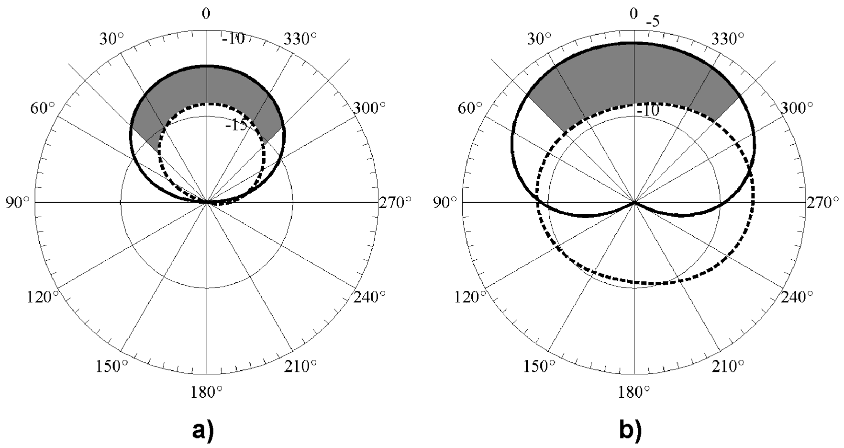

Figure 7.13: Phased NSA_4(continuous lines) for NVIS links around $\phi_0 = 0°$ at $\theta_0 = 10°$ compared with the embedded pattern having the highest gain at such a direction (dashed lines). *a)* $f = 4MHz$, two ports used, $\alpha_3 = \alpha_2$, $VSWR = 2.6$, $I = 63\%$. *b)* $f = 6MHz$, four ports used, $\alpha_1 = 0$, $\alpha_2 = 59°$, $\alpha_3 = 70°$, $\alpha_4 = 344°$, $1.9 < VSWR < 3$, $I = 108\%$.

Chapter 8

Experimental evaluation

This Chapter presents the experimental evaluation of the bifolded antenna and of the NSA. In particular, scale bifolded antenna models were built and measured both above a finite copper ground plane and onboard a scale model of the aircraft carrier G. Garibaldi. Also a full-size scale bifolded prototype was experimentally evaluated in transmission and the results were compared with those of a commercial HF broadband whip antenna.

For what concerns the NSA, two different scale models, in which the central superstructures resemble a funnel and a big mast, were built and measured above a finite copper ground plane [55]. In all the considered cases a good agreement between simulations and measurements is found and the slight differences can be due to the non-ideality of the electrical components, to fabrication inaccuracies and to the use of a non-anecoic measurement environment.

8.1 Bifolded measurements

8.1.1 Scale model on PEC

The optimized topology presented in Fig.3.7 and here reported for clarity (Fig.8.1), in which loading resistors are placed close to the ground plane and only three LC circuits are used, is here considered.

The 1:50 scale prototype in Fig.8.2 was measured on a 1m x 1m copper ground plane and within the scaled up frequency band 100-2000 MHz.

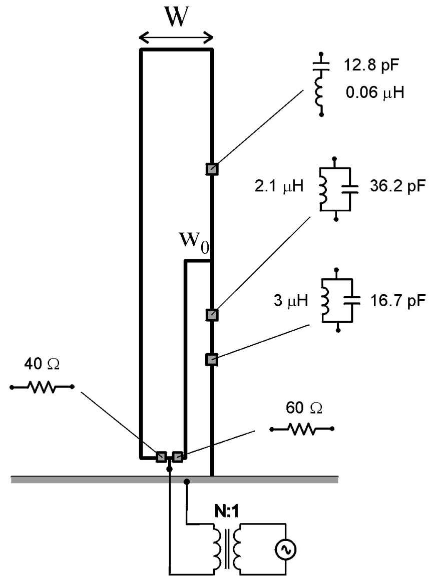

Figure 8.1: Loading topology of the bifolded monopole when resistors are constrained close to the ground plane. The transformation step-up ratio has been set to 4 and $w_0 = (2/5)W$.

It is worth noticing that the inductors and capacitors' values are required to be scaled down of the same factor. The conductor is a 2mm-diameter silvered-copper wire and loading electric devices are sustained by a dielectric substrate.

After the antenna connector de-embedding, the measured input impedance and VSWR in Fig.8.3 and Fig.8.4, respectively, are in good agreement with the numerical MoM model.

In order to check in first approximation the bifolded radiation along the horizon, measurement of the scattering parameter S_{12} between the antenna and a short probe monopole was carried out. Due to the nearly omnidirectional horizontal radiation of the bifolded, an arbitrary direction was chosen for measurement and simulation. The simulation was performed in the free space by placing the two antennas on a copper ground plane of size 1m x 1m. A good agreement between measurement and simulation can be observed.

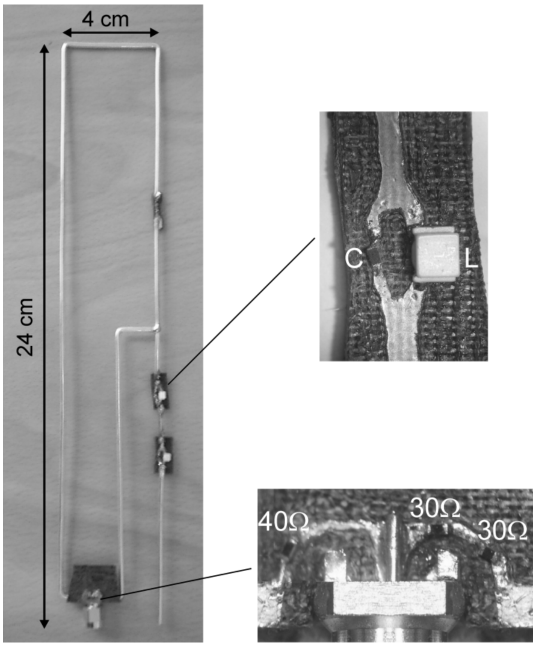

Figure 8.2: Scale model (1:50) of the bifolded antenna in Fig.8.1. On the right, some details about the loading circuit realization.

8.1.2 Scale model on scale ship prototype

In Chapter 7 it was numerically verified that the antenna input impedance is not sensibly modified after the on-ship installation and in this paragraph, therefore, only the horizontal patterns are investigated. Measurements were carried out in a military site of the Italian Navy, properly equipped to perform shipborne antenna measurements onboard realistic scale ship models. Bifolded prototype was mounted on the scale brass model of the aircraft carrier G. Garibaldi in the same position as in Chapter 7, and the overall system was placed on a rotating platform (Fig.8.6). A calibrated transmitting broadband antenna (log-periodic) was placed at 50m from the bifolded and at 1m-elevation from a conductive ground made of zinced cement representing the sea. Measurements were performed in reception mode during a complete turn of the rotating platform.

Fig.8.7 shows the comparison between measurements and simulations of the normalized horizontal radiation patterns. The measured patterns well agree with numerical data and are not so uniform as in the perfect ground

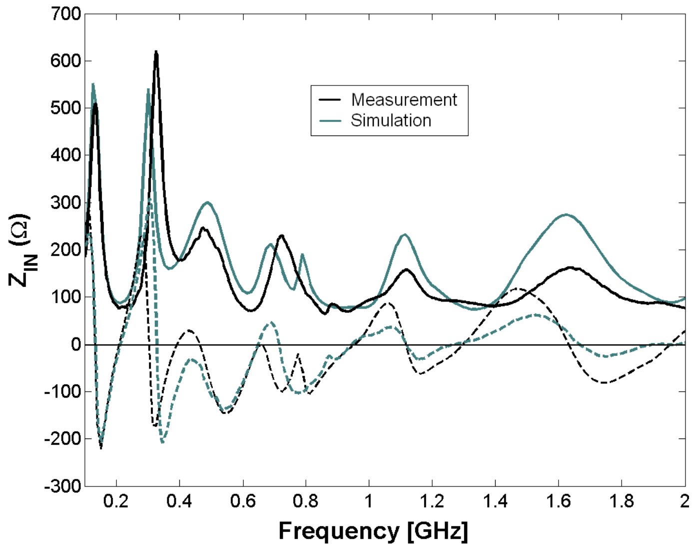

Figure 8.3: Input impedance of the bifolded monopole in Fig.8.2. Simulated data (gray curves) are compared with measurements (black curves). Solid lines tag the real part of the inut impedance while dashed lines indicate the imaginary part.

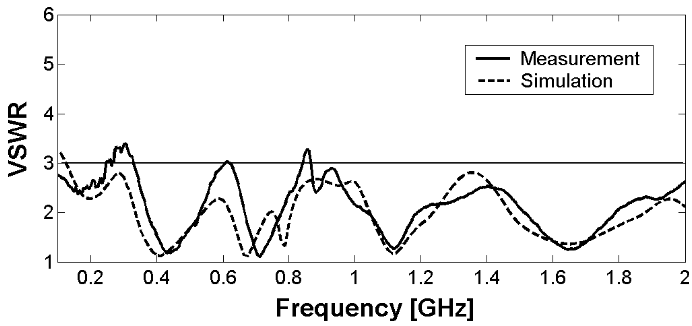

Figure 8.4: VSWR referred to 200Ω of the bifolded monopole in Fig.8.2. Simulated data (dashed line) are compared with measurements (solid line).

plane configuration because of the shadowing effects of the naval superstructures. The considered frequencies corresponds to 3, 15 and 25 MHz of the HF band.

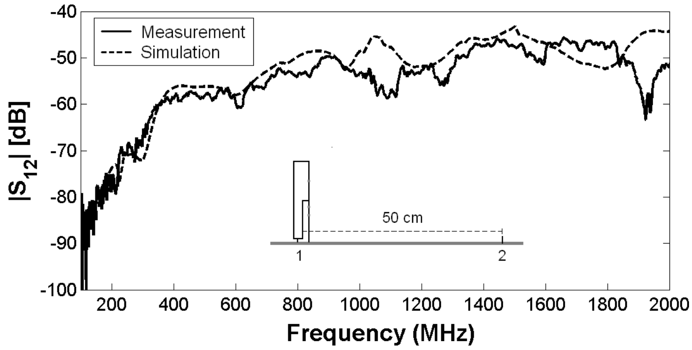

Figure 8.5: Amplitude of the scattering parameter S_{12} referred to 50Ω between the bifolded in Fig.8.2 and a short probe monopole of height 2.3cm. Simulated data (dashed line) are compared with measurements (solid line).

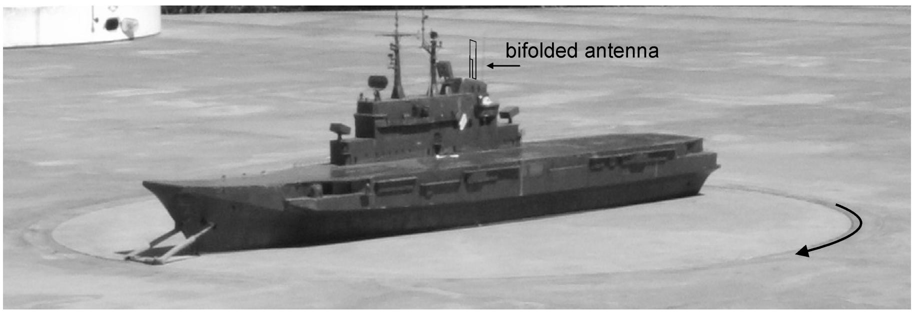

Figure 8.6: Bifolded model mounted on 1:50 scale brass model of the aircraft carrier G. Garibaldi.

8.1.3 Full-size scale model

Fig.8.8 shows the full-size scale bifolded prototype, manufactured by Selex Communications of Pomezia (RM). The box at the antenna basement contains resistors, devices for heat dissipation, and the broadband transformer. This paragraph considers the measurement of radiated field by comparison with a commercial HF broadband 10m-whip, the valcom antenna.

Transmission measurements were performed by feeding bifolded and valcom antenna with the same 150W input power. Antennas, 20m apart, simultaneously transmitted on close channels ($\Delta f = 15KHz$) from Pomezia. The receiving antenna was a tunable short whip connected to a spectrum analyzer and located on Torvaianica; the link length was about 6Km. Fig.8.9

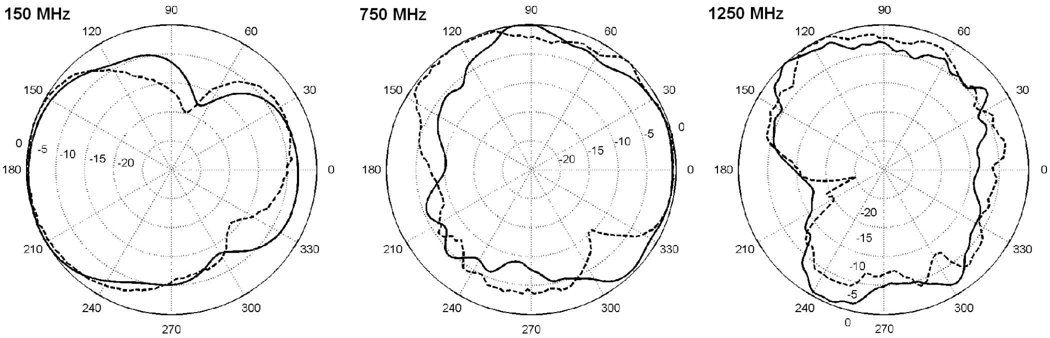

Figure 8.7: Normalized radiation patterns on the horizontal plane at some frequencies. Simulated data (solid line) are compared with measurements (dashed line).

shows the received power from the probe antenna in the HF band. At lower frequencies (2-4 MHz) bifolded seems to work much better than valcom, with a difference of more than 10 dB in the received power. In the range 5-7 MHz the received power is about the same and the radiation seems to depend on the propagation channel more than the antenna typology. In the rest of the band, bifolded radiation is on average higher than that of the valcom antenna.

8.2 NSA measurements

8.2.1 Scale models on PEC

This paragraph experimentally demonstrates the NSA concept and verifies the main electromagnetic features by characterization and fabrication of 1:50 scale NSA prototypes. Two NSA models, resembling a funnel and a big mast, are considered. The sub-radiators are manufactured by printing a metallic trace on a thin dielectric substrate. Simplifications of the NSA geometry, of the loads topology and position on the wires, and the use of a planar technology permit to minimize the fabrication inaccuracies.

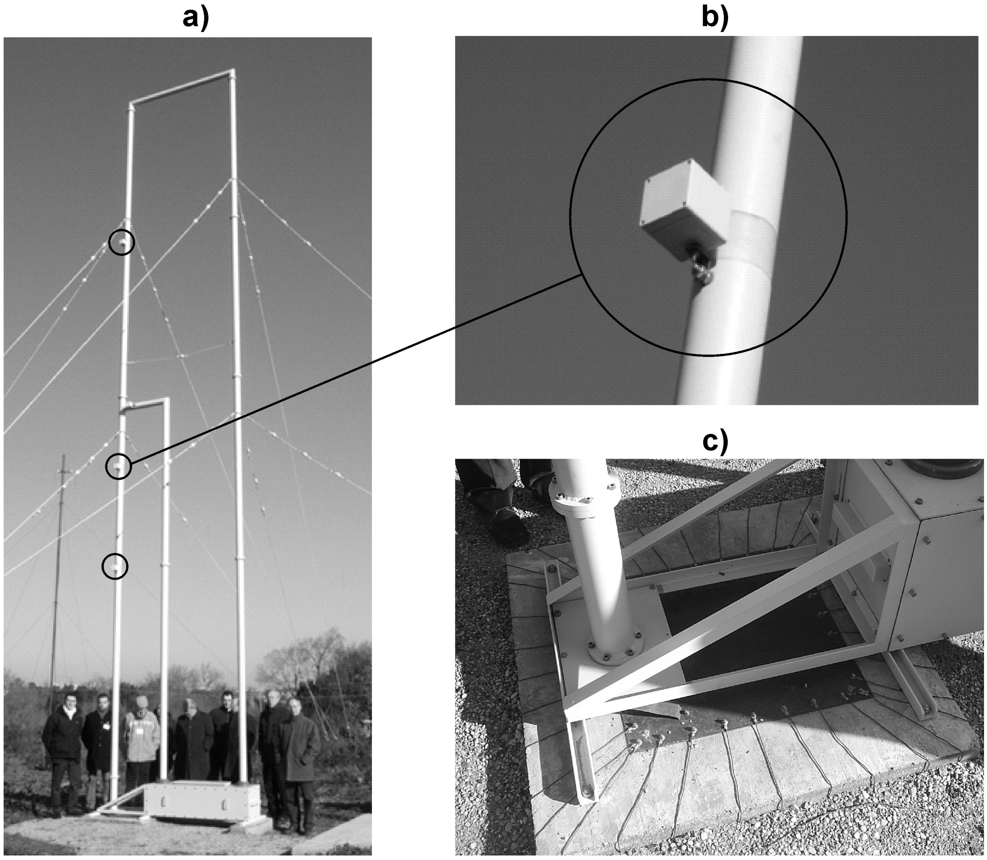

Figure 8.8: *a)* Full-size scale bifolded prototype; circles indicate trap positions. *b)* Detail of a trap. *c)* Detail of the antenna basement, where metallic 20m-wires depart in order to reproduce a conductive ground.

Prototype design and fabrication

Following the layouts in the previous Chapters, two different geometries are considered for the central body (Fig.8.10). The first one is a cylindrical funnel-like structure having about the same height as the loaded subradiators, while the second one is a mast-like structure having about double height with respect to the loaded wires.

With the purpose of obtaining prototypes of reasonable size and feasible electric values for inductors and capacitors, the scaling factor was fixed to 50, which is a typical value for scale models as discussed in [7] and in the previous paragraphs. Accordingly, the frequency band ranges from 100 MHz to 1500 MHz. The loaded conductors are designed as planar traces printed on a thin

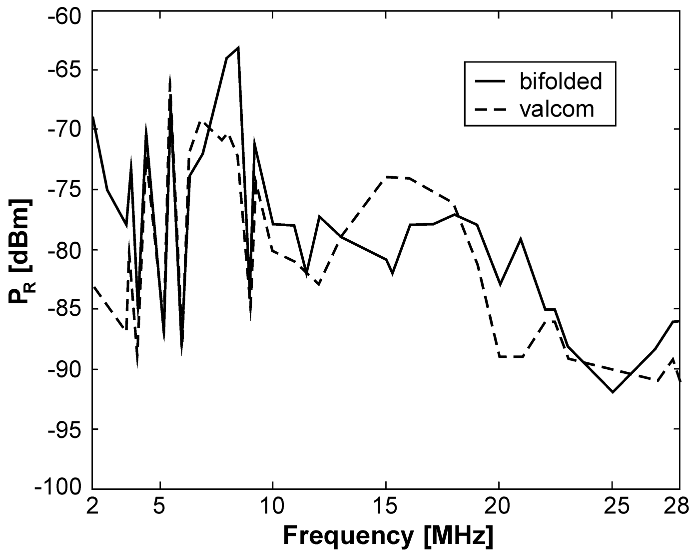

Figure 8.9: Radiation measurements in transmission mode. Comparison between bifolded and valcom antenna.

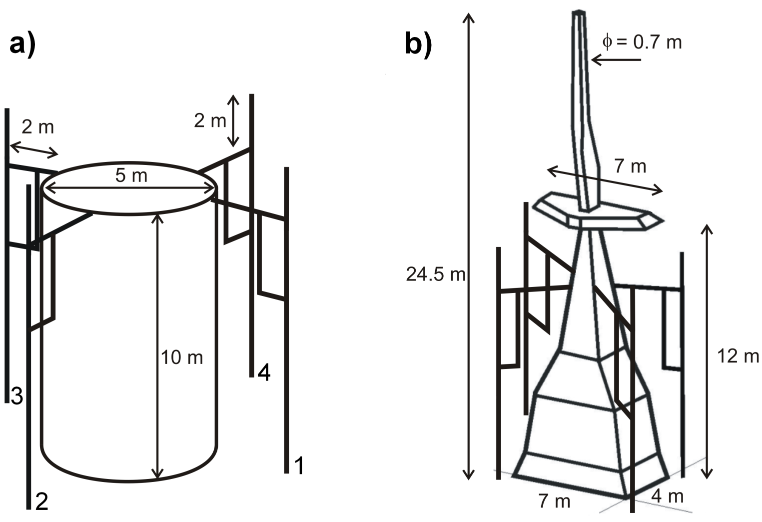

Figure 8.10: *a)* HF-NSA obtained from a funnel-like structure. The four input ports at the base of each sub-radiator are clockwise numbered. *b)* HF-NSA obtained from a mast-like structure.

dielectric substrate (thickness=1.524 mm and ε_r=2.4) as shown in Fig.8.11. The planar technology, in fact, simplifies the assembling of the electrical components and gives a good mechanical stability to the NSA prototype.

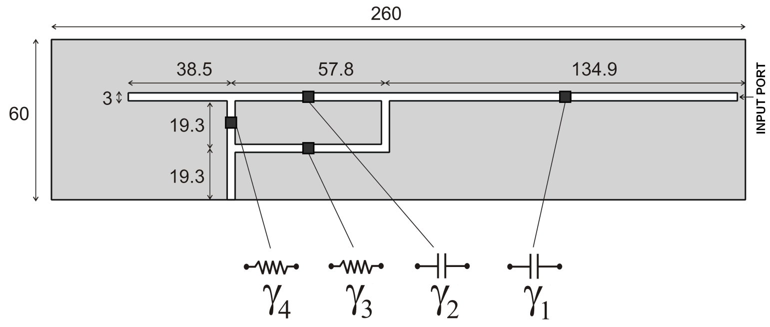

Figure 8.11: Layout of the planar sub-radiator, consisting in a metallic trace on a thin dielectric substrate, loaded with four electrical components in the middle of the related segments. Dimensions are in mm.

A Finite Difference Time Domain (FDTD) [56] electromagnetic solver is used to re-design the NSA loading in presence of dielectric materials with respect to the HF case. The antennas are assumed to be placed over an infinite perfect ground plane. For the mast-like configuration, the central structure is obtained as the combination of a frustum of cone and a pipe. It is worth recalling that, in the optimization procedure in Chapter 3 and 7, the loading impedances could be placed at any position on the wires and generally four lumped elements were enough to achieve the required NSA performances. Here, for fabrication opportunity, such loads have been instead fixed to the centre of each wire. After the optimization of their values and topology, low-valued inductors in the resonant series-connections were dropped out without any significant change in the system performance. The resulting loading set is therefore only given by two capacitors and two resistors (Fig.8.11). The performances of the optimized single-feed scale NSAs in terms of gain at the horizon and VSWR (Fig.8.12 and Fig.8.13) are fully comparable with those of the HF structures previously discussed, where a VSWR<3 and similar values of gain were found in the whole band. These diagrams also show the expected sensitivity of the antenna VSWR to the electric value tolerances. The nominal values of the optimized electrical components used in the simulations of Fig.8.12 and Fig.8.13, as well as the real components used in the fabrication, are given in Tab.8.1 for both the radiating structures. According to the sensitivity analysis, the slight discrepancies should not sensibly affect the measurement results.

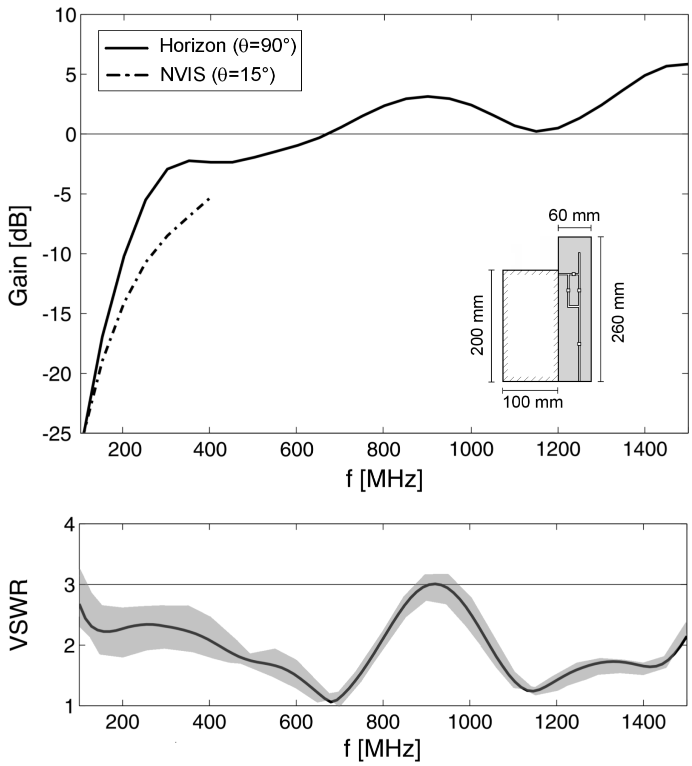

Figure 8.12: Simulated performances of the single-feed scale funnel-like NSA. The shadowed region gives the sensitivity of the VSWR to a random ±15% deviation of the electric components values from the nominal optimized results. VSWR is referred to 200Ω line impedance.

Measurements

The electromagnetic performances of the prototypes have been analyzed by measurements of input impedance, inter-port coupling and near field radiation. Measurements were performed by means of the *Agilent Technologies E5070B* Vector Network Analyzer, by placing the scale NSA models at the centre of a copper ground plane of size 1m x 1m. Experimental data are compared with numerical simulations, wherein the antennas were placed over a perfect electric conductor of the same size.

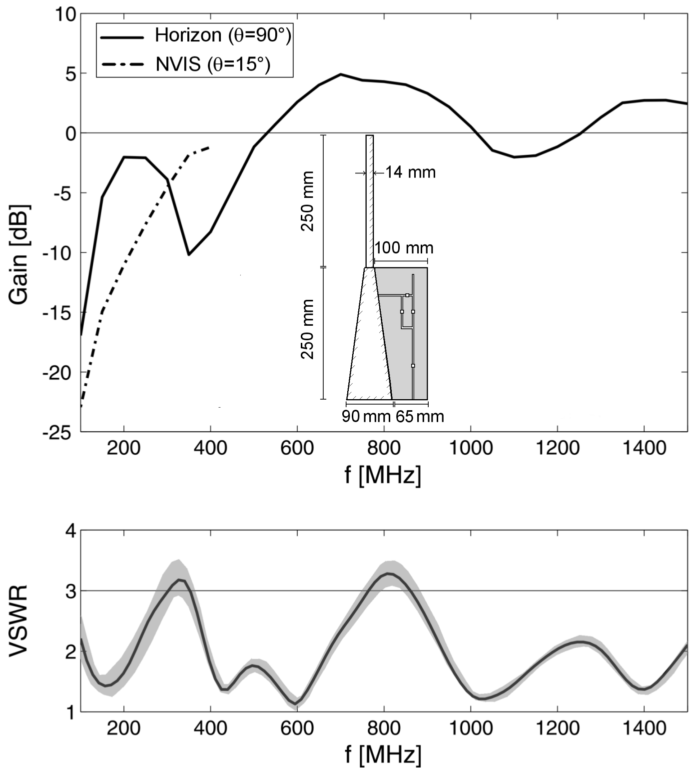

Figure 8.13: Simulated performances of the single-feed scale mast-like NSA. The shadowed region gives the sensitivity of the VSWR to a random ±15% deviation of the electric components values from the nominal optimized results. VSWR is referred to 200Ω line impedance.

Input impedance - Preliminarily, NSA models with only one sub-radiator were manufactured (Fig.8.14a and Fig.8.14b) and measured. A good agreement can be appreciated in Fig.8.15 between measured and computed input impedance in the range 100 MHz - 1500 MHz for both structural antennas.

The measurement was repeated for the 4-port prototypes (Fig.8.14c) with the purpose to analyze the scattering matrix and the embedded VSWR. Also in this case, measurements and numerical simulations compare well (Fig.8.16 and Fig.8.17). The inter-port coupling is less than -10 dB at all frequencies and the embedded VSWR is smaller than 3 in most part of the considered band, as predicted in the theoretical results in Chapters 4 and 7. The slight differences in the four measured embedded VSWR curves are probably due to the fabrication inaccuracies and to the interactions with a non-anecoic

Table 8.1: Nominal and real values of the electrical components of the optimized scaled NSAs. Loads are shown in Fig.8.11.

	funnel-like		**mast-like**	
	nominal	*real*	*nominal*	*real*
γ_1	12.8 pF	12.4 pF	8.9 pF	8.2 pF
γ_2	1.0 pF	1.0 pF	4.9 pF	5.6 pF
γ_3	67.1 Ω	66.5 Ω	110 Ω	110 Ω
γ_4	50.9 Ω	49.9 Ω	110 Ω	110 Ω

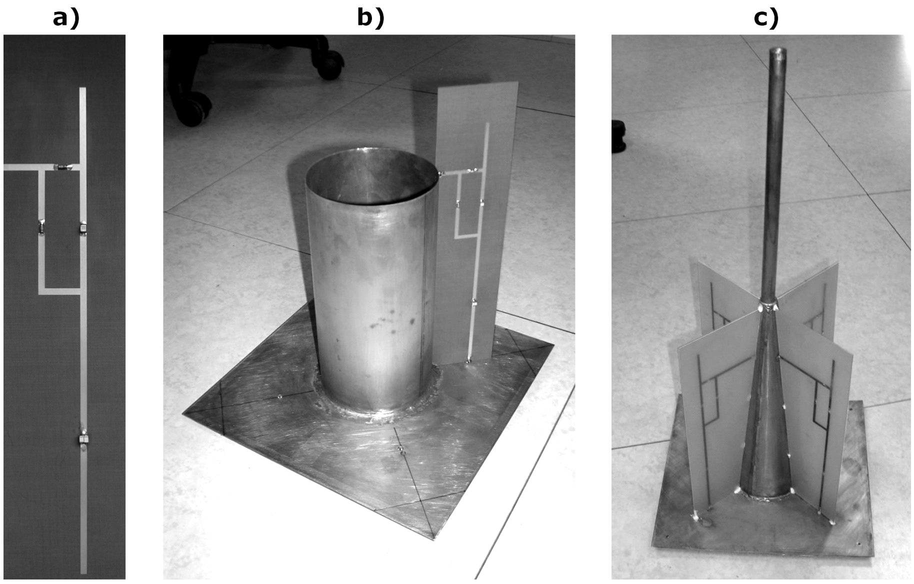

Figure 8.14: *a)* Example of a 1:50 scaled sub-radiator: copper trace printed on a teflon dieletric substrate (thickness=1.524 mm and ε_r=2.4). A width of 3 mm is found to be equivalent to the scaled wire radius [17]. *b)* Example of 1:50 scaled model of the single-feed funnel-like NSA. *c)* Example of 1:50 scaled model of the 4-port mast-like NSA.

environment.

Radiation - The radiation of the NSA structures has been analyzed in the near field region, within a typical lab environment. The near-to-far field transition, estimated for the full-size scale NSAs over an infinite perfect ground,

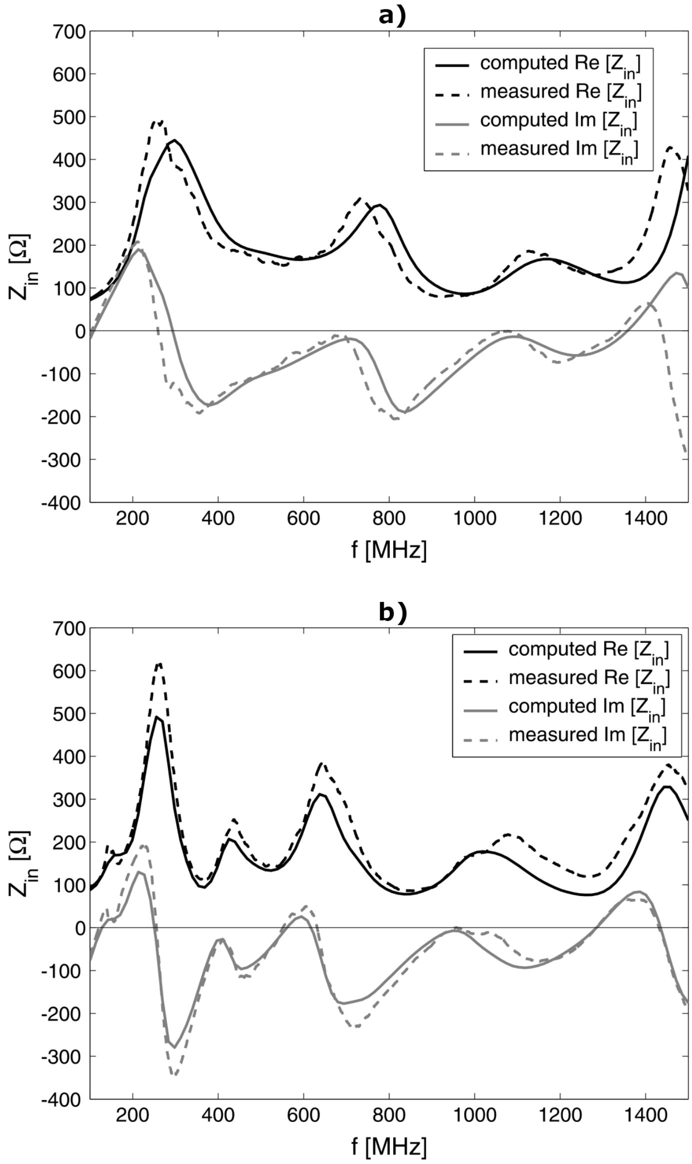

Figure 8.15: Measurement of input impedance on the single-feed NSAs compared with FDTD simulations. *a)* Funnel-like NSA. *b)* Mast-like NSA.

extends from about $8m@2MHz$ up to $115m@30MHz$, for the funnel-like structure, and from $30m@2MHz$ up to $480m@30MHz$, for the mast-like one. The near field measurement gives therefore useful information about the compliance of the transmitters with the field exposure limitations onboard the ship, and about the co-habitation with other onboard equipments. The measurement procedure considers the NSA radiation from a single port when

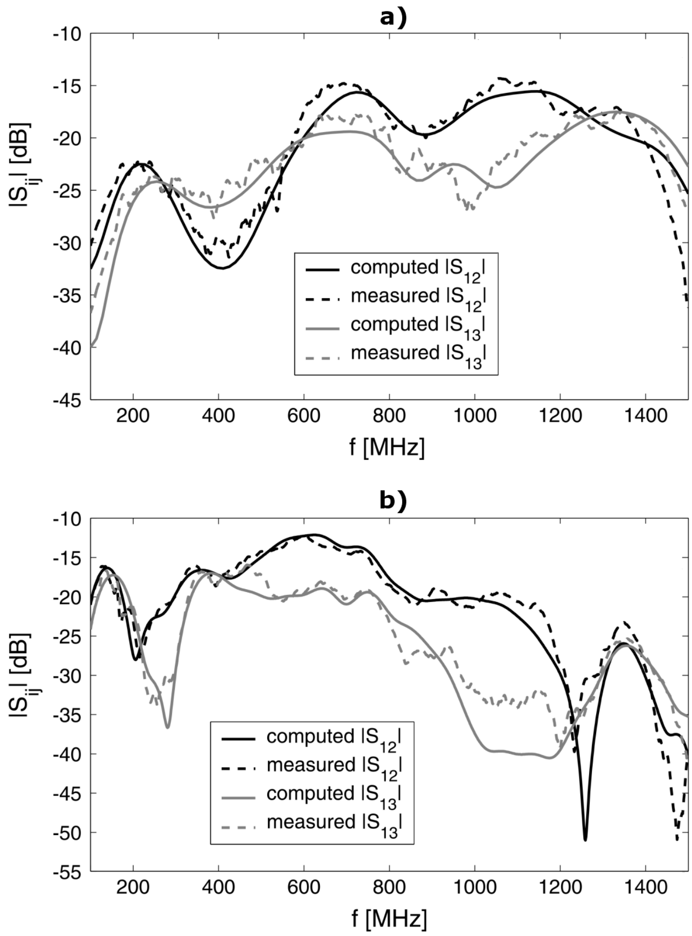

Figure 8.16: Measurement of the scattering parameters on the 4-port NSAs compared with FDTD simulations. *a)* Funnel-like NSA. *b)* Mast-like NSA. In both cases $S_{12} = S_{14}$ due to the simmetry of the structures. Data are referred to a 200Ω line impedance and ports are numbered as in Fig.8.10a.

the others are terminated to a 200 Ω line impedance. The field probe is a short monopole of height $h = 2cm$, which is smaller than $\lambda/10$ in the whole considered band. The monopole is placed at a fixed radial distance $r = 0.388m$ from the NSA geometrical centre in two different positions ($\Delta\phi = 45°$), as shown in Fig.8.18a. During the measurement, the ground plane was locally extended all around the probe to minimize the diffractions from the metallic edges.

The near field data on the horizontal plane are retrieved from the mea-

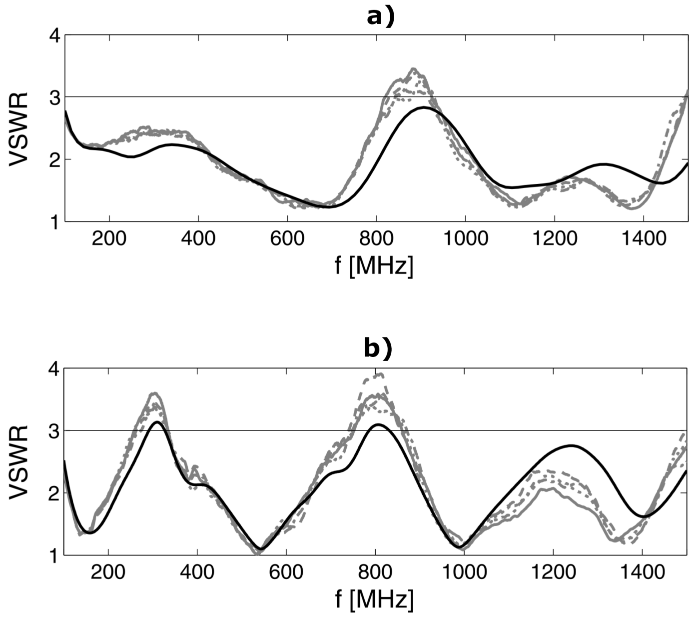

Figure 8.17: Measurement of the embedded VSWRs on the 4-port NSAs (grey lines) compared with FDTD simulation (black line). *a)* Funnel-like NSA. *b)* Mast-like NSA. Data are referred to a 200Ω line impedance.

surements of the mutual coupling S_{0n}, between the n-th sourced port of the NSA and the probe, which receives the vertical component of the radiated field E_z. The strength of E_z at the position of the probe is given by [57]

$$|E_z| = (AF_M)V_R \tag{8.1}$$

where AF_M is the *antenna factor* of the monopole and V_R is the magnitude of the voltage drop at the receiver load R. As described in [58], the antenna factor of a monopole is $AF_M = \left|\frac{R+Z_M}{R}\right| \frac{1}{h_e}$, where $R = 200\Omega$, Z_M is the monopole input impedance, and $h_e = h/2$ is its effective height [57]. The power delivered to the receiver $P_R = \frac{1}{2}\frac{V_R^2}{R}$ is related to the input power P_{IN} at the n-th transmitting antenna port by $P_R = |S_{0n}|^2 P_{IN}$. By combining these relations to express $V_R = |S_{0n}| \sqrt{2RP_{IN}}$, (8.1) becomes

$$|E_z| = \frac{|R + Z_M|}{h} |S_{0n}| \sqrt{\frac{8P_{IN}}{R}} \tag{8.2}$$

The rotational symmetry among the NSA ports permits to estimate the radiation on the horizontal plane along some directions by a small set of measurements. In a first set-up, the probe is placed in position M (Fig.8.18a) and the scattering parameters S_{01}, S_{03} and S_{04} are measured. Then the probe is moved in position N and S_{01} and S_{03} are obtained. By taking advantage of the port periodicity, the five previous measurements can be easily referred to a single port, e.g. port 1, as shown in Fig.8.18b, where $M1$, $N1$ and $M2$ are the positions of three observation points on the circumference of radius $r = 0.388m$ (about $20m$ for the full-size scale antenna). In this way the antenna radiation is estimated at five angularly equispaced directions, by means of just two set of measurements. It is worth noticing that, for the full-size scale funnel-like configuration, the observation points on the circumference are in the far field zone of the NSA in the range 2-6 MHz. Fig.8.19 and Fig.8.20 show the comparison between computed and estimated fields around the NSAs for $P_{IN} = 1W$ input power at port 1. A good agreement is observed in the whole band, particularly in positions N and M, where the probe is closer to the sourced port and, thus, the coupling with the surrounding environment is less effective. (8.2) gives a useful information about the near field strength onboard a ship (at a distance of about $20m$ from the NSA). For instance, for typical $P_{IN} = 1KW$ input power, the curves in Fig.8.19 and Fig.8.20 have to be increased of 30 dB and a frequency-averaged value of about 45-50 dBV/m is found in the various observation points. It is also confirmed that, as expected from a broadband antenna, the field strength exhibits small variations in the considered frequency band. Moreover, up to about 300 MHz, where the assumption of far field is reasonable, the measurements seem to corroborate the azimuthal omnidirectionality of the embedded NSA radiation found in Chapter 4, with maximum fluctuations of less than 10 dB.

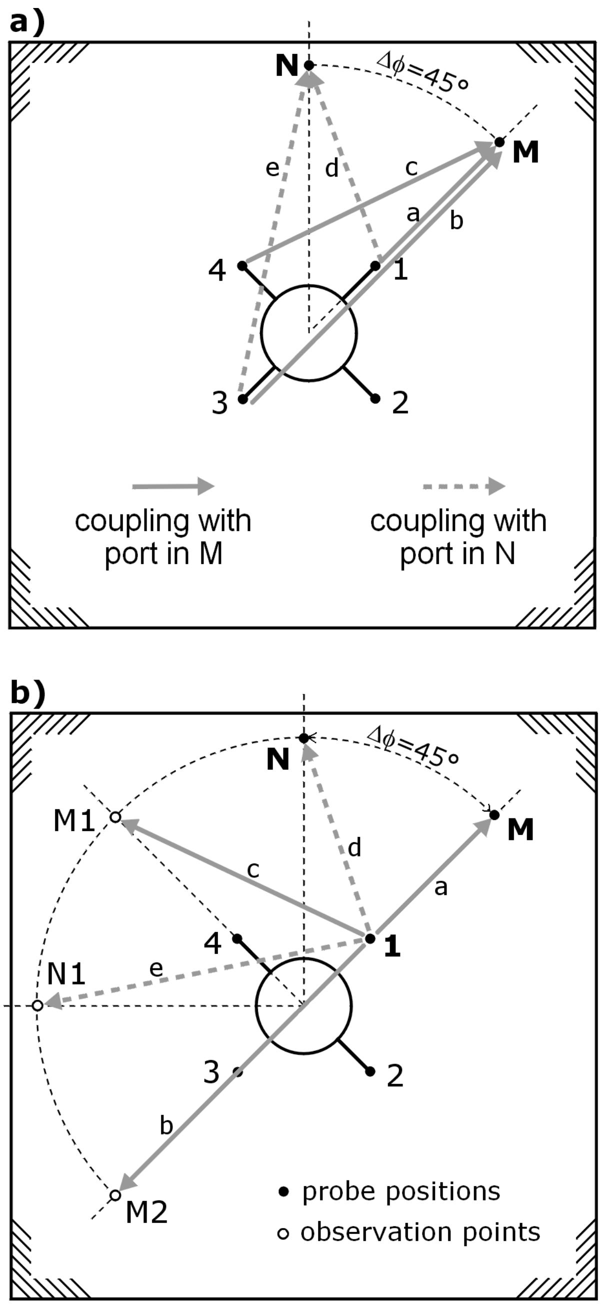

Figure 8.18: *a)* Scheme for the near field measurement using a short monopole, placed in two different positions (M and N). *b)* Estimation of the antenna radiation in five different directions in the half horizontal plane (eight directions all around the NSA); the vectors c, b, e are rotated and translated to be centred in the port 1.

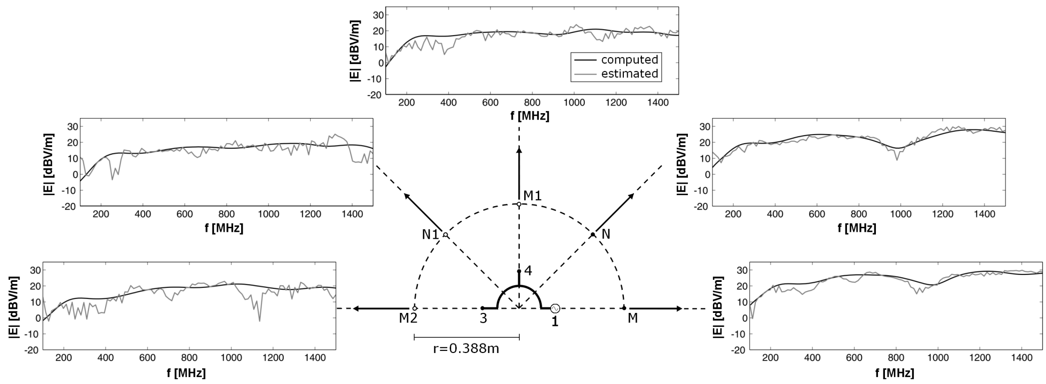

Figure 8.19: Measurement of the near field radiation on the horizontal plane for the funnel-like NSA, compared with FDTD simulations on an infinite perfect ground, along five different directions when port 1 is sourced with $P_{IN} = 1W$.

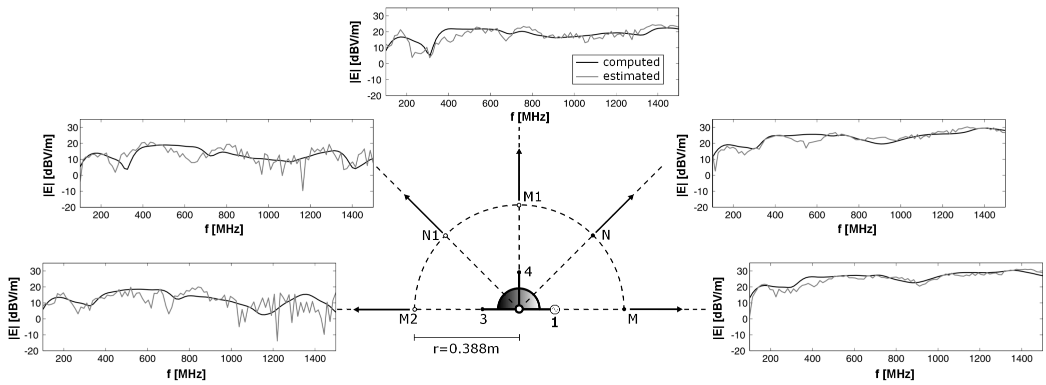

Figure 8.20: Measurement of the near field radiation on the horizontal plane for the mast-like NSA, compared with FDTD simulations on an infinite perfect ground, along five different directions when port 1 is sourced with $P_{IN} = 1W$.

Conclusions

The design methodologies discussed in this work have led to broadband antennas with unconventional features suitable for naval communications.

The antenna impedance loading technique is exploited for different purposes. It is found that the use of a small number of electric circuits (four or five) placed on properly shaped wire antennas is sufficient to cover the whole HF band and to moderately shape the radiation pattern to achieve, for example, NVIS and Seawave links at the same time. The tuning of the electrical components, moreover, is used to compensate the modification of the antenna performances, particularly the input impedance, when the radiator is placed in electromagnetic scenarios different from the original one. For instance, the tuning of the HF bifolded is performed to minimize the coupling with a top-mounted discone antenna for VHF/UHF bands.

The best way to compensate the electromagnetic performance modifications due to the presence of large metallic objects near the antenna consists in considering them as an active part of the antenna since the design stage. This strategy has led to the design of the naval structural antennas where an existing metallic superstructure, such as a funnel or a big mast, is connected to some loaded wire conductors and is exploited to maximize the overall radiating structure performances.

By driving the structural antennas with multiple feeding-ports, additional degrees of freedom in the synthesis procedure are exploited. In particular, when these multi-port radiating structures are fed incoherently, a sensible increase of the radiated efficiency with respect to the conventional single-port broadband radiators can be obtained. The coherent feeding strategy, instead, permits to shape the beam in a similar way as in the conventional array configurations. In particular, it is possible to perform sectorial coverages or broadcasting communications by compensating the radiation pattern distortion due to the shadowing effects of the naval superstructures.

In order to shape the beam without causing the port-mismatching, due to the close proximity of the radiating elements and the strong interactions with the surrounding environment, constrained array synthesis strategies have been succesfully adopted.

Despite the fabrication inaccuracies, the non-ideality of the electrical components, and the use of a non-anecoic measurement environment, the experimental evaluation on scaled and full-size prototypes of the new antennas has shown a good agreement with simulations, that corroborates the effectiveness of the employed methodologies.

The innovative antennas that resulted from the design techniques presented in this Ph.D. work promise to overcome the limitations of the actual shipborne systems, providing a great operational flexibility and a smart power handling with a modest space requirement. The power supply, the transmitters and the amplifiers can be therefore concentrated within a small space with a great simplification on the distribution and control networks.

Appendix A

BLADE: a Broadband Loaded Antenna DEsigner

In the last years, some popular electromagnetic solvers, such as the public domain 4-NEC2 [59] or the commercial SUPERNEC® [60], have been equipped with GA-based optimizers conceived for general purpose applications. They offer a moderate customization of the whole optimization set-up, including the expression of the objective function. Moreover, they require intensive and repeated fullwave electromagnetic analysis and therefore they are not particularly suited to broadband optimizations due to the large time involved.

This Appendix presents a versatile electromagnetic tool, named *BLADE* [61], especially dedicated to the combined design of loaded antennas equipped with a matching network for broadband or multiband applications. It implements a Genetic Algorithm optimizer to automatically select the great number of parameters relating to the traps and to the matching network, and uses a reduced antenna port model to quickly evaluate the antena system performances. The tool allows the user to rationalize the whole antenna design and to efficiently handle all the available degrees of freedom. A particular care was addressed to the possibility of setting the range of the electrical components to be optimized, in order to assure a practical feasibility. Moreover, the user can easily customize the objective function containing the electromagnetic requirements and can examine the entire optimization process by means of a monitor module. The tool has a graphical interface designed in MATLAB® and can be directly linked to the popular NEC2 [23] solver. Nevertheless, the possibility to handle reduced port models of the antenna, permits to use any kind of numerical solver for the electromagnetic analysis.

At the beginning of this Appendix, the concepts of impedance loading and broadbanding are recalled, then an optimization method is presented, based on the Genetic Algorithm, to determine the best topology, position and electrical values of lumped impedances (traps) and of a matching network with respect to a particular objective function. The modular architecture of the tool is then described and some examples of broadband and multiband antenna designs in complex environment are shown to demonstrate the potentiality of the tool.

A.1 Impedance loading and broadbanding

Impedance loading, widely argued in literature, seems to be an interesting solution to design multiband, broadband and compact antennas. An electrically loaded antenna is obtained by placing lumped or distributed impedances, generally denoted as RF traps (parallel LC circuits [62], transmission line stubs [9], [63], dielectric and magnetic beads [10]), on simple wire radiators in order to properly modify the current distribution along the conductors with the purpose of enhancing the desired antenna performances. Together with the antenna loading, the broadbanding strategy can also provide an "on-body" matching network [64], [22]. Some constructive realizations of lumped impedances on monopoles operating in the VHF/UHF band are shown in [65]. Antenna loading is even attractive for antenna miniaturization purpose, within the theoretical limitations of small antennas [66], [67]. In [68], it has been demonstrated that by using distributed impedances, more than a 30% reduction in monopoles length can be achieved preserving nearly the same radiation characteristics. The problem of the antenna size is a critical issue in the HF band, particularly when the available space for antenna installation is limited, such as in naval scenarios [7], [69]. Finally, the design of loaded antennas reveals rather flexible when tunable components realize the traps. In this case, changes in the electromagnetic environment surrounding the antenna, can be compensated by a new design of the antenna loading preserving acceptable performances.

In all the optimizations here considered, only lumped impedances are used to load the wire antennas and, because of the multiplicity of parameters relating to the broadband radiating system (traps and matching network), a powerful design procedure based on a Genetic Algorithm (GA) driven optimization is performed [22], [31], [30], [68].

A.1.1 Trap concept

The trap is a circuit that anti-resonates at a given frequency assuming an infinite impedance. The most common trap, whose constructive implementation is described in [62], is represented by the parallel inductor-capacitor connection (LC circuit) which anti-resonates at $f = 1/2\pi\sqrt{LC}$. By properly integrating one or more of these traps into a wire antenna it is possible to strongly modify its electromagnetic features. Fig.A.1 helps to recall the basic idea of the trap-loaded antenna. A quarter-wave monopole of length l, having the first resonance at f_0, exhibits a rather high input resistance at the second resonance $2f_0$. If a parallel LC trap (designed to anti-resonate at $2f_0$) is placed in the middle of the monopole, the current distribution at f_0 is not strongly perturbed because of the low impedance of the trap. At $2f_0$, instead, the current in the upper part of the antenna is nullified and it radiates as a quarter-wave monopole of length $l/2$ even at this frequency. In this case, the use of a single trap has led to a dual-band antenna that can be considered as the composition of two quarter-wave monopoles of different size.

A.1.2 Broadbanding strategy

The integration of one or more loading circuits along the antenna wires permits to control, dynamically with the frequency, the current distribution and consequently the input impedance, the radiation pattern and the efficiency. The traps are generally used to improve the antenna bandwidth or to achieve multiband features. Though the parallel LC circuit is the most common kind of trap, other topologies, including lossy circuits, can be used

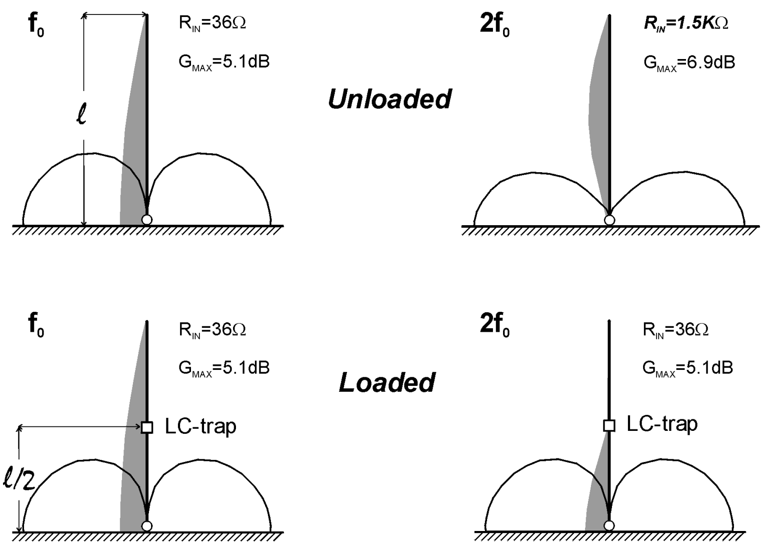

Figure A.1: The concept of trap. In the upper part, the current amplitude (shadowed region) and the radiation pattern of a conventional monopole at the first and second resonance. In the lower part, the features of a trap-loaded monopole which exhibits the same radiation pattern and impedance at the two frequencies.

too. For example, parallel inductor-resistor circuits have been proposed in [65]. The optimizations performed in the next paragraphs, provide three different topologies of load: the parallel and series LC circuits, that respectively act as an open- and a short-circuit at their resonant frequency (Fig.A.2) and as reactive loads elsewhere, and the isolated resistors, useful to achieve a frequency-dependent attenuator distributed all over the antenna. By the series connection of these basic circuits, even more complex topologies can be attained. These new composite loads can exhibit multiple resonances (see Fig.A.2, where the series connection of a parallel and a series LC circuit is considered), adding further degrees of freedom in a synthesis procedure. Different kind of traps, involving transmission line stubs, have been considered in [9], [63]. These devices require additional wire segments to be added to the original antenna and possess an infinite set of resonances defined by a small set of degrees of freedom. Only lumped traps will be considered here since their input impedance can be better controlled all over a wide band. Besides the antenna loading, also a matching network [64], [22] can be introduced between the loaded antenna and the transmitter in order to further reduce the VSWR. The general components of a matching network are a lossless ladder network, an impedance transformer and a frequency-independent attenuator (Fig.A.3).

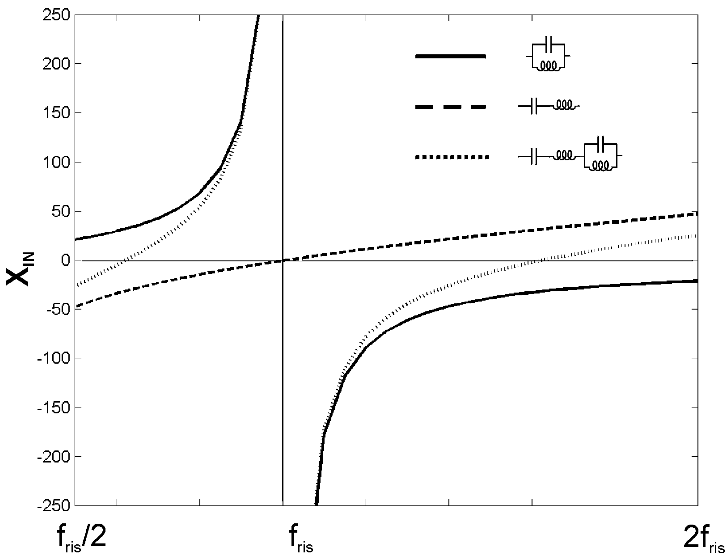

Figure A.2: Input reactance of simple and combined loading circuits.

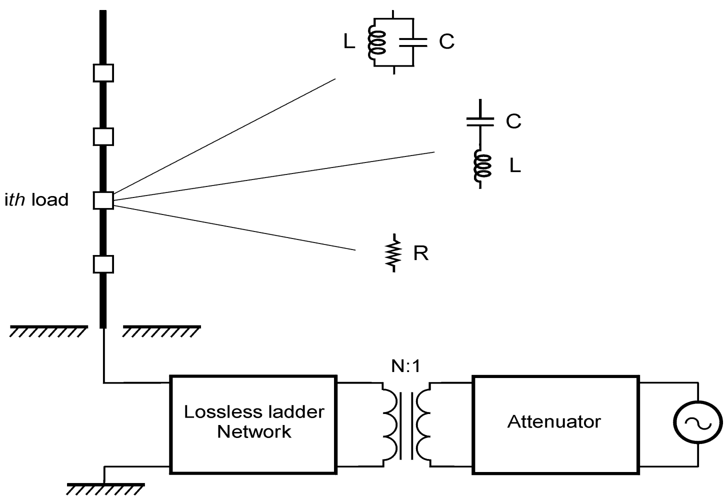

Figure A.3: General composition of a broadband antenna system.

A.1.3 GA Design optimization

Designing a broadband/multiband loaded antenna system to satisfy certain requirements, generally entails the solution of a non-linear optimization problem. The optimizer has to determine a large set of optimal parameters, i.e., the locations and the electrical values of the loads, and the components of the matching network. For instance, the design of an antenna loaded with 4 parallel LC traps and connected to a 3rd order ladder network involves the simultaneous optimization of 15 parameters. An efficient and commonly used procedure, when a great number of unknowns has to be determined, can be based on the Genetic Algorithm [31]. The solution of the optimization problem involves a search for the maximum (or the minimum) of a judiciously selected objective function (or fitness function) over the space of design parameters. The objective function primarily depends on the antenna requirements and it is typically expressed in the form of a summation

$$F = \sum_i w_i G_i \tag{A.1}$$

Each of the G_i terms reflects a desirable antenna feature that needs to be improved, and w_i is the related weighing coefficient. The choice of the objective function reflects on the final result of the entire optimization and therefore all the parameters included have to be carefully selected, with particular attention to the weighing coefficients. Often, the expression of the objective function becomes definitive after some attempts consisting in adjusting the weighing coefficients at the end of each optimization and consequently this is the most critical part of the GA.

The tool here presented is based on a combined MoM/GA approach. Since the optimization procedure in principle demands thousands of antenna analysis as the circuit parameters are changed, it is useful to define a reduced port model of the antenna in order to speed up the process. The antenna port model is obtained by solving the problem for the unloaded structure at each frequency and storing all the inverted MoM matrices. Then, for each new set of loads, the solution can be constructed from that of the unloaded antenna by using both the Sherman-Morrison-Woodbury-based scheme [22] or even a simpler approach, discussed in [30], which requires the inversion of small matrices of size only depending on the number of the employed loads.

A.2 Optimizer architecture

The optimization tool is developed in MATLAB® [70] and is equipped with a modular interface assembled by means of the MATLAB GUIDE facility that allows the user to easily set-up the optimization process, to monitor it during its evolution, and to post-process the results. Besides the graphical interface, the tool offers the possibility to insert all the input data directly by a script file for off-line driven optimization. This paragraph introduces both the general architecture of the tool and the functionality of each module. First of all, *BLADE* can process two different inputs: a text file written by the NEC2 code, defining the antenna geometry to be optimized, or a reduced port model of the unloaded antenna, separately produced by any electromagnetic solver. In the first case, the optimizer displays the NEC2 structure (Fig.A.4) and by the *Antenna* module the user sets all the parameters required to the NEC2 engine to directly produce the reduced antenna port model. The second step consists in the overall broadband antenna system optimization set-up. All the parameters are grouped into independent modules, comprising the *Loads* module, the *Network* module, the *Requirements* module and the *GA* module as shown in Fig.A.4. This modular approach allows the user to handle all the involved parameters in a versatile and efficient way. In particular, the Requirements module assists in the definition of the objective function and in the calibration of the weighing coefficients. Once the whole set-up is completed, the optimization process starts and a *Monitor* module permits to control the progresses. The optimization results can be managed by a *Post-processing* module.

A.2.1 Antenna module

This module is used to set all the parameters relating to the antenna (Fig.A.5) when the reduced port model has to be built by *BLADE* itself. At this purpose it is possible to explicitly indicate which parts of the antenna can potentially host the loading circuits or let the whole structure to be loaded. Finally, it is possible to constrain some resistors on the antenna, by specifying their locations and values. In the case of high power dissipation, e.g. in the broadband HF antennas, constraining the resistors close to the ground plane

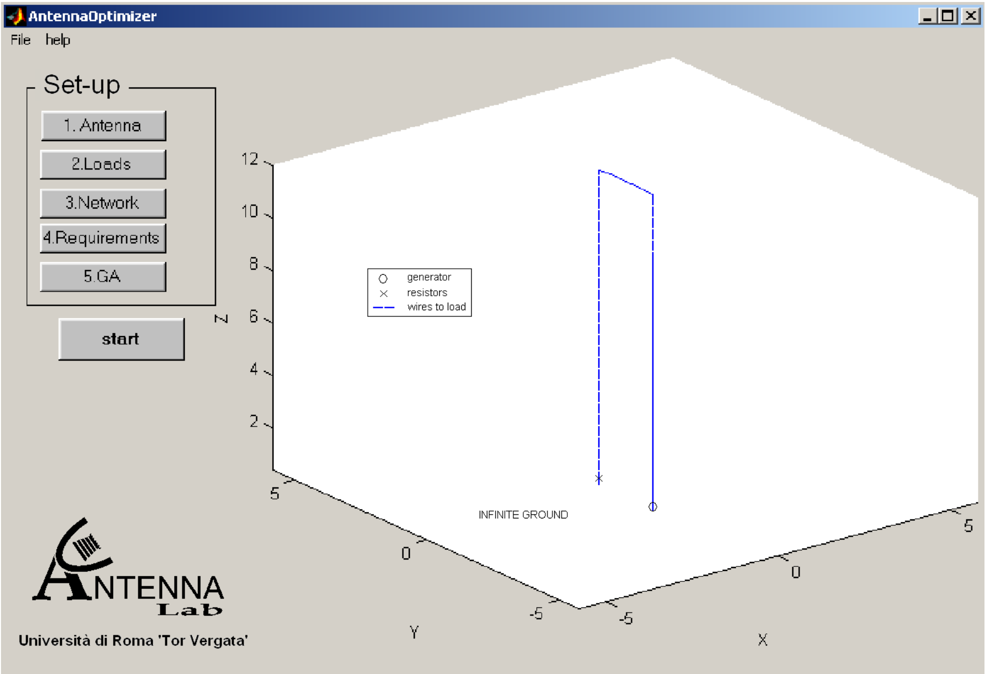

Figure A.4: Optimization set-up window and geometry of an antenna to optimize. The circle is for the source position, the 'x' indicates the constrained resistors and the segmented wires tag the parts of the antenna which can be loaded.

can simplify the cooling equipment. Once all the antenna parameters have been set, Fig.A.4 is updated and the generator, the resistors, the wires to load and the antenna environment are shown.

A.2.2 Loads module

The Loads module is used to define all the parameters relating to the lumped impedances that will load the selected antenna wires. As visible in Fig.A.6, the user can provide the maximum number of loads and their topology (resistors and parallel and series LC circuits). Moreover, it is possible to set feasibility bounds for the electrical components, to customize their binary coding and to indicate the Q-factor of the inductors. It is useful to remember that large values of inductance require large coils with respect to the wavelength that can get undesired self-resonances [29]. Concerning the resis-

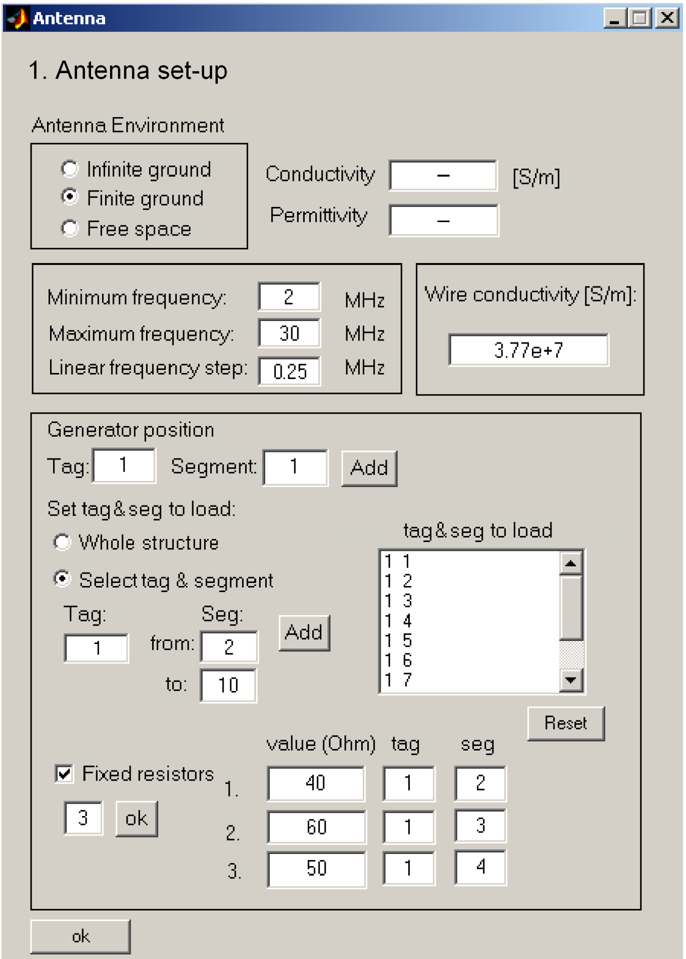

Figure A.5: Antenna module: the parts of the antenna to be loaded (according to the NEC2 tag formalism) and the positions of the fixed resistors can be defined.

tor limitations, instead, large resistances could require cooling systems to be distributed along the wires for high power dissipation.

A.2.3 Network Module

This module is used to assembly the matching network which is generally composed by the cascade, between the transmitter and the antenna, of a lossless ladder network, an impedance transformer and an attenuator (Fig.A.3). As visible in Fig.A.7, the user can decide to optimize the electrical compo-

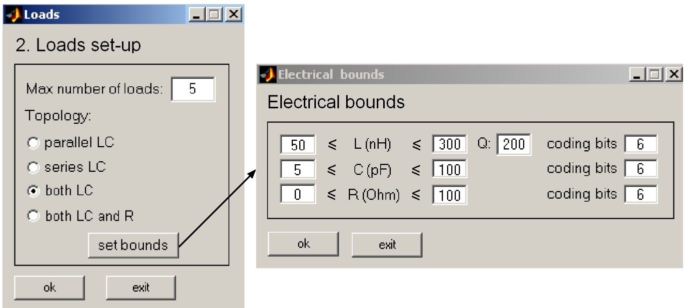

Figure A.6: Loads module: set-up of the loads topology and values.

nents of the lossless network, choosing among low-pass and high-pass filters of the 3rd and the 5th order, the impedance transformer step-up ratio, and the attenuation constant. The bounds and the coding bits of the lossless network components are the same as for the loads.

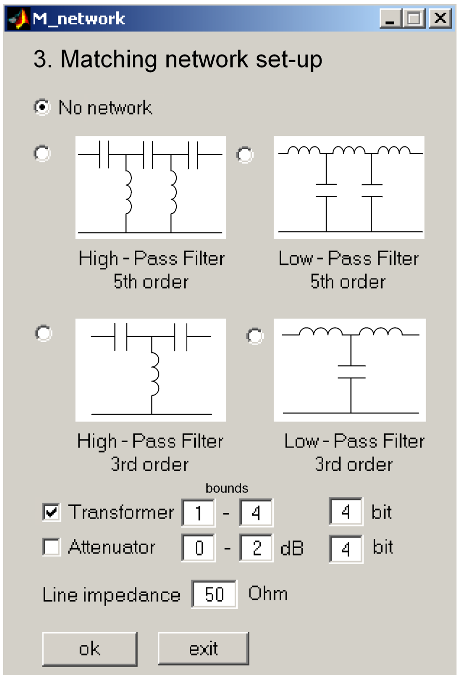

Figure A.7: Network module: set-up of the matching network.

A.2.4 Requirements module

This module allows the user to manually assembly the objective function to be minimized, whose general expression is shown in the upper part of Fig.A.8. This function evaluates the goodness of each individual with respect to the optimization problem. N_f is the total number of frequency samples in the selected range (tagged by the index n), $F_v^{(n)}$, $F_\eta^{(n)}$ and $F_g^{(n)}$ are the functions shown in (A.2)-(A.4), respectively controlling the antenna matching, the efficiency and the gain along a given direction. In these functions, s_0, η_0 and G_0 are frequency-independent thresholds, whose values depend on the system requirements. In particular, the VSWR has to be constrained under s_0, while the efficiency and the gain have to be confined above η_0 and G_0, respectively. Functions $w_v^{(n)}$, $w_\eta^{(n)}$, $w_g^{(n)}$ selectively weigh $F_v^{(n)}$, $F_\eta^{(n)}$ and $F_g^{(n)}$ in different parts of the band, while coefficients C_v, C_η, C_g are frequency-independent weights which add further degrees of freedom. Finally, F_L tries to minimize the number of loading impedances placed on the antenna and w_L is the related weight. Such an objective function reaches its minimum when all the antenna specifications are met, namely when the functions (A.2)-(A.4) are simultaneously zero.

$$F_v^{(n)} = \begin{cases} 0 & \text{if } VSWR^{(n)} < s_0 \\ \frac{VSWR^{(n)}-s_0}{VSWR^{(n)}} & \text{otherwise} \end{cases} \tag{A.2}$$

$$F_\eta^{(n)} = \begin{cases} 0 & \text{if } \eta^{(n)} > \eta_0 \\ \frac{\eta_0-\eta^{(n)}}{\eta_0} & \text{otherwise} \end{cases} \tag{A.3}$$

$$F_g^{(n)} = \begin{cases} 0 & \text{if } G^{(n)} > G_0 \\ \frac{G_0-G^{(n)}}{G_0} & \text{otherwise} \end{cases} \tag{A.4}$$

As visible in Fig.A.8, the user can assembly the objective function by selecting the VSWR, the efficiency and the direction (θ, ϕ) where the gain has to be optimized, and by defining the thresholds G_0, η_0, s_0 and all the weights above mentioned. In particular, the frequency-independent weights have to satisfy the relation $C_v + C_\eta + C_g + w_L = 100\%$, while the frequency-dependent

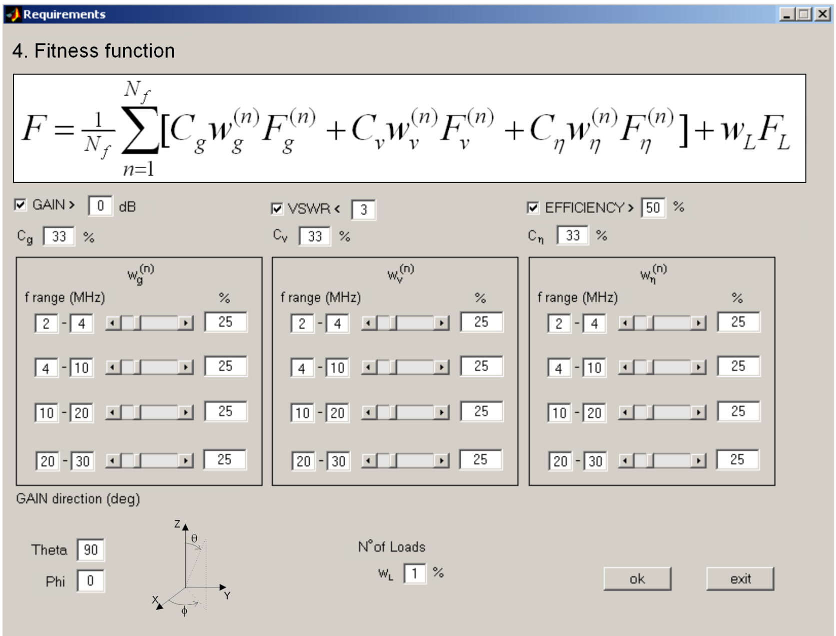

Figure A.8: Requirements module for the customization of the fitness function.

parameters can take different values for each sub-band, whose sum is 100% again. This arrangement of the fitness function permits to obtain broadband or also multiband (up to 4 bands) antennas. The four frequency ranges of each performance to be optimized are independent and could be either contiguous or separated to further customize the optimization strategy. Explicative examples about the role of the objective function in the optimization outcome will be shown later on.

A.2.5 GA module

The GA module is used to customize the parameters of the Genetic Algorithm. As visible in Fig.A.9, first of all the user has to set the number of individuals of each population (which has to be approximately equal to the number of bits of the resulting chromosome), and the probabilities concerning the genetic operators [31]. In particular, the generation gap indicates the fraction of the population to be reproduced. Next, an escape test has to be defined. The Genetic Algorithm stops whether one or both the following conditions are met: the maximum number of iterations is reached and the best individual remains the same for a given number of iterations.

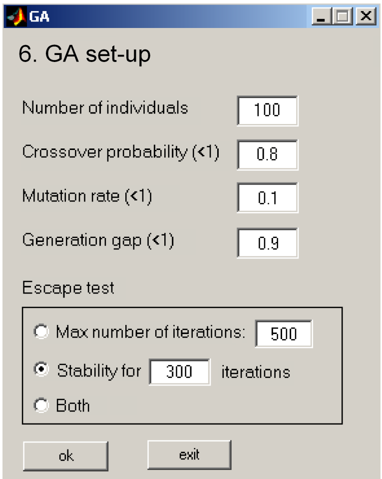

Figure A.9: GA module: the default number of individuals is automatically evaluated starting from the number of bits of the resulting chromosome.

A.2.6 Monitor module

Once the optimization set-up has been completed, the evolutive process can start and a monitoring window is displayed (Fig.A.10). In the upper part, the antenna performances to be optimized and relating to the best individual of the current generation are plotted and compared with those of the unloaded antenna system. In the central part, the histogram on the left represents the values of the objective function (which has to be minimized) of each individual of the current generation. On the right, a visualization of the individuals in the constraint space gain-vswr-efficiency is shown. In the lower part of the monitoring window the actual best fitness and the best antenna loading are represented.

A.2.7 Post-processing module

If the antenna model is built by NEC2, the post-processing module can be useful to calculate the full performances of the optimized antenna system both at a single frequency (Fig.A.11) and within a frequency range.

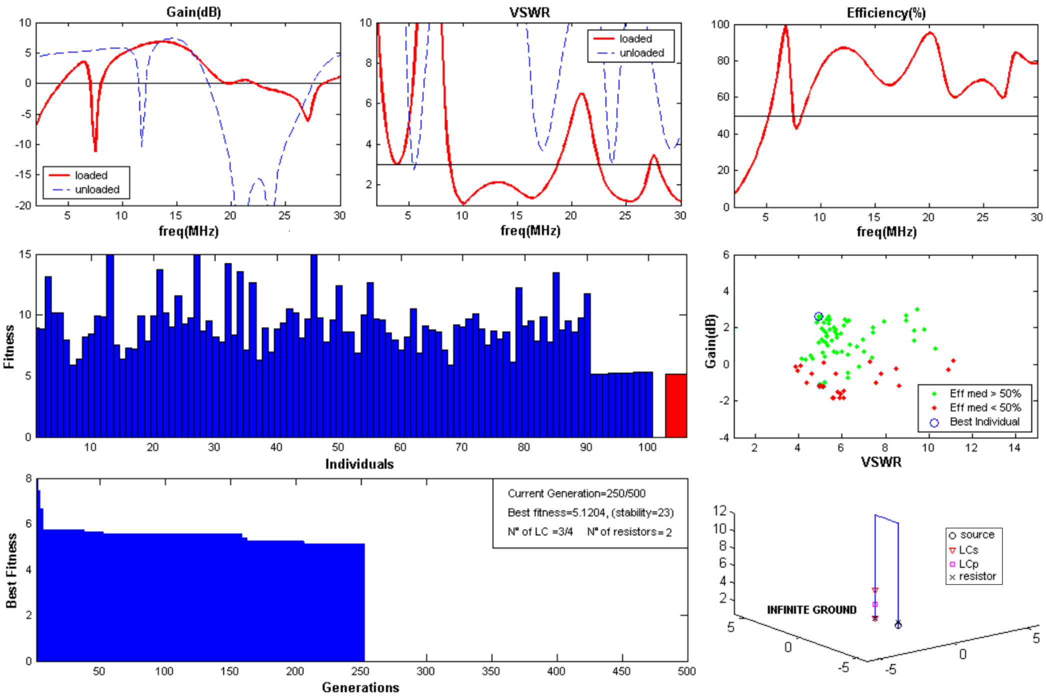

Figure A.10: Monitor module for the GA evolution control.

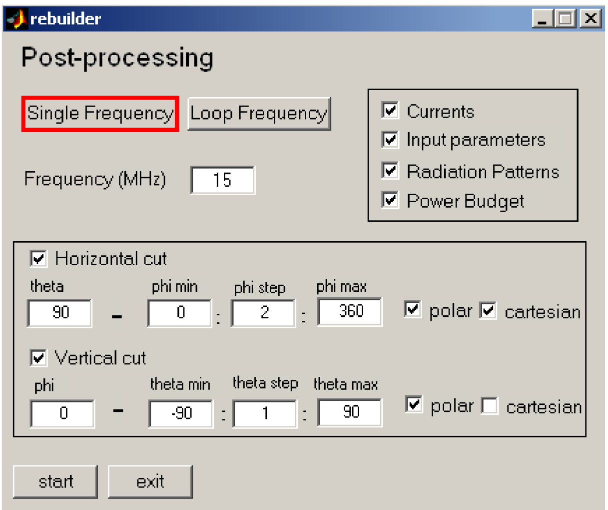

Figure A.11: Post-processing module: single frequency analysis.

A.3 Application Examples

The potentialities of *BLADE* are now discussed by means of two examples concerning the antenna optimization over mobile platforms: a medium-size ship and a vehicle. In both cases the reduced antenna port model within the complex scenario is accomplished by the NEC2 solver.

A.3.1 A broadband antenna for naval communications

The purpose of this design is to enlarge the bandwidth of a conventional HF folded monopole of height 8m when embedded into a naval scenario (Fig.A.12) maximizing, at the same time, its gain and efficiency. The antenna has been optimized in the whole 3-30 MHz range on the basis of the following requirements: VSWR<3, gain at horizon in the bow direction and efficiency higher than 0 dB and 50 %, respectively. The wire model of the ship has been borrowed, after some changes, from the 4NEC2 example catalog. The whole structure is supposed to be in aluminium and connected to a perfect ground plane simulating the sea. The folded monopole is excited by a voltage source at the base of the left vertical conductor and the loading circuits may be placed at any of the segments decomposing the antenna wires. Two 75 Ω resistors has been constrained, in the *Antenna* module of Fig.A.5, at the lower ends of the vertical conductors in order to improve the antenna bandwidth and simplify the cooling equipment. The reduced antenna port model has been generated by *BLADE* with 1 MHz frequency step. The optimizer will allocate an impedance transformer and up to 4 loads, chosen as series and parallel LC circuits. Neither a ladder lossless network nor an attenuator are considered in the *Network* module of Fig.A.7. The electrical components have been subjected, in the *Loads* module of Fig.A.6, to the following constraints: $50nH < L < 300nH$, $5pF < C < 100pF$, $0 < R < 100\Omega$. For what concerns the *Requirements* module of Fig.A.8, the VSWR has been weighed more than gain and efficiency (Fig.A.13), particularly at lower frequencies where the antenna is small with respect the wavelength and therefore rather difficult to match. The chromosome to be optimized is finally composed of 90 bits and therefore a population of 100 individuals has been chosen in the *GA* module of Fig.A.9. After 200 iterations *BLADE* has selected 3 LC traps and, as visible in Fig.A.12, two of them, on the left vertical conductor, share the same location by a series connection originating a more complex circuital topology as seen in Fig.A.2. The optimized impedance transformer value has been set to 4:1. The antenna performances, compared with those of the unloaded antenna in the same electromagnetic scenario, are shown in Fig.A.14. The VSWR is smaller than 3 all over the HF band and also the antenna gain and efficiency satisfy the requirements in almost the whole HF range. The poor performances at the lower frequencies are due to the small size of the antenna with respect to the wavelength. It has to be noted that a further improvement of the final results can be obtained by adjusting the weighing coefficients of the objective function in further optimizations. For instance, the user can try to improve the efficiency around 16 MHz by increasing the related weighing coefficient in this sub-band.

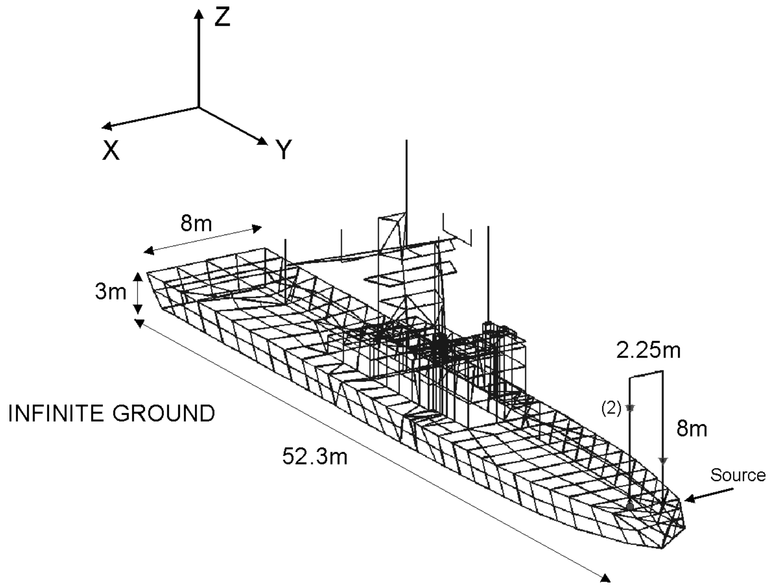

Figure A.12: Folded monopole of size 8m x 2.25m mounted on a medium-size ship. The tag '(2)' indicates that two traps have been placed by *BLADE* in the same position.

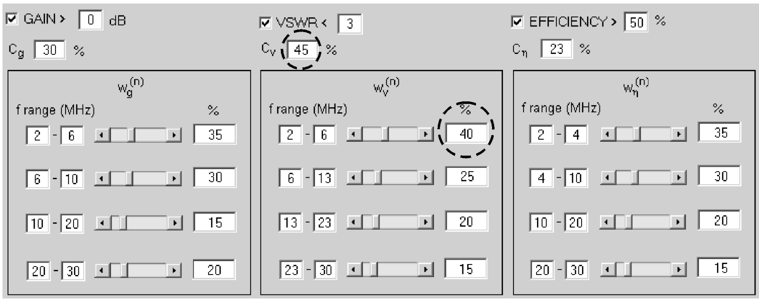

Figure A.13: Naval antenna: requirements and weighing coefficients. Additionally, $w_L = 2\%$, for the minimization of the loads number. Dashed circles highlight that the VSWR requirement has been emphasized more than the gain and the efficiency, particularly at the lower frequencies.

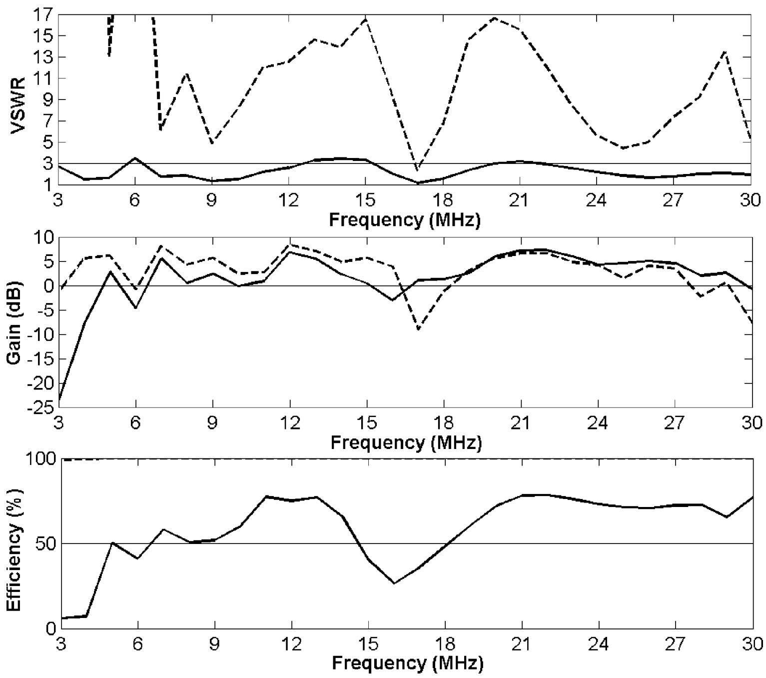

Figure A.14: Naval antenna: performances after the optimization of the loads and of the impedance transformer (solid line) compared with those of the antenna without loads and impedance transformer (dashed line). VSWR curves refer to 50Ω.

A.3.2 A dual-band antenna for vehicular communications

This example checks the potentiality of *BLADE* to design dual-band antennas. In particular, an HF monopole of height 5m mounted on the roof of a vehicle and excited at the base is considered (Fig.A.15). The antenna has been optimized in order to match the following requirements: VSWR<3, gain at horizon in the $\phi = 270°$ direction and efficiency respectively higher than 4 dB and 90 % in the non contiguous frequency ranges 13-17 MHz and 26-30 MHz. The whole antenna has been selected to host up to three lossless loading circuits (series and parallel LC traps), and the matching network has been endowed with only an hi-pass filter of the 3rd order. The ranges of the electrical components' values are the same as in the previous example. The reduced antenna port model has been generated by *BLADE* with 0.4 MHz frequency step. For what concerns the objective function, the dual-band requirements have been obtained by weighing VSWR more than gain and efficiency and by setting to zero all the weighing coefficients in the two sub-bands where the antenna is not required to communicate (10-13 MHz and 17-26 MHz), as described in Fig.A.16. Moreover, because the first resonance of the monopole ($f_0 = 15\ MHz$), where it is naturally matched, occurs in the first band to optimize, a more significant weight (60 %) has been associated to the other band. The resulting chromosome has 72 bits and therefore a population of 80 individuals has been chosen. After 100 iterations, only one parallel LC trap has been selected by the optimizer and the use of the ladder lossless network has permitted to enlarge the bandwidth of each sub-band. The antenna performances, compared with those of the unloaded antenna without matching network in the same electromagnetic scenario, are shown in Fig.A.17. VSWR shows the dual-band operation in the required frequency ranges where both the antenna gain and efficiency fully match the requirements.

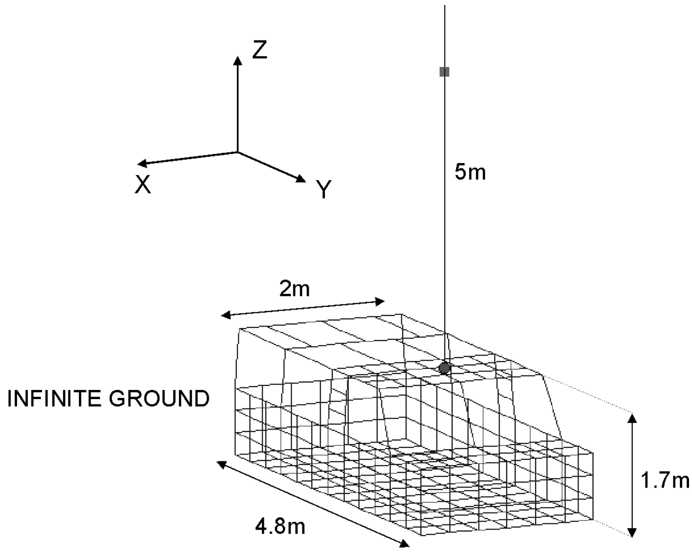

Figure A.15: Monopole of 5m on a vehicle assumed to be 0.5m upon a PEC.

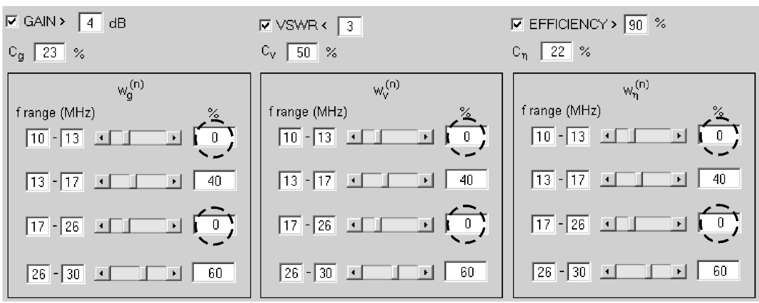

Figure A.16: Vehicular antenna: requirements and weighing coefficients to obtain a dual-band radiator. For the minimization of the loads number, $w_L = 5\%$ has been set. Dashed circles highlight that a null weight has been given to the non-interesting bands.

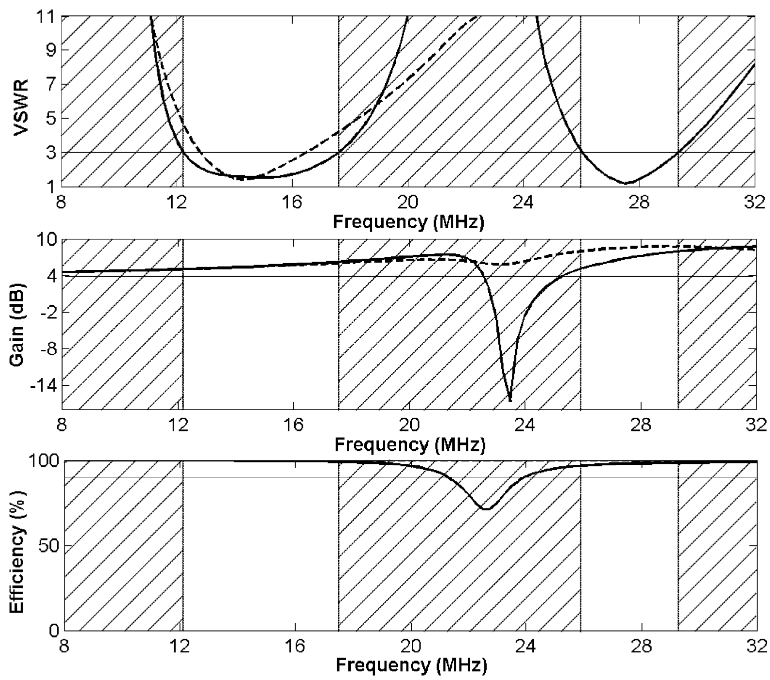

Figure A.17: Vehicular antenna: performances after the optimization of the loads and of the matching network (solid line) compared with those of the antenna without loads and matching network (dashed line). VSWR curves refer to 50Ω. The frequencies where the antenna has not been controlled by the optimizer have been shadowed.

Appendix B

Details on the penalty functions

B.1 Bifolded antenna and NSA$_1$ loading

Equations (B.1)-(B.3) define the normalized threshold functions in (3.1), while (B.4) represents the penalty associated to the number of effective loading impedances.

$$F_{VSWR}^{(n)} = \begin{cases} 0 & \text{if } VSWR^{(n)} < s_0^{(n)} \\ \frac{VSWR^{(n)} - s_0^{(n)}}{VSWR^{(n)}} & \text{otherwise} \end{cases} \tag{B.1}$$

$$F_{\eta}^{(n)} = \begin{cases} 0 & \text{if } \eta^{(n)} > \eta_0^{(n)} \\ \frac{\eta_0^{(n)} - \eta^{(n)}}{\eta_0^{(n)}} & \text{otherwise} \end{cases} \tag{B.2}$$

$$F_{G\theta}^{(n)} = \begin{cases} 0 & \text{if } G_{\theta}^{(n)} > G_{0\theta}^{(n)} \\ \frac{G_{0\theta}^{(n)} - G_{\theta}^{(n)}}{G_{0\theta}^{(n)}} & \text{otherwise} \end{cases} \tag{B.3}$$

$$F_{traps} = \frac{N_{tr}}{N_{\max}} \tag{B.4}$$

$VSWR^{(n)}$, $\eta^{(n)}$ and $G_{\theta}^{(n)}$ are the voltage standing wave ratio, efficiency and ϕ-averaged gain (linear) at elevation angle $90° - \theta$, calculated in the nth frequency sample. Generally, $s_0^{(n)}$, $\eta_0^{(n)}$and $G_{0\theta}^{(n)}$ are frequency-dependent thresholds, whose values depend on the system requirements. For what concerns equations (B.1)-(B.3), the penalty is zero when a requirement is met, otherwise the penalty linearly increases with the distance from the threshold value.

$G_\theta^{(n)}$ in (B.3) controls the ϕ-averaged gain at different elevation angles depending on the operating frequency. In (B.5), gain is optimized around the zenith at lower frequencies to achieve NVIS links, and at the horizon in the rest of the band.

$$G_\theta^{(n)} = \begin{cases} G_{10^\circ}^{(n)} & 2 \leqslant f < 10 \ (MHz) \\ G_{90^\circ}^{(n)} & 10 \leqslant f \leqslant 40 \ (MHz) \end{cases} \tag{B.5}$$

More complicated controls on gain requirements could be performed: for instance, it could be useful to simultaneously optimize the gain at two different elevation angles or to obtain a good pattern uniformity at the horizon for broadcast communications. In these cases, new functions will be defined instead of (B.3) and (B.5).

N_{tr} and N_{max} in (B.4) are, respectively, the number of loading impedances actually employed and the maximum number of loading impedances chosen.

It is worth noticing that all the functions in (B.1)-(B.4) are defined to be in the [0,1] interval.

B.2 On-PEC NSA$_N$ excitation

Equations (B.6)-(B.9) define the normalized threshold functions in (6.4) and refer to a fixed frequency.

B.2.1 Matching penalty F_{VSWR}

$$F_{VSWR} = \frac{1}{N} \sum_{i=1}^{N} p_{VSWR}^{(i)} \tag{B.6}$$

$$p_{VSWR}^{(i)} = \begin{cases} 0 & \text{if } VSWR^{(i)} < s_0 \\ \frac{VSWR^{(i)} - s_0}{VSWR^{(i)}} & \text{otherwise} \end{cases} \tag{B.7}$$

N is the number of NSA ports, $VSWR^{(i)}$ refers to the ith port and s_0 is a threshold value that has not to be exceeded.

B.2.2 Horizontal gain penalty F_{Gh}

$$F_{Gh} = \frac{1}{N_\phi} \sum_{n=1}^{N_\phi} p_{Gh}(\phi_n) \tag{B.8}$$

$$p_{Gh}(\phi_n) = \begin{cases} 0 & \text{if } (\phi_n \in BW) \cap (G_h(\phi_n) > MLL) \\ 0 & \text{if } (\phi_n \in \overline{BW}) \cap (G_h(\phi_n) < SLL) \\ \frac{MLL - G_h(\phi_n)}{MLL} & \text{if } (\phi_n \in BW) \cap (G_h(\phi_n) < MLL) \\ \frac{G_h(\phi_n) - SLL}{G_h(\phi_n)} & \text{if } (\phi_n \in \overline{BW}) \cap (G_h(\phi_n) > SLL) \end{cases} \tag{B.9}$$

N_ϕ is the number of ϕ_n points in the 2π-angle, G_h (ϕ_n) is the horizontal gain (linear) computed in the point ϕ_n, MLL and SLL are thresholds defining the desired level of the main lobe and of the side-lobes, respectively, BW defines the desired angular region for the main lobe and $\overline{BW}$ is the complementary angular region ($\overline{BW} = 2\pi - BW$) for the side-lobes (see Fig.6.4).

F_{VSWR} and F_{Gh} are defined to be in the [0,1] interval.

B.3 On-ship NSA$_N$ excitation

Equations (B.10)-(B.17) define the normalized threshold functions in (7.1) and refer to a fixed frequency.

B.3.1 Matching penalty F_S

$$F_S = \frac{1}{N_P} \sum_{i=1}^{N_P} p_S^{(i)} \tag{B.10}$$

$$p_S^{(i)} = \begin{cases} 0 & \text{if } VSWR^{(i)} < s_0 \\ \frac{VSWR^{(i)} - s_0}{VSWR^{(i)}} & \text{otherwise} \end{cases} \tag{B.11}$$

N_P is the number of excited ports, $VSWR^{(i)}$ refers to the ith port and s_0 is a threshold value that has not to be exceeded.

B.3.2 Uniformity penalty F_U

$$F_U = \begin{cases} 0 & \text{if } G_{EFF} > g_{TH} \\ \frac{g_{TH} - G_{EFF}}{g_{TH}} & \text{otherwise} \end{cases} \tag{B.12}$$

$$G_{EFF} = G_{AV} U, \qquad U = \frac{1}{N_\phi} \sum_{n=1}^{N_\phi} \delta_U(\phi_n) \tag{B.13}$$

$$\delta_U(\phi_n) = \begin{cases} 0 & \text{if } G_H(\phi_n) < \frac{G_{MAX}}{g_U} \\ 1 & \text{otherwise} \end{cases} \tag{B.14}$$

$G_H(\phi_n)$ is the horizontal gain ($\theta = 90°$) along the direction ϕ_n, G_{MAX} is the maximum value of the G_H curve and g_U is a threshold value set on the basis of the uniformity requirement with respect to the maximum gain (a typical value is $g_U = 0.1$). N_ϕ is the number of points where the azimuthal gain is evaluated, U is the pattern uniformity, i.e. the percentage of the whole azimuthal angle where G_H meets the uniformity requirement, G_{AV} is the ϕ-averaged value of G_H, and G_{EFF} is an effective average gain which correctly penalizes those patterns that, although uniform in azimuth, exhibit a low average gain. Finally, $g_{TH} = u_{TH} \cdot g_{AV}$ is a threshold value for the effective gain G_{EFF}, where u_{TH} and g_{AV} are the desired values of the pattern uniformity function U and of the average gain G_{AV}, respectively.

B.3.3 Horizontal gain penalty F_A

$$F_A = \frac{1}{N_{\Delta\phi}} \sum_{n=1}^{N_{\Delta\phi}} p_A(\phi_n) \tag{B.15}$$

$$p_A(\phi_n) = \begin{cases} 0 & \text{if } G_H(\phi_n) > g_A \\ \frac{g_A - G_H(\phi_n)}{g_A} & \text{otherwise} \end{cases} \tag{B.16}$$

$N_{\Delta\phi}$ is the number of ϕ_n points in the angular sector $\Delta\phi$, centered at the ϕ_0 direction, where the horizontal gain G_H ($\theta = 90°$) has to be maximized. g_A is a threshold value establishing the desired gain level in such an angular sector.

B.3.4 NVIS penalty F_V

The definition of F_V is the same as F_A with the NVIS gain $G_V(\phi_n)$ at $\theta = 10°$ instead of $G_H(\phi_n)$.

B.3.5 Excited ports penalty F_N

$$F_N = \frac{N_p - 1}{N - 1} \tag{B.17}$$

N_p is the number of simultaneously excited ports and N is the total number of ports of the NSA.

F_S, F_U, F_A, F_V and F_N are defined to be in the [0,1] interval.

Acknowledgments and Credits

This work has been funded by SELEX COMMUNICATIONS, a Finmeccanica Company, and has been carried on in close collaboration with the Software Defined Radio team of Mr. G. Falcione. The author wishes to thank prof. G. Marrocco, prof. F. Bardati, prof. P. Tognolatti and Mr. M. Proia for suggestions and valuable discussions. Moreover, the author wishes to mention the degree thesis of Mr. V. Martorelli, Mr. D. Di Lanzo and Ms. M. Marrocco, that he consulted and that contributed to the development of his overall research activity.

Bibliography

[1] W.E. Sabin, E.O. Schloenike, “Single-Sideband Systems and Circuits“, 2nd edition, McGraw-Hill, Technology & Industrial Arts.

[2] E. Buracchini, ”The software radio concept”, *IEEE Communications Magazine*, Vol. 38 , pp. 138-143, Sept. 2000.

[3] J. Mitola, ”The software radio architecture”, *IEEE Communications Magazine*, Vol. 33, Issue 5, pp. 26-38, May 1995.

[4] J. Mitola II and Z. Zvonar, ”Software Radio technologies”. New York: IEEE Press, 2001.

[5] W.H.W. Tuttlebee, ”Software-defined radio: facets of a developing technology”, *IEEE Personal (or Wireless) Communications*, Vol. 6, Issue 2, pp. 38-44, April 1999.

[6] Bruce A. Fette, ”Cognitive Radio Technology”, *Communications engineering series*, Newnes (Elsevier), 2006.

[7] S.R. Best, ”On the use of scale brass models in HF shipboard communication antenna design”, *IEEE Antennas and Propagation Magazine*, Vol. 44, pp. 12-22, Apr 2002.

[8] R.C. Johnson, H. Jasik, ”Antenna Engineering Handbook”, Mc Graw-Hill, New York, 1984, pp. 26-20 to 26-27.

[9] R.K. Royce, ”A compact wide-band HF transmitting antenna”, *Proc. Antennas and Propagat. Soc. Int. Symp.*, Vol.19, pp. 582-585, 1981.

[10] T.F. Kemmedy, S.A. Long, J.T. Williams, "Modification and control of currents on monopole antennas using magnetic bead loading", *IEEE Antennas and Wireless Propagat. Letters*, Vol.2, pp. 208-211, 2003.

[11] J.V.N. Granger, "Shunt-excited flat-plate antennas with applications to aircraft structures", *Proc. of IRE*, Vol.38, No.3, pp.280-287, Mar. 1950.

[12] I. Carswell, "Current distribution on wing-cap and tail-cap antennas", *IRE Trans. on Ant. and Propag.*, Vol. 3, No. 4, pp. 207-212, Oct. 1955.

[13] R.L. Tanner, "Shunt and notch-fed HF aircraft antennas", *IRE Trans. on Ant. and Propag.*, Vol. 6, No. 1, pp. 35-43, Jan. 1958.

[14] C.E. Baum, "Airframes as Antennas", *Sensor and Simulation Notes*, May 1995, Note *381*.

[15] J. Dresel, A.R. Clark and A.P.C. Fourie, "Applying soft magnetic materials to conductive surfaces to realise a novel conformal HF antenna concept", *IEEE AFRICON*, Vol. 2, pp. 1069-1074, Sept./Oct. 1999.

[16] G. Marrocco, P. Tognolatti, "New method for modelling and design of multiconductor airborne antennas", *IEE Proc.-Microw. Antennas Propag.*, Vol. 151, No. 3, June 2004, pp. 181-186.

[17] C. A. Balanis, "Antenna Theory: analysis and design", John Wiley & Sons, Second Edition, 1997.

[18] K.P. Murray, B.A. Austin, "HF antennas on vehicles - a characteristic modal approach", *IEE Colloquium on HF Antennas Systems*, pp. 2/1-2/4, Dec. 1992.

[19] R. J. Garbacz, "A generalised expansion for radiated and scattered fields", Ph.D. dissertation, The Ohio State University, 1968.

[20] M. Anstey, S.A. Saoudy, "Radiation charactersitics of a ship-mounted high frequency ground wave radar antenna", *Antennas and Propag. Soc. Int. Symp.*, Vol. 3, pp. 1852-1855, July 1996.

[21] C.E. Baum, "Ship Platform for HF/VHF Arrays", *Sensor and Simulation Notes*, August 1995, Note *383*.

[22] A. Boag, A. Boag, E. Michielssen, R. Mittra, "Design of electrically loaded wire antennas using genetic algorithms", *IEEE Trans. Antennas and Propagat.*, Vol. 44, pp. 687-695, May 1996.

[23] G.J. Burke, A.J. Poggio, "Numerical Electromagnetic Code (NEC) method of moments", pt. I, II and III, Naval Ocean Syst. Center, CA, Tech. Doc. 116, 1980.

[24] R.F. Harrington, "Field Computation by Moment Methods", Malabar, FL: Krieger, 1982, Ch. 6.

[25] F.I. Tseng, D.K. Cheng, "Pattern synthesis of circular arrays with many directive elements", *IEEE Trans. Antennas and Propag.*, pp. 758, Nov. 1968.

[26] L. Mattioni, G. Marrocco, "Design of a Broad-band HF Antenna for Multi-mode Naval Communications", *IEEE Antennas and Wireless Propagation Letters*, Vol.4, pp.179-182, 2005.

[27] G. Marrocco, L. Mattioni, F. Bardati, P. Tognolatti, G. Falcione, R. Perelli, G. Colasanti, M. Proia, "Wideband multifunction antenna operating in the HF range, particularly for naval installations", *International Patent* WO 2006/123311 A2.

[28] G. Marrocco, "Gain-optimized self-resonant meander line antennas for RFID applications", *IEEE Antennas and Wireless Propagat. Letters*, Vol.2, pp. 302-305, 2003.

[29] S. Ramo, J.R. Whinnery, T. Van Duzer, "Fields and eaves in communication electronics", Wiley & Son, New York, 1994, pp. 198-200.

[30] Z. Altman, R. Mittra and A. Boag, "New designs of ultra wide band communication antennas using a genetic algorithm", *IEEE Trans. Antennas and Propagat.*, Vol. 45, pp. 1494-1501, Oct. 1997.

[31] Y. Rahmat-Samii, E. Michielssen, "Electromagnetic Optimization By Genetic Algorithms", John Wiley & Sons, New York, 1999.

[32] L. Wanzheng, J. Yan, Y. Anmin, L. Shuanhong, "A Novel Short-Wave Broadband Antenna", *IEEE Ant., Prop. and EM Theory*, 5th Int. Symp., pp. 366-369, ISAPE 2000.

[33] L. Januszkiewicu, S. Hausman, "Combined Spiral-Discone Broadband Antenna for indoor applications", *IEEE Personal, Indoor and Mobile Radio Comms (PIMRC)*, 15th Int. Symp., Vol. 1, pp. 422-426, Sept. 2004.

[34] L. Mattioni, G. Marrocco, "Design of a Broad-band HF Antenna for multi-mode Naval Communications – Part II: Extension to VHF/UHF ranges", *IEEE Antennas and Wireless Propagation Letters*, Vol. 6, pp. 83-85, 2007.

[35] G. Marrocco, L. Mattioni, "Naval Structural Antenna Systems for Broadband HF Communications", *IEEE Trans. on Antennas Propagat.*, Vol. 54, No. 4, pp. 1065-1073, April 2006.

[36] G. Marrocco, L. Mattioni, F. Bardati, P. Tognolatti, G. Falcione, R. Perelli, G. Colasanti, M. Proia, "Wideband structural antenna operating in the HF range, particularly for naval installations", *International Patent* WO 2006/134543 A1.

[37] G.V. Borgiotti, Q. Balzano, "Mutual coupling analysis of a conformal array of elements on a cylindrical surface", *IEEE Trans. on Ant. and Propag.*, Vol. AP-18, No. 1, pp. 55-63, Jan. 1970.

[38] Yoon-Won Kang, D.M. Pozar, "Correction of error in reduced sidelobe synthesis due to mutual coupling", *IEEE Transactions on Antennas and Propagation*, Vol. 33, Issue 9, pp. 1025-1028, Sep. 1985.

[39] R.G. Rojas, Y.C. Chen, "Improved computer simulation of the TCAS III circular array mounted on an aircraft", *Antennas and Propagation Society International Symposium*, Vol. 3, pp. 1200-1203, 26-30 Jun. 1989.

[40] R. Vescovo, "Constrained and unconstrained synthesis of array factor for circular arrays", *IEEE Transactions on Antennas and Propagation*, Vol. 43, Issue 12, pp. 1405-1410, Dec. 1995.

[41] P. Ioannides, C.A. Balanis, "Uniform circular arrays for smart antennas", *IEEE Antennas and Propagation Magazine,* Vol. 47, Issue 4, pp. 192-206, Aug. 2005.

[42] H. Steyskal, "Circular array with frequency-invariant pattern", *Antennas and Propagation Society International Symposium*, Vol.3, pp. 1477-1480, 26-30 June 1989.

[43] N. Goto, Y. Tsunoda, "Sidelobe reduction of circular arrays with a constant excitation amplitude", *IEEE Transactions on Antennas and Propagation*, Vol. 25, Issue 6, pp. 896- 898, Nov. 1977.

[44] F. Watanabe, N. Goto, A. Nagayama, G. Yoshida, "A pattern synthesis of circular arrays by phase adjustment", *IEEE Transactions on Antennas and Propagation*, Vol. 28, Issue 6, pp. 857-863, Nov. 1980.

[45] You Chung Chung, R.L. Haupt, "GAs using varied and fixed binary chromosome lengths and realchromosomes for low sidelobe spherical-circular array pattern synthesis", *Antennas and Propagation Society International Symposium*, Vol. 2, pp. 1030-1033, 16-21 Jul. 2000.

[46] P. Hannan, D. Lerner, G. Knittel, "Impedance matching a phased-array antenna over wide scan angles by connecting circuits", *IEEE Transactions on Antennas and Propagation*, Vol. 13, Issue 1, pp. 28-34, Jan 1965.

[47] M.G. Bray, D.H. Werner, D.W. Boeringer, D.W. Machuga, "Matching network design using genetic algorithms for impedance constrained thinned arrays", *IEEE Antennas and Propagation Society International Symposium*, Vol. 1, pp. 528-531, June 2002.

[48] W. Kahn, "Impedance-match and element-pattern constraints for finite arrays", *IEEE Transactions on Antennas and Propagation*, Vol. 25, Issue 6, pp. 747-755, Nov. 1977.

[49] M. Shimizu, "Determining the excitation coefficients of an array using genetic algorithms", *IEEE Antennas and Propagation Society International Symposium*, Vol. 1, pp. 530-533, June 1994.

[50] O.M. Bucci, G. Franceschetti, G. Mazzarella, G. Panariello, "A general projection approach to array synthesis", *Antennas and Propagation Society International Symposium*, Vol. 1, pp. 146-149, 26-30 Jun 1989.

[51] O.M. Bucci, G. Franceschetti, G. Mazzarella, G. Panariello, "Intersection approach to array pattern synthesis", *IEE Proceedings of Microwaves, Antennas and Propagation*, Vol. 137, Issue 6, pp. 349-357, Dec. 1990.

[52] G. Marrocco, L. Mattioni, V. Martorelli, "Naval Structural Antenna Systems for Broadband HF Communications - Part II: Design Methodology for Real Naval Platforms", *IEEE Trans. on Antennas Propagat.*, Vol. 54, No. 11, pp. 3330-3337, Nov. 2006.

[53] C.C. Lu & W.C. Chew, "A multilevel algorithm for solving boundary-value scattering", *Micro. Opt. Tech. Lett.*, Vol. 7, No. 10, pp. 466-470, July 1994.

[54] "FEKO User's Manual, Suite 5.1", EM Software & Systems-S.A. (Pty) Ltd., Stellenbosch, South Africa, Dec. 2005, http://www.feko.info.

[55] L. Mattioni, G. Marrocco, D. Di Lanzo, "Naval Structural Antenna Systems for broadband HF communications – part III: Experimental evaluation on scale prototypes, to appear on *IEEE Transactions on Antennas and Propagation*.

[56] A. Taflove, "Advances in Computational Electrodynamics: The Finite-Difference Time-Domain Method", Artech House, Norwood, MA, 1998.

[57] T. Macnamara, "Handbook of Antennas for EMC", Artech House Publishers, 1995, Boston-London, Chapter 4, pp.253-260, pp.112.

[58] J.H. Kim, J. Il Park, "Development of standard monopole antenna for antenna factor measurement", *Proceedings of International Symposium on Electromagnetic Compatibility*, pp. 134-137, 21-23 May 1997.

[59] http://home.ict.nl/˜arivoors/

[60] www.supernec.com

[61] L. Mattioni, G. Marrocco, "*BLADE*: A Broadband Loaded Antennas DEsigner", *IEEE Antennas and Propagat. Magaz.*, Vol. 48, Issue 5, pp. 120-129, Oct. 2006.

[62] D.D. Reuster, K.J. Cybert, "A High-Efficiency Broadband HF Wire-Antenna System", *IEEE Antennas and Propagat. Magaz.*, Vol. 42, No. 4, pp. 53-61, Aug 2000.

[63] D.L. Smith, "The Trap-Loaded Cylindrical Antenna", *IEEE Trans. Antennas and Propagat.*, Vol. 23, No. 1, pp. 20-27, Jan. 1975.

[64] K. Yegin and A.Q. Martin, "Very broadband loaded monopole antennas", Department of Electrical and Computer Engineering, Clemson University, Clemson, SC29634.

[65] S.D. Rogers, C.M. Butler, A.Q. Martin, "Design and Realization of GA-Optimized Wire Monopole and Matching Network With 20:1 Bandwidth", *IEEE Trans. Antennas and Propagat.*, Vol. 51, No. 3, pp. 493-502, March 2003.

[66] H.A. Wheeler, "Small Antennas", *IEEE Trans. Antennas and Propagat.*, vol. 23, No. 4, pp. 462-469, July 1975.

[67] H.A. Wheeler, "Fundamental Limitations of Small Antennas", *Proceedings of the I.R.E.*, pp. 1479-1484, Dec. 1947.

[68] P.L. Werner, D.H. Werner, "Design Synthesis of Miniature Multiband Monopole Antennas With Application to Ground-Based and Vehicular Communication Systems", *IEEE Antennas and Wireless Propagat. Letters*, Vol. 4, pp. 104-106, 2005.

[69] T. Jagannath, P.P. Kulkarni, V.M. Tyagi, "HF Broadband Antenna Design Considerations on Warships", Naval EMC Centre, Mumbai, India, *Proceedings of the International Conference on Electromagnetic Interference and Compatibility '97*, pp.421-428.

[70] http://www.mathworks.com/

Publications and Conferences

International Journal Contributions

L. Mattioni, G. Marrocco, "Design of a Broadband HF Antenna for Multimode Naval Communications", *IEEE Antennas and Wireless Propagation Letters*, Vol. 4, pp. 179-182, 2005.

G. Marrocco, L. Mattioni, "Naval Structural Antenna Systems for Broadband HF Communications", *IEEE Transactions on Antennas and Propagation*, Vol. 54, No. 4, pp. 1065-1073, April 2006.

G. Marrocco, L. Mattioni, V. Martorelli, "Naval Structural Antenna Systems for Broad-band HF Communications – Part II: Design methodology for real naval platforms", *IEEE Transactions on Antennas and Propagation*, Vol. 54, No.11, pp. 3330-3336, Nov. 2006.

L. Mattioni, G. Marrocco, "BLADE: A Broadband Loaded Antenna DEsigner", *IEEE Antennas and Propagation Magazine,* Vol. 48, No. 5, pp. 120-129, Oct. 2006.

L. Mattioni, G. Marrocco, "Design of a Broad-band HF Antenna for multi-mode Naval Communications – Part II: Extension to VHF/UHF ranges", *IEEE Antennas and Wireless Propagation Letters*, Vol. 6, pp. 83-85, 2007.

L. Mattioni, G. Marrocco, D. Di Lanzo, "Naval Structural Antenna Systems for broadband HF communications – part III: Experimental evaluation on scale prototypes, to appear on *IEEE Transactions on Antennas and Propagation.*

International Congress Contributions

L. Mattioni, G. Marrocco, "New multi-function broadband antennas for HF naval communications", *IEEE AP-S International Symposium and USNC/URSI National Radio Science Meeting*, Washington DC, Washington, 3-8 July 2005.

G. Marrocco, L. Mattioni, "The concept of multi-port structural antenna system for HF naval communications", *IEEE Antennas and Propagation Society International Symposium,* Albuquerque, New Mexico, 9-14 July 2006, pp. 2243-2246.

L. Mattioni, G. Marrocco, G. Falcione, "The Bifolded antenna for Software Defined Radio Naval Systems", *IET / IRST 2006 (10th conference on Ionospheric Radio System & Tecniques),* London, England, 18-21 July, pp. 54-58, 2006.

G. Marrocco, L. Mattioni, G. Falcione, "Making multi-port Broadband Structural HF Antennas out of Naval superstructures", *IET / IRST 2006 (10th conference on Ionospheric Radio System & Tecniques),* London, England, 18-21 July 2006, pp.59-63.

L. Mattioni, G. Marrocco, "Design, analysis and experimental evaluation of a new broadband antenna for naval systems", *23rd International Review of Progress in Applied Computational Electromagnetics (ACES),* Verona, Italia, 19-23 March 2007, pp. 1773-1778.

L. Mattioni, D. Di Lanzo, G. Marrocco, "Theory, Design and Testing of the Broadband Naval Structural Antenna", *2nd European Conference on Antennas and Propagation (EuCAP),* Edinburgh, Scotland, Fr2.6.9, 11-16 Nov 2007.

National Congress Contributions

L. Mattioni, G. Marrocco "Sintesi di antenne navali HF a banda ultralarga", *XV RiNem 2004 (Riunione Nazionale di Elettromagnetismo),* Cagliari, Italia, 13-16 Sep 2004, pp. 93-96.

L. Mattioni, G. Marrocco, "Nuove antenne HF a larga banda per comunicazioni navali", congress organized by Mariteleradar, '*Telemil05: nuovi sviluppi tecnologici nelle telecomunicazioni e possibili applicazioni militari'*, Livorno, Italia, 15-16 June 2005.

M. Ciattaglia, L. Mattioni, G. Marrocco, "Analisi e sintesi di antenne a banda larga e ultra larga", *Assemblea SIEM (presentazione dell'attività di ricerca delle sedi),* Torino, Italia, 11-13 Sep 2005.

L. Mattioni, G. Marrocco "Antenne navali strutturali a larga banda", *XVI RiNem 2006 (Riunione Nazionale di Elettromagnetismo),* Genova, Italia, pp. 29-32, 18-21 Sep 2006.

G. Marrocco, L. Mattioni, D. Di Lanzo, F. Bardati, "Array navali strutturali a larga banda per sistemi Software Defined Radio", *XIII giornata di studio sull'ingegneria delle microonde – progettazione e sviluppo di moderni sistemi d'antenna (EIEm),* Fisciano (SA), Italia, 14-15 May 2007, pp.165-168.

Technical Reports

L. Mattioni, G. Marrocco, "Sintesi di antenne filari a larga banda per comunicazioni navali", Università "Tor Vergata" (DISP), Roma, Italia, *RR-04.49* (ING-INF/02), Mar. 2004.

D. Scarana, G. Marrocco, L. Mattioni, "Nuove antenne per comunicazioni veicolari", Università "Tor Vergata" (DISP), Roma, Italia, *RR-06.56* (ING-INF/02), Nov. 2006.

L. Mattioni, G. Marrocco, "Antenna multi-banda per terminali mobili", Università "Tor Vergata" (DISP), Roma, Italia, *RR-06.57* (ING-INF/02), Nov. 2006.

Intenational Patents

G. Marrocco, L. Mattioni, F. Bardati, P. Tognolatti, G. Falcione, R. Perelli, G. Colasanti, M. Proia, "Wideband structural antenna operating in the HF range, particularly for naval installations", WO 2006/134543 A1.

G. Marrocco, L. Mattioni, F. Bardati, P. Tognolatti, G. Falcione, R. Perelli, G. Colasanti, M. Proia, "Wideband multifunction antenna operating in the HF range, particularly for naval installations", WO 2006/123311 A2.